# MICROSTRUCTURAL CHARACTERISATION AND MODELLING

# OF DILUTE MAGNESIUM-TIN-ALUMINIUM ALLOYS



BY

## GARETH DOUGLAS

A thesis submitted to the University of Birmingham for the degree of

## DOCTOR OF PHILOSOPHY

**School of Metallurgy and Materials**

**College of Engineering and Physical Science**

**University of Birmingham**

**September 2017**

# UNIVERSITY OF BIRMINGHAM

**University of Birmingham Research Archive**

**e-theses repository**

Thank you to my two families.
The one I was given and the one I made along the way.


For my Grandmother who passed away shortly after my Viva.

# UNIVERSITY OF BIRMINGHAM

# RESEARCH THESIS
## *Author's Declaration*

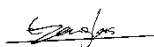**Full name** (block capitals, surname first): DOUGLAS, GARETH JAMES MEREDITH

**Full title of thesis/dissertation** (block capitals): MICROSTRUCTURAL CHARACTERISATION AND MODELLING OF DILUTE MAGNESIUM-TIN-ALUMINIUM ALLOYS

**College/School/Department** (block capitals): SCHOOL OF METALLURGY AND MATERIALS

**Date of award of degree** (leave blank):

1. I understand that one printed and one electronic copy of my thesis/dissertation (the Work) will be deposited in the University Library (the Library) and in a suitable electronic repository, for permanent retention.
2. Without changing the content, the Library or any third party with whom it has an agreement to do so, may convert either copy into a format or medium for the purpose of long-term retention, accessibility and preservation.
3. The Library will publish, and/or arrange with appropriate third parties for the non-exclusive publication of, a bibliographic description of the thesis/dissertation, and the author's abstract.
4. Unless arrangements are made to the contrary, (see paragraph 6. below), the Library is authorised to make the Work available for consultation in the Library, and via a recognised inter library loans system. The Library is authorised to make the electronic copy of the Work freely accessible to individuals and institutions - including automated agents - via the Internet.
5. Rights granted to the University of Birmingham through this agreement are entirely non-exclusive. I retain all my rights in the Work in its present version or future derivative works.
6. I understand that I may apply to the University to retain the right to withhold access to the content of my thesis/dissertation. Access to the paper version may be withheld for a period which shall not normally exceed four calendar years from the congregation at which the degree is conferred. The actual length of the period will be specified in the application, together with the precise reasons for making that application. The electronic copy may be withheld from dissemination via the web or other networks for any period.
7. I have obtained permission for any use made of substantial amounts of published or unpublished copyright material (text, illustrations, etc) where the rights are owned by a third party, other than as permitted under either The Copyright Designs and Patents Act 1988 (as modified by any related or successor legislation) or the Terms and Conditions of any Licence governing its use.
8. The content of the copies I shall deposit with the Library will be the final version of my thesis, as approved by the Examiners.
9. I understand that the Library and administrators of any electronic theses repository do not hold any obligation to take legal action on behalf of myself, or other rights holders, in the event of a breach of intellectual property rights, or any other right, in the material deposited.
10. I understand that, in the event of my thesis/dissertation being not approved by the Examiners, this declaration will become null and void.

**Signature:** *(signature)*         **Date: 18/05/18**

---

# ABSTRACT

The ageing process of two magnesium alloys with compositions of Mg-1.75Sn-1.93Al and Mg-1.29Sn-2.85Al(at%) have been investigated. Three ageing times, 40, 72 and 160 hrs, were selected to correspond to the early growth, peak hardness and coarsened stage of the alloys and the hardness measured. Subsequently, the precipitates in the alloys have been classified by 4 morphologies, basal plates, $\langle 11\bar{2}0 \rangle$ laths, pyramidal laths and prismatic rods. and identified as Mg$_2$Sn before the number density and size of the precipitates was measured. This has been achieved through a combination of X-ray Diffraction, Scanning Electron Microscopy and Transmission Electron Microscopy. Moreover, an Orientation Relationship of $(0001)_{\alpha}//(111)_{\beta}, [11\bar{2}0]_{\alpha}//[110]_{\beta}$ was found to be common to three of the four morphologies with the pyramidal laths not conforming to a well-defined orientation relationship. This is then linked through observation to the lack of a common habit plane or growth direction for these pyramidal precipitates.

The obtained data has then been used to model the nucleation and growth of the precipitates using a Kampmann-Wagner Numerical framework, where key parameters such as the diffusion rate of Sn and the interfacial energy of the precipitates were fitted. This leads into a simulated strength against the ageing time which has been compared to the initial hardness measurements made. This has good agreement with not only the overall number density and precipitate sizes but also the size distribution of the precipitates

The effect of the two microstructures on the differing mechanical properties has been discussed, highlighting the importance of number density over the different precipitate morphologies observed, and future experiments outlined.

# Table of Contents

# List of abbreviations and symbols

| | | | |
|---|---|---|---|
| ASTM | American Society for Testing and Materials | LSW | Lifshitz-Slyozov-Wagner |
| BCC | Body Centred Cubic | OR | Orientation Relationship |
| BSE | Backscatter Electron | RE | Rare Earth |
| CBED | Convergent Beam Electron Diffraction | SADP | Selected Area Diffraction Pattern |
| CCD | Charge coupled device | SAED | Selected Area Electron Diffraction |
| CP | Continuous Precipitate/Precipitation | SE | Secondary Electron |
| CRSS | Critically Resolved Shear Stress | SEM | Scanning Electron Microscope/Microscopy |
| DP | Discontiuous Precipitate/Precipitation | STEM | Scanning Transmission Electron Microscope/Microscopy |
| EDX | Energy Dispersive X-ray Spectroscopy | TEM | Transmission Electron Microscope/Microscopy |
| EELS | Electron Energy Loss Spectroscopy | UTS | Ultimate Tensile Stress |
| FCC | Face Centred Cubic | XRD | X ray Diffraction |
| FIB | Focused Ion Beam | YS | Yield Stress |
| HAADF | High Angle Annular Dark Field | ZA | Zone Axis |
| HCP | Hexagonal Close Packed | α Phase | Magnesium |
| HOLZ/LOLZ | High/Low Order Laue Zone | β Phase | $Mg_2Sn$ |
| KM | Kossel-Mollenstedt | γ Phase | $Mg_{17}Al_{12}$ |
| KWN | Kampmann-Wagner Numerical | | |

| | | | |
|---|---|---|---|
| $A, A'$ | Aspect Ratio | $l$ | Length |
| $a, b$ | constants | $l_c$ | Capillary Length |
| $A_j$ | Absorption Factor | $L$ | Load |
| $\boldsymbol{b}$ | Burgers vector | $L_k$ | Lorentz Polarisation factor |
| $C_{44}$ | Elastic Constant | $M$ | Taylor Factor |
| $C_i$ | Concentration | $N_{v/a}$ | Number Density (Volume/Area) |
| $\Delta C_k$ | Gibbs Thompson additional factor | $P_{mn}$ | Preferred Orientation Factor |
| $d$ | Planar spacing | $Q_d$ | Activation Energy for Nucleation |
| $d_{hkl}$ | Planar spacing of plane hkl | $r$ | Radius of a precipitate |
| $d_p$ | Precipitate diameter | $r_c$ | Radius of curvature |
| $D_p$ | Critical Particle Diameter | $R_g$ | Universal Gas Constant |
| $D_0$ | Diffusion Rate | $R_{SA}$ | Ratio of surface areas |
| $dr/dt$ | Growth rate | $s_i$ | Deviation Parameter |
| $f$ | Volume Fraction | $S_m$ | Peak Shape factor |
| $f_j$ | fitted volume fraction of phase j | $t_p$ | Precipitate thickness |
| $F_{m,n}$ | Structure factor | $T$ | Temperature |
| $g_\oplus$ | Acceleration due to Earth's Gravity | $V_j$ | Volume of unit cell of phase j |
| $g$ | Primitive cell factor | $V_m$ | Molar Volume |
| $G$ | Shear Modulus | $W$ | Least Squares Fitting Parameter |
| $\Delta G$ | Gibbs Free Energy | $x, y$ | Cartesian Co-ordiantes |
| $\Delta G*$ | Critical Gibbs Free energy | $Z$ | Zeldovich Factor |
| $hkl$ | Miller indices | $\beta$ | Beta Factor |
| $H_v$ | Vickers Hardness | $\gamma$ | Surface energy |
| $I/I_0$ | Nucleation Rate/Initial Nucleation Rate | $\varepsilon$ | Misfit Strain |
| $I_i$ | X-Ray intensity (XRD) | $\theta_B$ | Bragg's Angle |
| $j$ | Phase index | $\lambda$ | Mean precipitate spacing |
| $k$ | Arbitrary constant | $\nu$ | Poissons ratio |
| $k_B$ | Boltzmann's constant | $\xi$ | Extinction distance |

| | | | |
|---|---|---|---|
| $\sigma$ | Stress component | $\tau_i$ | Incubation time |
| $\tau$ | Critically Resolved Shear Stress | $\Omega$ | Supersaturation factor |

# 1 INTRODUCTION

Magnesium (Mg), highly reactive, relatively weak and easily corroded, does not seem like the most obvious construction material, but its intrinsic low specific gravity ($1.738kg/m^3$) makes it a potentially fantastic base for alloys where low weight is paramount, such as in the aerospace or automotive industries. Not existing in its pure form naturally, magnesium was first isolated in 1808 by Sir Humphrey Davis using electrolysis. Burning with a brilliant white light, it was initially used as an incendiary in flashbulbs and pyrotechnics up until the turn of the 20th century and the advent of the aeroplane.

Due to the poor power output of early aircraft engines, weight reduction was of vital importance. Elektron was the first alloy widely used, developed in 1910 by Gustav Pistor and Wilhelm Moschel with an initial composition of approximately 90wt% Mg, 9wt%Al with the remaining 1wt% being other components- surprisingly close to AZ91 which remains the most popular magnesium alloy by usage[1]. Early magnesium alloys were extremely volatile at high temperatures, with fires not uncommon in aeroplanes, yet despite this it was used throughout the 1930s, 40s and 50s in aerospace and the high performance automobile industry before being dropped in favour of cheaper aluminium alloys[2], and reduced to a supporting component in alloys such as Birmabright (1-7wt% Mg, 90+wt% Al) and Magnalium (between 5 and 50wt% magnesium, balance aluminium with trace amounts of Copper, Nickel and Tin)[3]. It is still commonly used in Al alloys (primarily 5xxx and 6xxx series as well as 2xxx, 3xxx, 7xxx to a lesser extent) to improve ductility and the alloys' age hardening response[4,5] as well as being used to remove sulphur from iron melts[6].

Despite magnesium's early adoption, it still falls far behind aluminium and steel in terms of usage as a construction material but since the early 1990's it is increasingly being thrust to the forefront of lightweight materials research due to rising fears over climate change and dwindling fossil fuel reserves. Greater research interest has led to improved corrosion resistance[7–9], improved strength[10,11] and, critically, reduced flammability.[9,12,13] For example in 2014 it was deregulated for use in commercial aircraft after being proven to be sufficiently resistant to flames. Similarly, magnesium is now recognised as having a huge potential as a material for biocompatible implants.[14–17]

Unfortunately, the reactive nature of magnesium means a cover gas, typically the environmentally unfriendly $SF_6$, must be used to prevent oxidation of the melt, meaning that large-scale castings are restricted. The $SF_6$ itself is a potent greenhouse gas, 23,900 times more harmful than $CO_2$ and research is on going into greener alternatives.[18]

Magnesium alloys are now categorised via an ASTM standard rather than their historic names. This consists of a prefix of letters denoting the main alloying elements in order of highest quantity by weight, followed by numbers representing the approximate weight percentage of each. Similarly a suffix is sometimes added to indicate the ageing condition. This is summarised in Table 1.1.

This chapter will briefly introduce the key aspects surrounding magnesium alloys including their structure, deformation behaviour and common alloying elements before detailing current research surrounding the magnesium tin alloys that are the focus of the following work.

**Table 1.1** *ASTM standard references for magnesium alloys*[2]*.*

| | Element | | Element | | Heat Treatment |
|---|---|---|---|---|---|
| A | Aluminium | M | Manganese | F | As Fabricated |
| C | Copper | Q | Silver | 0 | Annealed |
| D | Cadmium | R | Chromium | H | Strain Hardened by cold work |
| E | Rare Earths | S | Silicon | | |
| F | Iron | T | Tin | H1 | Strain Hardened only |
| J | Strontium | W | Yttrium | | |
| K | Zirconium | X | Calcium | T | Heat Treated |
| L | Lithium | Z | Zinc | W | Solution Treated |

# 2 LITERATURE REVIEW

This is an introduction to the state of research on magnesium alloys with a focus on, initially, the current approach to alloys for elevated temperature applications, before discussing the use of Sn as both an addition to current magnesium alloys and part of a new generation of Mg-Sn alloys. Mg-Sn-Al alloys like those investigated in this study are being considered as an alternative to currently available magnesium alloys. This is particularly important where temperatures above 100°C are encountered as alloys such as the AZ series suffer from a sharp loss of mechanical strength above this temperature. Mg-Sn alloys contain $Mg_2Sn$ precipitates that do not suffer this same issue, however they grow at a rate that is prohibitively slow in the binary alloy. Mg-Sn-Al ternaries have been shown to age more rapidly. This will be investigated on a microscopic scale in order to understand why ageing is more favourable. Three factors affect the strengthening that precipitates provide in Mg alloys, namely the number density of precipitates, their size and lastly their morphology[10,19,20].

Beginning with the morphology, the orientation relationship of different morphologies will be observed using Transmission Electron Microscopy (TEM) to link the different species of precipitates and compare this to observations in the literature of both the binary and ternary alloys. Moreover, measurements of the precipitates size and number density will be made via a variety of techniques in order to compare this to measured hardness of the alloys. This will also inform a model of the microstructure developed as part of the work. The aim is to provide better understanding of the factors effecting the morphology, growth rate and number density of precipitates to better inform the development of age hardened Mg-Sn-Al alloys.

## 2.1 Structure and Strengthening Mechanisms of Magnesium

Magnesium takes a hexagonal close packed (H.C.P.) structure, with lattice parameter a= 0.32092 nm, and a/c ratio of 1.624[18,21], close to the perfect ratio at room temperature. With lower symmetry than face centred cubic(F.C.C.) and body centred cubic (B.C.C.) systems, the number of slip systems is limited, contributing to low ductility in magnesium. The most common deformation mechanism is basal glide. This occurs through the <a> type dislocation: $(0001)\frac{1}{3}\langle11\bar{2}0\rangle$. Non basal slip systems are possible, with the first order prismatic $\{1\bar{1}00\}\frac{1}{3}\langle11\bar{2}0\rangle$ and pyramidal slip $\{1\bar{1}01\}\frac{1}{3}\langle11\bar{2}0\rangle$ both occurring, again via <a> type dislocations [21,22]. These are detailed below in Table 2.1 and Fig 2.1 While the slip planes rely on the same type of dislocation, they are not equally common; this is dictated by the critical shear stress, $\tau$ [23]. Very simply put, the stress required to activate a slip system is inversely proportional to the spacing between the planes, $a$, on which the glide occurs due to the lesser interaction between the individual atoms[24]. This is given by the theoretical critical shear stress, with the Burgers vector, $b$, and the shear modulus, $G$, acting as proportionality factors for different materials:

$$\tau = \boldsymbol{b}.\frac{G}{2\pi}.a \qquad\qquad [2.1]$$

The basal plane, being easily the most widely spaced, is the most common slip system in magnesium, with the prismatic plane requiring a critical resolved shear stress (CRSS) around 100 times greater than basal slip, though at 300°C the required CRSS drops to only four times greater than that for basal slip [25,26]. This gives an explanation for the increased ductility of magnesium at higher temperatures, at which it is typically wrought to produce a final product, as further slip systems are more easily activated.

Strain along the <c> direction cannot be accommodated by <a> type dislocations: this

gives rise to the <c+a> type dislocations[27], which have been found on the first order $\{10\bar{1}1\}\langle11\bar{2}3\rangle$[28,29] and second order $\{11\bar{2}2\}\langle11\bar{2}3\rangle$ pyramidal planes[29,30]. However these are rarely seen[30] in magnesium or other H.C.P. materials such as titanium; instead twinning is preferred due to the relatively lower activation energy.

Therefore only 2 independent slip systems (as the third is simply the combination of the first two) are present in magnesium at room temperature. Thus considering the von Mises criterion for deformation[31], only when <c+a> pyramidal slip or twinning is activated can we consider that the material is fully ductile.

***Table 2.1:*** *Summary of slip modes in magnesium. The crystallographic elements give the plane in which the slip occurs and the direction.*

| Direction | Plane | Crystallographic Element | Number of Independent Modes |
|---|---|---|---|
| | Basal Slip | $(0001)\langle11\bar{2}0\rangle$ | 2 |
| a | Prismatic Slip | $\{1\bar{1}00\}\langle11\bar{2}0\rangle$ | 2 |
| | Pyramidal Slip | $\{1\bar{1}0l\}\langle11\bar{2}0\rangle$ | 4 |
| c+a | Pyramidal Slip | $\{hkil\}\langle11\bar{2}3\rangle$ | 5 |
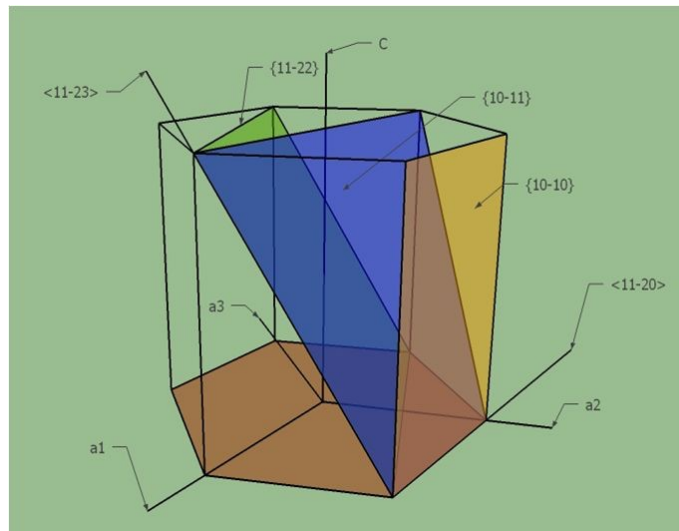


***Fig 2.1*** *Slip systems in H.C.P.*

Temperature is not the sole determining factor[26,32–35] for the CRSS needed to activate the various slip planes. It is very rare for metals used in everyday applications not to include several different elements. While magnesium alloys are somewhat less diverse than the broad array of steels or aluminium (Al) alloys on offer, there still is a wide variety of alloys, each with its own strengths and weaknesses. One of the main benefits of alloying, aside from solute strengthening, is the appearance of second phases and precipitates. Much study has been dedicated to understanding the precipitation process both as a result of solidification and after artificial ageing processes. Below is a brief introduction to magnesium alloys and their mechanical properties followed by a review of the effects different elements have when added to magnesium (Mg) with emphasis on those seen in ternary alloys with magnesium and tin (Sn). Ultimately it is my aim to investigate the precipitation mechanisms in dilute Mg-Sn-Al ternary alloys.

## 2.2 Macroalloying of Magnesium - Aluminium and Zinc

Most commonly, magnesium is alloyed with aluminium, as shown by the fact it is the major component in both the AZ and AM series. Al is known to increase castability and corrosion resistance and to contribute to strengthening in solid solution[33,36]. Soluble up to 11.6% at 710K[37] but rapidly dropping to 2.9% at 473K, as shown by the Mg-Al binary phase diagram in Fig.2.2, Al forms a $Mg_{17}Al_{12}$ ($\gamma$) precipitate when aged. This possesses a B.C.C. structure with space group $I\bar{4}3m$ and lattice parameter a=1.056 nm. The $\gamma$ phase forms different precipitate morphologies that fall into two main categories, continuous and discontinuous, which form competitively depending on the Al content of the alloy and ageing temperature. The ageing conditions[38–40] as well as pre-processing[41,42] and microalloying[43–49], determine the relative abundance of each category of precipitate.
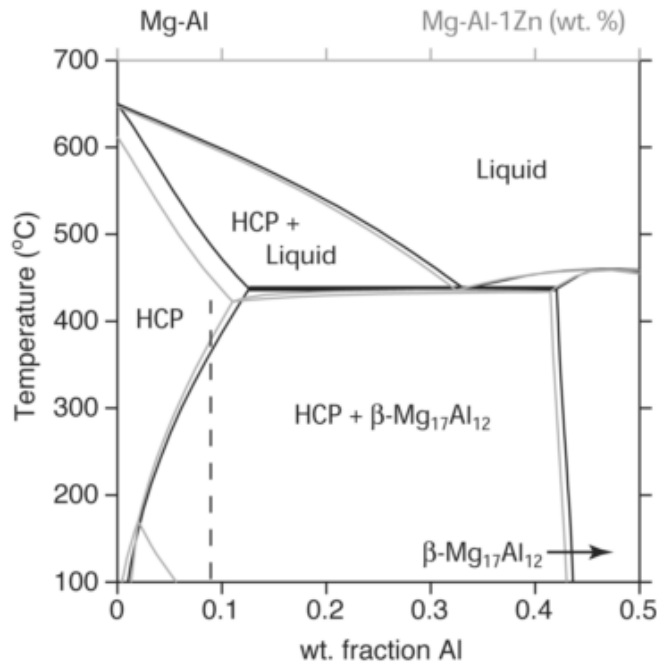
**Fig 2.2** *Mg rich end of the Mg-Al binary phase diagram*[37]. *The light grey lines represent an isopleth taken at 1%Zn to correspond to the AZ series.*

Continuous precipitates exist within the grains and contribute to strengthening via the Orowan mechanism[37]. They are known to nucleate mostly on defects, with two known morphologies, laths as shown in Fig 2.3b and rods[40]. The laths form on the basal plane, with a growth direction close to $\langle 11\bar{2}0 \rangle$ as shown in Fig 2.3a, and are much more widely seen at high temperatures, particularly above 350°C[37]. However the non-basal rods are more likely to form below 100°C, increasing further at lower temperatures[40] though the majority of the continuous precipitates still form as laths with an aspect ratio that decreases with temperature. In reality heat treatments at this temperature are impractically slow when considering peak hardness, thus typical ageing is carried out around 200°C where a mixture of continuous and discontinuous precipitates form. Most commonly the basal laths are observed to have orientation relationship (OR):

$$(0001)_{\alpha}//\{011\}_{\gamma}, [11\bar{2}0]_{\alpha}//[1\bar{1}1]_{\gamma} \qquad\qquad [\text{OR-}\gamma1]$$

though the prismatic rods have been shown to instead have the Crawley OR:

$$(0001)_\alpha//(1\bar{1}1)_\gamma, [10\bar{1}0]_\alpha//[110]_\gamma \qquad \text{[OR-}\gamma 2]$$

These two are not exclusive and as other ORs have been reported in Mg-Al alloys, this will be explored later when discussing the ORs in Mg-Sn alloys. Further information surrounding the ORs in AZ alloys can be found in the following references[40,41,50–55] and are summarised in Table 2.2, but a full discussion of this will be postponed to the section on ORs in Mg-Sn-Al alloys.
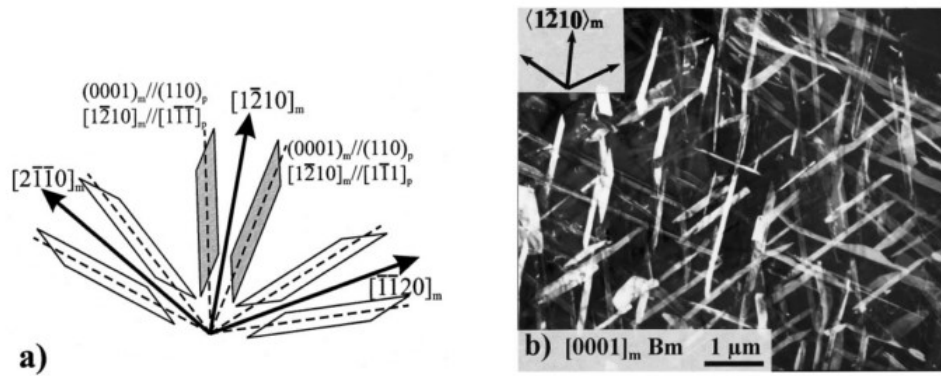


**Fig 2.3** *Schematic diagram of the morphology of continuous precipitates with the Burgers OR in AZ91 accompanied by B) a dark field image of continuous precipitates in a specimen aged for 8.3hrs at 200°C. Beam direction is 0001 with relation to the matrix.*[40]

**Table 2.2:** *ORs in Mg-Al binary and ternary alloys*

| Orientation Relationship | Name | Morphology | Ref |
|---|---|---|---|
| $(0001)_\alpha//\{011\}_\gamma, \langle11\bar{2}0\rangle_\alpha//\langle1\bar{1}1\rangle_\gamma$ | Burgers | Laths and some rods | [41,50] |
| $(0001)_\alpha//(11\bar{1})_\gamma, \langle11\bar{2}0\rangle_\alpha//\langle2\bar{1}1\rangle_\gamma$ | Crawley | Prismatic rods | [51,52] |
| $(\bar{1}\bar{1}21)_\alpha//(011)_\gamma, \langle1\bar{1}00\rangle_\alpha//\langle0\bar{1}1\rangle_\gamma$ | Porter | Basal rods | [50] |
| $(0001)_\alpha//(110)_\gamma, \langle11\bar{2}0\rangle_\alpha//\langle1\bar{1}2\rangle_\gamma$ | Gjönnes-Östmoe | Basal Laths | [53] |
| $(0001)_\alpha\ 2°(011)_\gamma, (01\bar{1}1)_\alpha//(110)_\gamma,$ $[2\bar{1}\bar{1}0]_\alpha//\ [1\bar{1}1]_\gamma$ | Potter | Basal Laths | [54] |

Discontinuous precipitates(DP) on the other hand are detrimental to the mechanical properties of the alloy, in particular with relation to creep resistance, softening of DP at elevated temperature making grain boundary sliding more likely. This aside, the discontinuous precipitates form as nodules of dense precipitation on the grain boundaries, consisting of lamellae of near equilibrium α and γ.

The discontinuous precipitation process begins with γ precipitates forming on the boundary due to a far higher diffusion rate on the boundaries compared to volume diffusion. As the grain boundary migrates to a lower energy configuration, the γ precipitates that have nucleated on the boundary grow behind the moving grain boundary[56], forming as lamellae within a near equilibrium matrix, as shown in Fig 2.4. They are so called discontinuous as across the grain boundary there is a large deviation in composition.

*Fig. 2.4* *Morphology of Mg₁₇Al₁₂ discontinuous precipitate*[66]

DP occurs either due to ageing after solution treatment or through a low cooling rate after casting. Invariably it has been shown that discontinuous precipitates have [OR-γ1][54] suggesting that this is the most energetically stable state, given the fact that it is seen to occur when the system has the most energetic freedom i.e. at higher ageing temperatures where diffusion is more rapid and cooling in the as cast condition, and that other ORs are a result of inhomogeneous nucleation or a lack of energy to sufficiently rearrange.

Likewise this discontinuous morphology occurs more frequently at a high angle grain boundary[57], where grain boundary migration to create a more energetically stable microstructure is favourable. Aside from this some globular, incoherent precipitates have been known to form near to discontinuous precipitates[39] though the growth mechanism is yet to be well understood.

DP fail to form at very high ageing temperatures. This is attributed to two factors: the increase in volume diffusion rate with relation to grain boundary diffusion decreasing the driving force for the growth of the discontinuous type precipitates[38], and the increased difficulty for the discontinuous type precipitate to nucleate at a grain boundary due to the

increased rate of grain boundary migration. Both of these mechanisms act such that there is further solute available for the continuous precipitates to grow.

The formation of precipitates highly localised to the grain boundary in the discontinuous morphology leaves large areas in the centre of the grains that consist of only matrix, where the Al solute has been exhausted, through which dislocations can travel unimpeded. Thus, we have the situation where the continuous and discontinuous precipitation mechanisms act competitively dependent on the probability of nucleation and growth rate; this is largely dependent on the temperature at which the ageing takes place as shown in Fig 2.5. A lot of research effort has gone in to understanding and controlling this process in AZ91 and other Mg-Al alloys.
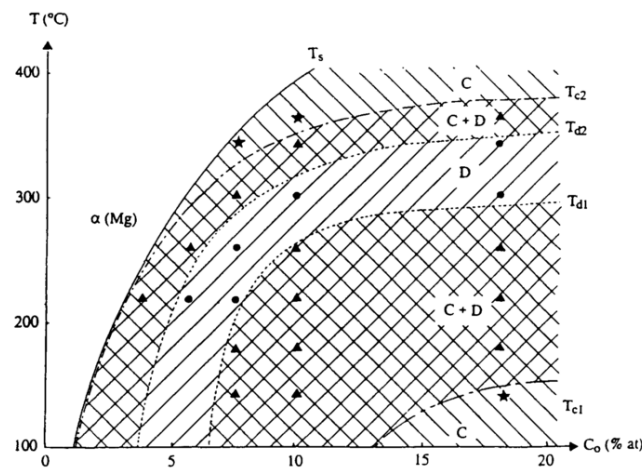


**Fig 2.5** *Diagram showing formation of DP (D) and CP (C) at different ageing temperature and Al content in Mg-Al binary alloys*[38]

Modern alloys, however, are far beyond simple binaries: zinc (Zn) for example is a common addition to magnesium alloys. The AZ series (AZ91, AZ61, AZ31) of alloys is by far[1] the most popular, with the additional zinc contributing to increased strength through the solid solution mechanism as well as improving corrosion resistance[7–9]. Above 2wt% Zn increases the likelihood of hot cracking, although the ZK series, as well as

various modification on this (eg ZC63, ZE41), have been well investigated to prevent this during forging.

In these alloys precipitation of the $MgZn_2$ phase occurs in two morphologies; basal plates and prismatic rods. There is still some debate about the exact crystal structure and whether it is different for the two morphologies[58–64] but it is widely reported to be a C-14 Laves structure (a=0.52 nm, c=0.85 nm, space group P63/mmc). This phase similarly contributes to hardness, particularly the prismatic rods due to their extended length in the <c> direction, up to 8μm, while still possessing a width of less than 100nm.

Likewise, it is well known[65–67] that in the AZ series, Zn can appear substitutionally in the γ phase to form a $Mg_{17}Al_{12-x}Zn_x$ ternary precipitate, most commonly reported as $Mg_{17}Al_{11.5}Zn_{0.5}$. Celotto and Bastow[66] show that this addition of zinc to the precipitate slightly increases the nucleation rate of the γ phase due to the zinc segregation.

## 2.3 High Temperature Magnesium Alloys

Despite much research, the high temperature use of magnesium-aluminium alloys is limited as the γ phase still lacks thermal stability above 130°C. Creep performance is poor[1,68,69] above this temperature, meaning the usage of Mg-Al alloys for components with high operating temperature, such as transmissions and engine blocks, is severely limited. Some success in increasing high temperature strength and reducing creep has been had by introducing extra alloying components such as calcium (Ca), strontium (Sr) and rare earth metals (RE)[43,70–73] to well established alloys, while other researchers[15,70,74–76] have sought to design new alloys based on these elements as additions.

Much in the same way as Zn can be introduced substitutionally into the γ phase, adding 0.3wt%Ca to AZ91 gives rise to a modified precipitate, with Ca replacing between 0.4 and

0.6 Mg atoms per unit cell of the γ phase[43,77]. This substitution increases the melting point of the phase as well as refining the size of the precipitates, thus giving an improvement in the mechanical strength of AZ91, especially at elevated temperature. Furthermore, Ca has been shown to suppress DP in AZ91, partially negating the detrimental effect of grain boundary sliding on creep resistance[43]. Greater amounts of Ca however can lead to other intermetallics such as $Al_4Ca$ and $Al_2Ca$[43,78]. These have been shown to further increase the hardness of the alloy as well as improve creep performance. Limitations occur however as large additions of Ca, above 1wt%, can lead to hot cracking and die soldering[70].

Rare Earth additions have similarly been shown to suppress DP as well as other γ phase precipitates in AZ91[43] with additional $Al_{11}RE_3$ and $Al_2RE$ intermetallics being formed in the as-cast alloy. These intermetallics will form preferentially, though $Mg_{12}RE$ precipitates are possible. Pettersen[79] determined that the ratio of RE to Al required for this is around 1.4. RE additions should always be treated with some scepticism: mostly these are achieved by the addition of mischmetal, an amalgamation of numerous different elements in varying amounts and therefore the composition of an AZ91 alloy with 1wt% RE can vary considerably. To add individual RE elements is cost prohibitive, though further research is being conducted into the effect of both individual elements and different combinations[15,76]. Some general conclusions can be drawn about the Mg-Al-RE system, though, as typically RE elements imbue similar properties; the ultimate tensile strength (UTS) will increase with Al and RE addition and the tensile yield strength (YS) is dependent on the RE content[80]. Likewise, Al decreases the creep resistance when added, whereas adding REs increases it, assuming all other conditions are fixed[70].

Khomamizadeh et al.[71] have measured the mechanical and creep properties of AZ91 with 1-3wt% RE at room temperature and 140°C. With up to 2wt% RE addition both YS and UTS increase when tested at 140°C before decreasing at 3wt%. Similarly, the elongation at 140°C is increased to a peak of 9% at 2wt% RE, while maintaining similar levels of elongation at room temperature to the AZ91 control sample. At room temperature, strengths remain comparable although elongation does decrease above 2wt%. Kabirian and Mahmud[81] similarly found that the optimum creep resistance for an AZ91 alloy augmented by REs is at 2wt%, demonstrating the limitations of this approach to alloy design. We instead briefly look toward Mg-Al-RE and Mg-Al-Sr alloys such as the AE and AJ series of alloys that were designed specifically with creep in mind. The creep properties of these alloys are well studied[68,70,75] as shown below in Table 2.3, being greatly superior to those found in AZ alloys.

**Table 2.3** *Creep properties of diecast Mg alloys*[70]

| Alloy | Tensile Creep, % | | | | | | Compressive Creep, % 70 MPa 200hrs |
|---|---|---|---|---|---|---|---|
| | 50 MPa 200hrs | | 50MPa 500hrs | | 70 MPa 100hrs | 70MPa 200hrs | |
| | 150℃ | 175℃ | 150℃ | 175℃ | 175℃ | 175℃ | 150℃ |
| AZ91D | 2.7 | * | 6.35 | - | - | - | 21 |
| AS41 | 0.05 | 2.48 | 0.07 | - | - | - | 6.13 |
| AS21x | 0.19 | 1.27 | - | - | - | 8.95 | 3.91 |
| AE42 | 0.06 | 0.033 | 0.08 | 0.44 | - | 0.18 | 2.16 |
| AX52 | - | - | - | - | 0.06 | - | - |
| AXJ531 | - | - | - | - | 0.06 | - | - |
| AJ52x | 0.04 | 0.05 | 0.03 | 0.09 | - | 0.14 | 0.24 |
| AJ62x | 0.05 | 0.05 | - | - | - | - | 1.73 |
| AJ62Lx | 0.13 | 0.29 | - | - | - | - | - |
| A380 | 0.08 | 0.04 | 0.10 | 0.05 | - | 0.22** | 0.03 |
| * Failed after 80hrs | | | **A383 alloy | | | | |

However, Powell et al[74] have shown that during creep testing of AE42 above 150°C, $Al_{11}RE_3$ precipitates decompose to $Al_2RE$, thus freeing up more Al in the solid solution, giving rise to γ phase. It was also shown, that this was solely due to the thermal

treatments, and not linked with the applied stress, by performing heat treatments comparable to the creep testing. What is more, the changes in the microstructure correlate with a marked decrease in the mechanical properties of the alloy as reported by Sieracki et al[82].

We thus see that, in addition to the expense of REs, the inclusion of Al in Mg-RE alloys limits the creep resistance provided by the RE. However, without the added Al, Mg-RE alloys lack the castability[70] required to be widely used. Moreover, problems occur during casting of Mg-Al-RE alloys as $Al_2RE$ can form when the cooling rate is low[70], removing RE from the solid solution without improving the creep or mechanical properties of the alloy. Nonetheless WE43, WE54 and AE44 show room temperature mechanical properties similar to AZ series alloys, with the additional benefit of superior mechanical properties at elevated temperature.[70,75,83]

Therefore, cheap alternatives to RE or Sr additions are sought, preferably that will not form intermetallics with Al, but preferentially with Mg, such that the benefits of the two phases are not mutually exclusive. Sn shows good solid solubility in magnesium, as high as 3.5at% at 561°C[84], but dropping to virtually 0at% below 200°C. Like many other elements, Sn has been introduced as a tertiary element in existing Mg-Al alloys and is known to increase hardness via solution strengthening[46,85–87]. Moreover, the $Mg_2Sn$ phase commonly found in Mg-Sn alloys has a melting point of 770°C[84], higher than that of most magnesium alloys. It follows that the mechanical properties of this intermetallic will be superior to Mg alloys strengthened by the γ phase at higher temperatures and thus of interest for applications where AZ91 or similar alloys would not be suitable.

As shown below in Fig 2.6, Sn additions to established alloys, Mg-Sn binary and ternaries will be explored in detail, firstly the mechanical properties on the macroscopic scale and

then this will be linked to the microstructure of the alloys. Moreover, the effects of microalloying will be discussed, linking the change in mechanical properties to alterations in the microstructure.
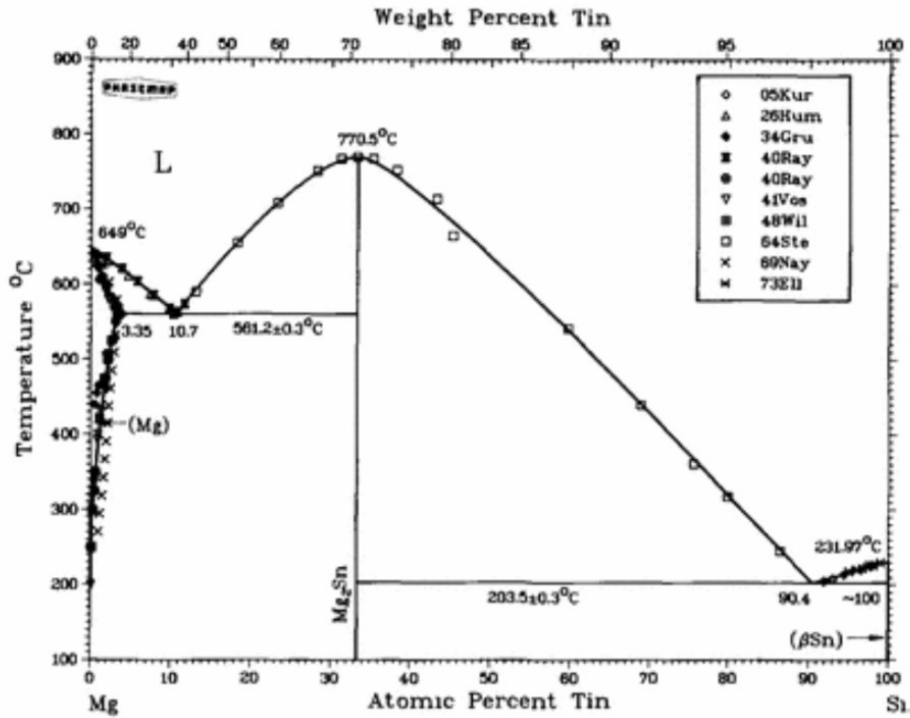


***Fig 2.6*** *Mg-Sn Binary Phase diagram*[84]

## 2.4 Tin as an Addition to Mg-Al and Other Mg alloys

Beginning with well established Mg-Al alloys, our initial consideration is of course the ternary phase diagram for Mg-Al-Sn shown in Fig. 2.7. This is somewhat sparse showing potential for only 3 phases in the Mg rich region, $\alpha$ matrix, the $Mg_{17}Al_{12}$ $\gamma$ phase and a $Mg_2Sn$ Zintl phase, hereafter referred to as the $\beta$ phase. This $\beta$ phase is desirable due to its higher melting point than $\gamma$ (437°C)[37,88]. The phase itself takes on an anti $CaF_2$ structure (a=6.759Å)[89] in which the large difference in electronegativity between the constituent atoms leads to the two valence electrons of the magnesium being mostly transferred to the tin, giving predominantly ionic bonding[89].

17

As of yet no Al-Sn phases have been reported in any Mg-Al-Sn ternaries, with instead a mixture of $\beta$ and $\gamma$ forming both in the as-cast and aged states. This does not preclude the two elements interacting, much in the way that Pb is known to affect the $\gamma$ precipitation process by restricting diffusion of solute atoms without forming any intermetallics[44,45]. Largely the literature will be divided into 2 sections below, Mg alloys where Sn is the minor component, including AZ series and other pre existing alloys and then Mg-Sn binaries and ternaries alloys where Sn is the major component. There are other compositions in the literature, for example Zn rich alloys that will be commented on where appropriate and likewise some of the effects of microalloying will be explored.
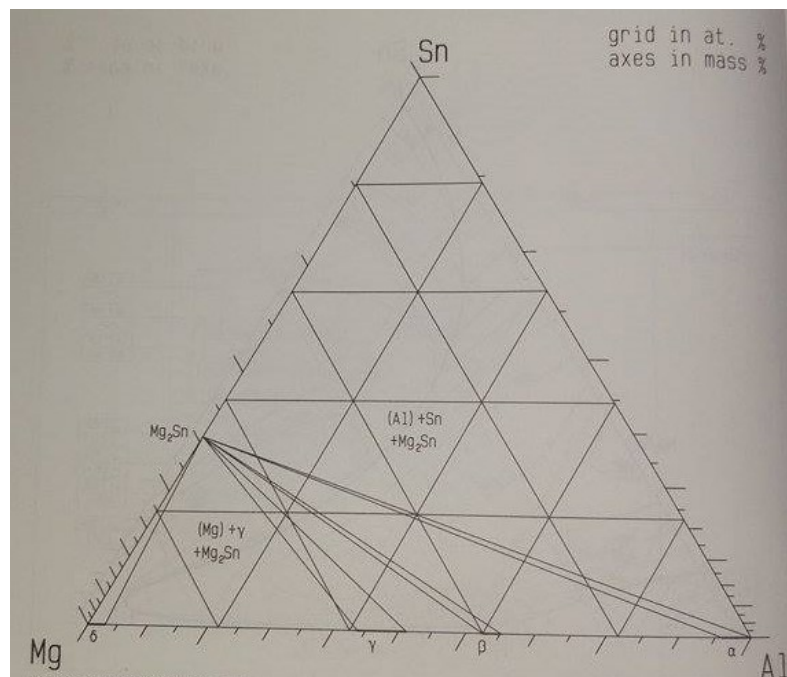


**Fig 2.7** *Isothermal section of Mg-Al-Sn ternary phase diagram near room temperature*[90]

Firstly, the addition of Sn to pre-existing Mg-Al alloys. As previously mentioned, the AZ series is by far the most common set of Mg alloys. A number of studies[46–49,91] have been conducted on AZ91 augmented by the addition of Sn, including as much as 5wt% Sn. In as-cast samples of AZ91 and similar alloys we expect that a $\gamma$ eutectic phase will be

present; the most noticeable effect of the Sn additions is the refinement of this phase. This effect is well documented in the AZ alloys, with micro additions of Pb, Si, Au[43–45] all restricting the growth of discontinuous precipitation during both cooling and heat treatment.

Similarly, Sevik[92] has reported a suppression of eutectic when adding Sn to AM60 as do Mingbo et al. for an AZ61-0.7Si alloy[93,94]. Likewise a Mg-6Zn-2Al alloy produced by Chen et al[95] shows a MgZn eutectic phase that is similarly suppressed by the addition of as little as 1wt%Sn, increasing amounts of Sn further reduce the amount of eutectic found in the as cast samples. This is explained by Mahmudi et al[91] as a consequence of Sn atoms' tendency to segregate to the liquid-solid interface during solidification, preventing the diffusion of other atoms into the solid phase. This effectively supercools the liquid metal in front of the solidification front which restricts the growth of the eutectic phase. The decrease in eutectic phase referred to above has been linked to an increase in hardness, as detailed in Table 2.4, but also to a change in the fracture properties of the alloys.

*Table 2.4* *Reported hardness of magnesium alloys containing Sn. (NB. Portions of the data are taken from graphs and as such are not precise values)*

| Alloy Composition (wt%) | Time (hrs) | Temperature °C | As Cast HV | Peak HV | HV increment | Ref |
|---|---|---|---|---|---|---|
| AT72 | 160 | Cast T4 410 +175 | 50 (1hr) | 54 | 4 | [96] |
| AT72 | 160 | Cast T4 410 +200 | 53 (1hr) | 68 | 15 | |
| AZ80 | 30 | 175 | 69 | 90 | 21 | [97] |
| TAZ180 | 30 | 175 | 69 | 93 | 24 | |
| TAZ280 | 30 | 175 | 69 | 95 | 26 | |
| TAZ480 | 30 | 175 | 71 | 97 | 26 | |
| AZ91 | 20 | 168 | 63 | 82 | 19 | [47] |
| AZT915 | 12 | 168 | 75 | 117 | 42 | |
| Mg-9Al-6Sn | 20 | 200 | 70 | 90 | 20 | [98] |
| Mg-9Al-6Sn-1Zn | 8 | 200 | 73 | 95 | 22 | |
| Mg-9Al-6Sn-3Zn | 8 | 200 | 82.5 | 102.5 | 20 | |

| Alloy | | | | | | Ref |
|---|---|---|---|---|---|---|
| Mg-4.5Zn-4.5Sn-2Al | | As Cast | 69 | | | [99] |
| Mg-4.5Zn-4.5Sn-2Al-0.2Ca | | As Cast | 71 | | | |
| Mg-4.5Zn-4.5Sn-2Al-0.4 Ca | | As Cast | 70 | | | |
| Mg-4.5Zn-4.5Sn-2Al-0.6 Ca | | As Cast | 62 | | | |
| Mg-4.5Zn-4.5Sn-2Al | | Rolled | 91 | | | |
| Mg-4.5Zn-4.5Sn-2Al-0.2Ca | | Rolled | 99 | | | |
| Mg-4.5Zn-4.5Sn-2Al | | As Cast | | 68 ± 3 | 3 | [100] |
| Mg-4.5Zn-4.5Sn-2Al | 15 | 150 | 70 ± 4 | 88 ± 4 | 18 | |
| Mg-4.5Zn-4.5Sn-2Al | 70 | | 70 ± 4 | 91 ± 3 | 21 | |
| Mg-4.5Zn-4.5Sn-2Al | 10 | 200 | 70 ± 4 | 84 ± 2 | 14 | |
| Mg-4.5Zn-4.5Sn-2Al | 50 | | 70 ± 4 | 87 ± 4 | 17 | |
| Mg-4.5Zn-4.5Sn-2Al | 10+7.5 | 200 (Preaged at 70) | 70 ± 4 | 91 ± 3 | 21 | |
| Mg | | Cast | | 40 | | [101] |
| Mg-1Sn | | Cast | | 52 | | |
| Mg-3Sn | | Cast | | 57 | | |
| Mg-5Sn | | Cast | | 67 | | |
| Mg-7Sn | | Cast | | 72 | | |
| Mg-10Sn | | Cast | | 74 | | |
| Mg-5Sn | 900 | 200 | 37.4±3.7 | 44.5±0.6 | 7.1 | [102] |
| Mg-5Sn-0.8Hf | 77 | 200 | 37.1±3.8 | 47.7±1.0 | 10.6 | |
| Mg-5Sn-1.5Hf | 77 | 200 | 32.7±1.9 | 44.9±1.5 | 12.2 | |
| Mg-10Sn | 220 | 200 | 39.8±4.2 | 53.9±2.2 | 14.1 | |
| Mg-10Sn-0.7Hf | 49 | 200 | 40.2±2.5 | 57±2.4 | 16.8 | |
| Mg-10Sn-1.5Hf | 96 | 200 | 40.1±2.3 | 58.1±1.5 | 18 | |
| Mg-6Sn-1Mn | ~180 | 200 | 45 | 59 | 14 | [103] |
| Mg-6Sn-1Mn-2Cu | ~180 | 200 | 52 | 70 | 18 | |
| Mg-6Sn-1Mn-2Cu-2Al | ~180 | 200 | 55 | 78 | 23 | |
| Mg-2.1Sn-0.1Mn-0.1Zn at | 200 | 200 | 43 | 63 | 20 | [104] |
| Mg-2.1Sn-0.1Mn-0.5Zn at | 100 | 200 | 48 | 71 | 23 | |
| Mg-2.1Sn-0.1Mn-1.0Zn at | 150 | 200 | 50 | 74 | 24 | |
| Mg-3Sn-1Al | 110 | 180 | 57 | 72 | 15 | [105] |
| Mg-3Sn-1Al-2Zn | 60 | 180 | 58 | 75 | 17 | |
| Mg-5.29Sn-0.29Mn-0.22Si | ~50 | 150 | 42 | 68 | 26 | [106] |
| Mg-5.29Sn-0.29Mn-0.22Si | ~50 | 250 | 42 | 70 | 28 | |
| Mg-5.29Sn-0.29Mn-0.22Si | ~50 | 350 | 42 | 70 | 28 | |
| Mg-7Sn-1Al-1Zn | 100 | 200 | 44 | 77 | 33 | [107] |
| Mg-6Sn | 1000 | 200 | 37 | 47 | 10 | [108,109] |
| Mg-6Sn-0.13Na | 58 | 200 | 36.4 | 63.2 | 26.8 | |
| Mg-8.64Sn | 240 | 200 | 45.1 | 54.4 | 9.3 | |
| Mg-2.0Sn-0.13Li-2.29In | 48 | 200 | 47.1 | 61.5 | 14.4 | |
| Mg-1.3Sn-1.0Zn | 300 | 200 | 40 | 56.8 | 16.8 | |
| Mg-1.3Sn-3.0Zn at | 211 | 200 | 40.1 | 70.1 | 30 | |
| Mg-1.3Sn-3.0Zn-0.17Na | 6.7 | 200 | 44.9 | 76.4 | 31.5 | |
| Mg-9.8Sn | ~1000 | 200 | 43 | 54 | 11 | [110] |

| | | | | | | |
|---|---|---|---|---|---|---|
| Mg-9.8Sn-0.5Al | ~1000 | 200 | 44 | 64 | 20 | |
| Mg-9.8Sn-1.0Al | 700 | 200 | 44 | 65 | 21 | |
| Mg-9.8Sn-2.0Al | ~1000 | 200 | 45 | 69 | 24 | |
| Mg-9.8Sn-3.0Al | ~80 | 200 | 49 | 73 | 24 | |
| Mg-9.8Sn-4.0Al | ~80 | 200 | 51 | 74 | 23 | |
| Mg-9.8Sn-3.0Al-0.15Ca | ~40 | 200 | 50 | 74 | 24 | |
| Mg-9.8Sn-3.0Al-0.3Ca | ~100 | 200 | 50 | 75 | 25 | |
| Mg-9.8Sn-3.0Al-0.4Ag | ~500 | 200 | 53 | 76 | 23 | |
| Mg-9.8Sn-3.0Al-0.4Ag-0.15Ca | ~150 | 200 | 48 | 75 | 27 | |
| Mg-9.8Sn-3.0Al-0.24Cu | ~500 | 200 | 50 | 72 | 22 | |
| Mg-9.8Sn-3.0Al-0.25Zn | ~500 | 200 | 48 | 74 | 26 | |
| Mg-9.8Sn-3.0Al-1.2Zn | ~400 | 200 | 45 | 81 | 36 | |
| Mg-9.8Sn-3.0Al-1.2Zn-0.15Ca | ~400 | 200 | 50 | 81 | 31 | |
| Mg-9.8Sn-3.0Al-0.2Mn | ~400 | 200 | 47 | 76 | 29 | |
| Mg-9.8Sn-3.0Al-1.0Mn | ~400 | 200 | 54 | 75 | 21 | |
| Mg-9.8Sn-1.2Zn | 50 | 200 | 48 | 72 | 24 | |
| Mg-9.8Sn-1.2Zn | 220 | 200 Double aged* | 50 | 80 | 30 | |
| +0.3Ca-0.8Ag-0.7Zr | ~200 | 200 | 52 | 82 | 30 | |
| +0.8Ag | ~28 | 200 | 49 | 82 | 33 | |
| +0.3Ca at | ~28 | 200 | 52 | 87 | 35 | |
| +~0.6Mm | ~200 | 200 | 49 | 71 | 22 | [111] |
| +0.5Cu | ~110 | 200 | 49 | 72 | 23 | |
| +0.5Cu-1.0Al | ~56 | 200 | 49 | 68 | 19 | |
| Mg-9.8Sn-1.2Zn | ~550 | 160 | 48 | 81 | 36 | |
| +0.3Ca-0.8Ag-0.7Zr | ~1400 | 160 | 53 | 87 | 34 | |
| +0.5Cu | ~100 | 160 | 53 | 87 | 34 | |
| +1.0Al | ~500 | 160 | 53 | 95 | 0 | |

Chen et al.[95] attempt to explain a twofold effect of the Sn, firstly relating its properties to those of Pb given the similar characteristics of the two atoms.  It is said that Sn restricts the diffusion of Al and Zn and increases the solid solubility of the Zn in the $\alpha$ matrix.  More interestingly, precipitates identified as $Mg_2Sn$ 'modified by Zn' were detected in the vicinity of the grain boundary, potentially due to this segregation of Sn to the solidification front.  Given the work of Liu et al[112] we know that Zn segregates to the surface of the $Mg_2Sn$ precipitates.  $Mg_2Sn$ forms during the casting of the alloy, it follows that each $Mg_2Sn$ precipitate would reduce the Zn in solid solution as the alloy cools, hence reducing that

available Zn to form a eutectic. Whether a similar explanation can be given for the suppression of the $\gamma$ eutectic and DP remains to be seen.

Mg$_2$Sn precipitates are also found in the as cast samples in the work of Luo et al.[113]. This study optimises the strength of Mg-Al-Sn ternary is optimised, with Mg-7Al-3/5Sn concluded as the two best candidates for room temperature strength, both exceeding the UTS, YS and elongation of AZ91. Of course this is only considering the as cast state. The only precipitation that is considered is that which occurs during solidification and thus is dependent on the casting conditions i.e. cooling rate. Table 2.5 below compares these properties with the measured volume fraction of the $\gamma$ and $\beta$ precipitates. This of course does not consider the effect that the $\beta$ will have on the mechanical properties at elevated temperatures.

**Table 2.5** *Tensile properties of as cast Mg-Al-Sn alloys at room temperature*[113]

| Alloy | Yield Strength (MPa) | Ultimate Tensile Strength (MPa) | Elongation (%) |
|---|---|---|---|
| Mg-5Al-1Sn | 64.7 ± 1.4 | 179.1 ± 17.0 | 8.32 ± 0.78 |
| Mg-5Al-3Sn | 75.7 ± 3.0 | 177.5 ± 9.9 | 7.49 ± 2.19 |
| Mg-5Al-5Sn | 82.5 ± 4.0 | 161.1 ± 5.6 | 4.8 ± 0.72 |
| **Mg-7Al-2Sn** | **91.9 ± 2.1** | **175.5 ± 6.2** | **5.34 ± 1.04** |
| Mg-7Al-3Sn | 88.8 ± 3.6 | 151.5 ± 2.7 | 3.11 ± 0.24 |
| **Mg-7Al-5Sn** | **110.1 ± 10.1** | **160.7 ± 5.5** | **3.18 ± 0.64** |
| Mg-9Al-2Sn | 102.5 ± 3.3 | 154.8 ± 2.0 | 2.05 ± 0.20 |
| Mg-9Al-4Sn | 120.4 ± 6.9 | 160.1 ± 7.0 | 1.46 ± 0.11 |
| Mg-9Al-5Sn | 127 ± 1.3 | 149.8 ± 2.1 | 1.08 ± 0.49 |
| AZ91 | 89.3 ± 4.4 | 150.8 ± 11.6 | 2.36 ± 0.49 |

## 2.5 Mg-Sn Binaries and Ternaries

Aside from the work of Luo et al, a number of studies of the mechanical properties of Mg-Sn alloys have been conducted[47,108–111]. The data is roughly split into two categories, those from tensile tests giving ductility, YS and UTS and those from Vickers hardness indents. The current study will use Vickers hardness to quantify the mechanical properties of the alloys, and thus only the literature which provides a direct comparison

will be discussed at this point. Modelling of the precipitation process on the other hand will feed into an Orowan type model, which will deal with the increment in yield strength. Hardness and yield strength can be broadly related but this relies on a coefficient that is unknown, widely accepted to be approximately 3[114].

Fig. 2.8 gives a summary of the range of hardness values found in the most common Mg-Sn alloys, included as well is a comparison with AZ91 and measurements taken from an AZ91 alloy with added Sn.

Hardness is obviously a coarse measurement and increments in hardness can arise through different mechanisms. Firstly we consider that Al, Sn and Zn[46,85–87] all act in solution to strengthen magnesium. This can be seen in Fig. 2.8 as adding a tertiary element to the Mg-Sn binary increases the lowest hardness, representing the solution treated state where no precipitates are expected. However, the focus of this study is the precipitation process in Mg-Sn alloys and thus we consider Orowan's mechanism.
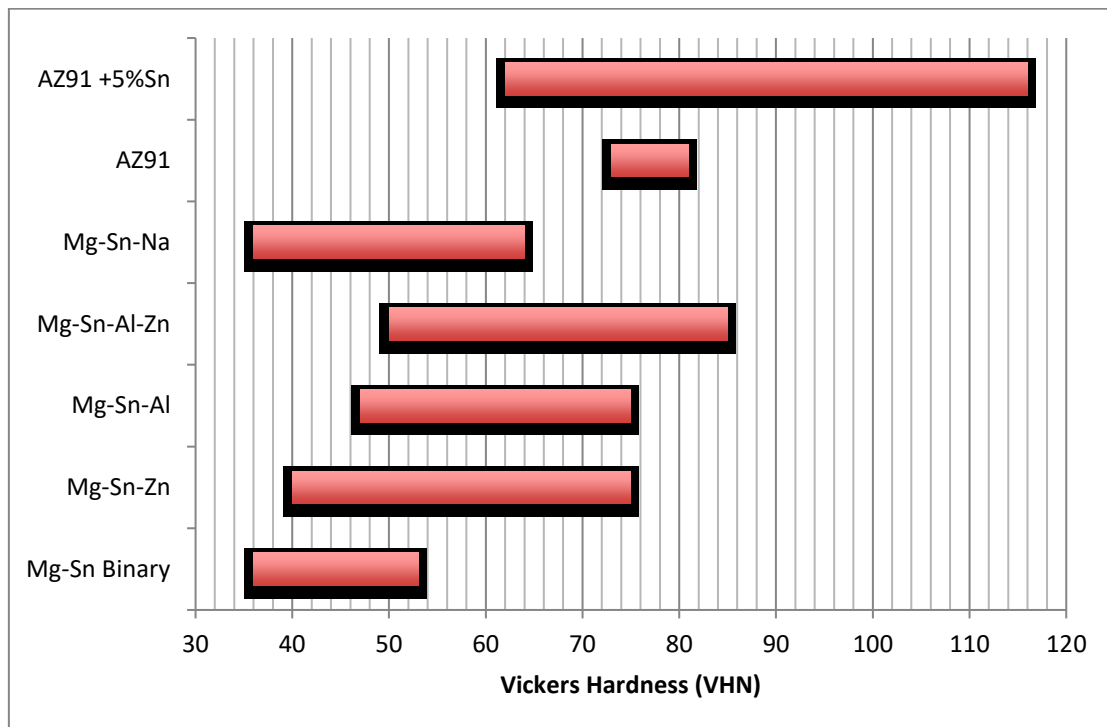


**Fig. 2.8** *Typical hardness ranges of Mg-Sn based alloys from the literature*[47,108–111]

Given that the shear modulus, $G$, and the Burgers vector, $b$ are properties of the material and dislocation respectively, there are two manners in which to increase the strength of the material: decrease the particle size, $d$, or reduce the mean particle spacing, $\lambda$, which is closely related to the number density, $N_v$. The two parameters are actually linked for constant solute content: an increase in $N_v$ given the same amount of solute available would as a consequence lead to smaller precipitates. This will be discussed more thoroughly later. First a quick review of the available literature on the number density of precipitates in magnesium alloys.

## 2.6  Number Density of Precipitates

Few studies of Mg alloys have stated quantitatively a number density of precipitates. It was established very early[108,109,115,116] that the binary Mg-Sn alloy produced a low number of coarse precipitates. The only work however to give explicit number densities in Mg-Sn alloys is that of Mendis et al.[108,109]and Huang[103] with the results given in Table 2.6 below. It is worth noting Mg-1.3Sn(at%) corresponds to one of the alloys in this study and thus a direct comparison will later be made between one of the compositions in the current work and the work of Mendis et al. [108,109] and of Huang et al.[103].

*Table 2.6* *Quantitative measurement of number density and precipitate dimensions for samples peak aged at 200°C*[40,102,103,108,109]

| Alloy Composition (at%) | Number Density (µm$^{-3}$) | Length (nm) | Width (nm) | Thickness (nm) | Length/ Width | Length/ Thickness |
|---|---|---|---|---|---|---|
| Mg-1.3Sn | 0.60 | 1500± 400 | 500± 80 | 54± 11 | 3 | 28 |
| Mg-1.3Sn-1.2Zn | | | | | | |
| Basal Laths | 1.35 | 650± 55 | 320± 45 | 60± 25 | 2 | 11 |
| [0001]$_{Mg}$ laths | 1.05 | 1105± 324 | | 180± 55 | | 6 |
| Mg-1.3Sn-0.15Na | 56.4 | 230± 50 | 90± 22 | 25± 8.5 | 2.55 | 9.2 |
| Mg-1.3Sn-1.2 Zn-0.19Na | 81.5 | 70± 25 | 63± 15 | 25± 6.8 | 1.1 | 2.8 |
| Mg-1.9Sn | 0.85 | 800± 230 | 170± 80 | 55± 31 | 4.7 | 14.5 |
| Mg-2Sn-0.48Li-0.53In | 25.5 | 37± 42 | 77± 28 | 26± 4.5 | 4.9 | 14.4 |
| Mg-1.3Sn-0.5Mn | 8.0 | 450± 180 | 105± 30 | 40± 15 | 4.3 | 11.3 |
| Mg-1.3Sn-0.5Mn-0.8Cu | 123.1 | 300± 100 | 50± 20 | 20± 10 | 6 | 15 |
| Mg-1.3Sn-0.5Mn-0.8Cu-2.0Al | 161.5 | 250± 100 | 40± 15 | 20± 10 | 6.3 | 12.5 |
| Mg-1.1Sn | - | 17± 7 | 12± 4 | - | 1.42 | - |
| Mg-1.1Sn -0.8Hf | 41.2 | 138± 34 | 38± 18 | - | 3.63 | - |
| Mg-1.1Sn -1.5Hf | 50.4 | 170± 56 | 43± 21 | - | 3.95 | - |
| AZ91 | 8 | - | - | - | - | - |

Likewise there are published number densities for AZ91 alloys[40]. While the precipitates have a different composition, the Orowan model is insensitive to these changes provided the morphology is similar. However, the discontinuous precipitation mechanism in the AZ91 series means that any comparisons should be made with caution as there is a more complex combination of strengthening mechanisms on the macroscopic scale due to the discontinuous precipitation reducing grain boundary sliding. It can be seen however by ageing to peak hardness (given as the 8.3hr sample in Celloto's work in Fig. 2.9) a number density of approximately *8µm$^{-3}$* is found in AZ91. This is larger than that found by Mendis et al.[108,109] in Mg-Sn binary and Mg-Sn-Zn ternary. We can clearly see the benefit of Na additions with the Mg-Sn-Zn-Na quarternary having a number density an order of magnitude greater than that Celotto found in AZ91. We again must remember however that the different morphologies of precipitate have a greater or lesser

effect on strengthening and thus any number density calculations should be sensitive to this morphology variance.
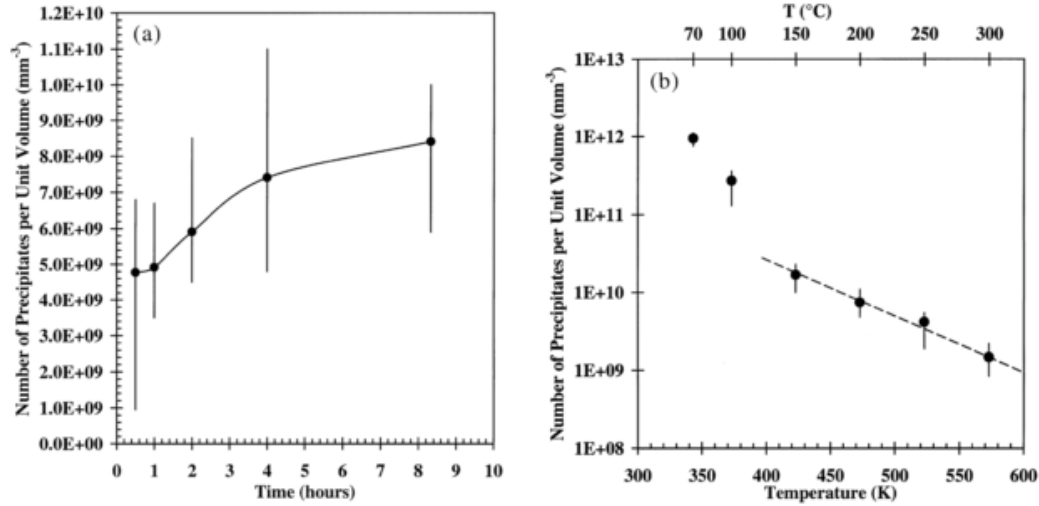


**Fig. 2.9** *Precipitate number density as a function of (a) ageing time at 200°C and (b) ageing temperature*[40]

Mendis et al.[108] further explore the significance that this increase in number density has on magnesium alloys, emphasising the importance of careful selection of both main alloying element and trace alloying elements. Clearly in the present case the main alloying element is dictated by the desire to investigate the Mg-Sn system, thus we focus instead on the mechanisms behind the increase in number density and the effect of microadditions and attempts made to model these mechanisms.

## 2.7 Modelling Strengthening

So far we have only mentioned Orowan strengthening in passing. Most materials scientists will be familiar with the form:

$$\sigma_{Orowan} = \frac{MG\boldsymbol{b}}{2\pi\lambda.\sqrt{1-\nu}} \qquad [2.2]$$

for the increment in strength, $\sigma_{Orowan}$, where $\nu, G$ and $\boldsymbol{b}$ are the Poisson ratio, shear modulus and Burgers vector of the matrix respectively. All of these can be easily obtained

from the literature[37,117,19,118] and are given in Table 2.7 for magnesium. Likewise $M$ is the Taylor factor: there is often not an agreed upon figure for this. For magnesium and magnesium alloys, this is given as between 2 and 5 depending on the reference used[37,117,19,118]. The remaining parameter $\lambda$, the mean interparticle spacing, changes depending on how the alloy has been processed and relates back to the number density.

*Table 2.7:* *Constants for magnesium and magnesium alloys*

| Table of Constants | Value in Magnesium and Magnesium Alloys |
|---|---|
| $b$, Burgers vector (basal) | 0.321 nm [37,118] |
| $G$, Shear Modulus | 17.2 GPa  [37,118] |
| $v$, Poissons ratio | 0.29[119], 0.35[37,118] |
| $M$, Taylor Factor | 2.1-5[37,117,19,118] |

Unfortunately, the Orowan equation is at times an oversimplification of the actual case. The above relies on the assumption that the precipitates are small and spherical in a homogeneous matrix. Most modern applications of Orowan strengthening include a matrix distortion parameter caused by the finite size of the precipitates representing the increase in energy per unit volume as a consequence of dislocations formed around the precipitates. This is given as a logarithmic term:

$$\sigma_{Orowan} = \frac{MG\boldsymbol{b}}{2\pi\lambda.\sqrt{1-v}}.\ln\left(\frac{d_p}{\boldsymbol{b}}\right) \qquad [2.3]$$

where $d_p$ represents the mean particle diameter. Ferguson et al.[120] however argue that this is not appropriate as it does not account well for the size dependence of the precipitate. They propose that a $d_p^{-1/2}$ factor as identified by Ashby[121] is more appropriate, although this is less commonly used.

H.C.P. materials present further difficulty as not only do they contain non-spherical precipitates but also have numerous different slip planes. As such, various modifications exist, depending on the situation. For magnesium the most obvious issue lies in the variety of slip planes and the non-symmetric morphology of the precipitates. This is a subject that has attracted some attention[10,20,122–124]. Different morphologies have been assessed for their effectiveness on a variety of slip planes. The interparticle spacing, λ, is either given as a function of volume fraction or, as in this case, as a function of number density, $N_V$:

$$\lambda = \frac{1}{\sqrt[3]{N_V}} \qquad [2.4]$$

As the size of the precipitates approaches a similar magnitude to the spacing between them, especially the case for high aspect ratio precipitates, we must compensate[20,120] for the finite size of the precipitates. The value must be adjusted to account for the mean radius of a precipitate, $d_p$, as follows:

$$\lambda = \frac{1}{\sqrt[3]{N_V}} - d_p \qquad [2.5]$$

For a sphere, $d_p$ is easily determined, but in magnesium alloys we are almost invariably faced with more complicated morphologies and different slip planes. Typically[20,122,123] this is accounted for by examining the spacing on each slip plane to geometrically calculate the spacing on each plane. Nie[20] does this for basal slip and Wang et al[122] extend this to non-basal slip systems. A summary of these is given in Table 2.8.

**Table 2.8.** *Different formulations of mean interparticle spacing for different slip planes and precipitate morphologies. $l_p$ = centre to centre spacing of precipitates, $D_p$= diameter of precipitate , $d_p$= effective diameter of precipitate, $t_p$ = precipitate thickness, $N_A$= number density $(m^{-2})$ and $f$ = percentage volume fraction of secondary phase*

| Formula | Precipitate Morphology | Slip Plane | Reference |
|---|---|---|---|
| $$\lambda = l_p - d_p = \frac{1.075}{\sqrt{N_A}} - \frac{\pi d_p}{4}$$ | Spheres in a triangular array | Any | [20] |
| $$\lambda = l_p - \frac{d_p}{2} - \frac{\sqrt{3}\,t_p}{2}$$ | Prismatic plates | Basal | [20] |
| $$\lambda = l_p - d_p$$ | Basal Plates | Basal | [20] |
| $$\lambda_{eff} = \frac{2}{3}\lambda_1 + \frac{1}{3}\lambda_2$$ $$\lambda_1 = l_p - \left(\frac{1}{4} - \frac{\cos(120-\theta)}{2}\right)D_p$$ $$-\left(\frac{\sqrt{3}}{2\sin\psi_1} + \frac{\sin(120-\theta)}{\sin\psi_2}\right)$$ $$\lambda_2 = l_p - \cos\theta - \frac{\sin\theta}{\sin\psi_2}t_p$$ $$l_p\left(\frac{8f}{3\sqrt{3}\pi D_p t_p}(\sin\psi_1 + 2\sin\psi_2)\right)^{-\frac{1}{2}}$$ $$d_p = \sqrt{D_p t_p}$$ | $(10\bar{1}0)$ Plates $\psi_1$=90° (2nd order), 28.1° (1st order) $\psi_2$ = 42.5° (2nd order) 63.8° (1st order) $\theta$ = 42.4° (2nd order) 74.8° (1st order) $(11\bar{2}0)$ Plates $\psi_1$=36.1° (2nd order) 90° (1st order) $\psi_2$ = 64.8° (2nd order) 40.2° (1st order) $\theta$ = 73.2° (2nd order) 39.2° (1st order) | Pyramidal | [122] |
| $$\lambda_{eff} = \frac{2}{3}\lambda_1 + \frac{1}{3}\lambda_2$$ $$\lambda_1 = l_p - \frac{D_p}{2} - \frac{\pi D_p}{8}$$ $$\lambda_2 = l_p - \frac{2}{\sqrt{3}}t_p$$ $$l_p = \left(\frac{2\sqrt{3}\,\pi\,D_p t_p}{4f\,(t_p + \sqrt{3}D_p)}\right)^{\frac{1}{2}}$$ $$d_p = 0.635\sqrt{D_p t_p} + \frac{D_p}{3}$$ | $(10\bar{1}0)$ Plates | Prismatic | [122] |
| $$\lambda_{eff} = \frac{2}{3}\lambda_1 + \frac{1}{3}\lambda_2$$ $$\lambda_1 = \sqrt{\left(l_p\sin60 - \frac{t_p}{2}\left(\frac{1}{\sin\psi_1} + \frac{1}{\sin\psi_2}\right)\right)^2 + (l_p\cos60)^2}$$ $$\lambda_2 = l_p - \frac{\pi D_p}{4}$$ $$l_p = \sqrt{\frac{\sqrt{3}\,\pi\,D_p t_p}{4f}}$$ | $(11\bar{2}0)$ Plates $\psi_1$=90° $\psi_2$ = 30° | Prismatic | [122] |
| $$\lambda = l_p - D_p$$ $$l_p = \sqrt{\frac{\pi D_p t_p}{2\sqrt{3}\,f\cos\psi}}$$ | [0001] rods $\psi$ =45.6° (2nd order) 51.1° (1st order) | Pyramidal | [122] |
| $$\lambda_{eff} = \sqrt{0.403\frac{D_p t_p}{f} - 0.576 D_p\sqrt{\frac{D_p t_p}{f}} + 0.274 D_p^2}$$ $$+ 0.317\sqrt{\frac{D_p t_p}{f}} - \frac{t_p}{3}$$ $$\lambda_1 = \sqrt{\left(l_p\sin60 - \frac{\pi}{4D}\right)^2 + (l_p\cos60)^2}$$ | [0001] rods | Prismatic | [122] |

| | | | |
|---|---|---|---|
| $$\lambda_2 = l_p - t_p$$ $$l_p = \sqrt{\frac{\pi D_p t_p}{2\sqrt{3}\,f}}$$ | | | |
| $$\lambda_{eff} = \frac{2}{3}\lambda_1 + \frac{1}{3}\lambda_2$$ $$\lambda_1 = \sqrt{\left(l_p sin60 - \frac{t_p}{sin\psi}\right)^2 + \left(l_p cos60\right)^2}$$ $$\lambda_2 = l_p - \frac{\pi}{4}D_p$$ $$l_p = \sqrt{\frac{\pi D_p t_p}{2\sqrt{3}\,f sin\psi}}$$ | Basal plate $\psi$ =45.6° (2nd order) 51.1° (1st order) | Pyramidal | [122] |
| $$\lambda = \sqrt{0.403\frac{D_p t_p}{f} - 0.733\,t_p\sqrt{\frac{D_p t_p}{f}} + t_p^2 + 0.317\sqrt{\frac{D_p t_p}{f}} - 0.262 D_p}$$ | Basal plate | Prismatic | [122] |
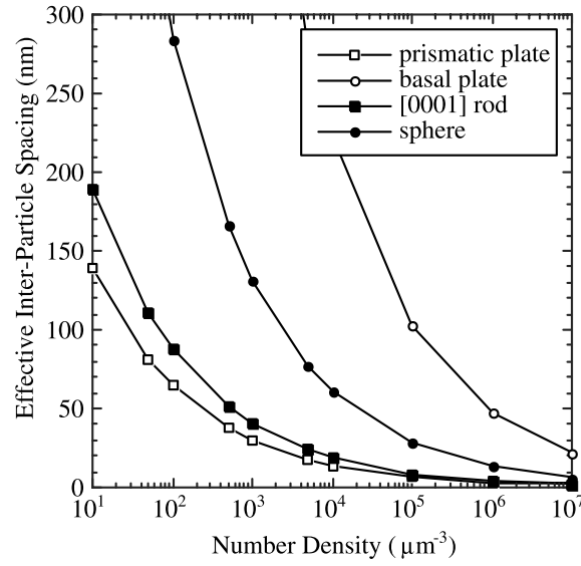


***Fig 2.10***: Comparison of the effective inter precipitate spacing for a constant volume fraction and number density[20]. $f = 0.04$ and aspect ratio, $A$ 1:40
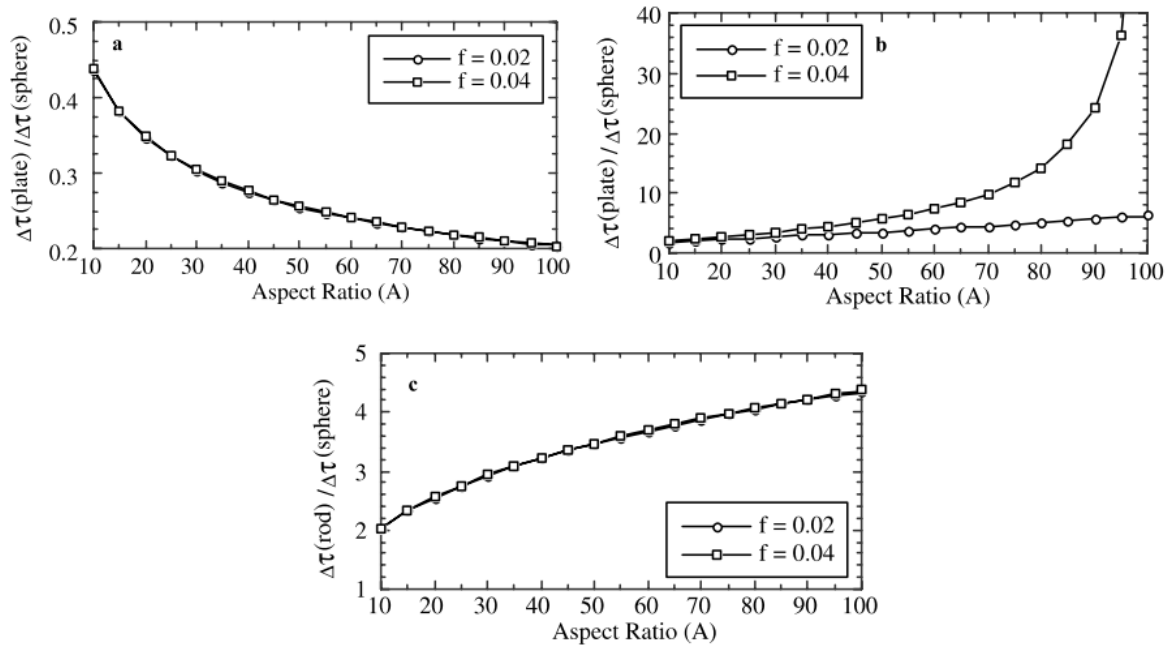
***Fig 2.11:*** *Comparison of effective strengthening from a)*(0001) *plates, b)* {10$\bar{1}$0} *or* {11$\bar{2}$0} *plates and c)* [0001] *rods as a function of A with two volume fraction, f* = 0.02, 0.04 [20]

Nie[20] gives a comparison of the effectiveness of each morphology in the basal slip plane, as seen in Fig 2.10, showing the greater effectiveness of prismatic plates as well as extending this to look at the effect of different aspect ratios as seen in Fig 2.11. This type of treatment is extended by Wang et al[122] to look at non-basal slip modes as shown in Fig 2.12. Here the effect of greater volume fraction is seen for two different aspect ratios of precipitate, in particular plate shaped precipitates on the prismatic planes greatly increase in effectiveness for higher volume fractions.

Hidalgo-Marique et al. [123]completes this by comparing this theoretical treatment with a Mg-RE alloy containing prismatic plate precipitates, reporting that the model is effective for precipitate strengthening for dislocations. Some doubts remain however as to how applicable this method is when calculating the strengthening effect for twinning.

As can be seen it is quite possible to model the strengthening by different precipitate morphologies within a matrix by adjusting Orowan's equation. However, it is time

consuming to take measurements from a large number of different samples and relies on some educated guess work to find the peak ageing time and how to improve the strengthening effectiveness of the microstructure. As such accurate modelling of a microstructure is desirable to give a roadmap to alloy design. One of these models successfully applied to AZ91 is the Kampman-Wagner Numerical(KWN) model.
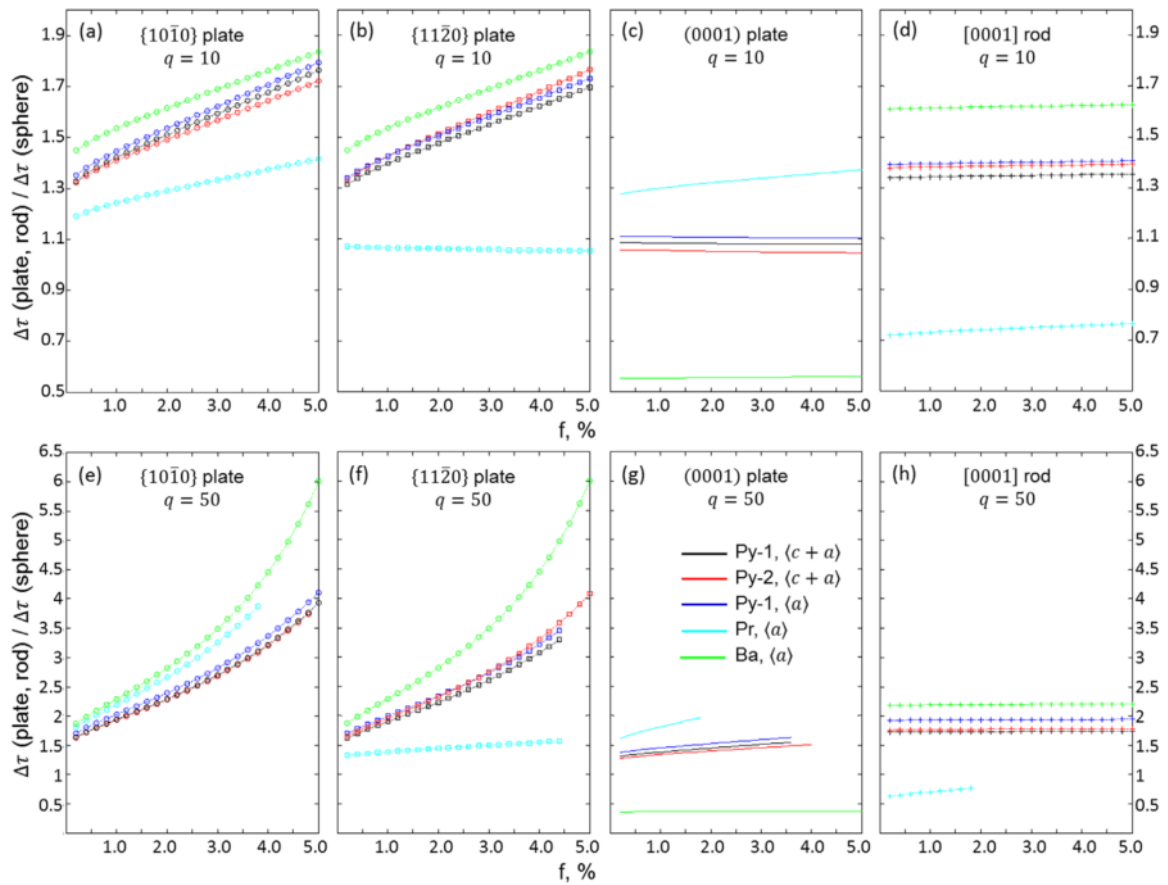


***Fig 2.12:*** *Comparison of effective strengthening by different precipitate morphologies as a function of volume fraction f for two different values of A, 10 and 50 (labelled as q on the graphs)*[122]

## 2.8   Modelling Growth and Coarsening of the Precipitates

Classically the age hardening mechanism is split into three distinct phases, nucleation, growth and coarsening each determined by their own equations, for example Lifshitz-Slyozov-Wagner (LSW) coarsening. Conversely the Kampmann-Wagner numerical

(KWN) model[118,125–131] considers all three simultaneously in order to build up a more complete picture of the microstructure as a function of time during heat treatment of the alloys.

The KWN model still relies on well established theories. Robson et al[129] for example use a nucleation rate $I$ calculated as a function of the number of nucleation points $N_v$, the Zeldovich factor $Z$ and the temperature $T$:

$$I = N_v Z \beta \exp\left[-\frac{4\pi r^*}{3k_B T}\right] \exp\left[-\frac{\tau_i}{t}\right] \qquad [2.6]$$

Also included are a critical incubation time $\tau_i$, the Boltzman constant $k_B$, critical radius for nucleation $r^*$ and another factor $\beta$. Mhyr et al.[127] by comparison use:

$$I = I_0 \exp\left[-\frac{\Delta G^*}{RT}\right] \exp\left[-\frac{Q_d}{RT}\right] \qquad [2.7]$$

where $I_0$ is a fitted constant, $R$ the universal gas constant, $\Delta G^*$ the energy barrier for nucleation of a precipitate and $Q_d$ the activation energy for diffusion of the solute. Both are based on classic nucleation theory and the choice is a mixture of preference and availability of data on the alloy.

Conversely the growth of precipitates is always controlled [118,125–131] by the same mechanism, relying on the calculated supersaturation of the alloy, $\Omega$, as a function of the equilibrium content in the precipitate, $c_e^\beta$, the instantaneous solute content in the matrix, $c_i$ and the solute content at the precipitate/matrix interface, $c_r^\alpha$:

$$\Omega = \frac{c_i - c_r^\alpha}{c_e^\beta - c_r^\alpha} \qquad [2.8]$$

Generally the growth is given as a function of the diffusion rate, $D_0$ and a leading constant $k$:

$$\frac{dr}{dt} = kD_0\Omega \qquad [2.9]$$

The growth mechanism used inherently causes the precipitates to coarsen as $c_r^\alpha$ is a function of the precipitate size. Smaller precipitates have a larger $c_r^\alpha$ value and as the value of $c_i$ decreases, it will cause negative growth rates in the smaller precipitates while the larger precipitates will continue to grow. For the case of a spherical precipitate the exact growth rate is given[127,129,131]] as:

$$\frac{dr}{dt} = \frac{D_0}{r}\Omega \qquad\qquad [2.10]$$

where $r$ is the radius of the precipitate. It is the common approach [118,127,131] to grow the precipitates as spheres as the value of $c_r^\alpha$ is constant for the whole surface. Methods are being developed to calculate this value for each face of precipitate due to anisotropy in the matrix[132]. In itself this is being used to explain the different morphologies found, although Hutchinson et al.[37] used a simpler approach to simulate laths in AZ91. By predetermining the precipitate shape and aspect ratio, the growth in only one dimension is required. This is achieved by using the Zener-Hillert equation, typically used for Widmanstatten plates[133] for the change in length $dL/dt$:

$$\frac{dL}{dt} = \frac{D_0}{2r}\Omega \left(1 - \frac{r_c}{r}\right) \qquad\qquad [2.11]$$

where $r$ now refers to the radius of curvature of the lath tip, as seen in Fig 2.13. $r_c$ is the critical radius of curvature at which the precipitate is neither growing nor shrinking. Unfortunately when $r = r_c$ this solution does not account for the effect of capillarity[133], being weaker on the long sides of the lath and as such Hutchinson et al[37] do not account for the possibility that the precipitate will continue to grow in the perpendicular direction. Nonetheless this model has been shown to match with reasonably accuracy the microstructure observed in AZ91.
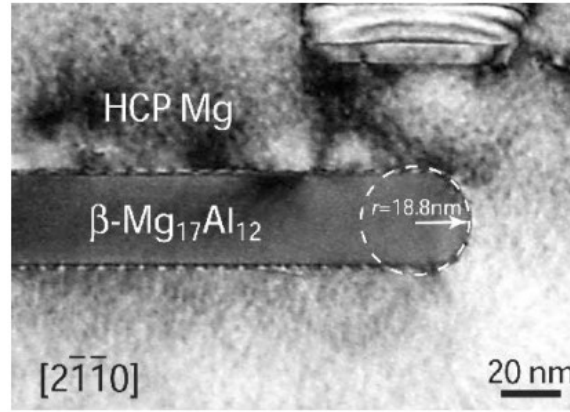
**Fig 2.13:** *Tip of Mg₁₇Al₁₂ plate in AZ91 showing the measured radius of curvature taken from the* $[2\bar{1}\bar{1}0]$ *zone axis. The long edge of the precipitate falls along* $[0\bar{1}10]$ *[37]*

So far we have only stated that the value $c_r^\alpha$ is dependent on the Gibbs-Thomson equation which is widely approximated[127–129] as a function of the surface tension of the precipitate, $\gamma$ and the equilibrium solute content at the precipitate/matrix interface $c_\infty^\alpha$:

$$c_r^\alpha = c_\infty^\alpha \exp\left(\frac{2\gamma V_m}{RTr}\right) \qquad [2.12]$$

where $V_m$ is the molar volume of the precipitate phase. This approximation, though used in a number of applications of the KWN model, doesn't account for stress between the matrix and the precipitate which could have a large implication on coarsening when the Gibbs free energy becomes lower with lower supersaturation. One of the major assumptions of the KWN model is that the same mechanism is used for both growth and coarsening. Aaron and Kotler[134] suggest in fact that the dissolution of precipitates is not the same as growth. They propose an extra term, $\Delta C_K$, be added to the Gibbs Thomson equation to account for the delay in solute transferring from the precipitate to the matrix:

$$c_r^\alpha = c_\infty^\alpha \exp\left(\frac{2\gamma V_m}{RTr}\right) + \Delta C_K \qquad [2.13],$$

the form of $\Delta C_K$ depending on the mechanism by which solute is removed from the precipitate. A summary of the different mechanisms is given in Table 2.9.

*Table 2.9:* *Effect of different atomic detachment methods on the solute content at the precipitate/matrix, $K_x$ are fitted constants*

| Atomic Detachment Method | Additional Term |
|---|---|
| Uniform atomic dissolution | $dr/dt = -K_0 \Delta C_K$ |
| Screw dislocation | $dr/dt = -K_1 \Delta (C_K)^2$ |
| Ledge growth mechanism | $dr/dt = -K_2 (\Delta C_K)^{\frac{1}{2}} \exp\left(\frac{K_3}{\Delta C_K}\right)$ |

Likewise Eqn [2.12] does not account for stress in the system due to lattice misfit. Li et al. [132] suggest that the Gibbs-Thomson equation can be expressed as a function of the capillary length $l_c$ to include the misfit strain, $\varepsilon$, term:

$$c_r^\alpha = c_\infty^\alpha \left(1 + \frac{a l_c}{r} + b \, \frac{l_c \varepsilon^2 C_{44}}{\sigma}\right) \qquad [2.14]$$

where $a$ and $b$ are fitted constants, $C_{44}$ the elastic constant of the precipitate phase (assuming this is approximately the same as the matrix) and $\sigma$, the surface energy per unit length. The relative magnitude of $\Delta C_K$ and the stress term in Eqn [2.14] must all be considered when modelling the precipitate growth; this will be investigated below. Thus through careful measurement of the precipitates in the model alloy, the growth and coarsening of the precipitates in the alloy can be modelled. One final issue that must be discussed is the orientation relationships in Mg-Sn alloys.

## 2.9 Orientation Relationships

In general, most ORs are discovered through observation, though a certain amount of commonality exists when considering typical crystal structures. For example common sense dictates that the orientation relationship between F.C.C. and H.C.P. structures will involve the close packed $(111)_{F.C.C.}$ plane being parallel to the $(0001)_{H.C.P}$ plane. Efforts have been made to generalise ORs[135–138], though as of yet there is no widely accepted framework. Likewise a substantial effort has been made to consider the geometry of the

crystal structures using techniques such as O-lattice theory[139–142], edge to edge matching[136,143–148] and coincident lattice sites[149,150]in order to predict and explain ORs. While this is limited as it does not consider the chemical potential involved in these interfaces, it has been successful in explaining known orientation relationships, as well as, to an extent, precipitate morphologies where an 'easy' growth direction can be identified, where the lattice mismatch is minimised. As of yet the ability to reliably predict ORs in new crystal combinations eludes researchers.

Our situation is more complicated as Mg$_2$Sn, the $\beta$ phase, has a more complex and less common structure, fluorite (CaF$_2$). Very few precipitates of this crystal structure exist and thus there is no well acknowledged set of orientation relationships as there is for more common crystal structures. The structure shares many similarities with the F.C.C. and B.C.C. structures and thus the relations between these two structures and H.C.P. is a good starting point to consider.

Derge et al., then later Henes and Gerold[151,152] identify 4 ORs in the Mg-Mg$_2$Sn system through X-Ray Diffraction (XRD) of binary alloys, but given the number of different precipitate morphologies, this leaves many unknowns about the microstructure. Moreover, a relationship between ageing temperature and the relative proportions of each OR was established that has not yet been fully investigated via TEM. Below 130-200°C the two relationships $(0001)_a//(110)_\beta, [11\bar{2}0]_a//[1\bar{1}1]_\beta$ (OR-1) and$(0001)_a//(110)_\beta, [11\bar{2}0]_a//[001]_\beta$ (OR-2) were found at a ratio of approximately 2:1 at 160°C. Above 200°C however there are two more ORs present, $(0001)_\alpha//(111)_\beta, [11\bar{2}0]_\alpha//[\bar{1}10]_\beta$ (OR-3) and $(0001)_\alpha//(111)_\beta, [11\bar{2}0]_\alpha//[1\bar{1}\bar{2}]_\beta$ (OR-3*). While it is reported that the intensity of the two additional ORs increase more rapidly as the temperature is raised

above 200°C, the intensity even at 300°C is below that of OR-2. A summary of the ORs will

be detailed in Table 2.10.

The 4 ORs are split into two pairs, one for the range 130-300°C and the other for 200-

300°C. Each of the pairs has a common close packing plane. As mentioned above the

$(0001)_{\alpha}//(111)_{\beta}$ archetype found in the HCP/FCC system is only possible at higher

temeratures whereas $(0001)_{\alpha}//(110)_{\beta.}$, more commonly associated with H.C.P./B.C.C.

systems is seen at the lower temperatures and more commonly. We will later see that the

majority of orientations are either $(0001)_{\alpha}//(111)_{\beta}$ or $(0001)_{\alpha}//(110)_{\beta}$, though as the

majority of studies are conducted at 200°C, this temperature dependence cannot be easily

identified. Given the above, we first refer to the available literature to give an overview of

the known ORs and where possible relate this to precipitate morphology.

### 2.9.1 Precipitate Classifications and Reported Orientation Relationships

Due to the lack of symmetry in the magnesium unit cell, the morphology of the precipitates

in the as aged state has a significant effect upon the macroscopic strength as explored in

section 2.7 above. Unfortunately, in the majority of Mg alloys, Mg-Sn included, secondary

phases precipitate as laths or rods in the basal plane [10,144] which are far less effective

at strengthening than their non-basal counterparts. Much effort[20,153,154] has thus

been devoted to better understanding and manipulating the precipitation mechanism,

particularly in order to encourage non-basal precipitates, in an attempt to improve the as-

aged strength of the alloy. In order to clarify the terminology used, the known

morphologies will be described below along with the alloys that they are attributed to and

the orientation relationships that are found in Mg-Sn alloys. This will be later summarised

for ease of reference in Table 2.10.

## 2.9.2 Precipitates with Basal Habit Plane

First we explore the precipitates that form on the basal plane of the magnesium matrix. These come in two morphologies, plates and laths/rods. Even a cursory glance at a micrograph taken with a g-vector parallel to the basal plane will demonstrate that the basal plane is by far the most common habit plane for precipitates, though this has only been quantified in a single Mg-1.3%Sn-1.2%Zn alloy by Mendis et al.[108,109], in which the respective number densities are similar (1.35 and 1.05µm$^{-1}$), this being an exceptional case.
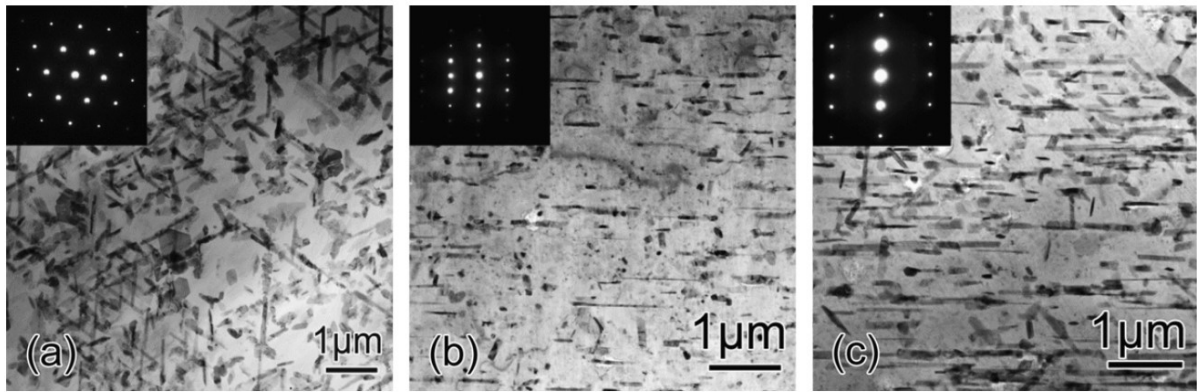


***Fig. 2.14:*** *BF image of peak aged Mg-2.2%Sn-3%Al-0.5Zn alloy aged at 200°C as viewed from a) $[0001]_\alpha$, b) $[11\bar{2}0]_\alpha$ and c) $[10\bar{1}0]_\alpha$*

To begin with plates have a tendency to mirror the magnesium unit cell, with a hexagonal projection when observed in the c direction, with the sides parallel to $\{11\bar{2}0\}_\alpha$. Typically the thickness of the plates in the c direction is of the order of 10s of nm, with a diameter of approximately 1-1.5µm depending on the thermal history and composition of the sample[40,110]. These plates have been observed in Mg-Sn binary alloys[109,110,116,155,156] as well as in numerous ternary alloys[106,108,157].

While the plates are noticeably different from the other precipitate morphologies, the distinction between laths and rods is not always made. Traditionally a lath would be considered to be very flat, having a dimension in the c-direction of the order of a couple

of nanometres compared to a much larger width and length.  In a Mg-1.3Sn binary[108] this is true, with the respective length and width of the laths being around 1500nm and 500nm in peak aged condition compared to a thickness of 54nm, a ratio of approximately 27:9:1; on the other hand, the inclusion of ternary and quarternary alloying have varying effects on these dimensions with, for example a Mg-1.3Sn-2.0Al-0.8Cu-0.5Mn[103] alloy containing laths with a width of 40nm and thickness of 20nm respectively, while maintaining a length of 250nm a ratio of 25:4:2.  A summary of the available data from the literature on the sizes of precipitates is given above in Table 2.6.  For now, the basal precipitates will be considered as laths given their morphology in the binary alloy.

Lath shaped precipitates are common in most Mg alloys, and are seen in the Mg-Sn binary[109,110,155,156] as well as ternaries containing Al[104,110,155], Zn[108,111,116,157] and Mn[106,149,150].  Typically they will grow in all three $\langle 11\bar{2}0 \rangle_\alpha$ type directions and each author has their own preference when reporting the specific direction in the OR. In reality the OR can be rotated such that any one of the $\langle 11\bar{2}0 \rangle_\alpha$ directions is parallel to the direction in the precipitate crystal.  However, for the reader's benefit and for consistency, the below have all been stereographically rotated such that the growth direction is given as $[11\bar{2}0]_\alpha$.  Below the observed relationships for plates and laths/rods that fall in the basal plane are reviewed.  Most often the heat treatments are conducted at 200°C until peak hardness and thus, for brevity, unless explicitly stated otherwise, this can be assumed.  Exact ageing times where given in the literature will be inserted below in Table 2.7, where the ORs for all precipitate morphologies will be summarised.

To begin with, the most commonly reported orientation relationship between these Mg$_2$Sn basal plates and the matrix is the Burgers relationship[108,111,149,150],

$$(0001)_\alpha//(110)_\beta, [11\bar{2}0]_\alpha//[1\bar{1}1]_\beta, \qquad \text{(OR-1)},$$

with this being widely reported elsewhere including the AZ series[40,41,146]. There are however a few reported deviations from this OR. The Burgers relationship has likewise been observed for basal lath morphology precipitates in a Mg-2.2Sn[156] and Mg-1.64Sn-1Mn alloy[149,150], though a small deviation of 0.21° is reported for the laths in the ternary alloy, this being explained by the authors within the context of a constrained coincident site lattice (CCSL) model.

Elsewhere El-Sayed et al.[110] also report laths with:

$$(0001)_\alpha//(110)_\beta, [11\bar{2}0]_\alpha//[1\bar{1}\bar{2}]_\beta \qquad \text{(OR-1*)},$$

known as the Gjonnes-Ostmoe OR[53], in a set of Mg-2.2Sn-0/1/3Al ternaries. These laths co-exist in the alloys with another set of laths with the OR:

$$(0001)_\alpha//(110)_\beta, [1\bar{2}10]_\alpha//[001]_\beta \qquad \text{(OR-2)};$$

Both $Mg_2Sn$ and the F.C.C. $Mg_{17}Al_{12}$ precipitates are present in El-Sayed et al.'s alloy, sharing the two ORs with no reported preference for either chemical composition or OR. $Mg_{17}Al_{12}$ has previously been observed with the Gjonnes-Ostmoe OR in Mg-Al alloys[146], but the morphology differs in the fact that it was in a lens shaped precipitate situated on the $\{\bar{1}100\}_\alpha$ prismatic plane. The reason for the change in morphology is not yet clear, nor why the basal plane is favoured in the Mg-Sn-Al alloy. The case that El-Sayed et al report with the OR varying throughout the sample is not isolated, Nie et al[156] report both OR-1 and OR-2 in a Mg-2.2Sn binary, with 75.1% of laths exhibiting OR-1 and the rest OR-2.

Shi et al.[149,150] also report OR-1* for a Mg–1.64Sn–1Mn alloy. This and the work of El Sayed et al.[110] are the only observations of OR-1* for precipitates with the basal lath morphology, but Sasaki[111] reports the same OR for the plate morphology in a Mg-2.2Sn-

0.5Zn-0/0.5Al. All three studies used the same ageing temperature, with El-Sayed et al. and Sasaki et al. using very similar compositions; the variation arises as the plate like precipitates are found in a sample that had been aged at 70°C for 24hrs prior to the treatment at 200°C. Thus the discrepancy can be attributed to this unusual ageing treatment, potentially altering the nucleation mechanism of the plate, though other precipitate morphologies display the same Ors as seen in a single ageing treatment at 200°C. It remains to be seen whether this orientation relationship is present for other conditions.

As an aside which will be discussed in more detail later, OR-1 is also displayed by both basal and prismatic laths in the work of Mendis[108], and prismatic and pyramidal precipitates share an OR in the work of Sasaki[111]. Thus we have numerous cases where an OR can be common to different precipitate morphologies or different precipitate compositions, even within the same sample. Also a particular precipitate type can exhibit different ORs in a single sample.

Continuing with the variations in ORs, above we introduced (OR-2), a commonly reported OR for laths lying in the basal plane. This has been reported in a Mg-2.2Sn binary[106] and Mg-Sn ternaries with both Al and Zn as well as in some alloys microalloyed with Mn[110,149,150] and aged at 200°C and in a Mg-1.1Sn-0.13Mn-0.20Si alloy aged at 250°C[106]; full details of the heat treatments are given in Table 2.7. Again this OR, known as the Pitsch-Schrader OR, is seen elsewhere though not in Mg-Al alloys[146]. The growth direction is not along a well-defined direction in the matrix, instead falling 5.26° from $[1\bar{1}1]_\beta$ in the precipitate crystal (the growth direction of OR-1).

Similarly, El-Sayed et al.[110] have reported the orientation relationship of :

$$(10\bar{1}0)_\alpha//(1\bar{1}0)_\beta, [1\bar{2}10]_\alpha//[001]_\beta \qquad\qquad \text{(OR-2')}$$

in Mg-2.2Sn-0/1/3Al aged at 200°C for laths in the basal plane. By crossing the vectors with the corresponding planes, we can infer that $[0001]_\alpha//[110]_\beta$, thus matching OR 2 reported above. This however is partially flawed as it is observed from the $[10\bar{1}0]_\alpha$ direction. This does not allow us to link this OR directly with a particular growth direction for the lath morphology as the projections of all of the $\langle11\bar{2}0\rangle_\alpha$ vectors are identical in direction when viewed from $[10\bar{1}0]_\alpha$.

A variation on OR-2 has been investigated by Shi et al[149,150]. in the Mg-1.64Sn-1Mn alloy. This represents a 90° rotation of the precipitate around the $(0001)_\alpha//(110)_\beta$ plane normal resulting in an OR of:

$$(0001)_\alpha//(110)_\beta, [1\bar{1}00]_\alpha// [001]_\beta. \qquad\qquad \text{(OR-2*)}$$

However the only observation of this OR occurred when the precipitate was in contact with another precipitate along the broad side of the precipitate with the other precipitate having OR 2. It is not clear whether this OR is possible in isolation or is a result of growing in contact with the other lath and thus is viewed with some scepticism as an OR in its own right.

Likewise the OR:

$$(0001)_\alpha//(111)_\beta , [11\bar{2}0]_\alpha//[\bar{1}10]_\beta, \qquad\qquad \text{(OR-3)}$$

is also commonly observed in basal laths for example in Mg-1.3/1.9Sn[109], Mg-2.2Sn-0/0.1/0.5Zn ternary[116], and Mg-2.2Sn-0/1/3Al as well as three different Mg-Sn quaternary alloys[107,110,158]. As previously mentioned the difference in the parallel planes has been previously linked to the ageing temperature; 200°C is given by Henes and Gerold[152] as the dividing line between the two domains, with $(0001)_\alpha//(111)_\beta$ occupying the higher temperature range. OR 3 and OR 2 may represent the two most favoured ORs for the basal laths; indeed OR3 is one of those presented by Henes and

Gerold for the 200-300°C range. However, Liu et al.[112] observe basal laths with OR 3 at both 200 and 160°C in a Mg-2.2Sn-0.5Zn alloy. We thus conclude that there are more effects present than simply the ageing temperature as $(0001)_\alpha//(111)_\beta$ is observed at a temperature lower than that given in the work of Henes and Gerold. This will be discussed in full in the following section.

Many reports of $(0001)_\alpha//(111)_\beta$ have been made in the Mg-Mg2Sn system, where there has been a survey of the microstructure. Both Derge et al. and Henes and Gerold[151,152] report the presence of:

$$(0001)_\alpha//(111)_\beta \, , [11\bar{2}0]_\alpha// \, [11\bar{2}]_\beta \, ; \tag{OR-3*}$$

in their Mg-Sn binary alloys when aged between 200-300°C. As of yet this has not been observed via electron microscopy, but as it can be clearly identified using XRD it is safe to assume that it is not sufficiently rare to have been missed by the previous studies and thus is likely to be a result of the higher aging temperature for which current studies are limited. What is more this is identical to the Crawley relationship as identified in AZ91[51,52,146] for precipitates on the prismatic plane. Whether this is the case in the Mg-Sn system is yet to be seen. It is worth noting that the OR represents a 90° rotation of the $(111)_\beta$ plane of OR-3, similar to the variation observed by Shi et al. for OR-2 when precipitates have co-nucleated. This might suggest that the OR is a result of co-nucleation of precipitates as seen by Shi and co-workers[149,150].

Incidentally, two small variations upon OR-3 are reported. Zhang et al.[106] reported an orientation relationship of:

$$(0001)_\alpha//(111)_\beta, [11\bar{2}0]_\alpha \sim 9° \text{ from } [1\bar{1}0]_\beta \tag{OR-3'}$$

in a Mg-1.1Sn-0.13Mn-0.20Si alloy for basal plates. There are no other common directions in the lattice, nor has this been observed elsewhere, though again this may be related to

the lack of studies at the higher temperature of 250°C. In order to confirm the reason for this change, i.e. the composition or the temperature, further evidence is required.

Liu et al.[112] observe a small (~70nm diameter) irregular hexagonal plate with the OR:

$$[11\bar{2}0]_\alpha //[\bar{1}10]_\beta, (0001)_\alpha \sim 13.7° \text{ from } (111)_\beta. \qquad \text{(OR-3'')}$$

Again, no other low index directions match in the matrix and precipitate, possibly accounting for its relatively small size.

Lastly, Zhang et al.[106] also present a basal lath OR not reported otherwise:

$$(0001)_\alpha //(110)_\beta, [1\bar{1}00]_\alpha //[\bar{1}13]_\beta; \qquad \text{(OR-4)}$$

This is unique as not only has this OR not been reported elsewhere, but also the growth direction is not of the $\langle 11\bar{2}0 \rangle_\alpha$ type as with all other observed laths but instead $\langle 10\bar{1}0 \rangle_\alpha$. Again the higher temperature used and the less investigated composition Mg-1.1Sn-0.13Mn-0.20Si could be contributing factors.

### 2.9.3 Precipitates with Non-Basal Habit Plane

Celotto[40] observed changes in morphology with temperature in AZ91. Laths growing in the basal plane were widely seen across all temperatures whereas non-basal rods with $[0001]_\alpha$ growth direction became less prominent with higher temperature, being very rare above 150°C despite being widely seen below it. Thus temperature dependence of both the morphology and OR of precipitates in magnesium alloys is not unheard of but as of yet there is little systematic investigation of these effects in Mg-Sn alloys.

As previously mentioned, non-basal precipitates are far less common than basal, not existing at all in the binary alloy. However these non-basal precipitates are of great benefit[38] to the strength of the alloys; the inclusion of ternary alloying elements, particularly Zn and Al, is associated with the presence of these non-basal precipitates. There are multiple morphologies of non-basal precipitates, as with the basal precipitates

investigated above, and these will be initially described. Firstly, rods of similar dimensions to the laths seen in the basal plane are known to grow on the prismatic planes [108,111] of Mg alloys. Moreover a number of Mg-Sn alloys[108,111,112] exhibit laths on pyramidal $\{11\bar{2}2\}_\alpha$ habit planes. These are easily identifiable by their shorter length and greater width than laths in the basal plane.

Aside from those precipitates with a long axis, precipitates described as polygons are present in some alloys[106] These usually are equiaxed and typically are not said to have a habit plane in the same manner as the elongated precipitates and thus are included here in the non-basal section. The majority of the non-basal precipitates draw from the same set of OR's described above for the basal precipitates and thus the focus will be on discussing the cause of the non basal precipitates as well as their coexistence with other precipitates, particularly where OR's are shared between multiple morphologies.

To begin with, we introduce the final OR that has yet to be mentioned. This OR has been reported in two similar forms both in Mg-2.2Sn-0.5 Zn alloys. Initially Sasaki et al.[111] reported a pyramidal lath (wrongly labelled as prismatic in the paper) with an OR of:

$$(1\bar{1}00)_\alpha // (111)_\beta, [11\bar{2}0]_\alpha // [0\bar{1}1]_\beta. \qquad \text{(OR-5)}$$

Similarly, Liu et al[156] report an OR for a pyramidal lath of

$$(0001)_\alpha \ 15.4° \text{ from} (111)_\beta, [11\bar{2}0]_\alpha // [0\bar{1}1]_\beta \qquad \text{(OR-5')}$$

There is actually very little difference between OR-5 and OR-5'; in both $[11\bar{2}0]_\alpha // [0\bar{1}1]_\beta$. While Liu et al. decide to note that $(0001)_\alpha$ falls 15.4° from $(111)_\beta$, in fact $(0001)_\alpha$ is closer to $(2\bar{1}\bar{1})_\beta$, being only 4.6° away.

What is more, Sasaki et al. emphasise the importance of the $(11\bar{2}2)_\alpha$ and $(1\bar{2}1)_\beta$ planes being near parallel due to the good matching between the atomic position on the two

phases. Using the stereographic projection, it can also be shown that $(11\bar{2}2)_\alpha$ is nearly parallel with $(1\bar{2}1)_\beta$ in Liu et al.'s observations, with approximately 5° misoriention between the two plane normals and thus we can conclude that while a small deviation does exist between the two, the OR has the same basis. This explains the preferred growth direction of the precipitate given the relatively low interfacial strain on $(11\bar{2}2)_\alpha$ (hence low interfacial energy). Moreover, both of the above have reported these pyramidal laths coexisting with basal laths and plates with OR-3, giving more credence to the fact that the two microstructures share properties.

Elsewhere, pyramidal laths and prismatic rods have been reported by Sasaki et al.[111] and Mendis and co-workers[108] in Mg-2.2Sn-0.5Zn and Mg-1.3Sn-1.2Zn. Both of these alloys have 3 types of lath shaped precipitate, basal, pyramidal and prismatic, that share 2 different ORs, with the basal laths favouring OR-3 and pyramidal laths exhibiting OR-1 in both cases. However, disagreement arises as to the OR of the prismatic rods with Sasaki et al. reporting OR-1 and Mendis et al. reporting OR-3. Interestingly the precipitates in both of these alloys share ORs between two morphologies and both show ORs with both $(111)_\beta$ and $(110)_\beta$ as the plane parallel to $(0001)_\alpha$. This shows the that temperature is not the sole reason for the change between $(111)_\beta$ and $(110)_\beta$, as hinted at by the work of Henes and Gerold.

Finally we report the ORs observed for polygon precipitates. Reports are limited with Zhang and co-workers[106] reporting polygons with OR-3 in a Mg-1.1Sn-0.13Mn-0.20Si alloy aged at 250°C. With no comparable observations, no conclusion can be drawn. In Table 2.10, the above orientation relationships have been summarised with full details of the relevant heat treatments.

**Table 2.10:** *Summary of orientation relationships observed for Mg₂Sn in the Mg-Sn family of alloys – need to complete with ageing times*

| OR ID | Orientation Relationship | Morphology | Composition | Ageing temp | Ref |
|---|---|---|---|---|---|
| OR-1 | $(0001)_\alpha//(110)_\beta$ $[11\bar{2}0]_\alpha//[1\bar{1}1]_\beta$ Burgers OR | | Mg-Sn Binary | 130-300°C | [152] |
| | | Basal Lath | Mg–1.64Sn–1Mn Small 0.21° deviation | 200°C 270hrs | [149,150] |
| | | | Mg-2.15Sn | 200°C | [156] |
| | | Pyramidal | Mg-1.3Sn-1.2Zn | 200°C | [108] |
| | | | Mg-2.2Sn-0.5Zn | | [116] |
| | | Prismatic | Mg-2.2Sn-0.5Zn | 200°C | [116] |
| OR-1* | $(0001)_\alpha//(110)_\beta$ $[11\bar{2}0]_\alpha//[1\bar{1}\bar{2}]_\beta$ Gjonnes Ostmoe OR | Basal Plate | Mg-2.2Sn-0.5Zn-0/0.5Al | 70°C/ 24hrs then 200°C | [111] |
| | | Basal Lath | Mg-Sn Binary | 130-300°C | [152] |
| | | | Mg–1.64Sn–1Mn | 200°C | [149,150] |
| | | | Mg-2.2Sn-0/1/3Al | | [110] |
| OR-2 | $(0001)_\alpha//(110)_\beta$ $[1\bar{2}10]_\alpha//[001]_\beta$ Pitsch Schrader OR | Basal Lath | Mg–1.64Sn–1Mn | 200°C | [149,150] |
| | | | Mg-2.2Sn-0/1/3Al, | | [110] |
| | | | Mg-2.15Sn | | [156] |
| | | | Mg-2.2Sn-0.1Mn-0/0.1/0.5Zn, | | [104] |
| | | | Mg-1.1Sn-0.13Mn-0.20Si | 250°C | [159] |
| OR-2* | $(0001)_\alpha//(110)_\beta$ $[1\bar{1}00]_\alpha//[001]_\beta$ | Basal Lath | Mg–1.64Sn–1Mn | 200°C | [149,150] |
| OR-3 | $(0001)_\alpha//(111)_\beta$ $[11\bar{2}0]_\alpha//[\bar{1}10]_\beta$ | | Mg-Sn Binary | 200-300°C | [152] |
| | | Basal Lath | Mg-1.3/1.9Sn Mg-1.3Sn-0.13Na | 200°C | [109] |
| | | | Mg-1.3Sn-1.2Zn-(0.19Na) | | [108] |
| | | | Mg-2.2Sn-0.5Zn-(1.0Al) | | [110] |

| OR | Relationship | Morphology | Alloy | Temperature | Ref |
|---|---|---|---|---|---|
| | | | Mg-2.2Sn-0/1/3Al | | [116] |
| | | | Mg-2.2Sn-0/0.1/0.5Zn | | [157] |
| | | | Mg-2.2Sn-3Al-0.5Zn | | [111] |
| | | | Mg-1.52Sn-0.94Al-0.39Zn | | [107] |
| | | | Mg-2.2Sn-0.5Zn | 160°C and 200°C | [112] |
| | | | Mg-1.75Sn-2.86Al-0.92Si | Die cast | [158] |
| | | Polygon | Mg-1.1Sn-0.13Mn-0.20Si | 250°C | [106] |
| | | Prismatic | Mg-1.3Sn-1.2Zn | 200°C | [108] |
| OR-3' | $(0001)_\alpha // (111)_\beta$ $[11\bar{2}0]_\alpha$ 9° from $[\bar{1}10]_\beta$ | Basal Plates | Mg-1.1Sn-0.13Mn-0.20Si | 250°C | [106] |
| OR-3'' | $[11\bar{2}0]_\alpha // [\bar{1}10]_\beta$ $(0001)_\alpha$ 13.7° from $(111)$ | Basal Plates | Mg-2.2Sn-0.5Zn | 200°C | [112] |
| OR-3* | $(0001)_\alpha // (111)_\beta$ $[11\bar{2}0]_\alpha // [11\bar{2}]_\beta$ Crawley OR | | Mg-Sn | 200-300°C | [152] |
| OR-4 | $(0001)_\alpha // (110)_\beta$ $[1\bar{1}00]_\alpha // [\bar{1}1\bar{3}]_\beta$ | Basal Lath {10-10} | Mg-1.1Sn-0.13Mn-0.20Si | 250°C | [106] |
| OR-5 | $(1\bar{1}00)_\alpha // (111)_\beta$ $[11\bar{2}0]_\alpha // [0\bar{1}1]_\beta$ | Pyramidal | Mg-2.2Sn-0.5Zn | 200°C | [111] |
| OR-5' | $[11\bar{2}0]_\alpha // [0\bar{1}1]_\beta$ $(0001)_\alpha$ 15.4° from $(111)_\beta$ | Pyramidal | Mg-2.2Sn-0.5Zn | 200°C | [112] |

## 2.10 Discussion of Morphologies

As mentioned above, Celloto's work[40] on FAZ91 indicated the importance of ageing temperature to the ratio between basal and non-basal precipitates, although there still is no confirmed relationship in Mg-Sn alloys. That being said, despite the increase in peak hardness gained from the lower ageing temperature, 200°C remains the standard temperature used for ageing AZ alloys due to the reduction in time to peak hardness. Most reported microstructural studies on Mg-Sn alloys relate to 200°C and therefore there is

the question of what happens with varying temperature. Certainly the first report of the ORs in Mg-Sn given by Henes and Gerold[152] indicates a transition of ORs at 200°C. This may explain certain inconsistencies in the ORs found, with the scarcity of certain ORs occurring in precipitat.es nucleated below the targeted ageing temperature, given that no heat treatment is perfect as a finite amount of time is required to heat and cool the sample. We can however assume, given that certain ORs are reported widely, that on the whole small alloying additions do not affect the ORs of specific morphologies but instead allow for a wider variety of morphologies to grow, as demonstrated by the lack of non-basal precipitates in the binary alloy and the stark increase in number density of precipitates in ternaries. While the rods are more efficient in blocking basal slip, the impracticality of ageing at such low temperatures for such long time periods mean that this is generally avoided.

It is recognised as well that, despite no change in the composition, habit planes, growth directions and orientation relationships vary within the same microstructure[108,111,156]; clearly we must be careful when generalising ORs or precipitate morphologies to a particular chemistry but instead recognise that orientation relationships are sensitive to precipitate morphology as well as ageing conditions. In order to properly understand how a microstructure evolves, we must consider both these parameters. As 200°C is considered a typical temperature for heat treatment of magnesium and is used in the majority of studies so far, the following comments will relate only to samples aged at this temperature.

One aspect that is analysed in detail by Zhang and co-workers[136] is the importance of the a/c ratio, as well as the ratio between the matrix and precipitate lattice constants, in determining orientation relationships in F.C.C/H.C.P. However their conclusion is that

with a c/a ratio of ~1.6 and the ratio between matrix and precipitate lattice constant ($a_M/a_P$) of ~0.5 there should be no stable ORs as no clearly favourable edge to edge matching can be found i.e. within 10% lattice mismatch. As shown by the literature this is not the case for the Mg-Mg$_2$Sn system, with no stable ORs; nonetheless their work demonstrates the importance of a/c ratio in determining OR based upon the edge to edge matching logic.
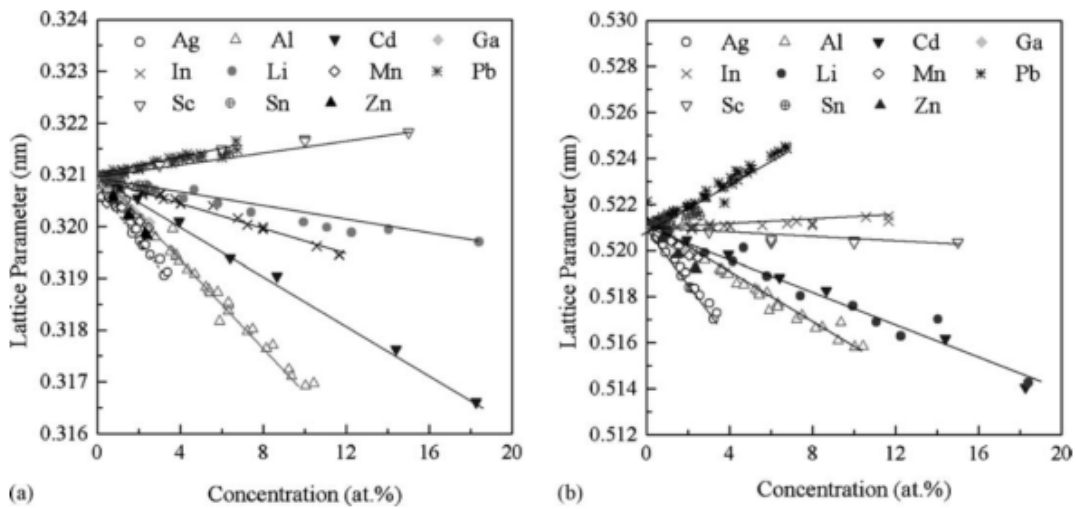


***Fig. 2.15:*** *Effect of various alloying additions on the a and c parameters of magnesium*[109]

Mendis et al.[108] examine this same effect, considering the effect that different alloying elements have on the a and c lattice parameters of the matrix and thus the spacing of the non-basal planes. It can be clearly seen in Fig 2.15 that even at low concentrations, both Zn and Al, as well as Mn are effective in reducing both the a and c dimensions of the matrix. It is well established[108,136] that the ratio $a_M/a_P$ is also important in adjusting precipitate morphology as well as determining the possible ORs; with different ORs it becomes possible that directions off the basal plane become easy growth directions, thus leading to precipitates with non-basal habit planes. Other elements that have yet to be investigated such as Ag, Li and Cd have so far not been investigated thoroughly, though

may cause a similar effect. It can be seen from Table 2.7 that the only alloys with pyramidal precipitates contain Zn[108,111,116,156].

## 2.11 Objectives

The challenges facing magnesium alloys are two-fold: firstly the tendency to form precipitates on the basal plane, thus not effectively impeding basal glide, so important in the deformation of H.C.P. materials and secondly the lack of cost effective alloys for producing lightweight components to operate at high temperature.

While RE and Sr additions have produced alloys with excellent mechanical properties at high temperature, these are exclusively used for niche applications such as in space exploration where their high cost is offset by the aggressive need for weight reduction to reduce fuel consumption. The common usage of Al as the sole precipitate forming addition is detrimental to this due to the inherent lack of thermal stability of the γ phase that is prominent in all Mg-Al alloys despite much research effort that has been devoted to improving this. On the other hand, Mg-Sn shows promise in offering alloys that have sufficiently favourable mechanical properties at high temperatures but can be produced in a cost effective manner with elements that are in higher abundance.

Mg-Sn is not without its flaws, despite the favourable solubility change between the melting point of the alloy and room temperature. Precipitates are coarse in the binary alloy and the mechanical strength is below that achievable by industrially used alloys such as the AZ, ZK and WE series. Thus an effort to better understand the microstructure and ageing behaviour of Mg-Sn is needed in conjunction with optimisation of mechanical properties in order to present Mg-Sn alloys as a viable alternative to existing alloys.

# 3 METHODOLOGY

## 3.1 Sample Production

Ingots were cast from Mg, Al and Sn, all above >99.5% purity. The pieces of magnesium were polished shortly before melting in order to remove the majority of the oxide present, reducing the potential for contamination of the melt. Two compositions were produced, Mg-1.75Sn-1.93Al (at%), (Mg-8Sn-2Al(wt%) Composition A) and Mg-1.29Sn-2.85Al(at%) (Mg-6Sn-3Al(wt%), (Composition B). These are nominal values based on the percentage of raw materials used.

Raw materials were placed in a vacuum induction furnace containing a mild steel crucible. The furnace was evacuated down to approximately 0.5 mbar before being purged with 600mbar of argon. This process was repeated 3 times before melting began to ensure the amount of oxygen and moisture was minimal. Once the metal was visibly melted in the crucible, it was held for 2 minutes before being poured into a 5mm thick rectangular steel mould with dimensions 100mm x 67mm x 34mm. The ingots were left to cool before being removed from the furnace. Subsequently they were cold rolled until visible cracking initiated with the thickness of the ingot reducing approximately 10%. The ingot was subsequently cut to 6 approximately equally sized pieces before remelting in order to ensure homogeneity. This process was then once again repeated.

An approximately 1cm section was cut through the middle of the ingot before being wrapped in tantalum foil and sealed in a quartz tube in a protective argon atmosphere at around 800mbar. The tantalum ensures that no reaction occurs between the quartz and the sample as $Mg_2Si$ has been known to form[160]. The sample was then solution treated at 510°C for 40hrs to remove any precipitation from the casting process before being

quenched in cold water.  The samples were cut into quarters for subsequent ageing at 200°C in a tube furnace.  Artificial ageing took place for 40, 72 and 160 hours respectively with the remaining material being examined to characterise the as solution treated state. These times were selected to roughly approximate the nucleation/growth phase, approximate peak hardness and the coarsening stage of precipitation.

## 3.2    Sample Preparation for SEM and Hardness Testing

Two sets of samples were prepared in broadly the same way, one set for OM and SEM observation and the other for hardness testing.  The main difference lies in the mounting of the specimens; in order to give an undistorted result in Vickers hardness testing it is vital the sample be flat and perpendicular to the indenter.  To ensure this, the samples were mounted using the Metprep Variset system.  The fact that mounting material is poured in a liquid state means that naturally the bottom surface will be flat and parallel to the bottom of the mold.  However the Variset mounting material is non-conductive, thus SEM samples were mounted on aluminium stubs after grinding and polishing.  The samples were attached using a small amount of superglue to prevent movement and silver DAG paint to ensure good conduction.

Both sets of samples were ground and polished in the usual manner, being first made planar with 400 grit SiC paper followed by successive steps of 800 and 1200 grit SiC paper before polishing with 3µm then 1µm diamond paste on two separate Struers Nap discs lubricated with ethanol.  The final step consists of a short polish on a Struers Chem disc with a small amount of OPS, though this was omitted for the hardness samples due to the length scales of interest being far greater than 1µm.  After each step the surface was then doused in ethanol to remove any debris before being rapidly dried using warm air to prevent drying marks.

### 3.3   Hardness Testing

Hardness testing was conducted using a Vickers indenter fitted in a Struers Durascan with a load of 0.1kg.  100 indents were made in a grid, with each indent separated by 300µm to ensure that no work hardening from previous indents was detected.  Results were then averaged (and a standard deviation calculated) to determine the hardness of the sample.

### 3.4   Number Density and Area Fraction

All SEM observations were made in a Tescan Mira XM-3 equipped with both secondary electron (SE) and backscatter electron (BSE) detectors, an Oxford Instruments X-max 80 energy dispersive X-ray spectrometer (EDX) and a Nordlys Nano electron back scatter detector (EBSD), both using the Aztec software package.  BSE images were taken at a regular view field of 10 x 7.5 µm across the sample and then processed using FIJI[161].  At least 20 BSE micrographs per sample of a fixed 10µm view field were taken at intervals between 100 and 200µm.  Number density was determined by manual counting of the precipitates whereas the area fraction was determined using a FIJI script.

### 3.5   X-Ray Diffraction Data

In order to ascertain and quantify the phases present in the as-cast and aged sample XRD can be employed.  While OM, SEM and especially TEM are limited to small areas, X-rays in the XRD interact with a volume of several hundred microns depending on how well collimated the beam is and the energy of the X-rays. XRD measurements were made using an Inel Equinox for an acquisition period of 30 minutes.  This utilizes a fixed detector that covers the angle between 0° and 135° degrees and a rotating sample holder.  A Cu anode was used with a Ge filter producing Kα radiation with a wavelength of 0.15418 nm.  Phase identification is relatively easy; the XRD data can be directly imported into the Match! software, allowing access to an extensive catalogue of crystallographic data.

Quantification of volume fractions however requires a far more extensive procedure. A number of methods have been proposed, some using single peaks for comparison, but the most common is based upon a Rietveld type approach[162–164], which will be explored below. This has the advantage of using the entirety of the pattern thus negating errors that can occur when using single peaks such as preferred orientation or peak broadening due to strain.

The Rietveld method relies on a modelled spectrum given a set of known crystal structures and attempts to minimize a least squares fitting function to best fit the acquired spectrum, in the process giving each crystal a different weighting, corresponding to quantity. Mathematically this least squares parameter, $W$, is calculated as:

$$W = \sum_i \frac{(I_i^{exp} - I_i^{calc})^2}{I_i^{exp}}, \qquad\qquad [3.1]$$

where $I^{exp}$ and $I^{calc}$ are the intensities, determined by experiment and calculation respectively. For this to work successfully we must however have an accurate means to produce $I_i^{calc}$. Here we give the classical diffracted intensity equation for a number of peaks, $k$, diffracted from an initial intensity of $I_0$, summed over a number of phases, $j$, each with a calculated unit cell volume $V_j$ and a fitted volume fraction $f_j$:

$$I_i^{calc} = I_0 \sum_n \frac{f_n}{V_n^2} \sum_m L_m |F_{n,m}|^2 S_m(2\theta_i - 2\theta_{m,n}) P_{m,n} A_n + B(2\theta). \qquad [3.2]$$

This in itself is the product of a number of functions summed with a background function $B(2\theta)$ which combine to fully describe the complex shape of the XRD spectrum. $L_k$ is the Lorentz polarization factor, $F_{m,n}$ the structure factor $S_m(2\theta_i - 2\theta_{m,n})$ a peak shape function, $P_{m,n}$ is a preferred orientation function and $A_j$ the absorption factor determined

by the detector geometry. Each of these will be described below.

### 3.5.1 Structure Factor

Structure factor is commonly used across both X-ray diffraction and TEM and will later be used in calculating the thickness of a TEM foil. It is calculated by considering scattering from each of the lattice points in the primitive cell. In the case of magnesium we have a rhombohedral unit cell with atoms located at (0,0,0) and (1/3,2/3,1/2). The structure factor can be expressed generally as:

$$F_{hkl} = \sum f_j \, e^{2\pi i(uh + vk + wl)}, \qquad [3.3]$$

where $f_j$ is the atomic scattering factor, which is a function of atomic number and $d_{hkl}$. Summing both atomic locations in our unit cell and multiplying through by the complex conjugate to give the square of the magnitude, we are left with the expression for the square of the absolute value of $F$ for magnesium:

$$\left| F_g \right|^2 = 4f_{Mg}^2 (\cos^2 \pi g), \qquad [3.4]$$

where, from the magnesium primitive cell:

$$g = \frac{h + 2k}{3} + \frac{l}{2}. \qquad [3.5]$$

In the case of the precipitates, this calculation can be repeated, where $f_j$ is selected for each lattice site based upon which atom is expected to sit in the given position. The $CaF_2$ structure is well known and relatively simple and thus we quote the result as:

$$F_{hkl} = \left[ f_{Sn} + f_{Mg} . 2 . \cos \frac{\pi}{2} (h + k + l) \right] \qquad [3.6]$$

This can be generalised to 3 possible results dependent on the sum of h,k,l:

$$F_{4n} = 4(f_{Sn} + 2f_{Mg}),\qquad\qquad [3.7a]$$

$$F_{2n} = 4(f_{Sn} - 2f_{Mg}),\qquad\qquad [3.7b]$$

$$F_{2n+1} = 4(f_{Sn} + 2f_{Mg}),\qquad\qquad [3.7c]$$

where n is any integer. These calculations however do rely on measurements of $f_j$, made on pure materials. It has previously been discussed that the crystals we deal with do not always have the precise composition we assign when making these calculations. However given that the alloys used are dilute, and the Al and Sn sit substitutionally on the magnesium lattice sites, it is a reasonable assumption that the structure factor will not vary greatly from that calculated.

### 3.5.2   Lorentz-Polarisation Factor, Shape Factors, Absorption and Preferred Orientation

Both the Lorentz-polarisation factor and the shape factor are loosely linked. Both arise due to the finite width of the peaks found within XRD. While mathematically we model both our lattice points and our Ewald sphere as infinitesimally small, they do in fact in the real case have a finite width. This is evidenced in the XRD spectra. A perfect case would yield a line corresponding to a $\delta$-function, but what is observed is a peak distributed over a small $2\theta$ range.

Our shape factor is a parameter allowing us to model this. We must remember that this arises not only from the finite size of the atoms involved but in a practical situation is also restricted as our detector elements have finite size and our beam is collimated to a finite width. Therefore we simply select a function with which to model this. In this work a Pseudo-Voigt peak type has been used due to its flexibility.

The Lorentz polarisation factor is a compound of two mechanisms,. Firstly the polarisation of the emitted electromagnetic wave from the electron, coming from the

scattering from an isolated atom; secondly there is the Lorentz factor, which arises due to the fact that the Ewald sphere and lattice points are not in fact infinitesimally small but have a finite width and size respectively. Fortunately neither factor varies in any way for different phases and thus can simply be stated as a function of Bragg's angle $\theta$:

$$L = \frac{1 + \cos^2 2\theta}{\sin^2 \theta \cdot \cos \theta.} \qquad [3.8]$$

As mentioned each peak was modeled using the Pseudo-Voigt expression, itself a compound of both Gaussian and Lorentz functions, allowing for asymmetry of the peak. Aside from the factors above this the quantification also considers absorption and preferred orientation factors. As the incident beam only impinges on a small area, only a finite number of grains were measured meaning not all reflections are excited equaly. Because of this preferred orientation must be considered. Partly due to the limited number of grains and partly due to the preference of the precipitates to sit on the basal habit plane, we must weight each of the diffraction peaks given the geometry of the sample. Moreover, as the x-rays are travelling through the sample and some attenuation will occur, this is accounted for via an absorption factor.

### 3.5.3   Implementation and Limitations

Diffract.Suite Topas was used for quantification of the respective diffraction patterns using an iterative approach. Initially the program was given the structure of the unit cells for each of the possible phases and told to subtract a background; the program could refine this in order to better fit to the peaks present using a least squares fitting function.

The fit was inspected and then preferred orientation functions were introduced and iterated to minimize the least squares fitting parameter to account for peaks that were larger than expected. The program could then again iteratively refine these weightings in order to minimize the least squares fitting function.

While XRD is a very useful tool its limitations should not be forgotten. The ideal case for XRD is a powder, where the crystals are small (a few μm) and randomly oriented. This is dissimilar to the case we present whereby we only inspect a number of grains, each with their own orientation. Because of the small number of grains inspected, each of different size, there will always be a preference toward certain orientations as seen by the detector. This is something that must be considered when quantifying the XRD spectra and is really one of the benefits of the Rietveld type model, which uses the entire spectrum.

### 3.6    Sample Preparation for TEM and Observation

For TEM samples, thin strips of material ~1-2mm thick were cut from the ingot using a low speed saw and a SiC blade and then polished down to approximately 150μm thickness. 3mm discs were then punched from the material for twinjet polishing and further gently ground down to below 100μm using 1200 grit SiC paper to prevent large amounts of work hardening. A Tenupol III was used with an electrolyte of 10g Lithium Chloride and 22g Magnesium Perchlorate dissolved in 1000ml methanol and 200ml butoxyethanol cooled to between -20°C and -30°C with liquid nitrogen. A voltage of ~40V is applied, producing a current of ~0.1A depending on how much the solution had been previously used. The parameters given above are only approximate as twinjet polishing is sensitive to many different variables, including the microstructure of the sample: as such it should be expected that a certain amount of skill is required on the part of the operator in order to produce a good sample. When the discs were perforated they were gently cleaned in ethanol, taking care not to damage the thin area, and dried on filter paper.

Samples were imaged as soon after twinjet polishing as possible to minimise oxidation and corrosion as well as being stored in a vacuum desiccator when not being used. If the

thin area was not sufficiently large or oxidation had occurred between polishing and observation, discs can be ion polished in a Gatan Precision Ion Polishing 691 system (PIPS), with beam energy 3.5 keV and incidence angle of 4° for 15 minutes on each side of the disc. This procedure can only be carried out a handful of times before the edges of the thin area begin to amorphise.

TEM observations were made using a JEOL 2100 and FEI Tecnai F20 both operated at 200kV. Moreover, the FEI Tecnai F20 is equipped with a scanning transmission electron microscopy (STEM) mode allowing images to be taken with a high angle annular dark field (HAADF) detector. This gives contrast proportional to the average atomic weight of each phase. The contrast provided in this mode can be used for qualitative analysis of previously identified phases which can be quantified with an Oxford Instruments X-max 80 EDX detector, using the Aztec software package, also installed on the microscope as well as via conventional crystallography to determine the structure of any phase.

In the case of the sample used to determine the orientation relationship, there was some difficulty in producing a sample with a foil normal that allowed imaging from the [0001] direction at low tilt angle. In this case a sample was cut using a FEI Quanta 3D FEG-SEM FIB equipped with an Omniprobe. The sample used was an old TEM foil known to have a foil normal close to $\langle 11\bar{2}0 \rangle_\alpha$, using EBSD conducted in the Tescan Mira XM-3 to determine the orientation of the crystal. The sample was rotated such that the foil normal was close to [0001]. Further details on the lift out method used and other similar methods are widely available from other sources[165–167] so will not be detailed here. Some broad points to consider, magnesium is far lighter and mills far more easily than other materials such as titanium or steel - this should always be considered when following any method

that is either generalised or appropriate for heavier material, where possible reducing the milling current. Likewise, given the larger extinction distance of electrons when compared to other materials, the sample does not have to be as thin as other materials, meaning that the thickness can be left at ~250nm and still be easily viewed using a 200kV microscope.

### 3.6.1   Sample Thickness Measurement

In order to ascertain the number density of precipitates in TEM, we must not only know the view field but also the sample thickness. The two most popular ways of achieving this are Electron Energy Loss Spectroscopy (EELS) or via Convergent Beam Electron Diffraction(CBED). For the purpose of this study CBED was used given there is no need for equipment beyond the standard TEM (and a CCD camera is useful!).

Many users will be familiar with CBED as a manner of navigating to the zone axes of samples, but CBED holds far more information than just the orientation.  The widest application is the use of CBED to produce patterns similar to those seen by Selected Area Electron Diffraction (SAED). However, unlike SAED, CBED patterns are derived from a much smaller volume, nanometres if the user has correctly aligned the microscope, as we are only limited by the beam dimensions, not the physical aperture size. Moreover CBED produces disks controlled by the size of the C2 aperture rather than the points seen in SAED. With a larger aperture we see overlapping disks giving a continuous Kossel pattern. Conversely if we reduce this aperture size we can get smaller disks (called a Kossel-Möllenstedt (KM) pattern) which are more similar to selected area diffraction pattern (SADP). These discs aside from giving the information expected from a SAED pattern, also contain further contrast information. Within a Kossel pattern it will be clear that there are multiple lines crossing the pattern. Unlike the Kikuchi bands seen these remaining lines

will appear singular as the separation between the $hkl$ and $\bar{h}\bar{k}\bar{l}$ bands is much larger due to the higher order hence larger Bragg's angle. The pairs will become clear in the K-M pattern. These lines arise from higher order Laue zones (HOLZ) as opposed to lower order Laue zones (LOLZ) which form the bands typically referred to as the Kikuchi pattern at the particular zone axis (ZA). When the pattern is entirely illuminated only the defect lines, i.e. the points which are diffracted due to satisfying the Bragg condition for the given plane, will be visible. The excess lines ie where the electrons have been diffracted to are lost due to the brighter illumination from the large Kossel disc. When we reduced our disk size, we can clearly observe the excess lines, separated from the illuminated deficiency line by the angle, $\theta_B$. What is more, provided that the sample is thicker than the extinction distance of the electron, a number of fringes are present within the disks. When observed on a ZA they are difficult to analyse due to a number of competing interferences, providing nothing more useful than decoration, but by illuminating a single HOLZ line, the fringes will form parallel lines. By centring the deficiency line in the transmission disk and measuring the separation between the primary (either excess of defect, the fringes will be present on each) line and each fringe, we find a number of measurements $\Delta\theta_B$ from which the thickness can be calculated. The deviation parmeter, $s_i$, when combined with the wavelength of the electrons, $\lambda$, and the interplanar spacing for the given g vector of the Laue zone used, $d_g$, can be calculated by:

$$s_i = \frac{\lambda}{d_g^2} \cdot \frac{\Delta\theta_B}{\theta_B} \qquad [3.9]$$

While not directly useful, a plot of $(s_i/n_i)^2$ against $1/n_i^2$, $n_i$ being the fringe number, should yield a straight line, whose y intercept is equal to $1/t^2$, $t$ being the sample thickness. It is often the case that the first fringe is not visible due to the lack of dynamic

range in the image, thus some fitting is needed on the part of the operator. The accuracy of the fit can be checked using the gradient of the line. If done correctly this should equal $1/\xi^2$, where $\xi$ is the extinction distance which can be calculated.

The ion polishing step in PIPS above was found to be vital in producing disks of sufficient quality to see KM fringes that are clear enough to get a reliable reading from. As such all samples used for the number density calculations where the disk thickness was required were polished using the Gatan PIPS. While this allows for the thickness of the sample to be calculate,d there are a number of assumptions made, primarily that the thickness does not greatly vary through out the sample. This is minimized by measuring the thickness in multiple loactions however must always be considered calculating number density from TEM.

## 3.7  Modelling

The final part of the thesis will attempt to fit a model to the growth and coarsening of precipitates in the Mg-Sn-Al alloys. This is based largely on the application of the KWN model as described in the literature review. A number of studies using this model for spherical precipitates exist in the literature[127,128] though few deal with non-spherical precipitates[37,118,131]. To begin with, a nucleation rate $I$ is calculated as a function of the number of nucleation points $N_v$, the Zeldovich factor $Z$ and the temperature $T$:

$$I = N_v Z \beta \exp\left[-\frac{4\pi r^*}{3k_B T}\right] \exp\left[-\frac{\tau_i}{t}\right] \quad\quad [3.10]$$

where $\tau_i$ is the incubation time for the nuclei. While this is calculate in the work of Robson et al.[129], in the present work this is fitted.  Also included are the Boltzman constant $k_B$, critical radius for nucleation $r^*$ and another factor $\beta$, which is itself a function, dependent on lattice constant $a$, diffusion rate $D_0$, tin concentration $c_i$ and the Gibbs free energy $\Delta G_v$.

$$\beta = \frac{16\pi \gamma_n^2 c_i D_0}{\Delta G_v^2 a^4} \qquad [3.11]$$

Likewise the Zeldovich factor can be calculated, using the volume of the α unit cell $V_\alpha$ which compensates for the decay of super saturated nuclei, this time including the precipitate surface energy γ:

$$Z = \frac{V_\alpha \Delta G_v^2}{8\pi \sqrt{\gamma_n^3 k_B T}} \qquad [3.12]$$

It is noted by Hutchinson et al [37] that a value of 0.05 is typical for a Zeldovich factor. One thing that must be discussed is the value of $N_v$: elsewhere the value of $N_v$ is either chosen[127] or fitted[118] with Robson et al[118] fitting a value of $10^{-9} m^{-3}$ for a Mg-Zn-Zr alloy. In the current work this was fitted with the caveat that the values is given as:

$$N_v = N_0 . CSn \qquad [3.13]$$

where $N_0$ is the fitted value. Up until now we have not examined the Gibbs free energy, $\Delta G_v$; while not included directly in the formulation of the nucleation rate, $\Delta G_v$ is critical to a fully working model. This is calculated via:

$$\Delta G_v = \frac{R_g T}{V_a} \left[ c_e^\beta \frac{\ln(c_i)}{\ln(c_e^\alpha)} + (1 - c_e^\beta) \frac{\ln(1 - c_i)}{\ln(1 - c_e^\alpha)} \right] \qquad [3.14]$$

with $c_e^\alpha$ / $c_e^\beta$ being the equilibrium atomic percentage in $\alpha$ and $\beta$ phases respectively. The value for $c_e^\beta$ is simply 1/3 whereas the equilibrium tin content is taken as 0.00035 as reported by Kang et al.[168] at room temperature as no elevated temperature solubility is reported. It is clear however from the binary phase diagram (Fig 2.6) that the solubility of Sn at the ageing temperature 200°C has not increased greatly compared to room temperature. Once the total number of nuclei has been determined, these will be divided up into three categories, representing the $\langle 11\bar{2}0 \rangle_\alpha$ laths, prismatic and pyramidal precipitates respectively as set by constant fractions given in Table 3.1.

It is at the growth stage that the model diverges most from models reported elsewhere. The calculations are well established for the case of a spherical precipitate in an isotropic medium as given in section 2.8, Eqns [2.8-2.11] above, but this needs to be modified in order to reflect the alloys in this study. Addressing first the precipitate shape; as in the work of Robson et al and Hutchinson et al[37,118,131], this is defined by a measured aspect ratio based on TEM observation. The parameter $\alpha$, is introduced such that Eqn [2.11] becomes:

$$\frac{dr}{dt} = \frac{D_0\,\alpha}{r}\,\Omega\,\left(1 - \frac{r_c}{r}\right) \qquad\qquad [3.15]$$

α, a dimensionless constant, will account for the variation between spherical growth and lath growth. Likewise the actual precipitate length is not used in Eqn [3.15]. Instead the radius, $r$, of a spherical precipitate of the same volume is used as per Robson et al[118,131]. A constant aspect ratio estimated from the TEM measurements. As with the nucleation, each precipitate type is then assigned a factor to moderate the growth as based upon the lengths of the precipitates; again these are given in Table 3.1 below. This is representative of the anisotropy in the matrix causing slower growth in certain directions.

**Table 3.1:** *Nucleation and growth factors as estimated from TEM observations*

| Precipitate Morphology | Percentage of Nuclei | Growth Factor |
|---|---|---|
| $\langle 11\bar{2}0\rangle_\alpha$ Laths | 0.75 | 1 |
| Pyramidal Laths | 0.2 | 0.6 |
| Prismatic Rods | 0.5 | 0.4 |

One major change from the reported KWN model is the manner in which the dissolution of the precipitates is treated. Coarsening has not received as much attention as the growth mechanisms in the majority of alloys, including Mg, and it is suggested[134] that the two cannot be described using identical equations except in special cases, something that the

66

KWN model assumes. The classic LSW model varies from growth models used typically being applied from an arbitrary point that the author deems coarsening initiates; likewise a number of different coarsening mechanisms are proposed by Aaron and Kotler[134] for different dissolution mechanisms which alter the Gibbs-Thomson equation. Similarly the Gibbs-Thomson equation can be rephrased to include a stress term[132], though the effect of this is said to be minor in most cases.

The method used in this work is much simpler; as pointed out by Aaron and Kolter [134]when they a compare plates and spheres, there is a great difference in surface areas. Growth is constricted in that in order to be favourable, the shape of the precipitate must such to minimise the surface energy, usually by growing favourably in a preferred direction. Dissolution on the other hand is less constrained by this as the solute is being removed from all surfaces. As such, given that we can express both the surface area of a sphere and a lath as a function of their radius and length respectively, we can calculate the difference in their surface areas. Firstly, we must find the ratio between the length of the lath and the sphere's radius. This is done by comparing the volume of the two shapes:

$$\frac{4}{3}\pi r^3 = l.w.h \tag{3.16}$$

We can express the width, $w$ and height, $h$ as a proportion of r using the aspect ratios, $A$ and $A'$ thus:

$$\frac{4}{3}\pi r^3 = l^3 A.A' \tag{3.17}$$

$$\frac{r}{l} = \sqrt[3]{\frac{3AA'}{4\pi}} \tag{3.18}$$

This is then used, firstly to calculate the lath length from the spherical volume but also to calculate the ratio between the two surface areas $R_{SA}$

$$R_{SA} = \frac{4\pi r^2}{2l^2(A' + A + A.A')} \qquad [3.19]$$

Substituting in [3.18] and using the aspect ratios $A = 10$ and $A' = \frac{10}{3}$ for the $\langle 11\bar{2}0 \rangle_\alpha$

laths we are left with $R_{SA} = 5x10^{-3}$. Thus when considering a negative growth rate, the

value is divided by $R_{SA}$ giving a modified version of [3.15] as:

$$\frac{dr}{dt} = \frac{D_0 \, \alpha \, \Omega}{r} \left( 1 - \frac{r_c}{r} \right) \text{ when } \Omega > 0 \qquad [3.15a]$$

$$\frac{dr}{dt} = \frac{D_0 \, \alpha \, \Omega}{r \, R_{SA}} \left( 1 - \frac{r_c}{r} \right) \text{ when } \Omega < 0 \qquad [3.15b]$$

## 3.8 Summary

A number of techniques are used considering different length scales. Each has advantages and disadvantages: for example while TEM provides a very accurate measurement of precipitate dimensions, the area inspected is always very small and care must be taken to see that the result is repeatable and indicative of the entire sample. Likewise due to the thickness of the sample and preparation method, precipitates can be truncated and different phases preferentially removed or even react with the electrolyte to form a different phase. At the other end of the spectrum, XRD provides an inspection of a large portion of the sample averaging inhomogeneities and avoiding most issues concerning polishing and sample preparation. This however is limited to a volume fraction only with no direct observation. Whether the secondary phase is one single eutectic network buried within the sample or millions of nanoscopic precipitates is an unknown.

The below will detail the findings using a variety of these methods. The first sections will focus on the more macroscopic techniques such as XRD, SEM and Vickers hardness. These will be used to consider the overall microstructure and link this to the hardness and the strength of the material. The precipitates will then be observed in more detail, identifying the different varieties and defining their crystal structure. The study then progresses to

look at the precipitates as a collective, establishing number density via both TEM and SEM as well as measuring the size distribution of the precipitates. The purpose of this is to feed into the last section, a model of both the precipitate nucleation and development over ageing time and finally bringing us full circle back to the mechanical properties of the alloy which will be modelled using the modified KWN model described above based upon the observations of the microstructure.

# 4 MORPHOLOGY, COMPOSITION AND CRYSTAL STRUCTURE OF PRECIPITATES

## 4.1 Outline

As previously outlined, precipitation hardening of Mg alloys is key to increasing their strength and is well studied for Mg alloys such as AZ91. The purpose of this study is to characterise the precipitates in Mg-Sn-Al alloys, with the ultimate aim of introducing them as a viable alternative to the AZ series for situations where operating temperatures rise above 100°C. In order to do this, more information is required on the mechanism through which precipitate nucleation occurs and the manner of growth of the precipitates. This will be acquired through two tertiary alloys, Mg-1.75Sn-1.93Al and Mg-1.29Sn-2.85Al(at%).

To begin with, the hardness of the alloys will be measured in order to ascertain the strengthening effect of the ageing treatment. 3 ageing times have been selected (40, 72 and 160 hrs) for a temperature of 200°C, based upon measurements on similar alloys in the literature, to correspond roughly to the three stages of ageing:

- Initial ageing where precipitates are nucleating and growing rapidly,
- peak hardness, where growth has been slowed by the lack of solute,
- and coarsening, whereby the number density of precipitates is beginning to reduce and the alloy is weakening

The precipitates responsible for the strengthening will then be identified and their composition and crystal structure, including their orientation relationship with the matrix, investigated via XRD, SEM and TEM.

With this knowledge in hand, chapter 5 will describe the evolution of the precipitates, taking into account their number density, size and habit plane, all of which alter their

effective strengthening[10,20,40]. This will later be developed into a model in chapter 6 which will firstly model the evolution of the precipitates over the ageing treatment and then latterly the strengthening caused by these precipitates. The microstructure of the alloy is typical of that seen for magnesium alloys, that is to say equiaxed grains, however in line with other Sn containing alloys, no eutectics are present. In this particular case, due to the lack of a grain refiner, the grains are coarse, typically millimetres in size. The as aged samples show needle like precipitates.

## 4.2 Hardness Measurement
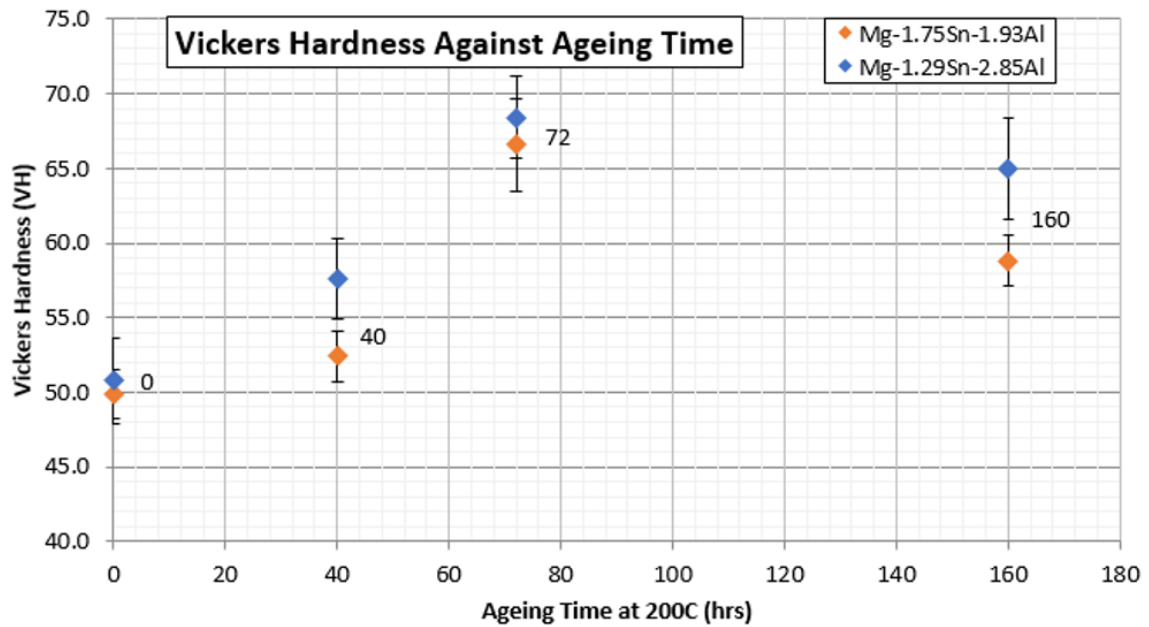


***Fig 4.1****: Vickers hardness averaged from 100 points using a 0.1kg load with standard deviation given as the error*

A minimum of 100 Vickers hardness indents were made on each sample and averaged to provide values of hardness; the results shown in Fig 4.1. Clearly it can be seen that the peak hardness is found at approximately 72 hours ageing as expected and this declines in the 160 hour sample. While the hardness of the two alloys is similar in the solution treated state, it's clear that the Mg-1.29Sn-1.93Al has a marginally higher peak hardness despite

the lower Sn content. Certainly it is also more resistant to weakening due to coarsening at 160 hours. Likewise the hardness of the Mg-1.29Sn-2.85Al sample is lower at 40hrs which may indicate nucleation of precipitate is slower in this alloy.

As can be seen in Fig 4.2 the values from this work fit reasonably well with those given for other Mg-Sn-Al ternaries, although the peak hardness is somewhat lower than for the Mg-Sn-Al alloys studied in the literature. We can be satisfied that the application of a heat treatment increases the hardness and thus the yield strength of the alloy. This is expected to occur by the formation of $Mg_2Sn$ as indicated by the phase diagrams in Fig 4.3. We thus advance to inspect the change in the microstructure due to the heat treatment that causes this increase in strength.
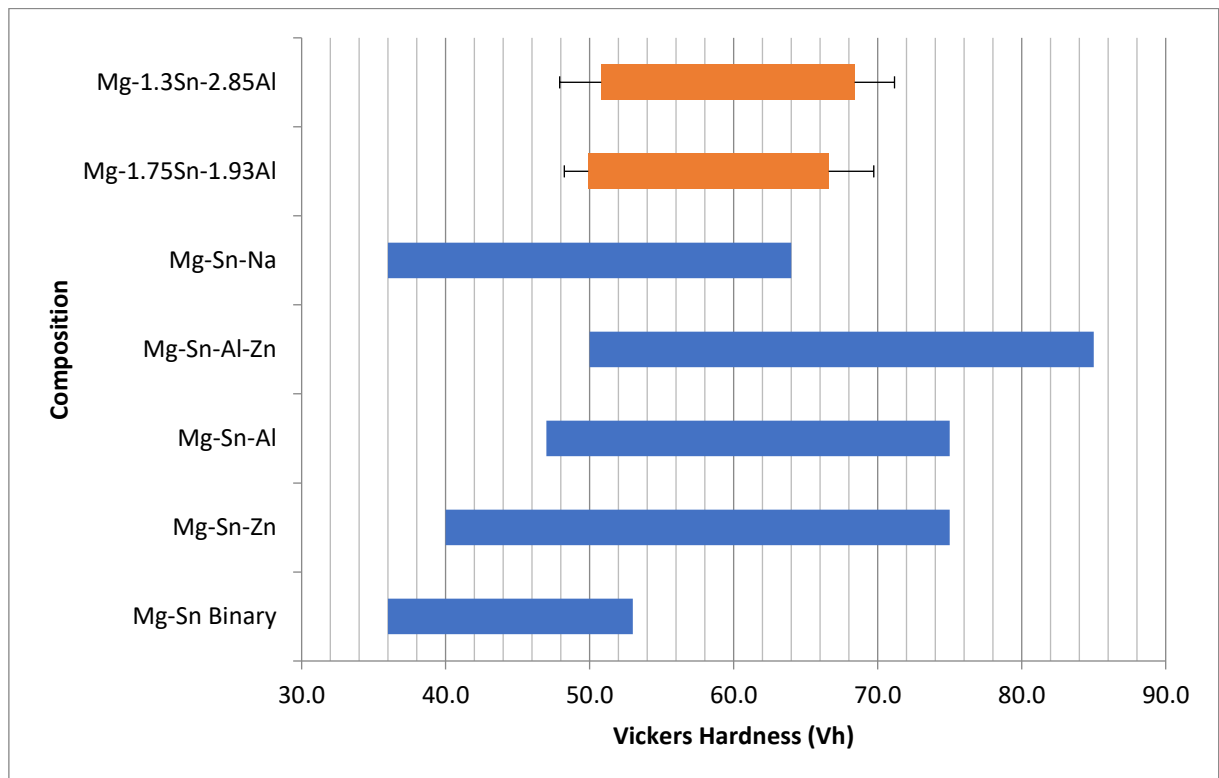


***Fig 4.2:*** *Comparison of literature*[47,108,109,111] *hardness values with present work (given in orange)*
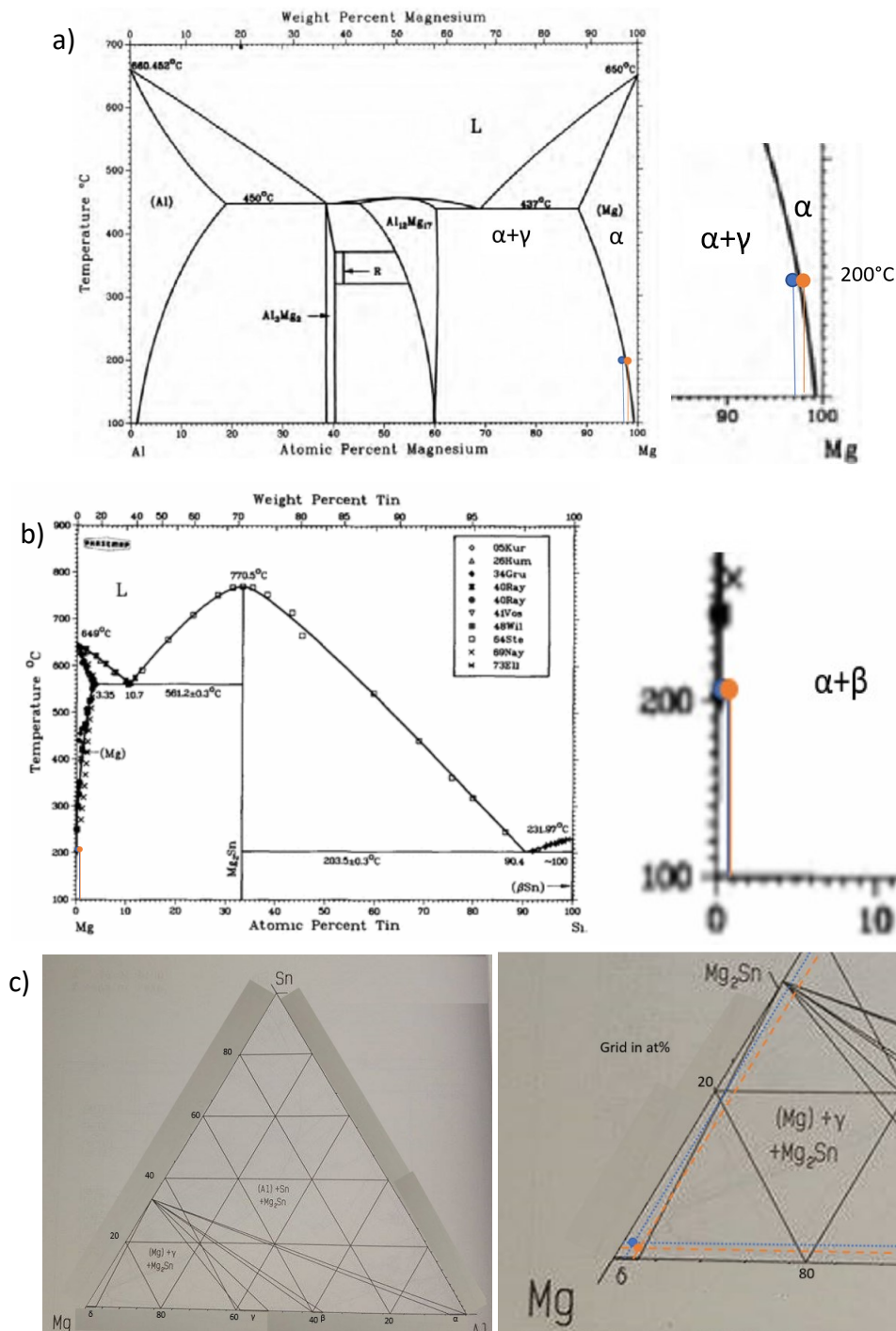
***Fig 4.3:*** *Binary phase diagrams for a) Mg-Al[169] and b) Mg-Sn[84] along with c) isotherm of Mg-Sn-Al ternary phase diagram at room temperature[90]. In all cases Mg-1.75Sn-1.93Al(at%) is marked in orange and the Mg-1.29Sn-2.85Al in marked in blue and a larger view of the area of interest is given. Due to the low solid solubility of tin at room temperature[168], δ represents the Mg+Mg₂Sn region*

Three methods have been used to inspect the precipitates, the following will firstly determine the phases present using XRD before observing these precipitate via SEM and then TEM. The TEM will then be used to explore the precipitate morphologies before confirming the precipitate crystal structure via electron diffraction.

### 4.3.1 XRD Phase Identification

The data extracted from the diffractometer was firstly imported into the Match! Software package, where the two expected phases, $\alpha$-Mg and $Mg_2Sn$, as well as $Mg_{17}Al_{12}$ were selected as possible phases. Given in Fig 4.4 are the results from each of the ageing times for both samples. While the 3 phases were selected, only $\alpha$-Mg and $Mg_2Sn$ are identified phases, with no peaks for $Mg_{17}Al_{12}$ being found, excluding those that overlap with the $\alpha$-Mg. In the two solution treated alloys (Fig 4.4a and 4.4e) only the $\alpha$-Mg was identified, with the aged samples also showing $Mg_2Sn$. The peak height ratios do no match well to that given for a powder diffraction pattern hinting at a texture in the alloy

e) Mg-1.29Sn-2.85Al
Solution Treated

f) Mg-1.29Sn-2.85Al
Aged for 40hrs

g) Mg-1.29Sn-2.85Al
Aged for 72hrs
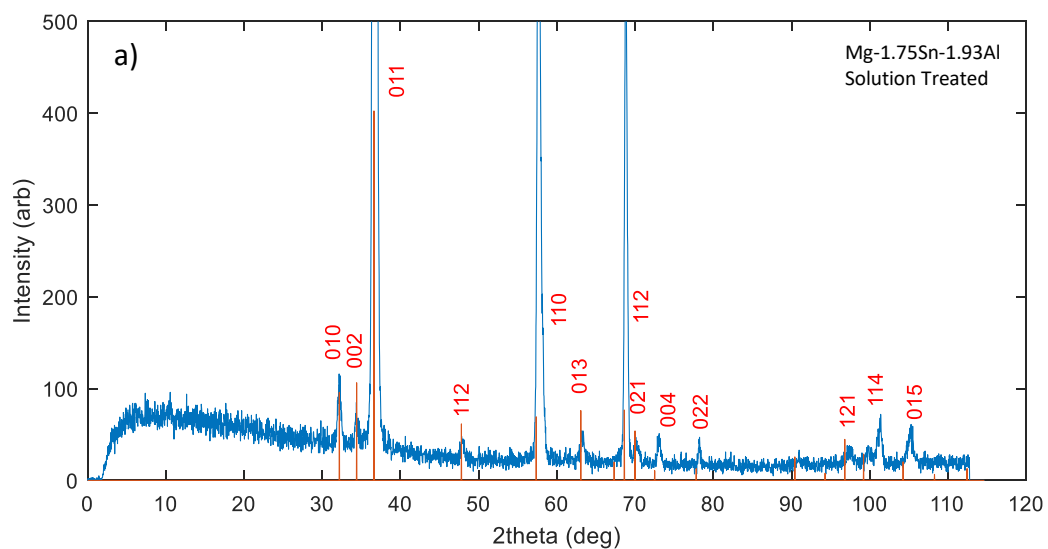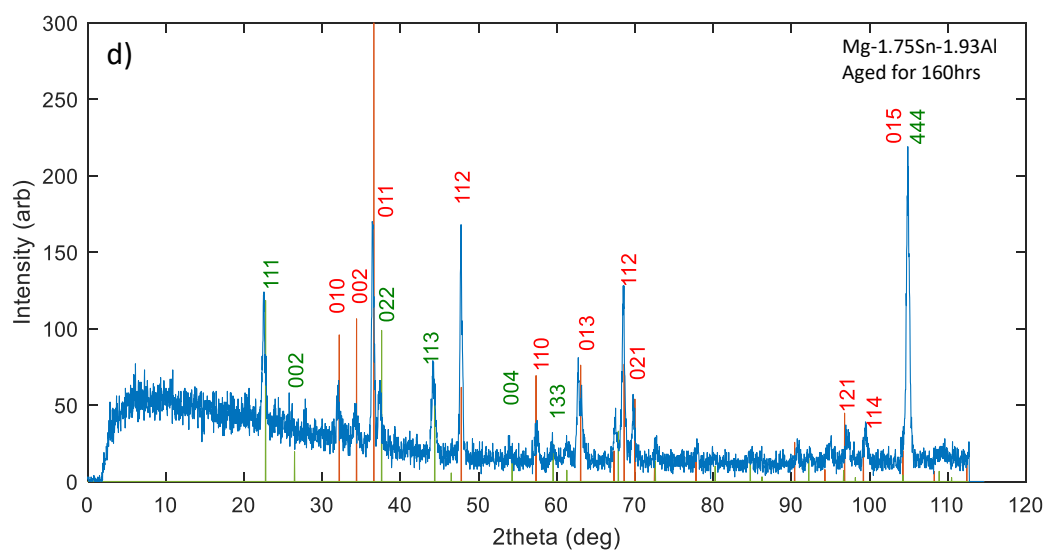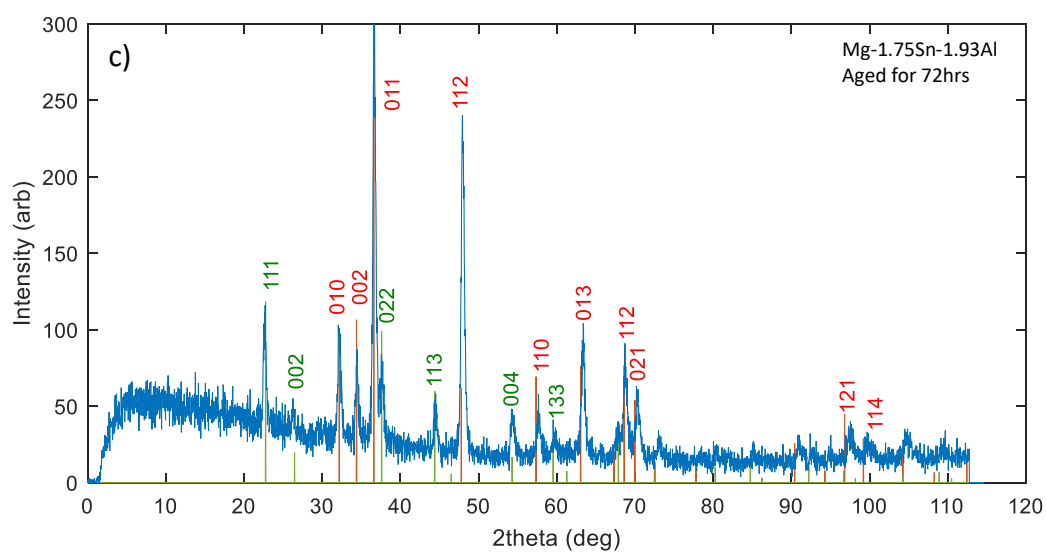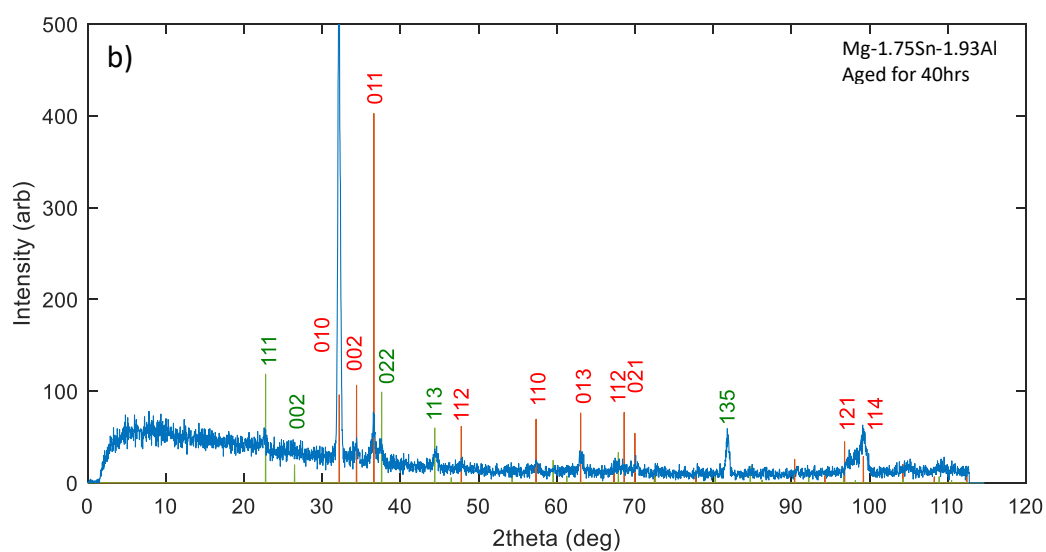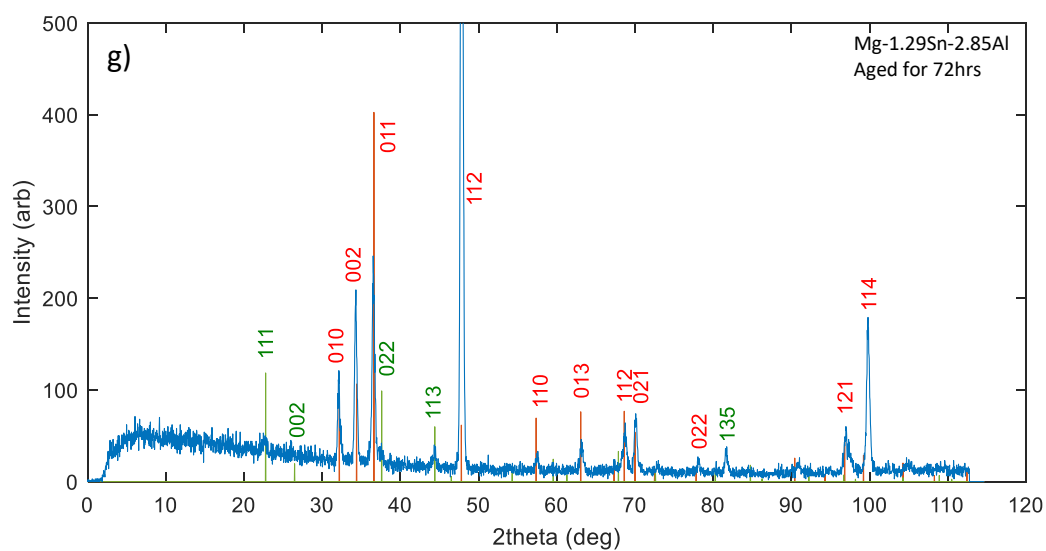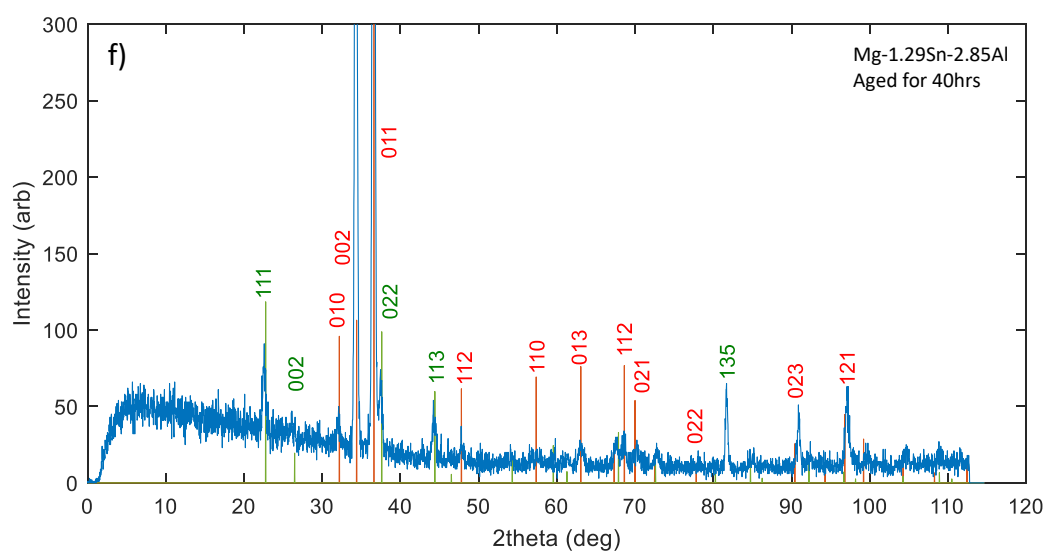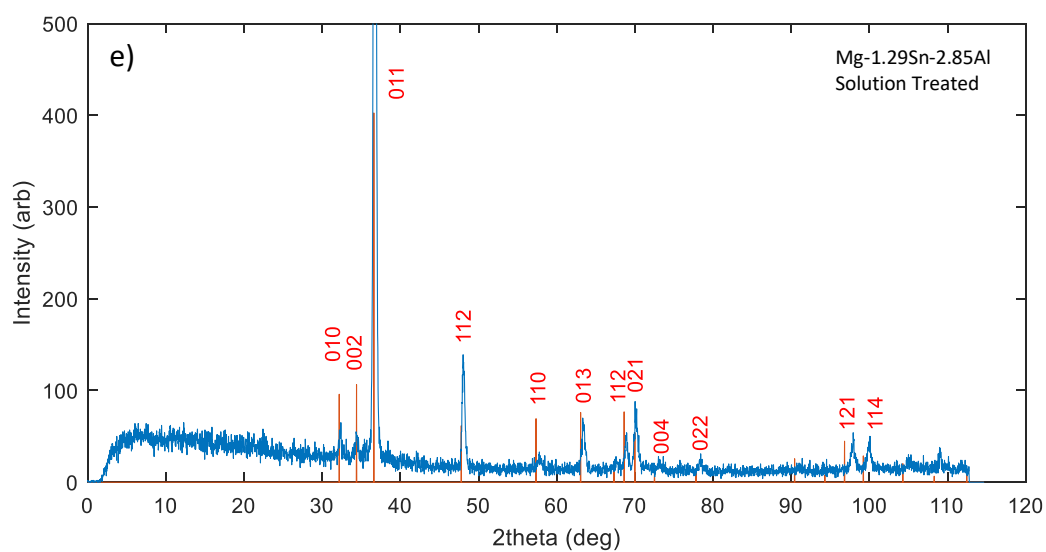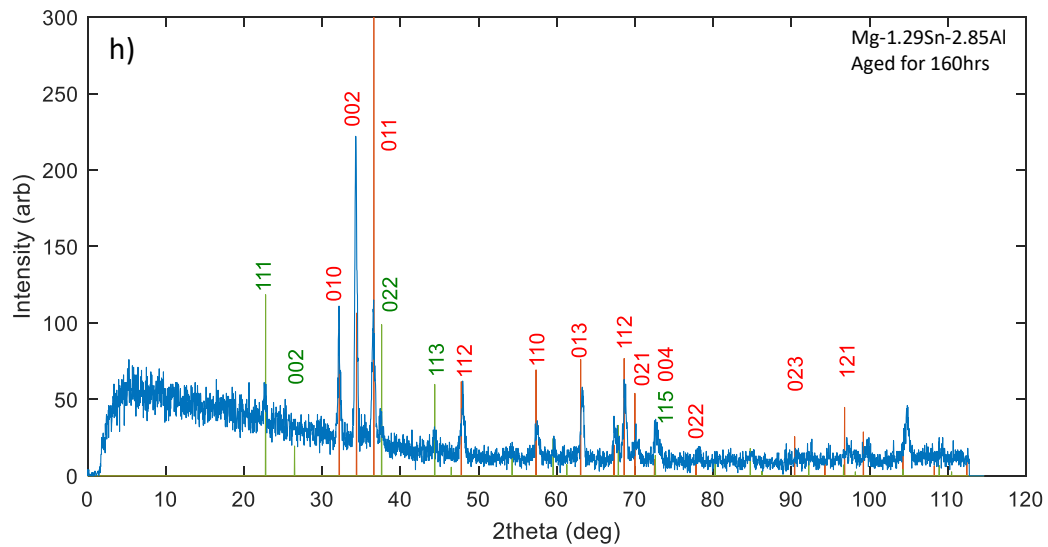
***Fig 4.4*** *XRD spectra showing α-Mg (green) and Mg₂Sn (red) peaks identified taken from Mg-1.75Sn-1.93Al in the a) solution treated state and aged for b)40, c)72 and d)160 hours and Mg-1.29Sn-2.85Al in the e) solution treated state and aged for f)40, g)72 and h)160 hours. The red and green lines given on the spectra represent the peak ratios as expected powder pattern,*

### 4.3.2   SEM Observation

While the confirmation of the phases present is established by the XRD, we are presented with no information as the appearance of this phase. As discussed in the literature review, there is great interest in morphology of the precipitates due to the effect on strengthening. Fig 4.5 and 4.6 give backscatter SEM images of the two alloy compositions throughout the ageing process. What can be clearly seen is the lack of secondary phase in the as solution treated sample, and then a steady growth from 40 to 72 and eventually 160 hours. While it is less clear on the 40 hour image, it is obvious from 72 hours onwards in both alloys that the precipitates have an elongated shape. This is not unusual for a magnesium alloy, with laths and rods being widely reported in Mg-Al, Mg-Zn, Mg-Sn and many other combinations.

As can be seen the precipitate dimensions are of the order of micrometers, however with the increasing ageing time, the width does not noticeably increase to the point where

SEM-EDX would be able to confidently identify the composition of the precipitates, as such TEM is required to produce a suitably small interaction area.
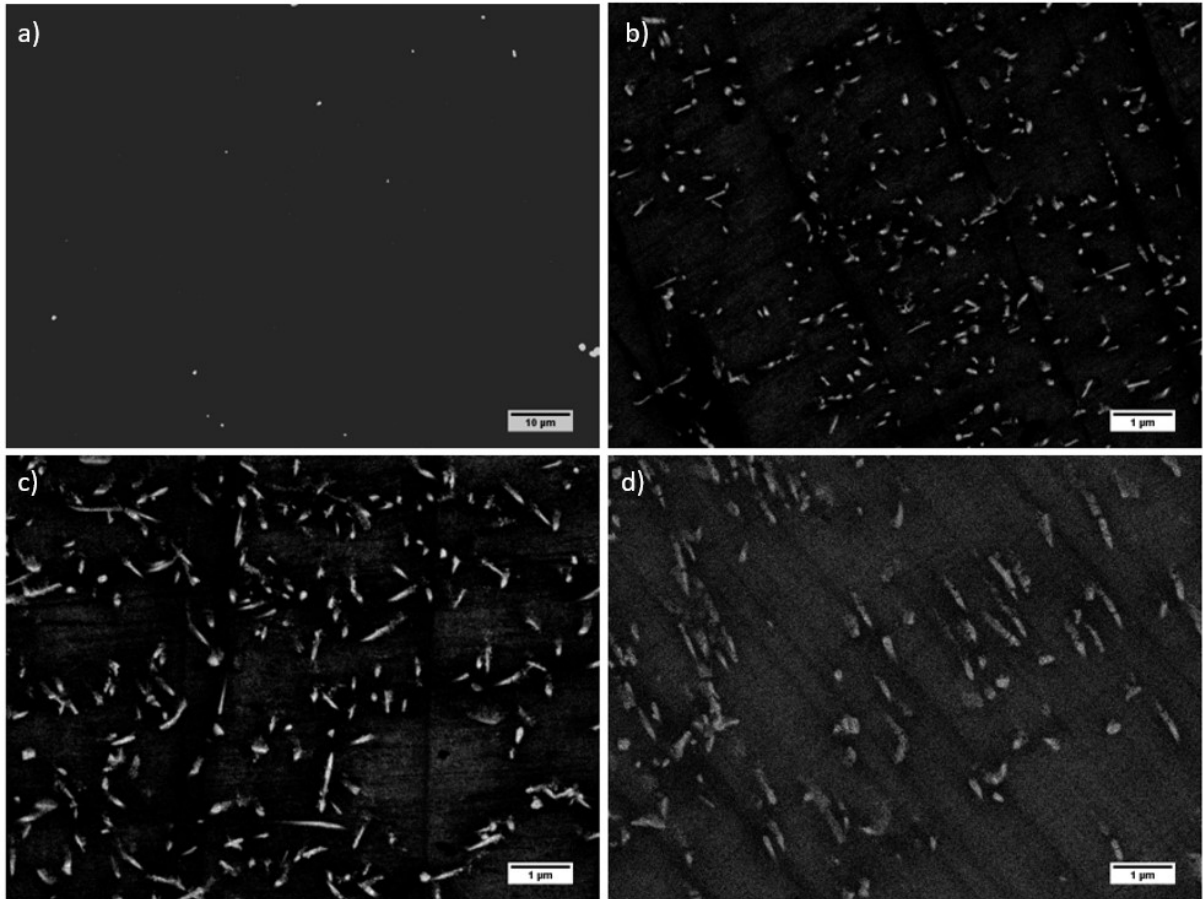


***Fig 4.5*** *BSE SEM images for Mg-1.75Sn-1.93Al sample aged for a) as cast, b) 40, c)72 and d)160 hrs respectively. While the lighter contrast is sourced from the precipitates on the later 3 images, on the as cast samples; they correspond to OP-S remaining from the polishing process*
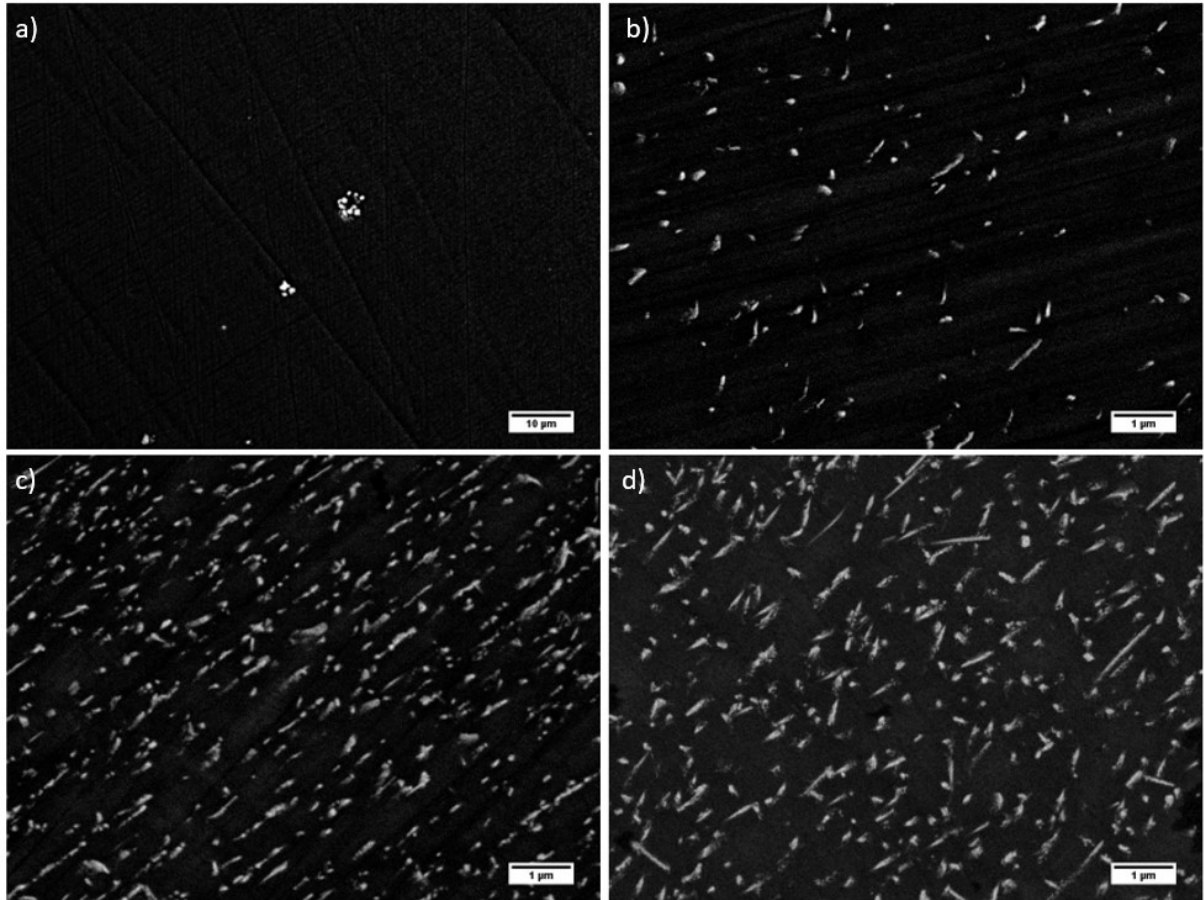
***Fig 4.6*** *BSE SEM images for Mg-1.29Sn-2.85Al sample aged for a) as cast, b) 40, c)72 and d)160 hrs respectively. While the lighter contrast is sourced from the precipitates on the later 3 images, on the solution treated sample; they correspond to OP-S remaining from the polishing process*

### 4.3.3   Precipitate Morphologies

Figs 4.7 and 4.8 show STEM HAADF images from the $[11\bar{2}0]_\alpha$ zone axis of the two alloys again for each of the ageing times. The solution treated sample is omitted due to the lack of a precipitate phase.
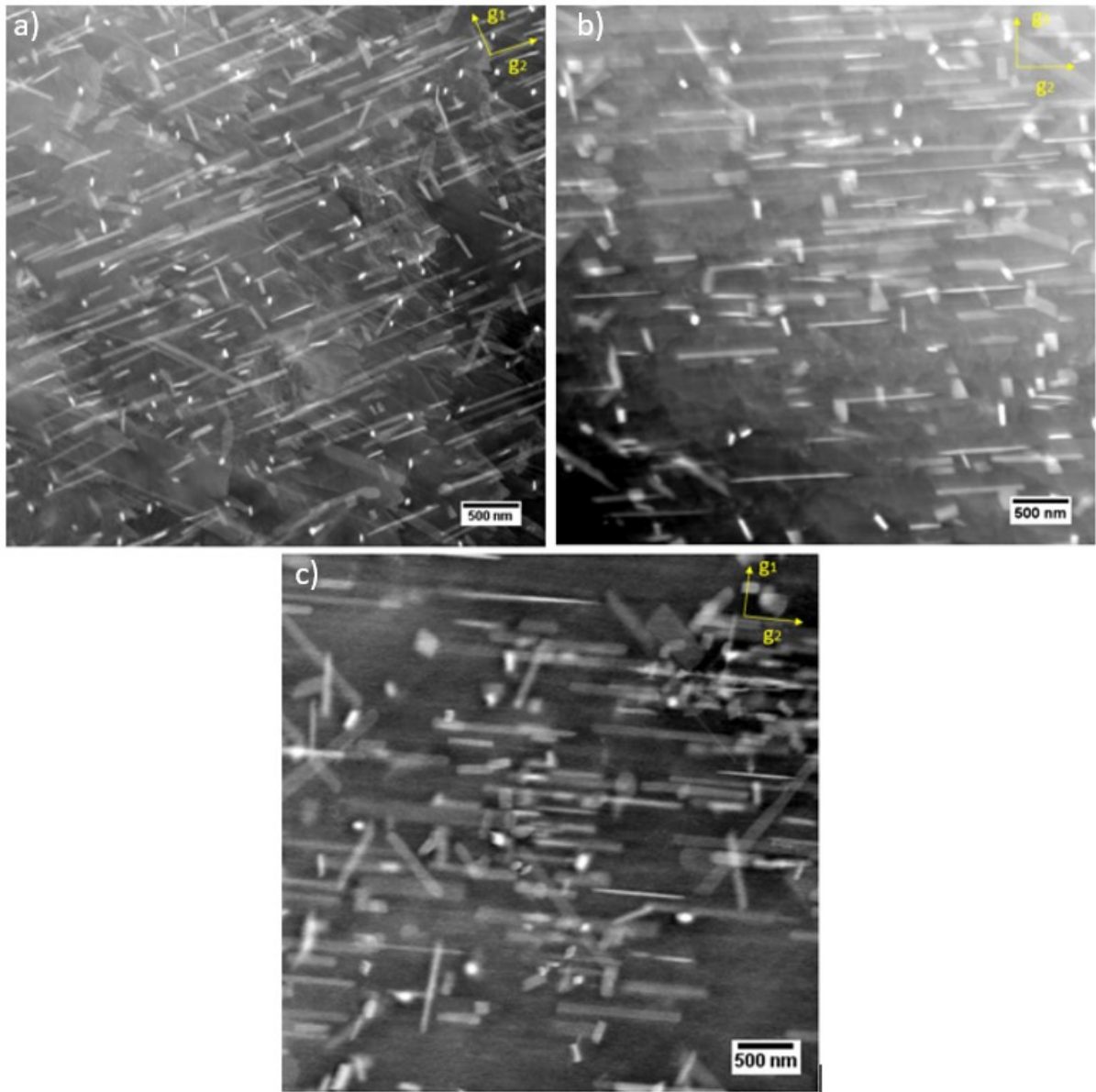
**Fig 4.7** *HAADF STEM images for Mg-1.75Sn-1.93Al sample aged for a) 40, b)72 and c)160 hrs respectively. All images are taken from $[11\bar{2}0]_\alpha$ with $g_1 = [0001]_\alpha$ and $g_2 = [\bar{1}100]_\alpha$*
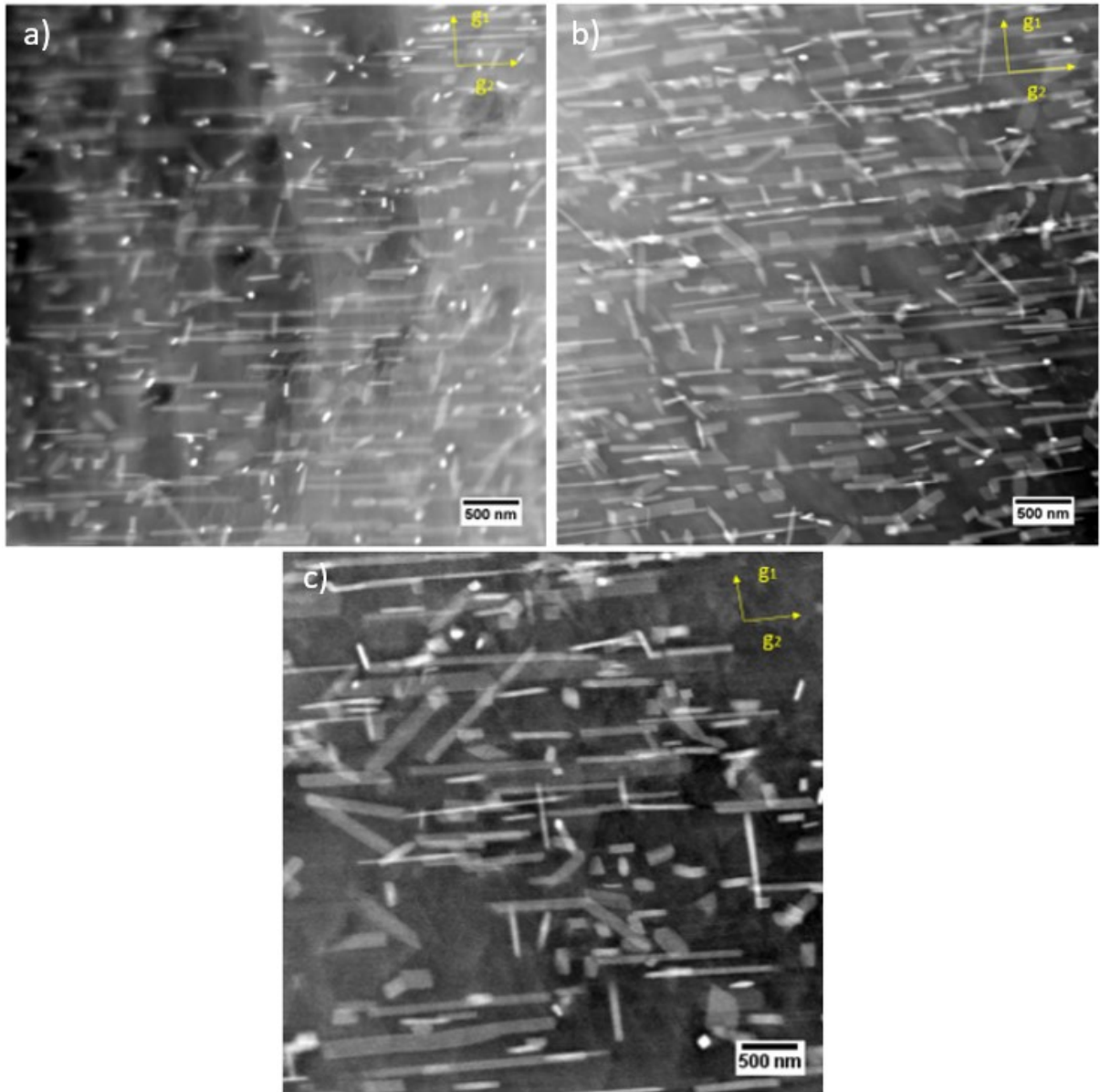
*Fig 4.8* HAADF STEM images for Mg-1.29Sn-2.85Al sample aged for a) 40, b)72 and c)160 hrs respectively. All images are taken from $[11\bar{2}0]_\alpha$ with $g_1$ = $[0001]_\alpha$ and $g_2$= $[\bar{1}100]_\alpha$

Thus far we have categorised the precipitates as a singular group. Broadly the precipitate morphologies are split in the literature into 4 categories, a schematic diagram of these can be seen in Fig 4.9.:

a)  laths with the long side parallel to $\langle11\bar{2}0\rangle_\alpha$, the literature assigns the habit plane as basal referred to as '$\langle11\bar{2}0\rangle_\alpha$ laths' in the current work,

b)  basal hexagonal plates with sides parallel to the $\langle 11\bar{2}0 \rangle$ directions, referred to as 'basal plates' in the current work,

c)  rods with the long axis parallel to the $[0001]_\alpha$ direction referred to as '<c> rods'. These have been referred to in the literature as prismatic rods due to their growth direction,

d)  rods that when observed from $[0001]_\alpha$ have a trace in the $\langle 11\bar{2}0 \rangle_\alpha$ direction giving a growth direction of $\langle 11\bar{2}X \rangle_\alpha$. The growth direction/habit plane are not widely discussed in the literature but these will be referred to as 'pyramidal laths.'
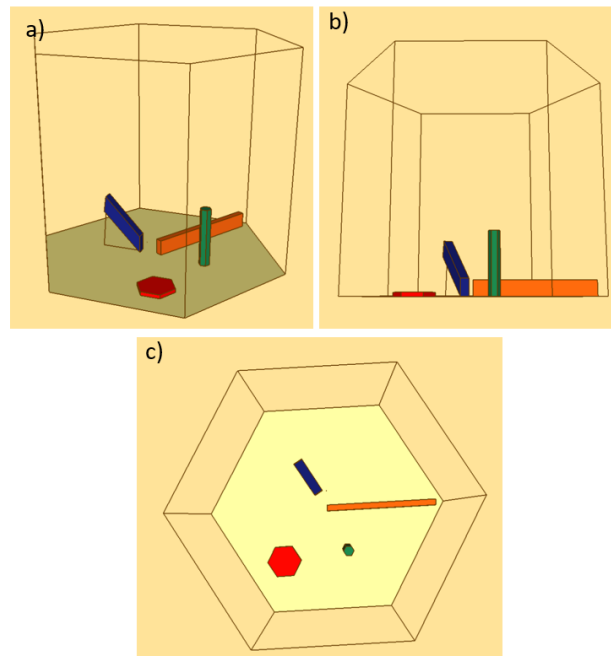


***Fig 4.9*** *Schematic diagrams from a) isometric, b) $[1\bar{1}00]_\alpha$ and c) $[0001]_\alpha$ showing the different precipitate morphologies, $\langle 11\bar{2}0 \rangle_\alpha$ lath (orange), hexagonal basal plate (red), prismatic rod (green) and pyramidal rods (blue)*

Some ambiguity exists in the literature where the habit planes have not necessarily been conclusively identified; certainly, in the case of category a) these have often been identified as basal laths. This will be investigated below for the different morphologies seen in the two samples.

## 4.3.3.1 $\langle 11\bar{2}0 \rangle$ Laths
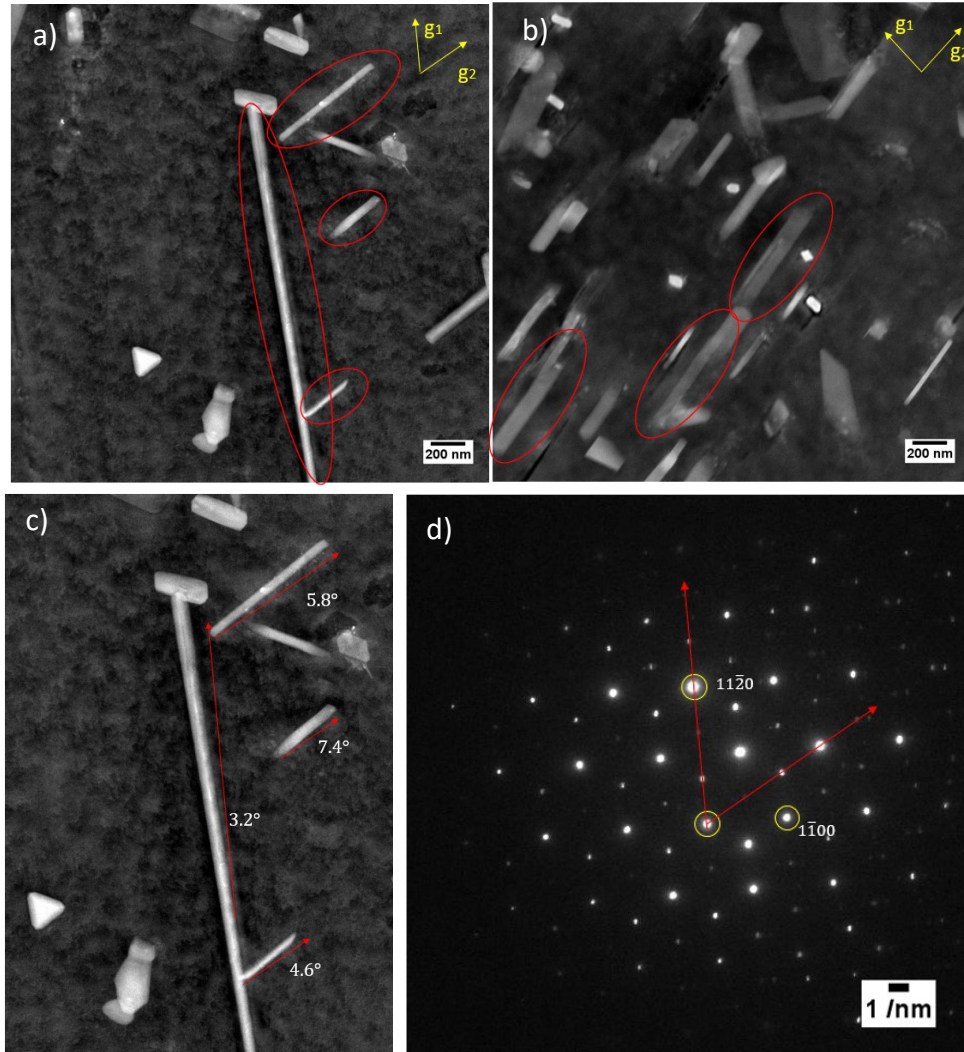


**Fig 4.10:** *Mg-1.75Sn-1.93Al alloy aged for 160 hours as seen from a)* $[0001]_\alpha$ *($g_1$ =$[2\bar{1}\bar{1}0]_\alpha$, $g_2$= $[11\bar{2}0]_\alpha$) and b)* $[2\bar{1}\bar{1}0]_\alpha$ *($g_1$ =$[0001]_\alpha$, $g_2$= $[01\bar{1}0]_\alpha$) zone axes.* $\langle 11\bar{2}0 \rangle_\alpha$ *lath is circled in red in both images. c) shows the angular deviation between the* $\langle 11\bar{2}0 \rangle_\alpha$ *directions with d)* $[0001]_\alpha$ *SADP.*

Taking a lath growing in the $[11\bar{2}0]_\alpha$ direction as our starting point, Fig 4.10a)&b) give a view from the $[0001]_\alpha$ and $[11\bar{2}0]_\alpha$ zone axes of the Mg-1.75Sn-1.93Al sample aged for 160hrs. It can be seen from Fig 4.10b) that in the width in the $[1\bar{1}00]_\alpha$ direction is smaller than the height in $[0001]_\alpha$ for the laths. Careful comparison of the growth direction with the diffraction pattern (Fig 4.10 c&d). shows a small variation between the growth direction of between 3 and 7.5° The morphology is confirmed by taking a tilt series of one

of these laths given in Fig 4.11 demonstrating the maximum length at the $1\bar{1}00$ zone axis and the shortest at approximately $[11\bar{2}0]_\alpha$.



$\sim 12\bar{3}0$    $\sim 1\bar{1}00$    $\sim 2\bar{1}\bar{1}0$    $\sim 21\bar{3}0$    $\sim 11\bar{2}0$
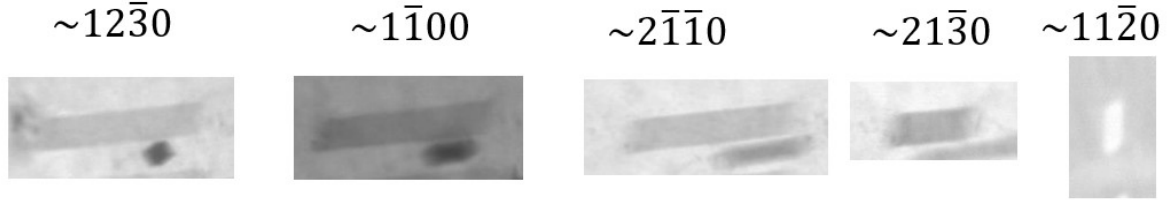
***Fig 4.11:*** *A tilt series of* $\langle 11\bar{2}0 \rangle_\alpha$ *lath (HAADF was used for* $[11\bar{2}0]_\alpha$ *due to poor contrast). ZA are approximate as the tilting axis was slightly off the* $(0001)_\alpha$ *kikuchi band*

**Table 4.1** *Measurements of the length of a* $\langle 11\bar{2}0 \rangle_\alpha$ *lath at different zone axes*

| *Zone Axis* | $12\bar{3}0$ | $1\bar{1}00$ | $2\bar{1}\bar{1}0$ | $21\bar{3}0$ | $11\bar{2}0$ |
|---|---|---|---|---|---|
| *Length (nm)* | *659* | *674* | *637* | *289* | *70* |

In a Mg-Sn binary alloy typically the width in the $[1\bar{1}00]_\alpha$ direction is much greater than the height in the $[0001]_\alpha$ direction, typically with an aspect ratio of around 10[109] as demonstrated in Fig 4.12. This poses an interesting problem as clearly the precipitates are still extended in approximately the $\langle 11\bar{2}0 \rangle_\alpha$ direction, however from what has been seen in Fig 4.10 and 4.11, unlike the literature, the habit plane is $\{1\bar{1}00\}_\alpha$ not basal. For the purpose of the study, and to avoid confusion with category c, they will be referred to as $\langle 11\bar{2}0 \rangle_\alpha$ laths.
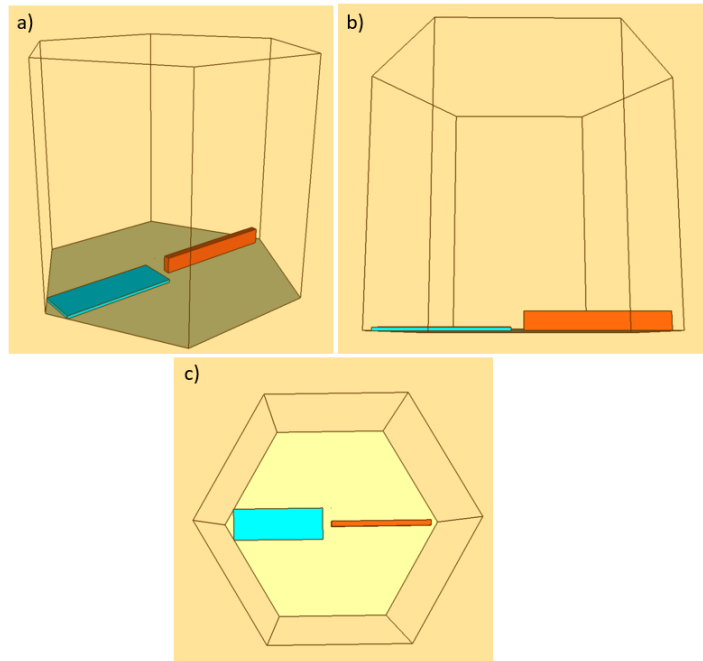
**Fig 4.12:** *a) isometric, b) $[1\bar{1}00]_\alpha$ and c) $[0001]_\alpha$ views showing the difference between $\langle11\bar{2}0\rangle_\alpha$ laths in the literature and the current work. In the binary the laths (blue) are clearly wider in the basal plane, however with increasing alloying content this width decreases. In the current work (orange) the width in the basal plane is similar to that for highly alloyed Mg-Sn-Al/Zn alloys however the laths have grown in the $[0001]_\alpha$ direction such that the habit plane is now $\{1\bar{1}00\}_\alpha$. Both still have a long axis roughly corresponding to $\langle11\bar{2}0\rangle_\alpha$.*

### 4.3.3.2   Basal plates

Next we consider the basal plate precipitates, a tilting experiment was conducted in a similar manner to above to demonstrate the habit plane of the precipitates. Clearly when observing from $[0001]_\alpha$ we can see a hexagonal shape of the plates as seen in Fig 4.13 however when tilted we can see the shortening of the precipitates indicating that the maximum dimensions are found at $[0001]_\alpha$, these measurements are given in Table 4.2. The facets of the plate are clearly irregular falling between 4 and 7.5° away from the plane, mirroring the observation of the $\langle11\bar{2}0\rangle_\alpha$ laths. Fig 4.14 gives a comparison between the facets and the $\{1\bar{1}00\}_\alpha$ planes; included also is a more regular basal precipitate from the Mg-1.29Sn-2.85Al sample aged for 160 hours. It can be seen that the matching is far closer in this precipitate with only one facet not aligning well to a $\{1\bar{1}00\}_\alpha$ plane,
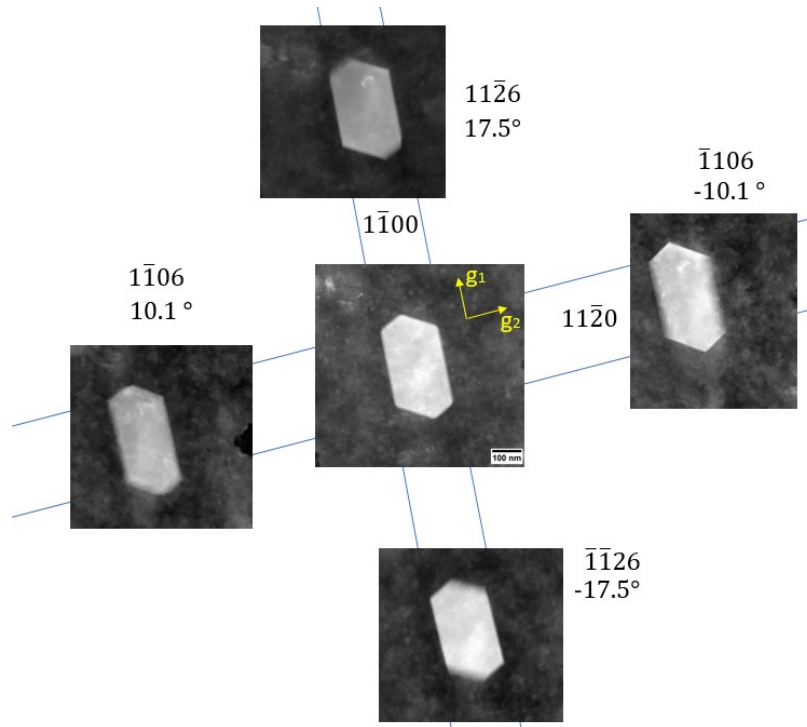
*Fig 4.13:* Tilt series of basal plate precipitate, central image is from $[0001]_\alpha$ with $g_1=[11\bar{2}0]_\alpha$ and $g_2=[\bar{1}100]_\alpha$. Images are taken from the Mg-1.75Sn-1.93Al sample aged for 160hrs.

*Table 4.2:* Dimensions of the basal plate precipitate from five different zone axes. The vertical measurement is taken as the left hand side of the precipitate and the horizontal perpendicular to this.

| Zone axes | Horizontal (nm) | Vertical (nm) |
|---|---|---|
| $[11\bar{2}6]_\alpha$ | 193 | 239 |
| $[0001]_\alpha$ | 194 | 266 |
| $[\bar{1}\bar{1}26]_\alpha$ | 191 | 244 |
| $[1\bar{1}06]_\alpha$ | 182 | 267 |
| $[\bar{1}106]_\alpha$ | 182 | 260 |
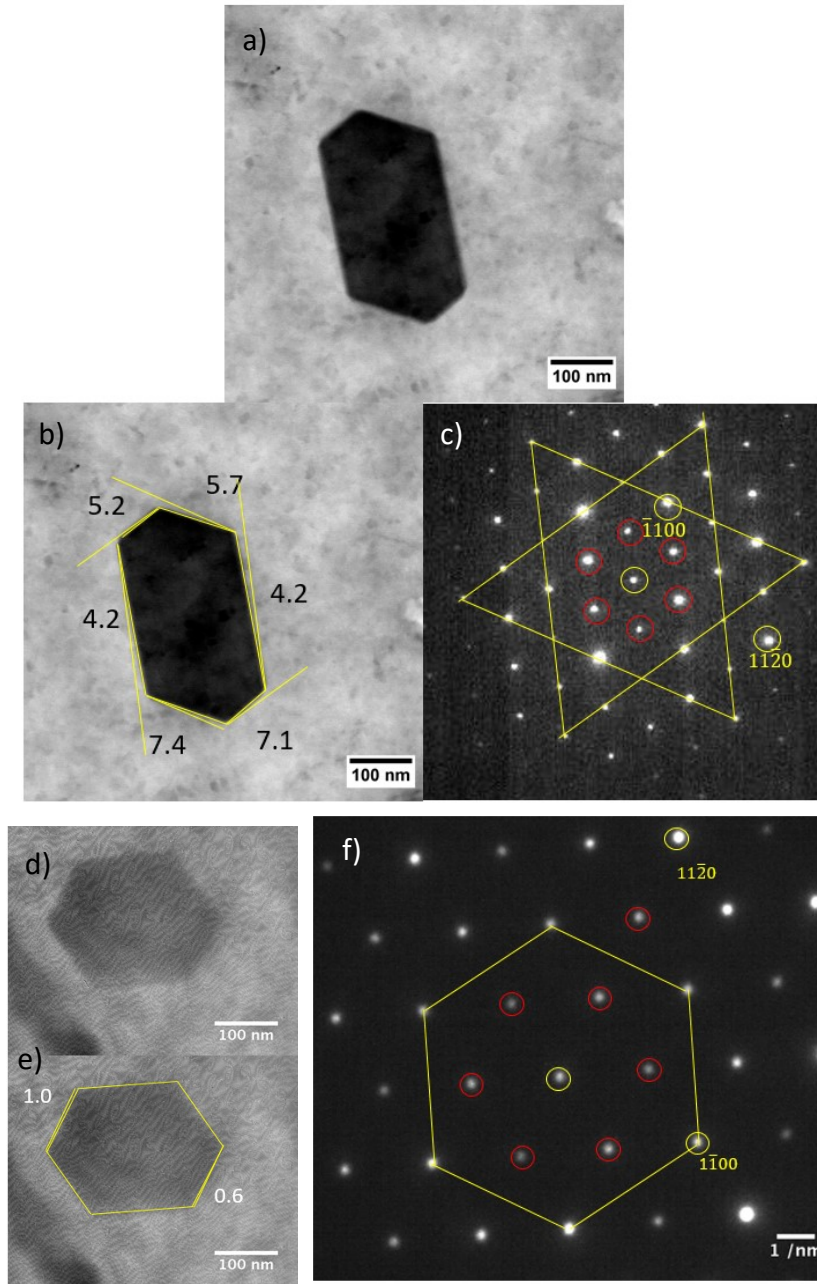
***Fig 4.14:*** *Two basal plates showing the edges deviation from $\{1\bar{1}00\}_\alpha$ planes. a) shows a basal plate in the Mg-1.75Sn-1.93Al alloy with b) the facets and $\{1\bar{1}00\}_\alpha$ planes marked as well as c)the accompanying SADP for the $[0001]_\alpha$ zone axis. There is clear deviations from the $\{1\bar{1}00\}_\alpha$ planes. d) however shows a basal plate from the Mg-1.29Sn-2.85Al alloy with e) the facets and$\{1\bar{1}00\}_\alpha$ planes and f) accompanying SADP. Here the deviation is much less common with only one pair of facets deviate from the$\{1\bar{1}00\}_\alpha$ planes. NB. precipitate reflections are circled in red.*

### 4.3.3.3   <c> Rods

Continuing we have the rods that grow in the $[0001]_\alpha$ direction. These can be observing

from $[0001]_\alpha$ to show the minimum size. The precipitate extends perpendicular to the tilt

axis during tilting; this is shown in Fig 4.15 with measurements given in Table 4.3. An issue arises that typically the length of the rods will exceed the sample thickness if the foil normal is close to $[0001]_\alpha$ meaning they are truncated in a sample with foil normal close to $[0001]_\alpha$. Despite the regular shape of this precipitate, the three facets all fall a few degrees from the $\{1\bar{1}00\}_\alpha$ planes as illustrated by Fig 4.16. Clearly measurement C increases greatly when tilted along the $(11\bar{2}0)_\alpha$ kikuchi band; C is close to perpendicular to the tilting axis indicating the rod shape. Similarly it can be seen in $[11\bar{2}6]_\alpha$ and $[\bar{1}\bar{1}26]_\alpha$ that a lengthening occurs perpendicular to the tilting axis, this is less obvious in the measurements however it can be clearly seen the top side in $[11\bar{2}6]_\alpha$ and the bottom in $[\bar{1}\bar{1}26]_\alpha$ are elongated. Again as shown for the previous two morphologies, there is a deviation between the faces of the precipitate and the $\{1\bar{1}00\}_\alpha$ planes of between 5 and 7.5°.
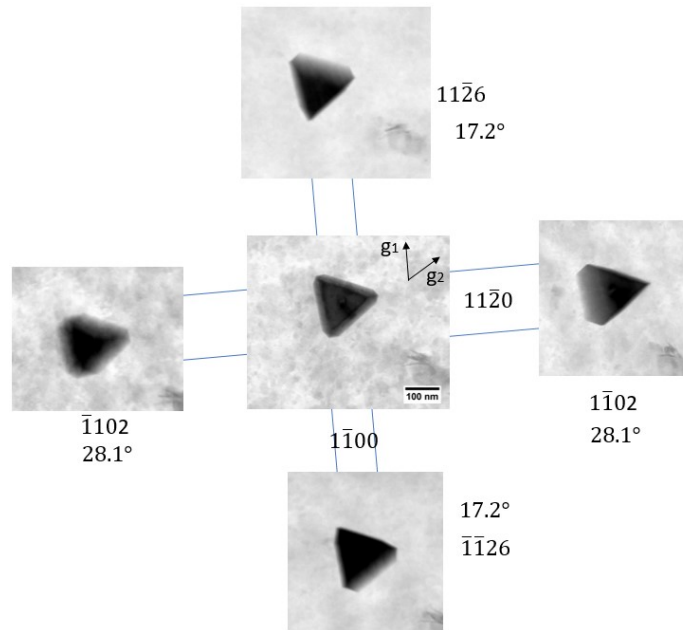


**Fig 4.15:** *Tilt series of <c>-rod precipitate, the central image is from $[0001]_\alpha$ with $g_1=[2\bar{1}\bar{1}0]_\alpha$ and $g_2=[11\bar{2}0]_\alpha$. These are taken from the Mg-1.75Sn-1.93Al alloy aged for 160hrs*

**Table 4.3**. *Table giving 3 measurements made from the three vertices to the opposite side. The vertices are labelled in Fig 4.16*

| Zone axes | A (nm) | B (nm) | C(nm) |
|-----------|--------|--------|-------|
| $[11\bar{2}6]_\alpha$ | 174 | 186 | 176 |
| $[0001]_\alpha$ | 176 | 174 | 180 |
| $[\bar{1}\bar{1}26]_\alpha$ | 183 | 167 | 178 |
| $[1\bar{1}02]_\alpha$ | 167 | 165 | 206 |
| $[\bar{1}102]_\alpha$ | 174 | 176 | 201 |
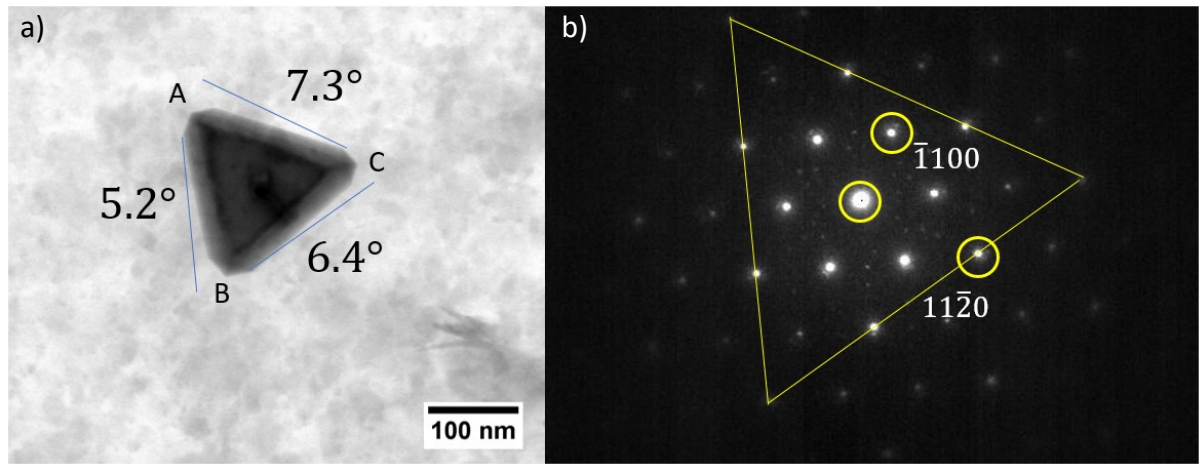


**Fig 4.16:** *a) <c> rod with $\{1\bar{1}00\}_\alpha$ marked with the angular deviation labelled and b) accompanying SADP*

### 4.3.3.4 Pyramidal Precipitates

Lastly we have the pyramidal rods, observing from $[11\bar{2}0]_\alpha$ (Fig 4.7 and 4.8 for the two alloys) it is clear that there are precipitates that do not fall into any of the three categories above however it is less obvious which plane that these lie on. The minimum/maximum thickness method used above is not necessarily the most suitable for pyramidal precipitates thus a 'facet method' is proposed whereby determining the trace direction from a pair of HAADF images of each of the sides of the precipitate can be used to calculate the faces of the precipitates. It is possible to use this method for any precipitate that is within the foil provided that tilt between the two images is not large meaning that the same facets are used in both images. Moreover, it makes the assumption that the

precipitate is a simple geometry e.g. cuboidal, such that the same facet is used after the sample has been tilted.

Sasaki et al[111] claim the pyramidal precipitates in their Mg-2.2Sn-0.5Zn alloy lie on the $\{11\bar{2}2\}_\alpha$ plane, though neither Liu et al or Mendis et al[108,109,112] confirm this or provide an alternative. Fig 4.16 is one such pyramidal precipitate in the Mg-1.29Sn-2.85Al alloy aged for 160hrs; HAADF images are shown with accompanying SADPs. Firstly, from the $[0001]_\alpha$ image, Fig 4.16, it is clear that the two edges fall along the projection of $[11\bar{2}0]_\alpha$ and $[\bar{2}110]_\alpha$.
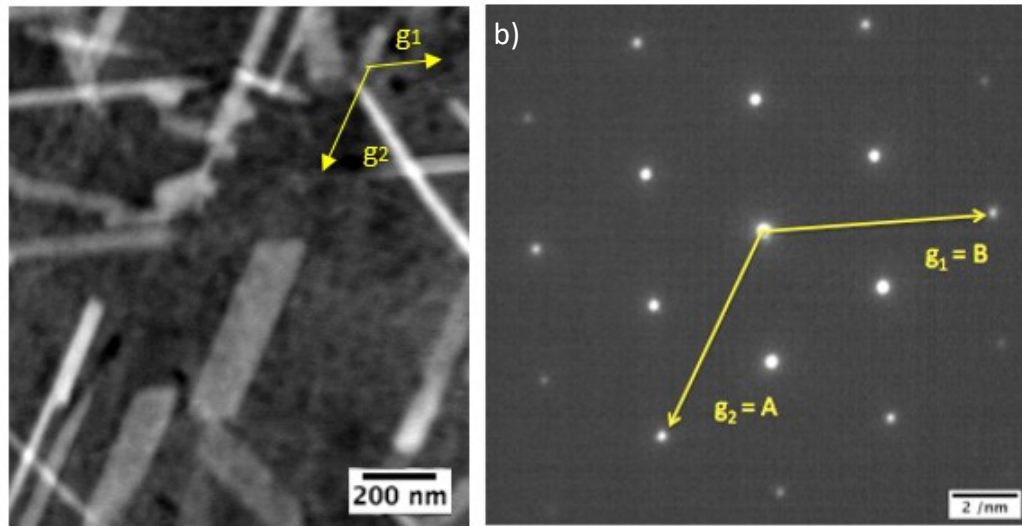


***Fig 4.16:*** *a)HAADF image ($g_1$=B =$2\bar{1}\bar{1}0_\alpha$ $g_2$= A = $\bar{1}\bar{1}20_\alpha$) and b)SADP from pyramidal lath precipitate*

The second image, Fig 4.17, the matter is marginally more complicated. Observing from the $(01\bar{1}2)_\alpha$ zone axis, we can see a second set of traces. Fig 4.18 shows that edge A lies on $[22\bar{4}3]_\alpha$ and edge B lies on the $[4\bar{3}\bar{1}1]_\alpha$. By crossing each pair of directions, we are left with $(1\bar{1}00)_\alpha$ and $(0\bar{1}12)_\alpha$ as the two facets of the precipitate. Crossing this pair and we are left with a direction of $[\bar{2}\bar{2}43]_\alpha$ which falls close to the $(11\bar{2}1)_\alpha$ plane. This can be shown diagrammatically on a stereogram in Fig 4.19.
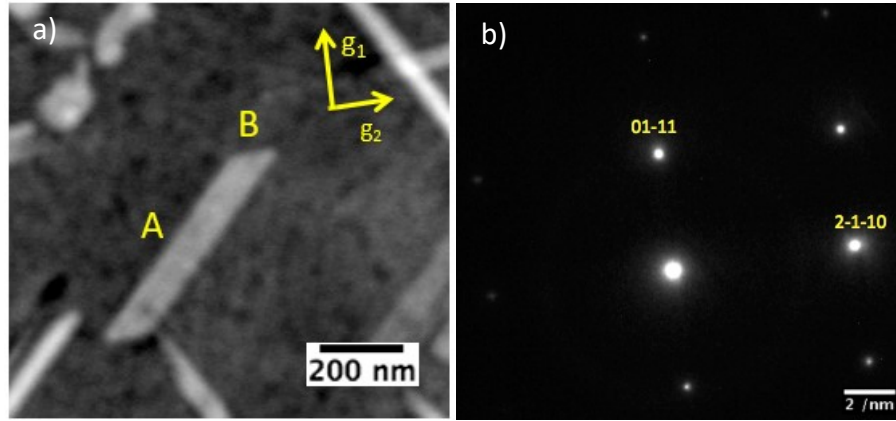
**Fig 4.17:** *a) HAADF image of pyramidal precipitate ($g_1$ =$[0\bar{1}11]_\alpha$, $g_2$ = $[2\bar{1}\bar{1}0]_\alpha$) with b) accompanying SADP from $[01\bar{1}2]_\alpha$, facets are labelled A and B respectively*
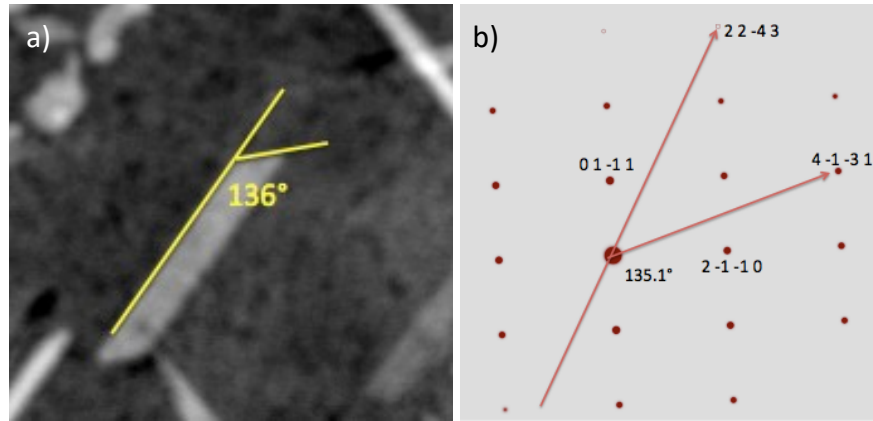


**Fig 4.18:** *a) facets on HAADF image matched to b) simulated diffraction pattern showing the edges near parallel to $[22\bar{4}3]_\alpha$ and $[4\bar{1}\bar{3}1]_\alpha$*
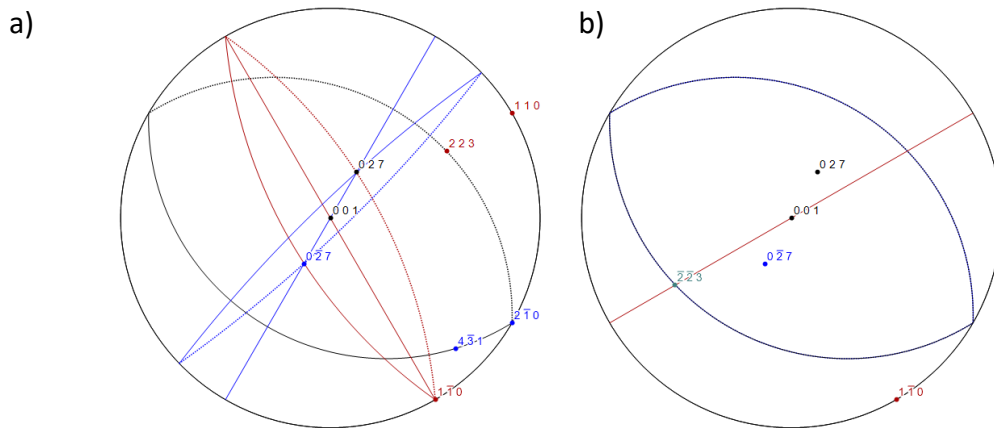


**Fig 4.19:** *a) Stereograph from $[0001]_\alpha$ zone axis showing facet A in red (110 and 223) and facet B in blue ($2\bar{1}0$ and $4\bar{1}1$). The resulting great circles give the facets as the $1\bar{1}0$ ($[1\bar{1}00]_\alpha$) and $02\bar{7}([01\bar{1}2]_\alpha)$. b) stereograph from $[0001]_\alpha$ shows the resulting plane normal gs $\bar{2}\bar{2}3$ which gives plane close to $(11\bar{2}1)_\alpha$*

However when observing from the $[11\bar{2}0]_\alpha$ direction (Fig 4.7 and 4.8), it is clear that the pyramidal precipitates lie on different planes. The growth direction of the pyramidal laths is $\langle 11\bar{2}X \rangle_\alpha$, as can be see from $[0001]_\alpha$ (Fig 4.16) as the long axis is along a $\langle 11\bar{2}0 \rangle_\alpha$ direction.

As the other two $\langle 11\bar{2}0 \rangle_\alpha$ directions are ±60° from the beam direction when observing from $[11\bar{2}0]_\alpha$ the trace of any of the $\langle 11\bar{2}X \rangle_\alpha$ (where X is an integer) planes would have the same elevation angle (angle between the trace of the plane and basal plane). Thus we can measure a large number of these elevation angles to determine if there is any trend in the habit planes, knowing the growth direction as $\langle 11\bar{2}X \rangle_\alpha$ we can actually convert the measured angle into the actual elevation angle with simple trigonometry.
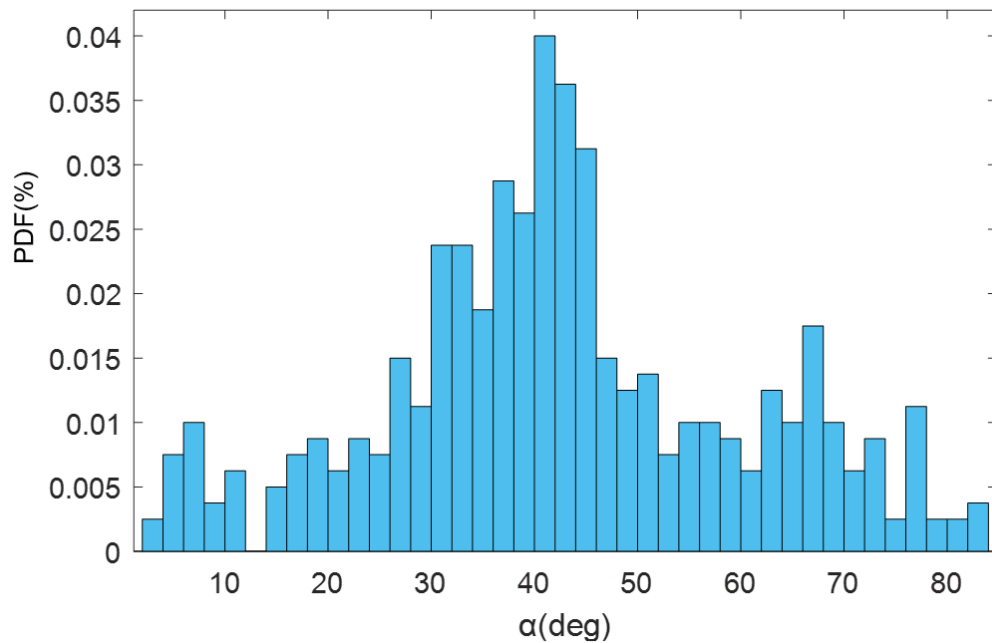


***Fig 4.20:*** *Histogram of actual elevation angles of pyramidal precipitates. Data is compiled for all the studied samples*

As such, a survey of a large number of precipitates has been conducted, identifying as best as possible the common growth directions as shown in Fig 4.20. It is clear that there is a

great deviance in the given angles. Clearly there is a complex reason for the great number of morphologies and habit planes.

### 4.3.4 Chemical Composition

The chemical composition was measured via EDX on the two 160 hour aged alloys to demonstrate that all of the precipitates are Sn rich; secondly, electron diffraction has been used to confirm the crystal structure of the precipitates and identify the orientation relationship between the precipitates and the matrix.

A quick EDX map easily demonstrates that the Al in the alloy is not localised to the precipitates as shown in Fig 4.21. Assuming that the precipitates in both samples are $Mg_2Sn$, EDX point scans should fall between the matrix composition and $Mg_2Sn$ depending on the percentage of the signal which arises from the precipitate and the matrix respectively. Plotting the results on a ternary phase diagram should result in the compositions measured falling on a line between the matrix composition and $Mg_2Sn$.
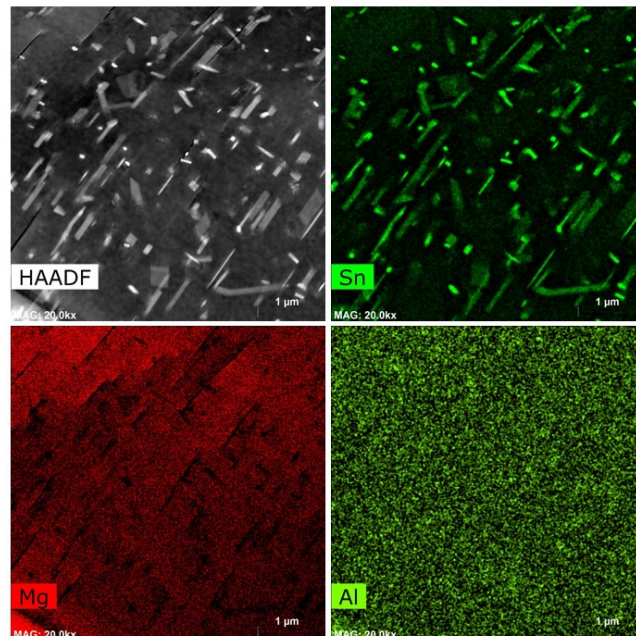


*Fig 4.21:* *EDX map of Mg-1.75Sn-1.93Al alloy aged for 160 hours. Clearly the Al is not concentrated in any area where as the Sn is clearly located in the precipitates.*

It should be noted that the EDX study will not discriminate between the precipitate morphologies observed in the previous section. Spectra have been taken from a variety of precipitate morphologies and on both alloy compositions aged for 160hrs on the basis that the precipitates will be largest, hence less of the matrix will be included in the interaction volume.

As can be seen in Fig 4.22, both alloy compositions give a clear indication that the precipitates are $Mg_2Sn$, as they fall close to the line between $Mg_2Sn$ and the alloys nominal composition. There is clearly some deviation from the line presented and it should be noted only to the aluminium rich (left) of the line. It should be remembered that the two compositions highlighted in Fig 4.23 are that of the as-cast alloys and as such the actual composition of the matrix after ageing will be pushed toward the Al corner of the ternary phase diagram as both Mg and Sn are tied into the precipitates. Further investigation of the crystal structure through electron diffraction is still required to unequivocally show the precipitates to be $Mg_2Sn$ with the $CaF_2$ crystal structure.
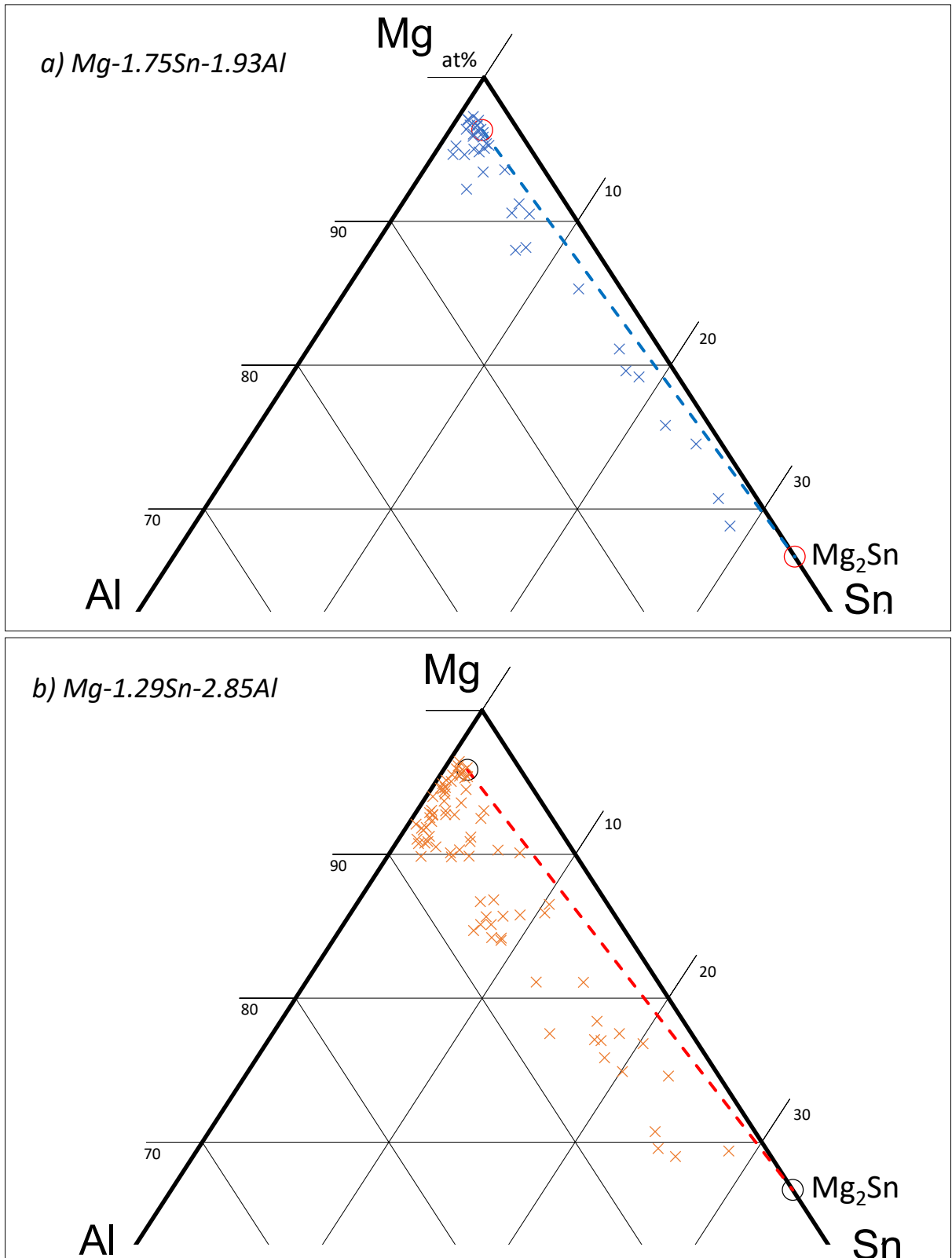
**Fig 4.22:** *Mg-Al-Sn phase diagram for a)Mg-1.75Sn-1.93Al and b)Mg-1.29Sn-2.85Al both showing composition from EDX point scans. In both cases the composition of the alloy and Mg$_2$Sn are given as hollow circles with a dotted line between them.*

### 4.3.5 Orientation Relationships and Crystal Structure

From the observations from the XRD and the EDX we concluded that the precipitates are

$Mg_2Sn$; this would give the precipitates a $CaF_2$ structure. Electron diffraction will allow us

to not only identify the crystal structure but also give the orientation between the

precipitates and the magnesium matrix. As can be seen from the literature survey there

are a number of possibilities reported for the orientation relationship (Table 2.7). What

is common between the majority of these is that the $0001_\alpha$ axis of the matrix corresponds

to a major zone axis of the precipitate, usually either $111_\beta$ or $110_\beta$, thus giving a

reasonable idea of where to start with the identification. The two most commonly

reported orientation relationships are:

$$(0001)_\alpha//(110)_\beta, \ [11\bar{2}0]_\alpha//[1\bar{1}1]_\beta \hspace{3cm} \text{(OR-1)}$$

and

$$(0001)_\alpha//(111)_\beta, \ [11\bar{2}0]_\alpha//[\bar{1}10]_\beta \hspace{3cm} \text{(OR-3),}$$

so it is expected that the OR is likely to be one of these. Thus, it seems prudent to observe

the different precipitates from the $0001_\alpha$ beam direction as a starting point. Fig 4.23 gives

a SADP from a $\langle 11\bar{2}0 \rangle_\alpha$ lath in the Mg-1.75Sn-1.93Al alloy showing a pattern

corresponding to OR-3. Additional diffraction spots fall on the forbidden $\langle 1\bar{1}0 \rangle_\beta$

reflections.

Observing from $[2\bar{1}\bar{1}0]_\alpha$ (Fig 4.24), the pattern becomes far more complicated with

additional reflections being present, however the OR still remains as OR-3. The extra

reflections are attributed to double diffraction. In order to ensure that the crystal

structure is $CaF_2$, 2 other ZA were identified as shown in Fig 4.25, it should be noted that

the $CaF_2$ structure cannot be discerned from F.C.C. using electron diffraction due to

identical symmetry and forbidden reflections. In theory the two can be discerned by

measuring the relative intensity of diffraction spots however this is high dubious using TEM and better ascertained using XRD.
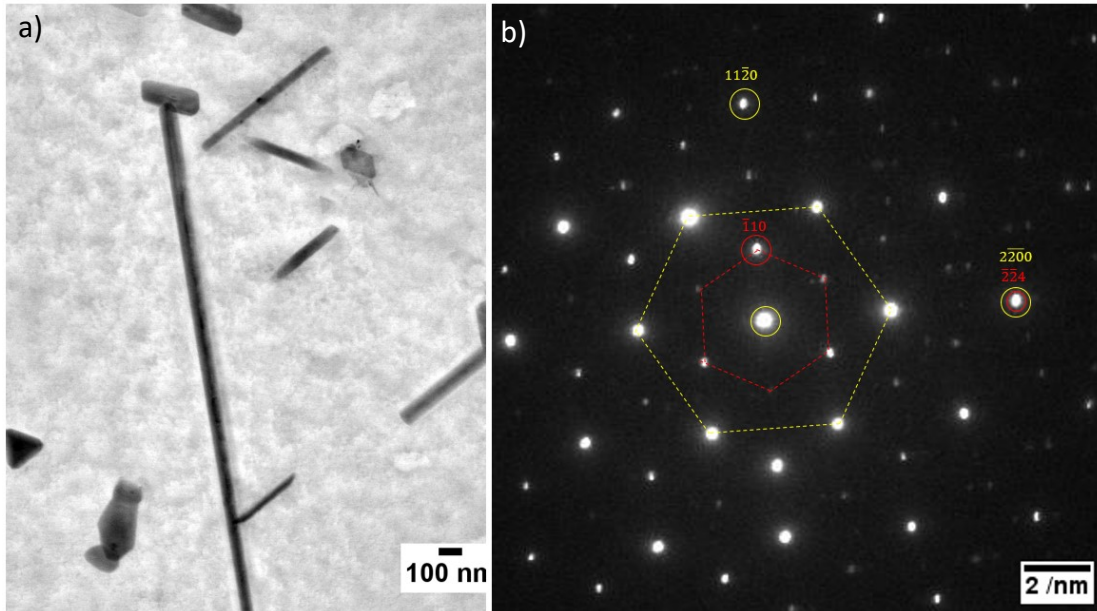


**Fig 4.23:** *a) BF image. (g₁ =[11$\bar{2}$0]$_\alpha$, g₂ = [1$\bar{1}$00]$_\alpha$) with b) [0001]$_\alpha$ DP from [11$\bar{2}$0]$_\alpha$ lath in Mg-1.29Sn-2.85Al alloy aged for 160 hours Diffraction spots circled in yellow are those of the matrix whereas red circled spots represent diffraction spots from the precipitate. Note that forbidden ⟨110⟩$_\beta$ reflections are visible*
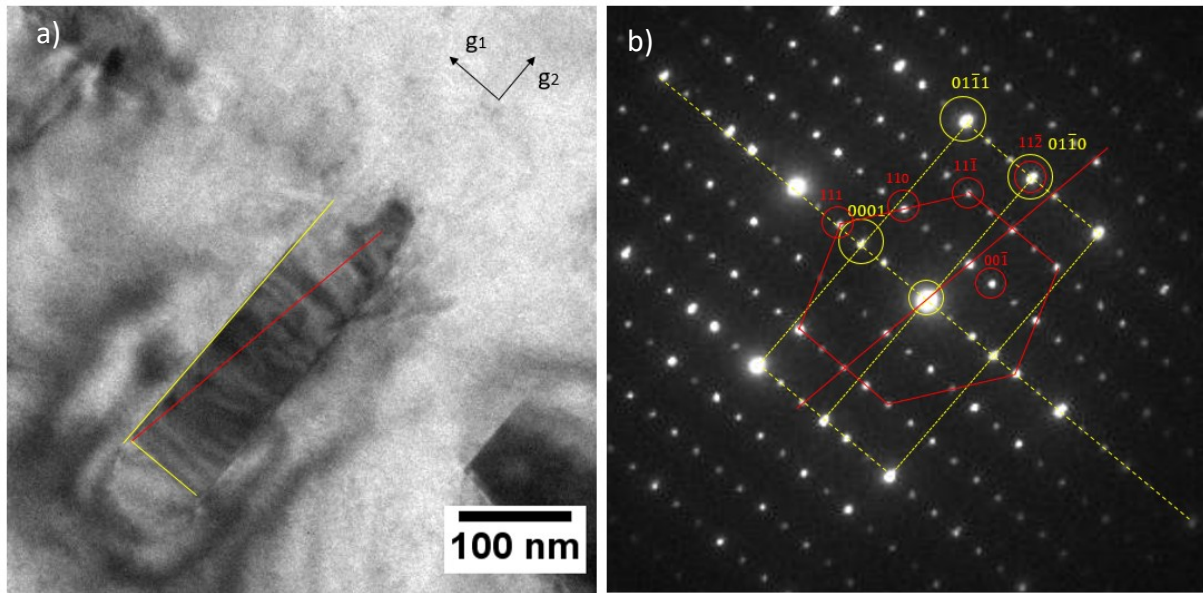


**Fig 4.24:** *a) BF image. (g₁ =[0001]$_\alpha$, g₂ = [01$\bar{1}$0]$_\alpha$) from [2$\bar{1}$$\bar{1}$0]$_\alpha$ ZA with b) DP from [11$\bar{2}$0]$_\alpha$ lath in Mg-1.75Sn-1.93Al alloy aged for 160 hours. Diffraction spots circled in yellow are those of the matrix whereas red circled spots represent diffraction spots from the precipitate.*
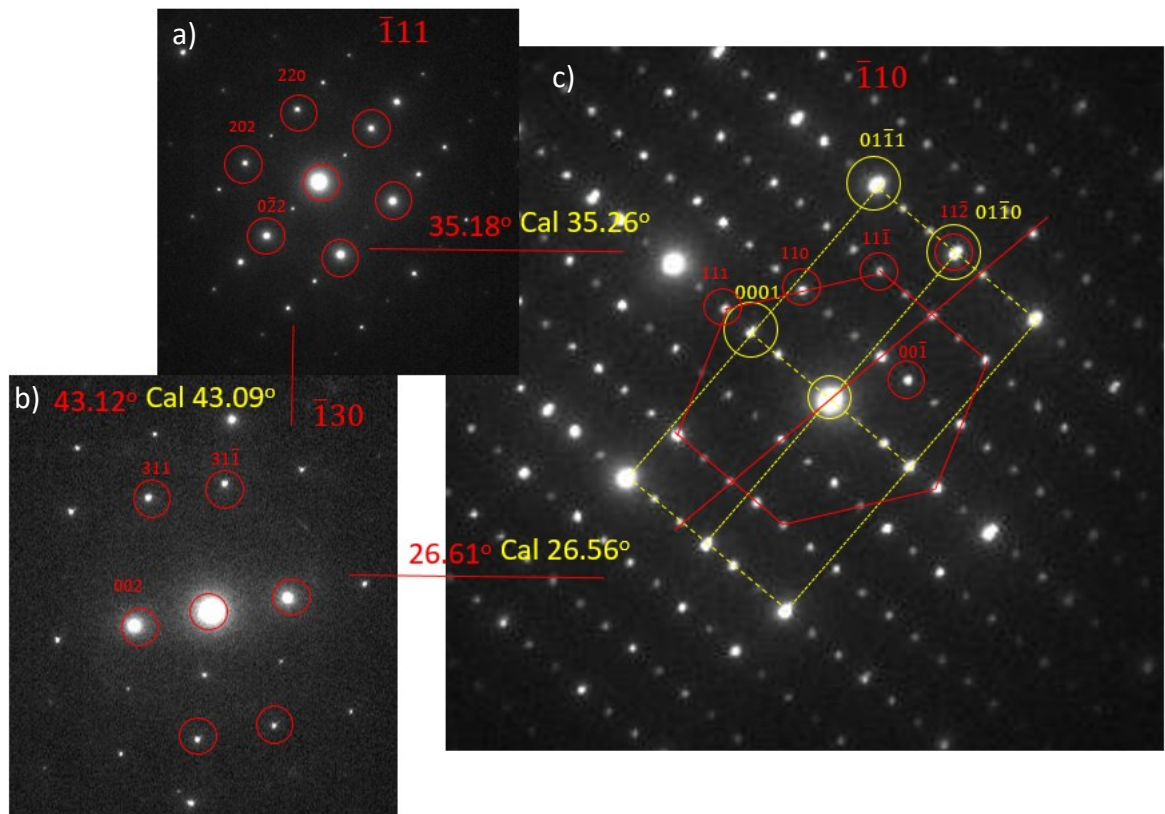
***Fig 4.25:*** *3 zones axes, a)* $[\bar{1}11]_\beta$*, b) )* $[\bar{1}30]_\beta$ *and c)* $[\bar{1}10]_\beta$ *confirming the crystal structure of the* $Mg_2Sn$ $[11\bar{2}0]_\alpha$ *lath. Diffraction spots circled in yellow are those of the matrix whereas red circled spots represent diffraction spots from the precipitate.*

The OR for the $\langle11\bar{2}0\rangle_\alpha$ laths in the Mg-1.29Sn-2.85Al sample, aged for 160 hours is confirmed as shown in Fig 4.26 from the $[0001]_\alpha$ direction. This treatment is extended to the basal plate and prismatic rod morphologies that are given below in Fig 4.27-30. All instances show the same OR.
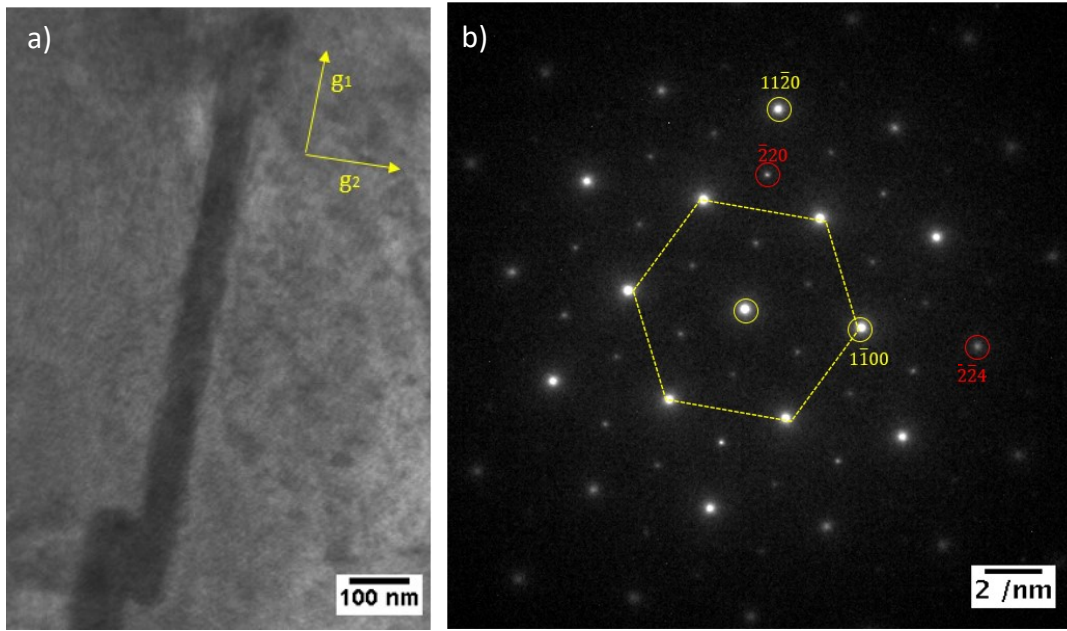
***Fig 4.26:*** *a) BF image. ($g_1$ =$[11\bar{2}0]_\alpha$, $g_2$ = $[1\bar{1}00]_\alpha$) with b) $[0001]_\alpha$ DP from $[11\bar{2}0]_\alpha$ lath in Mg-1.29Sn-2.85Al alloy aged for 160 hours. Diffraction spots circled in yellow are those of the matrix whereas red circled spots represent diffraction spots from the precipitate. Note that forbidden $\langle 110 \rangle_\beta$ reflections are visible*
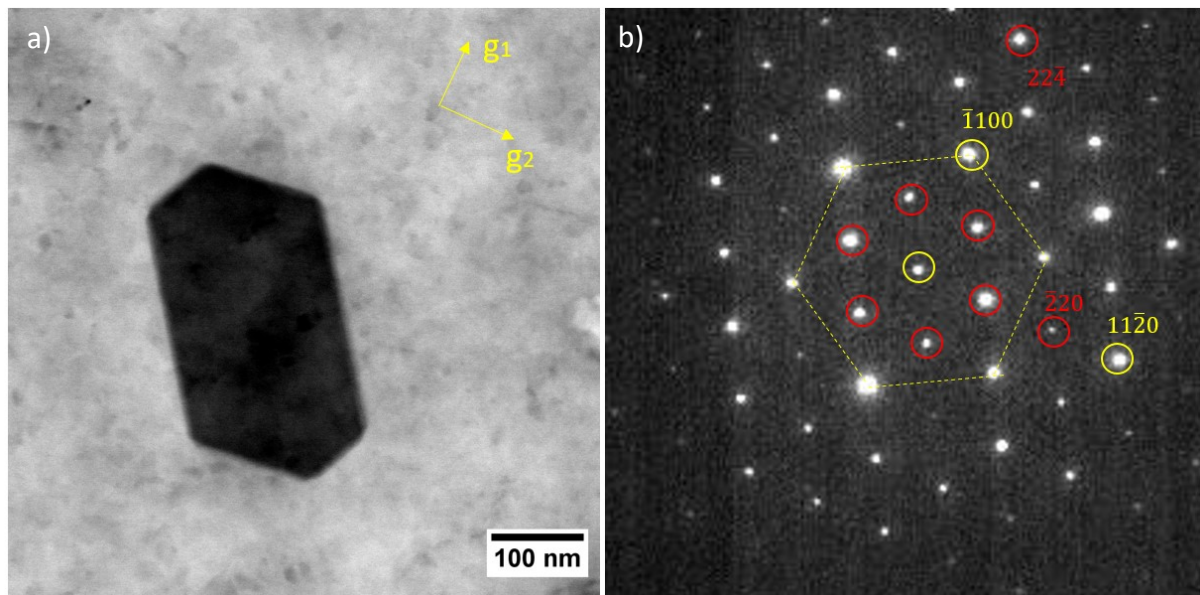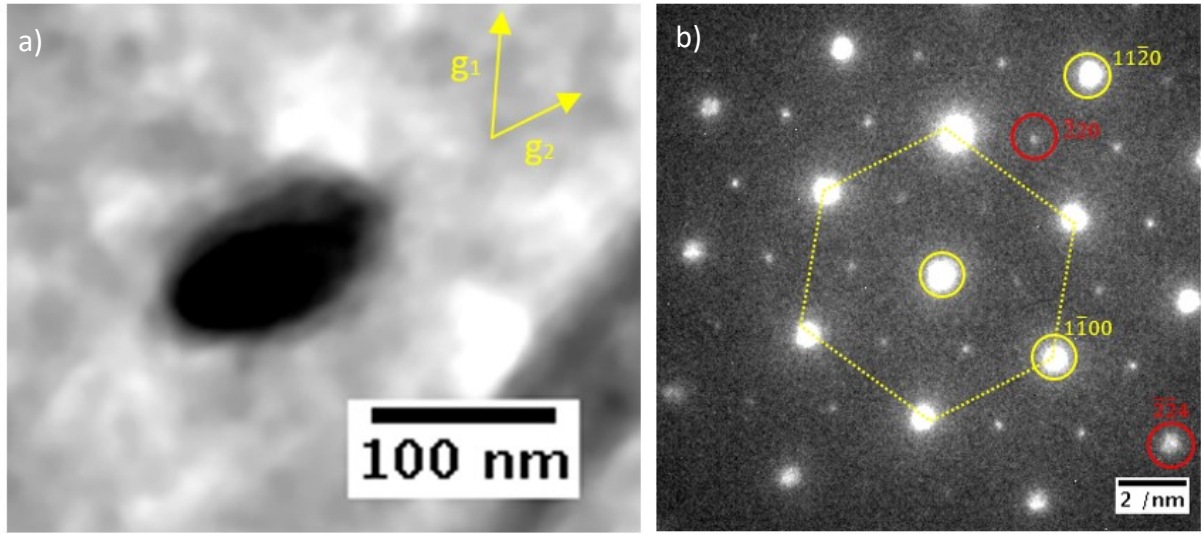


***Fig 4.27****: (a) BF image of hexagonal basal precipitate in Mg-1.75Sn-1.93Al alloy aged for 160hrs from beam direction $[0001]_a$, ($g_1$= $[\bar{1}100]_\alpha$, $g_2$= $[11\bar{2}0]_a$) with (b) SADP. Diffraction spots circled in yellow are those of the matrix whereas red circled spots represent diffraction spots from the precipitate*
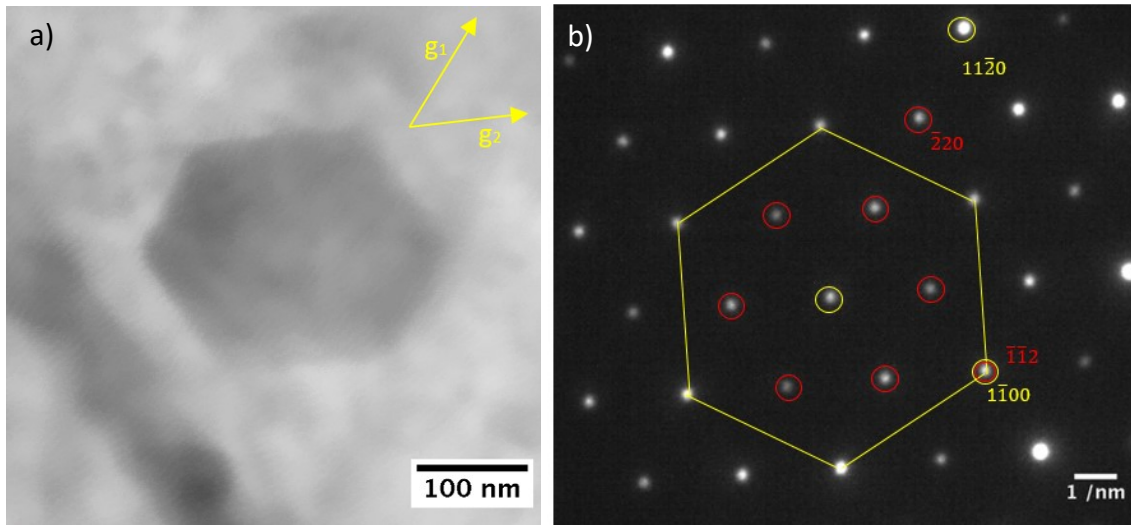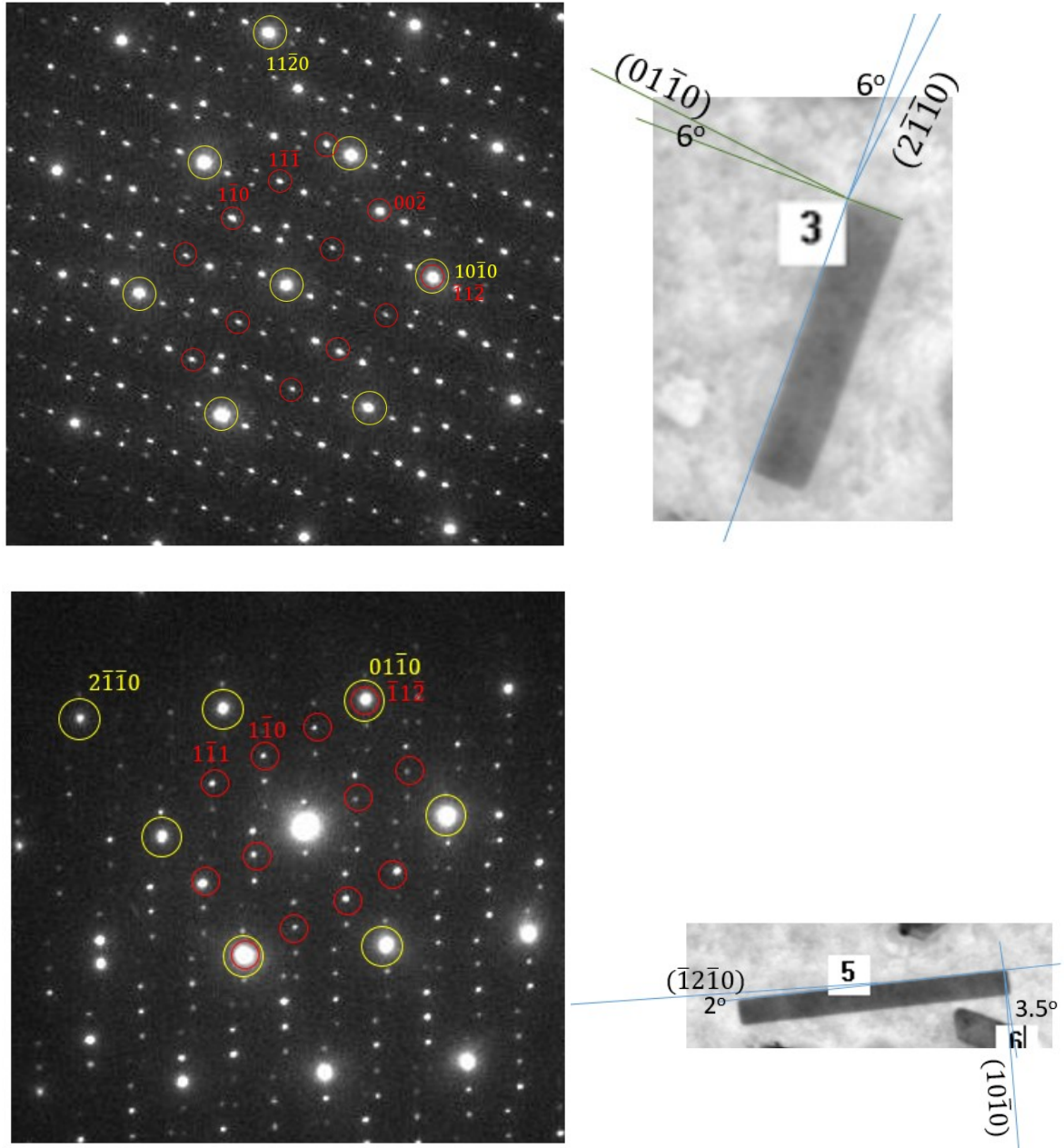
***Fig 4.28***: (a) *BF image of hexagonal basal precipitate in Mg-1.29Sn-2.85Al alloy aged for 160hrs from beam direction $[0001]_a$, ($g_1= [11\bar{2}0]_a$, $g_2= [\bar{1}2\bar{1}0]_a$) with (b) SADP. Diffraction spots circled in yellow are those of the matrix whereas red circled spots represent diffraction spots from the precipitate*
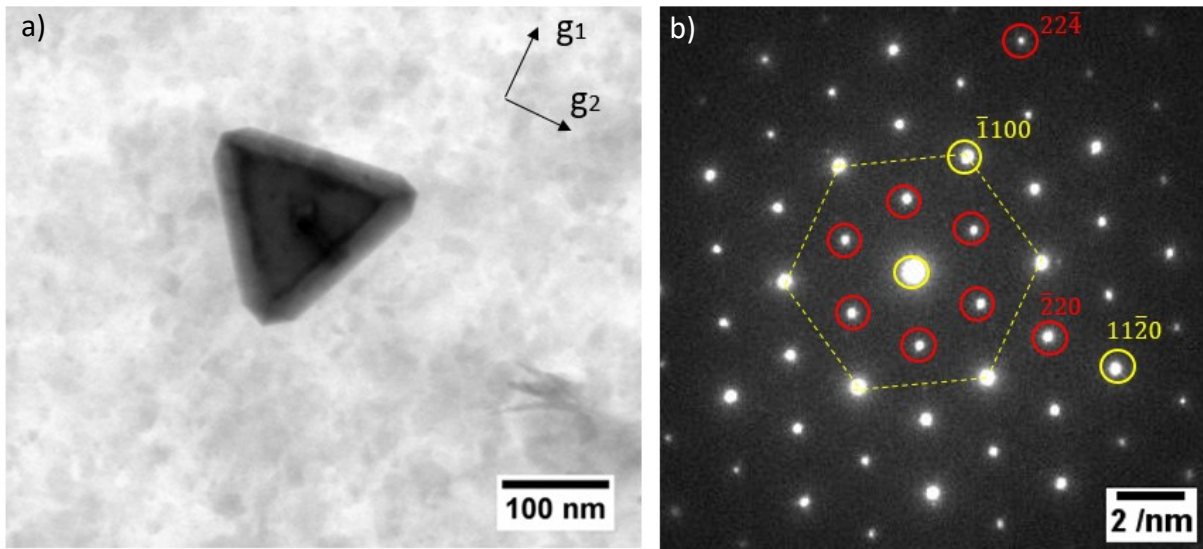


***Fig 4.29***: (a) *BF image of <c>rod precipitate in Mg-1.75Sn-1.93Al alloy aged for 160hrs from beam direction $[0001]_a$, ($g_1= [\bar{1}100]_a$, $g_2= [11\bar{2}0]_a$) with (b) SADP. Diffraction spots circled in yellow are those of the matrix whereas red circled spots represent diffraction spots from the precipitate*

***Fig 4.30***: (a) *BF image of <c>rod precipitate in Mg-1.29Sn-2.85Al alloy aged for 160hrs from beam direction* $[0001]_a$, *(g₁= $[01\bar{1}0]_a$, g₂= $[10\bar{1}0]_a$) with (b) SADP . Diffraction spots circled in yellow are those of the matrix whereas red circled spots represent diffraction spots from the precipitate*

### 4.3.6 Basal Laths

In addition to the above, there are instances of basal laths seen in the Mg-1.75Sn-1.93Al sample used in this study. These are far fewer in number than the other morphologies described, with only two instances being found. These are interesting as despite the other morphologies mostly exhibiting OR-3, these exhibit OR-1 as described in the literature. As with the other precipitates, the facets do not fall exactly on the low index planes but have a similar small deviation of up to 10°.

***Fig 4.31***: (a) *BF image of <c>rod precipitate in Mg-1.29Sn-2.85Al alloy aged for 160hrs from beam direction* $[0001]_a$, ($g_1$= $[01\bar{1}0]_a$, $g_2$= $[10\bar{1}0]_a$) *with (b) SADP . Diffraction spots circled in yellow are those of the matrix whereas red circled spots represent diffraction spots from the precipitate*
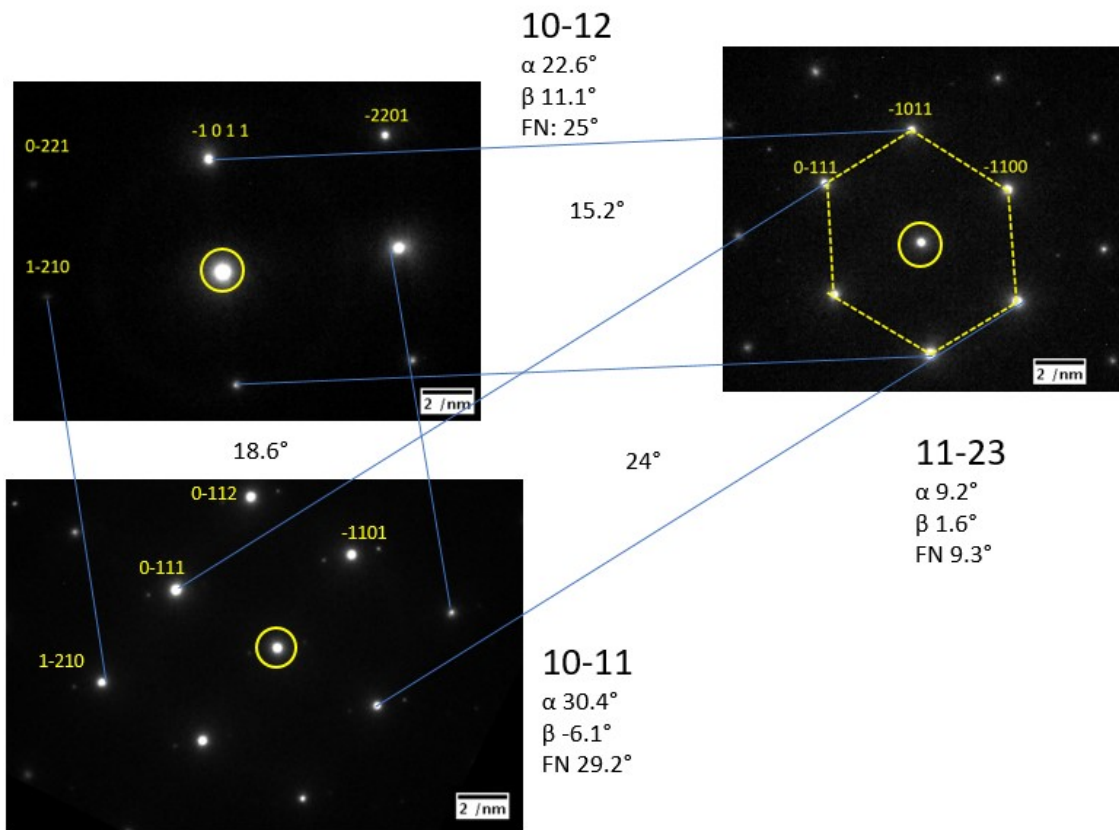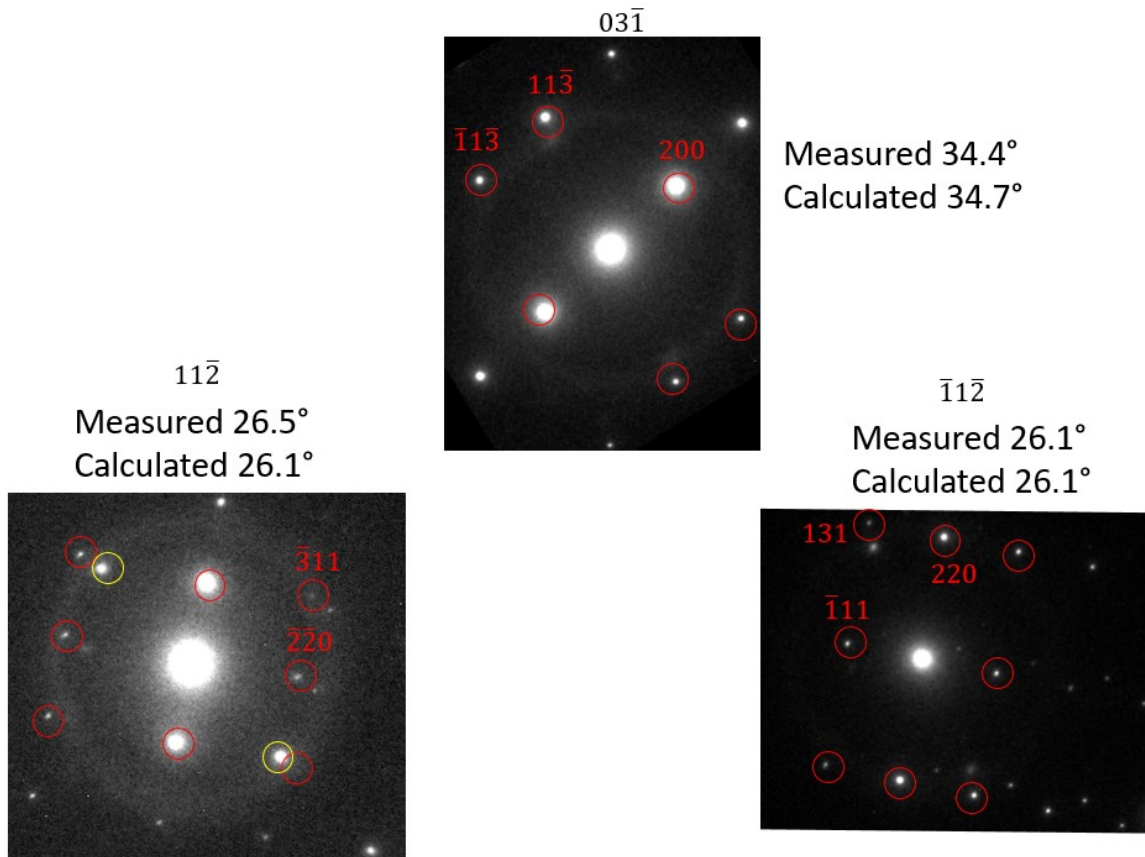
***Fig 4.32***: *3 diffraction patterns with angle to the foil normal used to calculate the foil normal of* $[10\ 24\ \overline{34}\ 43]_\alpha$

### 4.3.7  Pyramidal Laths

Unfortunately the pyramidal laths presented a much less simple OR that could not be determined from the $[0001]_\alpha$ beam direction . A number of different ZA for the precipitate were identified, though the majority did not readily correspond to the ZAs of the matrix. However, by mapping the tilt angles between the various ZA of both precipitate and matrix that are found as well as calculating the foil normal for both the matrix and the precipitate, it has been possible to construct a stereogram containing the orientation information for both lattices and subsequently express the OR using these corresponding poles.

Initially the determination of the foil normal from the matrix is relatively simple, as described by Loretto[170] as shown in Figs 4.32 and 4.33. This allows foil normals of

$[10\ 24\ \overline{34}\ 43]_\alpha$ and $[03\overline{4}]_\beta$ to be found for the FIB-TEM sample for the matrix phase and the pyramidal rod used in this study. Stereograms for each lattice to be constructed with the respective foil normal in the centre. By then considering the angle that can be measured between the ZAs of the two different crystals, the stereographs can be rotated and from this the OR ascertained as shown in Fig 4.32. While this method is useful, there is likely still an error of a degree or so given the discrepancy between the actual tilting in the stage and that calculated in the theoretical case; nonetheless this provides a useful tool with which to establish an OR which can aid in explaining the observed morphology. As can be seen there is no easily definable OR as with the other morphologies, with the only ZA close to corresponding being shown in Table 4.1.



*Fig 4.33*: *3 diffraction patterns with angle to the foil normal used to calculate the foil normal of* $[034]_\beta$

s

**Table 4.1:** *Table giving approximate misorientation between closely aligned zone axes in matrix and precipitate crystal structures*

| Matrix | Angle | Precipitate |
|:---:|:---:|:---:|
| $[0001]_\alpha$ | ~2° | $[\bar{2}1\bar{3}]_\beta$ |
| $[0001]_\alpha$ | ~20° | $[\bar{1}1\bar{1}]_\beta$ |
| $[0001]_\alpha$ | ~20° | $[\bar{1}0\bar{1}]_\beta$ |
| $[11\bar{2}2]_\alpha$ | ~5° | $[01\bar{1}]_\beta$ |
| $[10\bar{1}2]_\alpha$ | ~5° | $[\bar{1}2\bar{2}]_\beta$ |
| $[01\bar{1}0]_\alpha$ | ~5° | $[21\bar{1}]_\beta$ |
| $[\bar{1}100]_\alpha$ | ~10° | $[1\bar{1}\bar{1}]_\beta$ |

## 4.4 Discussion

Obviously given the range of OR's reported in the literature, not all Mg-Sn alloys conform to a single OR. The two studied alloys, however, exhibit OR-3 for 3 of the described morphologies as widely observed in other Mg-Sn ternaries. What is more, in keeping with the work of Mendis et al.[108], the ORs for the $\langle 11\bar{2}0 \rangle_\alpha$ lath and prismatic precipitates are the same despite their different morphologies. It is noted in the work of Nie et al[156] that the OR can vary within one sample. Nie found that the majority, 75.1%, of basal laths had OR-1 with 24.3% having OR-2 and the remaining 0.6% having unnamed ORs. In the current alloy, OR-3 has been observed throughout the sample on multiple precipitates. Two precipitates sitting on the basal plane was found to have OR-1 in the Mg-1.75Sn-1.93Al alloy.

OR-3 is most prominent in the current alloys, being observed for multiple precipitate morphologies. The OR is not surprising as diffraction spots for $[11\bar{2}0]_\alpha$ and $[\bar{3}30]_\beta$, and $[1\bar{1}00]_\alpha$ and $[\bar{1}\bar{1}2]_\beta$ overlap as illustrated by Fig 4.23, however the multiple morphologies observed would suggest that precipitates morphology is determined earlier in the ageing

process than the OR, mostly likely in the early stage of nucleation. OR-3 seems to be more favourable than OR-1 observed in the binary[156], although OR-3 is still possible in the binary as demonstrated by Henes and Gerold[152]. It is only apparent at higher ageing temperature, and accounts for a small fraction of the precipitates, suggesting that the energy required for nucleation is higher relative to OR-1. The addition of alloying elements clearly lowers the energy required for OR-3 below that of OR-1. It is suggested that the additional energy results from the enthalpy of mixing between the Al/Zn and Sn[110,155]. It is further noted that the nucleation rate of the precipitates is far higher than in the binary and therefore it is suggested that the quicker nucleation and the change in OR are both due to the same reason with there being additional energy to first of all create and sustain nuclei and secondly for those nuclei to rearrange to a form that will yield OR-3.

We can take this further by considering that the precipitates in the binary are solely basal. The alloying element is therefore again responsible for the non-basal precipitate morphologies. The OR in the case of the pyramidal precipitates in this work and in Liu[112] show very few low index directions coinciding between the two crystals. This as with the above OR is taken to be a consequence of the precipitate nucleating and growing in a shape before a clear OR is established. As the growth direction does not lie close to a low index plane in the matrix as demonstrated by Fig 4.20, the magnitude of the Gibbs free energy driving the growth of the $Mg_2Sn$ is sufficiently large to allow a precipitate with high surface energy to grow to a sufficient size quickly enough that it cannot rearrange to a precipitate with a lower surface energy as would be expected of OR-3. Therefore edge to edge matching, as used by Zhang and Kelly[50,144–146] and CCSL techniques, as described by Shi et al[149,150] are not suggested as a means for predicting ORs found in

Mg-Sn alloys but are useful to justify those observed. There is no benefit in further reporting the ORs of the various precipitates without a better understanding of the mechanism determining the precipitate morphology. Further investigation is required into the nucleation of the precipitates to explain the different morphologies. It is suggested that the early stages of growth are characterised, preferably via an in-situ TEM ageing experiment with a heating stage. This would allow the determination of the shape and OR of the precipitates in the early stages and directly link the resultant precipitate shape and OR. The nucleation mechanism should be compared between the binary and ternary to ascertain the effect of Al and Zn; this experiment may be prohibited by the time required for nucleation to occur in the binary.

## 4.5 Summary

To conclude, the species of precipitate has unequivocally been identified as that of $Mg_2Sn$ via XRD, STEM-EDX and electron diffraction. Four precipitate morphologies have been identified through a series of tilting experiments, with the facets investigated. The habit plane/growth direction of the pyramidal precipitates has been investigated to show that there is no one favoured plane. Moreover the OR for the $\langle 11\bar{2}0 \rangle_\alpha$ laths, basal plates and prismatic precipitate morphologies has been shown to consistently be OR-3 as favoured in other ternary alloys[107–112,116,152,157,158]. On the other hand, partially in line with the work of Liu et al[112], the pyramidal laths have been shown to have no well defined OR in the Mg-1.29Sn-2.85Al.
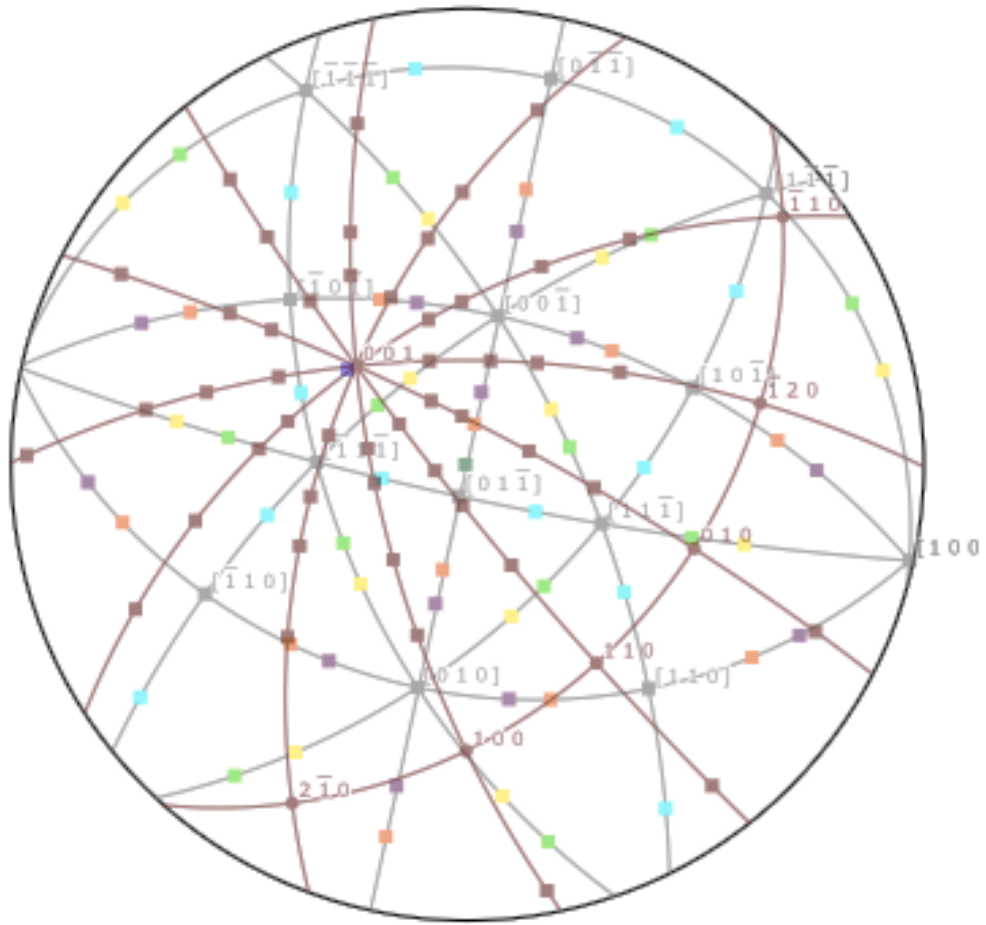
**Fig 4.32:** *Overlayed stereograms centred on foil normal. Foil normal is given as dark green. Burgundy represents the matrix with the following ZA marked* $\langle 10\bar{1}0 \rangle_\alpha, \langle 20\bar{2}1 \rangle_\alpha, \langle 10\bar{1}1 \rangle_\alpha, \langle 10\bar{1}2 \rangle_\alpha, \langle 10\bar{1}3 \rangle_\alpha, \langle 11\bar{2}0 \rangle_\alpha, \langle 11\bar{2}1 \rangle_\alpha, \langle 11\bar{2}2 \rangle_\alpha, \langle 1\bar{1}23 \rangle_\alpha$ *and* $\langle 11\bar{2}6 \rangle_\alpha$. *The major poles of the Mg2Sn precipitate are labelled with the following poles colour coded as below: Light green* $\langle 112 \rangle_\beta$, *yellow* $\langle 113 \rangle_\beta$, *light blue* $\langle 122 \rangle_\beta$, *orange* $\langle 201 \rangle_\beta$, *purple* $\langle 301 \rangle_\beta$.

# 5  PRECIPITATE NUMBER DENSITY AND SIZES

## 5.1  Introduction

So far we have established that in line with the literature and the associated phase diagrams that the two alloys, Mg-1.75Sn-1.93Al and Mg-1.29Sn-2.85Al(at%), both develop a $Mg_2Sn$ phase during ageing at 200°C. The ageing produces a greater hardening in the Mg-1.29Sn-2.85Al alloy despite the lower Sn content based on the hardness measurements. Firstly the volume/area fraction of precipitates will be established via XRD and SEM. This will be furthered developed by establishing a number density which is important in the context of the strengthening. This will be measured by both SEM and TEM. Likewise when establishing the orientation relationship, we have seen that numerous morphologies exist within the microstructure. The relative fractions of each morphology have not been established elsewhere and will be incorporated into the TEM number density measurements.

Similarly, it is well established that precipitates can strengthen via two mechanisms. When a dislocation interacts with a precipitate, one of two things can happen; either the precipitate will be small enough that the dislocation can shear the precipitate or the precipitate will large such that the dislocation will be impeded and form a dislocation loop. Only one of these mechanisms will be active at one time, which is determined by the size of the precipitate. Therefore we must consider the size of the precipitates to model the strength properly. This will establish a full picture of the microstructure of the alloy, providing data to be fed into the model that will be described in Chapter 6.

## 5.2    Volume and Area Fraction

Now that the precipitates have been identified as $Mg_2Sn$, it is possible to extract further information from the XRD spectra. The spectra was fitted using the Rietveld approach described in chapter 3[162–164] to give the volume fraction of each phase. The $\alpha$-Mg and $\beta$-$Mg_2Sn$ were incorporated into a TOPAS code kindly provided by Dr Daniel Reed.

Moreover, the area fraction of $Mg_2Sn$ precipitates was also measured using BSE SEM images. Both the area fraction and volume fraction are equal given a large enough sample area. A minimum of 20 BSE images, with a view field of 10x7.5µm, were taken of each sample at intervals of between 100-200µm to cover a wide area of the sample. These were then processed via a FIJI[161] macro, the results of which are given in Fig 5.1 with the XRD data.
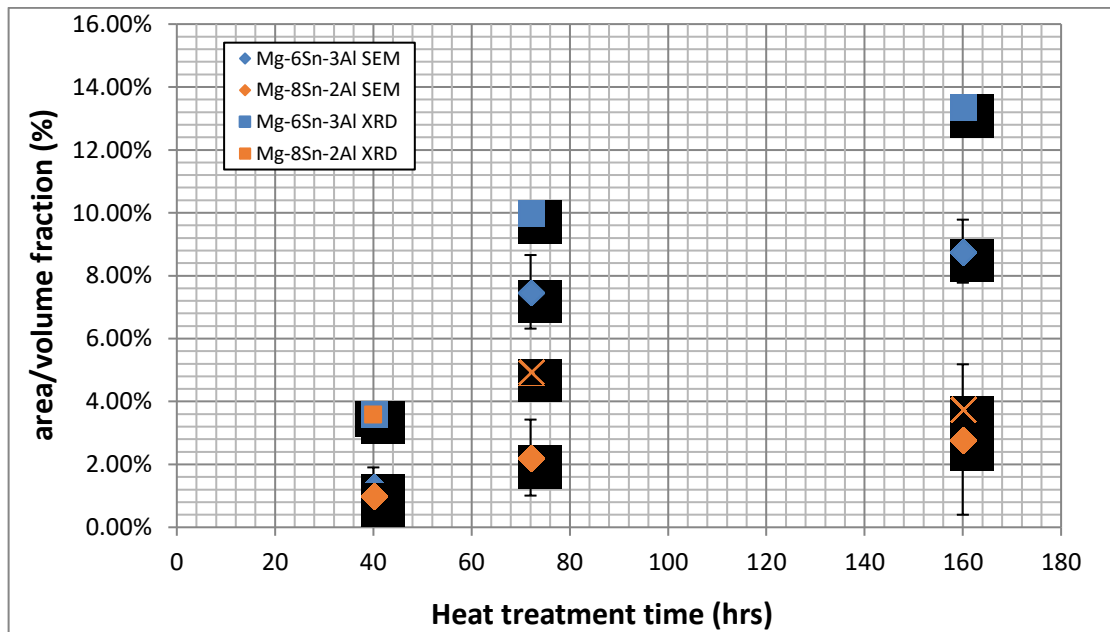


***Fig 5.1:*** *Comparison of area fraction measured by SEM BSE images and volume fraction as measured by XRD*

Considering the two measures in Fig 5.1, we can see, as with the hardness (Fig 4.1), there is little difference in the volume/area fractions of the two alloys aged for 40 hours, but there is a clear difference after with a larger discrepancy between the two alloys.

The XRD consistently gives a fraction greater than that given by the SEM as seen in Fig 5.2. A number of reasons may be given for the difference between the two results. Firstly, during the sample preparation, lift out of precipitates while polishing is not an uncommon phenomenon as shown in Fig 5.2a for example.

Secondly the precipitate size. While the resolution of the SEM used is of the order of 1-2nm, the images used had a view field of 10x7.5μm in order to capture a large area of the sample, meaning each pixel represented just under 10nm by 10nm (image resolution was 1024x768). This may have led to under counting when the precipitates were particularly small as due to the small amount of noise in the images, the area fraction macro was set to ignore precipitates below 10,000nm$^2$ i.e. 10 pixels by 10 pixels. Considering this and taking the set of images that gave the largest discrepancy (Mg-1.29Sn-2.85Al), the analysis was repeated with a precipitate size of 1000nm squared i.e. approximately 3x3 pixel. The result was marginally higher, 9.7% against the original 8.8%. This therefore again does not account for the greater fraction from the XRD analysis (13.4%). What is more it is clear from the images that many of the regions selected by the software do not contain precipitates as shown in Fig 5.2b, as the BSE contrast is not consistent across that area.

Obviously, a combination of this surface damage and the coarse resolution is responsible for the discrepancy however the XRD is not without fault. While the result is clearly less distorted by the sample preparation and detects smaller particles better, it is very much fallible when it comes to small volume fraction and as such the real results is likely to fall between the two results. What is clear however is that the sample with the lower Sn content has the larger volume fraction of precipitates. This is attributed to the Al content, which has already been suggested in the literature[110] to increase the precipitate nucleation rate in Mg-Sn-Al ternaries either due to reducing the solubility of Sn in the

111

matrix or by reducing the interfacial energy between Mg$_2$Sn and the matrix or possibly both. However the XRD cannot establish number density and size of precipitates and as such we look to SEM and TEM to establish the number density and size of the precipitates.
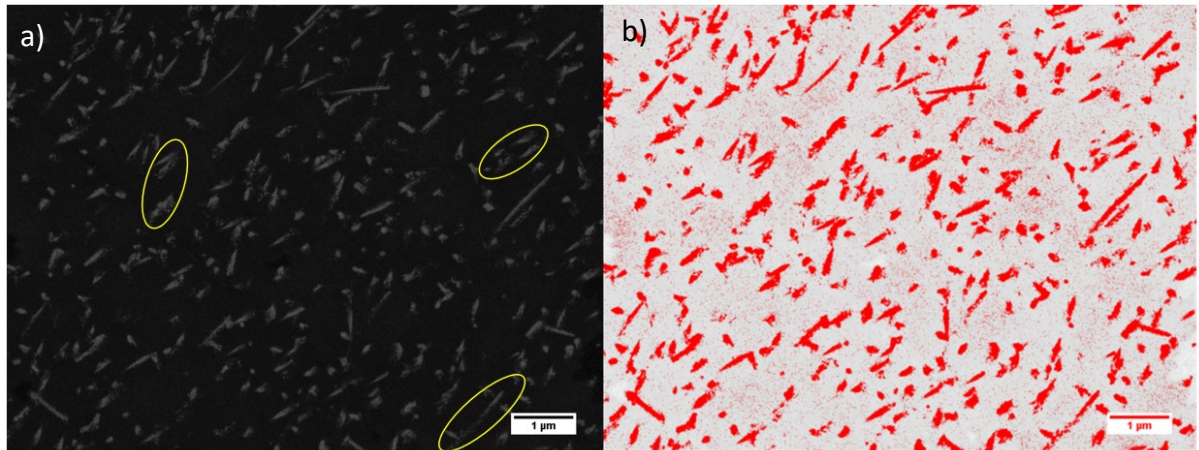


***Fig 5.2:*** a) *Example BSE image showing precipitates damaged by the sample preparation and b) 'speckle' from background changes in contrast as shown in processed BSE image. Area in red represents that determined by the software to be a precipitate with no minimum size filtering.*

## 5.3 Number Density

Two methods will be used to measure the number density of precipitates within the alloys. Initially the number density will be determined via SEM using the same BSE images used to determine the area fraction. Secondly TEM samples will be used to identify the number density of the different morphologies which will be important when considering the strengthening from these precipitates.

### 5.3.1 SEM

The number density of the two alloys, as measured by SEM BSE, are given in Fig 5.2. Most of the precipitates have a lath morphology and thus there are instances where the cross section seen appears to be much smaller. Unfortunately the different morphologies discussed in chapter 4 cannot be differentiated thus the number density given is inclusive of all the morphologies.
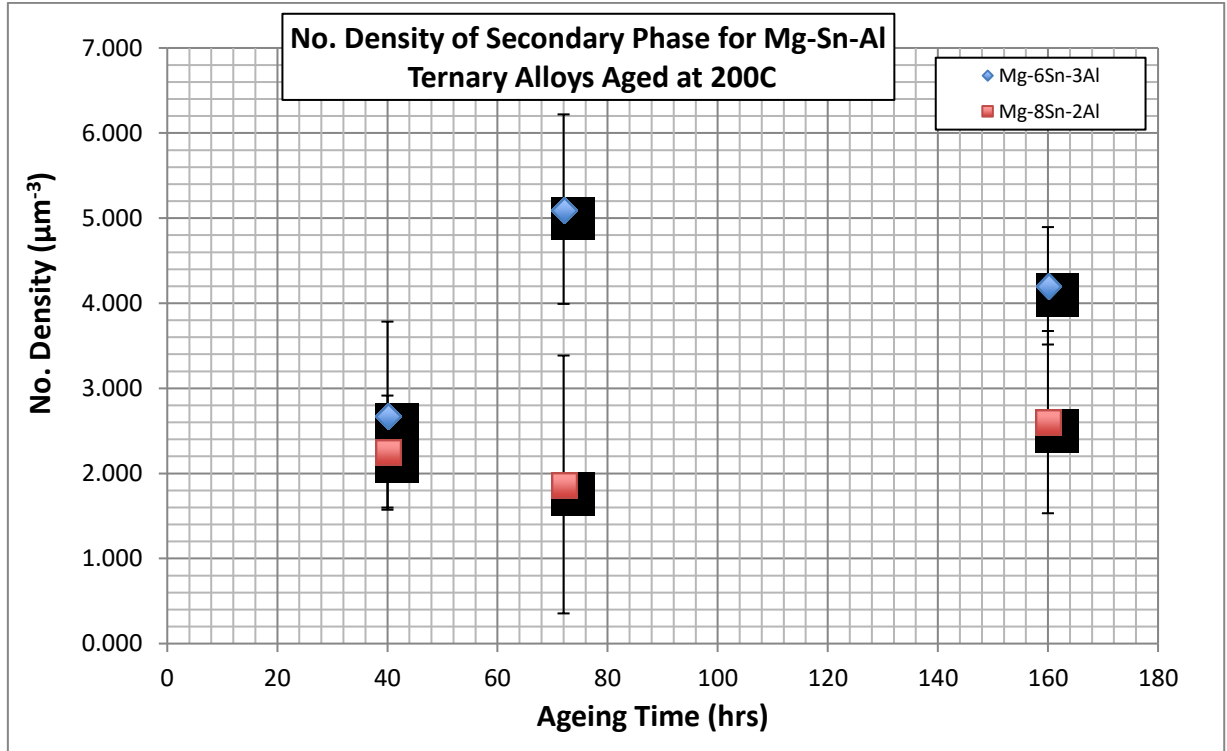
***Fig 5.3:*** *Number density of precipitates as measured in BSE imaging in SEM.*

### 5.3.2   TEM

Similarly, the number density via TEM was calculated using a set of HAADF images. Rather than define a volume to inspect as with the SEM, a minimum of 1000 precipitates were counted, though for the more densely populated samples this was far exceeded. Now that the morphologies have been identified, we must consider how these can be identified en mass in order to characterise the alloys. Three of these morphologies can be identified by observing using a ZA parallel to the basal plane. This is shown in Fig 5.4. The majority, highlighted in red, are either basal plates or $\langle 11\bar{2}0 \rangle_\alpha$ laths. Their long axes both fall on the trace of the basal plane. They account for around three-quarters of the precipitates. Observation in the $0001_\alpha$ direction (Fig 5.5) confirms that the majority of precipitates have long axes parallel to $\langle 11\bar{2}0 \rangle_\alpha$. Furthermore, it is clear that the lath shaped precipitates greatly outnumber the hexagonal plates.
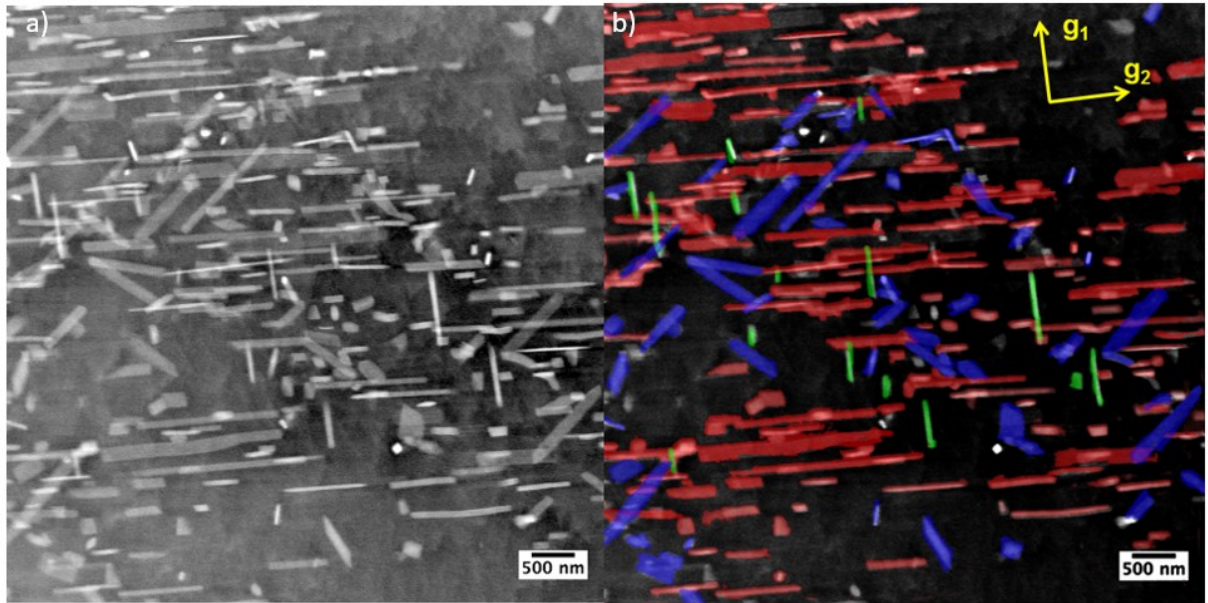
***Fig 5.4:*** *a)HAADF image and b)coloured version of Mg-1.29Sn-2.85Al alloy aged for 160 hrs at 200°C (B=[11$\bar{2}$0]$_\alpha$, g₁ = [0001]$_\alpha$ and g₂ = [1$\bar{1}$00]$_\alpha$). Numerous precipitates can be seen to have traces along the ⟨1$\bar{1}$00⟩$_\alpha$ direction (red), thus being either basal plates (category b) or ⟨11$\bar{2}$0⟩$_\alpha$ laths (category a). Also shown are <c> rods (category c) (green) and pyramidal laths (category d) (blue)*
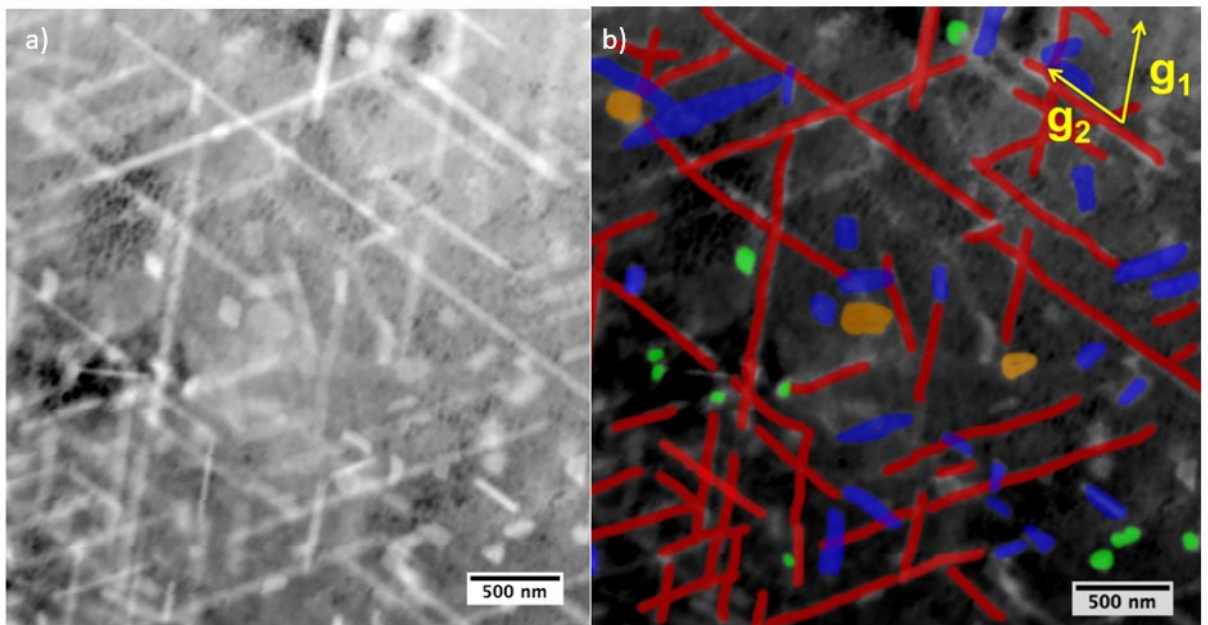


***Fig 5.5 :*** *a)HAADF image and b)coloured version of Mg-1.29Sn-2.85Al alloy aged for 160 hrs at 200°C (B=[0001]$_\alpha$, g₁ = [11$\bar{2}$0]$_\alpha$ and g₂ = [$\bar{1}$2$\bar{1}$0]$_\alpha$) ⟨11$\bar{2}$0⟩$_\alpha$ lath precipitates (category a) (red) are determined by their greater length than pyramidal precipitates (category c) (blue). Basal plates (category b)(orange) and <c> rods (category d) (green) are also highlighted*

Moreover, <c> rods, highlighted in green, are most easily identified by observing from the $0001_\alpha$ beam direction. HAADF allows for easy differentiation between these and basal plates as the contrast is much stronger where the precipitate is thicker in the observed direction. When observed from $[11\bar{2}0]_\alpha$ it is clear that the trace of these precipitates will be along the $[0001]_\alpha$ long axes. It should be noted that the width of the prismatic precipitates is far smaller than that of any of the other species of precipitate.

Finally, we have the last category, d, the pyramidal rods. Similar to the basal laths, when observed from the $[0001]_\alpha$ beam direction (Fig 5.4) have a long axis along the trace of $\langle 11\bar{2}0 \rangle_\alpha$ (Fig 5.4). From the image in Fig 5.4 however it is clear that any precipitates that do not have a long axis falling along $[1\bar{1}00]_\alpha$ or $[0001]_\alpha$ fall in to this category. It is thus clear that the direction of the long axis is can be categorised as $\langle 11\bar{2}X \rangle_\alpha$

There is however some overlap between the pyramidal rods and <c> rods as when observing from $[11\bar{2}0]_\alpha$ it is possible that the long axes would make the precipitate appear to have a long axis in the $[0001]_\alpha$ direction as $[11\bar{2}X]_\alpha$ is a possible growth direction. Here we rely on two assumptions. Firstly, as we are dealing with a TEM sample, our thickness is of the order of 100nm. Provided that the beam direction is kept close to the normal direction of the foil, any pyramidal precipitate will be greatly truncated when its long axis is growing out of the plane of the sample, especially as the lengths are up to and above 1μm. Secondly as noted above, the width of the <c> rods is much less than that of the prismatic rods, thus even if not truncated, the <c> rods should appear far narrower than the prismatic rods. Thus with a reasonable degree of certainty we can determine the precipitate category when observing from a $\langle 11\bar{2}0 \rangle_\alpha$ ZA. This will be useful later when the size and number density is determined via TEM.

Also, the chosen zone axis allows for size measurements. The symmetry of the system is such that the majority of precipitates grow close to $\langle 11\bar{2}0\rangle_\alpha$ or $\langle 11\bar{2}X\rangle_\alpha$ direction. This gives 3 possibilities. While one of these directions will be parallel to that of the beam, the other two will both lie 30° from the image plane. This allows for us to unambiguously calculate the length of the precipitates with only a single image. Conversely, imaging at $\langle 1\bar{1}00\rangle_\alpha$ beam direction would mean that a third of the $\langle 11\bar{2}0\rangle_\alpha$ would grow in the image plane but the other two thirds will have a reduced apparent length due to the growth direction being 60° out of the image plane as seen. This would lead to the length of the precipitates being misrepresented in the measurements as there is no way to tell the growth direction of a $\langle 11\bar{2}0\rangle_\alpha$ lath. This is demonstrated in Fig 5.6. The one downside to this is the ambiguity for any pyramidal precipitates that grow along $[11\bar{2}X]_\alpha$ whereby X is any number other than 0, when our beam direction is $[11\bar{2}0]_\alpha$. These will appear in the image to have a growth direction of $[0001]_\alpha$ as demonstrated in Fig 5.7. Unfortunately, without further complicating the issue this is unavoidable, it should also be considered that, as the foil normal fell close to $[11\bar{2}0]_\alpha$ in all cases, precipitates growing in $[11\bar{2}0]_\alpha$ or $[11\bar{2}X]_\alpha$ directions are likely truncated due to the small sample thickness, reducing the effect of these measurements. In order to compensate for this an 'other' category will be used when there is ambiguity, this allows the overall number density to be established while not skewing the fraction of each precipitate type.
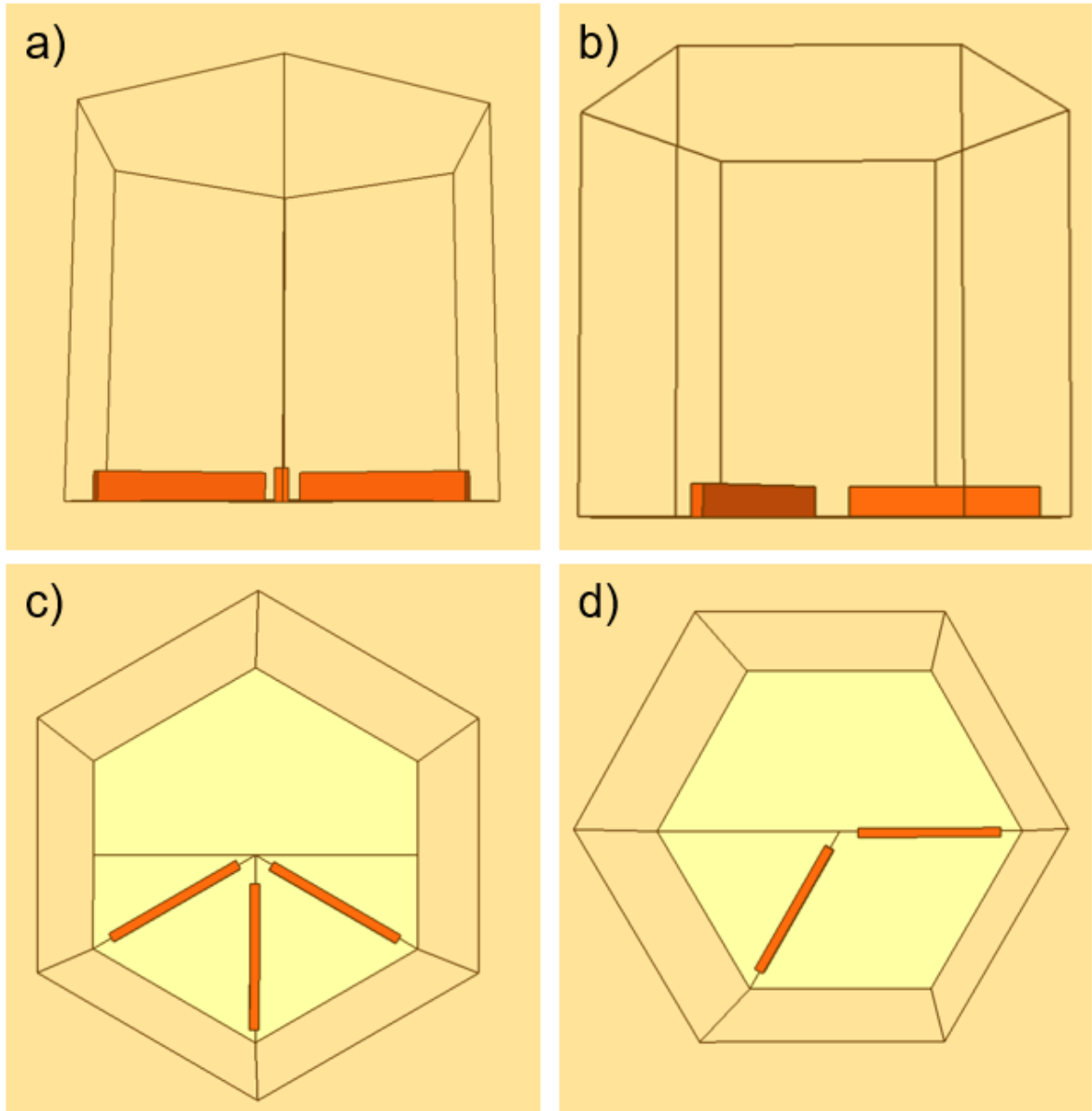
**Fig 5.6:** *Views of the three $\langle 11\bar{2}0 \rangle_\alpha$ lath varieties, equally sized, as seen from a)$[11\bar{2}0]_\alpha$, b) $[10\bar{1}0]_\alpha$. The $[11\bar{2}0]_\alpha$ lath in b) has been removed. While the laths in a) have the same apparent length, b) leaves ambiguity as to the actual length of the precipitate as the angle between the growth direction and the image plane varies. This is demonstrated from the $[0001]_\alpha$ images c) and d) on which the image plane is horizontal.*
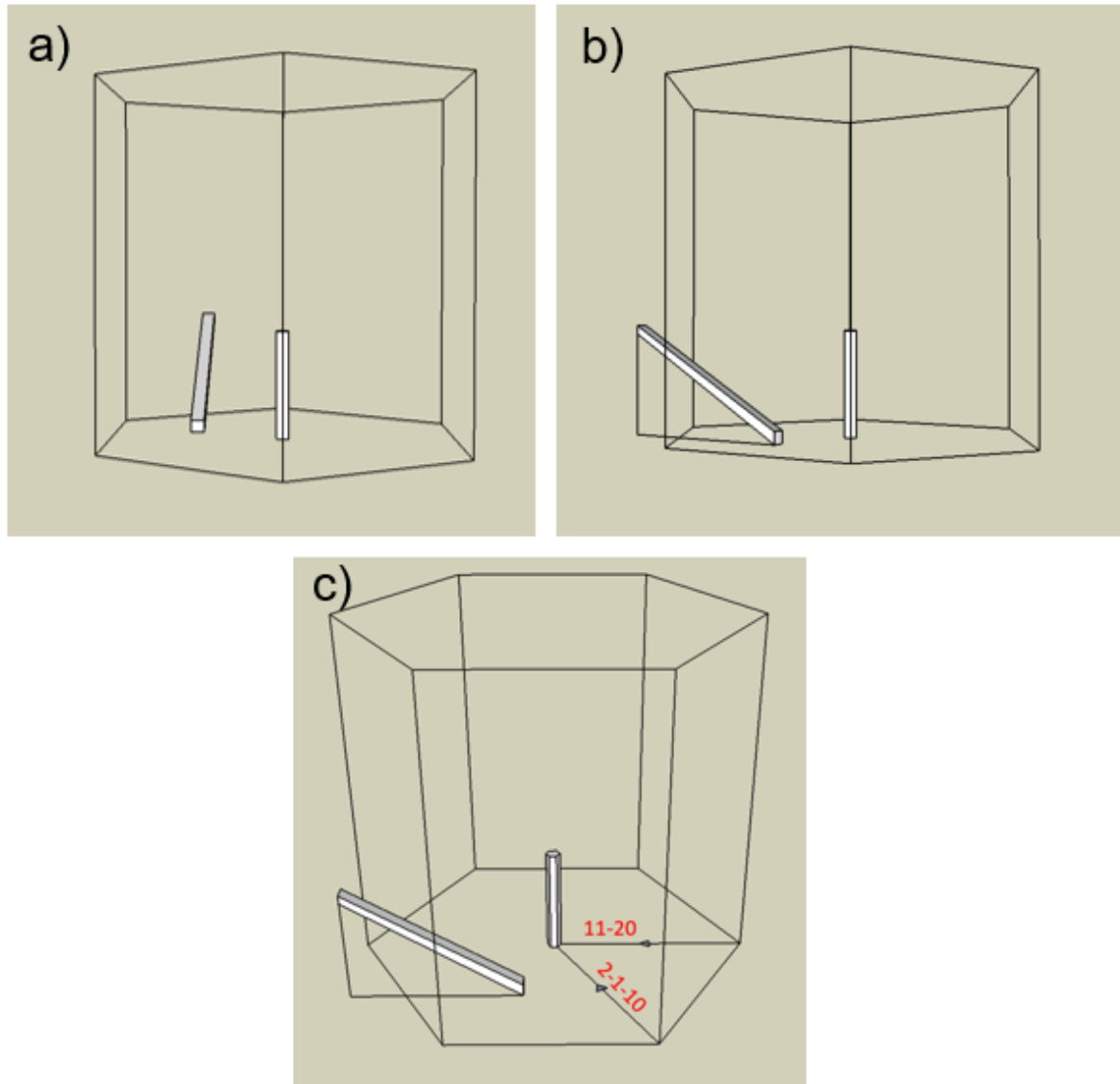
*Fig 5.7: Schematic diagrams showing pyramidal rod growing along $[11\bar{2}X]_\alpha$ and <c> rod from a) $[11\bar{2}0]_\alpha$, b) $[2\bar{1}\bar{1}0]_\alpha$ and c) $[1\bar{1}03]_\alpha$ with view directions marked. Note also that the trace of the pyramidal rod is given in the basal and prismatic planes. In a) there is no way to differentiate between the two precipitate types.*

Considering the sample thickness, unlike SEM where we are presented with an area, the TEM inspects a volume, thus in order to get a number density we must measure the thickness of the sample. There are two ways of achieving this in the TEM, either via EELS or CBED. For the purpose of this study CBED was used given the simplicity with which it can be achieved. The method as described in chapter 3 was followed, with Fig 5.8 showing

an example of the patterns as well as the fitting of the graph in order to determine sample thickness. A minimum of 3 CBED patterns were taken across the imaging area in order to obtain a reasonable estimate of the sample thickness.
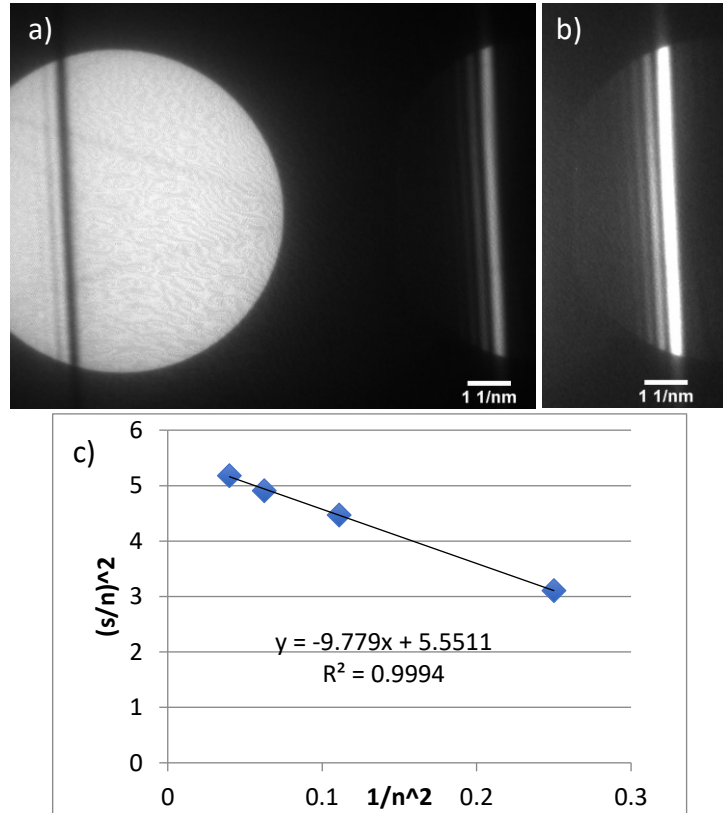


***Fig 5.8:*** *a) example CBED pattern from Mg-1.29Sn-2.85Al sample, aged 72hours, used to measure sample thickness t including b) enhanced image of disk to show fringes and c) plot of $s^2/n^2$ against $1/n^2$, the y intercept of which is $1/t^2$*

Given in Fig 5.9 is a comparison of the total number density found in the current alloy in comparison to similar Mg-Sn alloys. Values are taken from the 72 hour sample where the number density is at its highest. A further breakdown of the precipitate type and the time dependency is given in Fig 5.10 Unfortunately, not all of the precipitates were easily identifiable and as such when there is doubt, the precipitate type was assigned as other in order to give the overall number density.
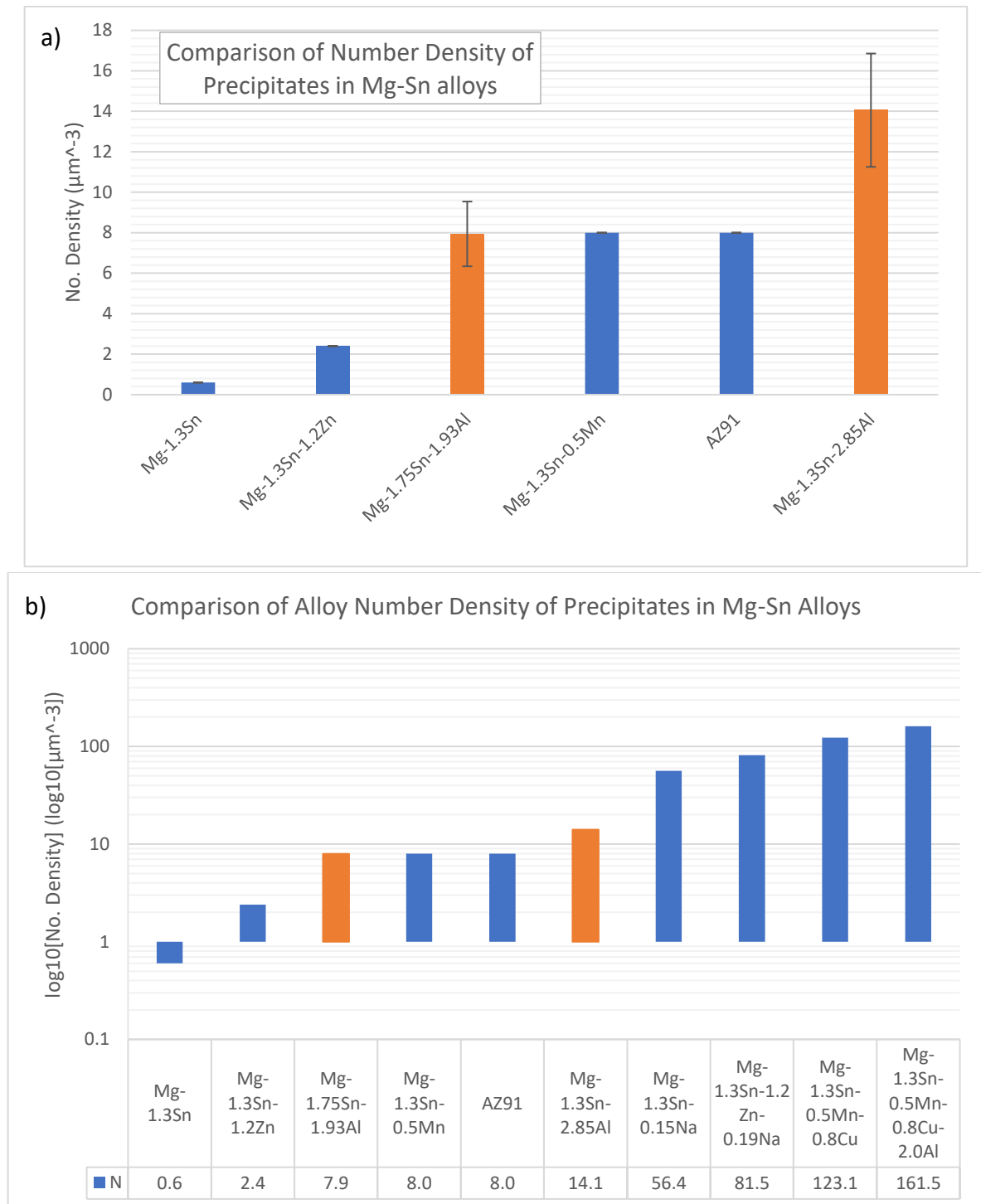
***Fig 5.9:*** *Number density of peak aged Mg-Sn alloys[40,103,108,109] along with AZ91[40] for comparison. a) gives the number density on a linear scale with those with similar number densities whereas b) gives a logarithmic scale to show alloys with far greater number densities. Alloys from the current work are shown in orange and represent the 72hrs specimens as determined by TEM.*
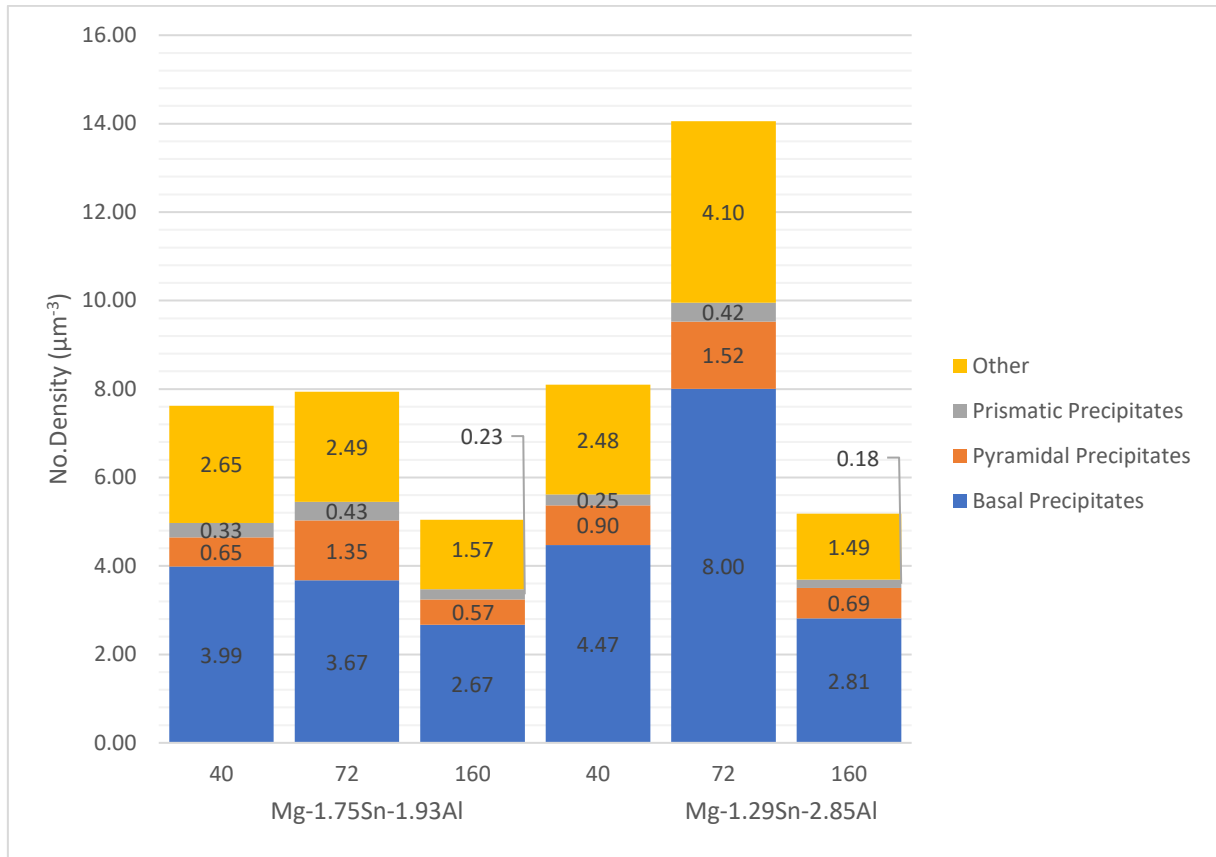
**Fig 5.10:** *Breakdown of precipitate number densities for different precipitate types as determined by TEM. Basal precipitates includes the $\langle 11\bar{2}0 \rangle_\alpha$ laths*

### 5.3.3 Comparison of Number Density Measurements

Neither is without flaws but the combination of the two will give a complete view of the

microstructure across the sample. Initially SEM was used due to the ease of sample

preparation and large measurement area. This however gives a measure that is per unit

area not unit volume and relies on how the alloy has been sectioned. While this is trivial

in the case of a spherical or even relatively equiaxed particle, the elongated precipitates

add an extra layer of complexity, especially with no knowledge of crystal orientation. TEM

on the other hand gives us far easier access to this information which, coupled with the

fact we are imaging a volume not an area, allows for the precipitates to be classified by

their morphology and habit plane/growth direction. While this makes the number density

far easier to calculate, there are pitfalls; typically with TEM the volume analysed is far

smaller than SEM and what is more, requires the foil thickness to be calculated. However the TEM allows far more effect size measurement, the results from which are given below.

## 5.4   Precipitate Dimensions

The number densities established the further remaining parameter that is needed to model the strength of the alloys is the actual size of the precipitates. This will be determined using the HAADF images used for the number density calculations. Due to the relatively lower numbers of the non-basal species, instead of measurements being taken over a set of images, the dimensions will be averaged over a minimum of 100 precipitates for $\langle 11\bar{2}0 \rangle_\alpha$ laths and pyramidal rods. Conversely only 50 <c> rods are measured due to the smaller number in the sample.

### 5.4.1   $\langle 11\bar{2}0 \rangle_\alpha$ Laths

The size of the $\langle 11\bar{2}0 \rangle_\alpha$ laths is relatively easy to acquire from the $[11\bar{2}0]_\alpha$ images. For the $\langle 11\bar{2}0 \rangle_\alpha$ laths, as previously discussed, there are three possible orientations that can be present in the alloy corresponding to the 3 $\langle 11\bar{2}0 \rangle_\alpha$ directions. Two of these fall 30° from the image plane with the final being perpendicular. Given the observation from $0001_\alpha$ (Fig 5.5), we know the width of the laths is below 100nm and as such can safely assume that anything above this is not a lath oriented in the beam direction. To begin with the height and apparent length of all the precipitates was measured, the length data is then processed to give an actual length for those precipitates. Fig 5.11 shows the length distribution for each sample given as a probability density function; the average dimensions are given in Table 5.1. For height an average is given due to the small variance in the data.
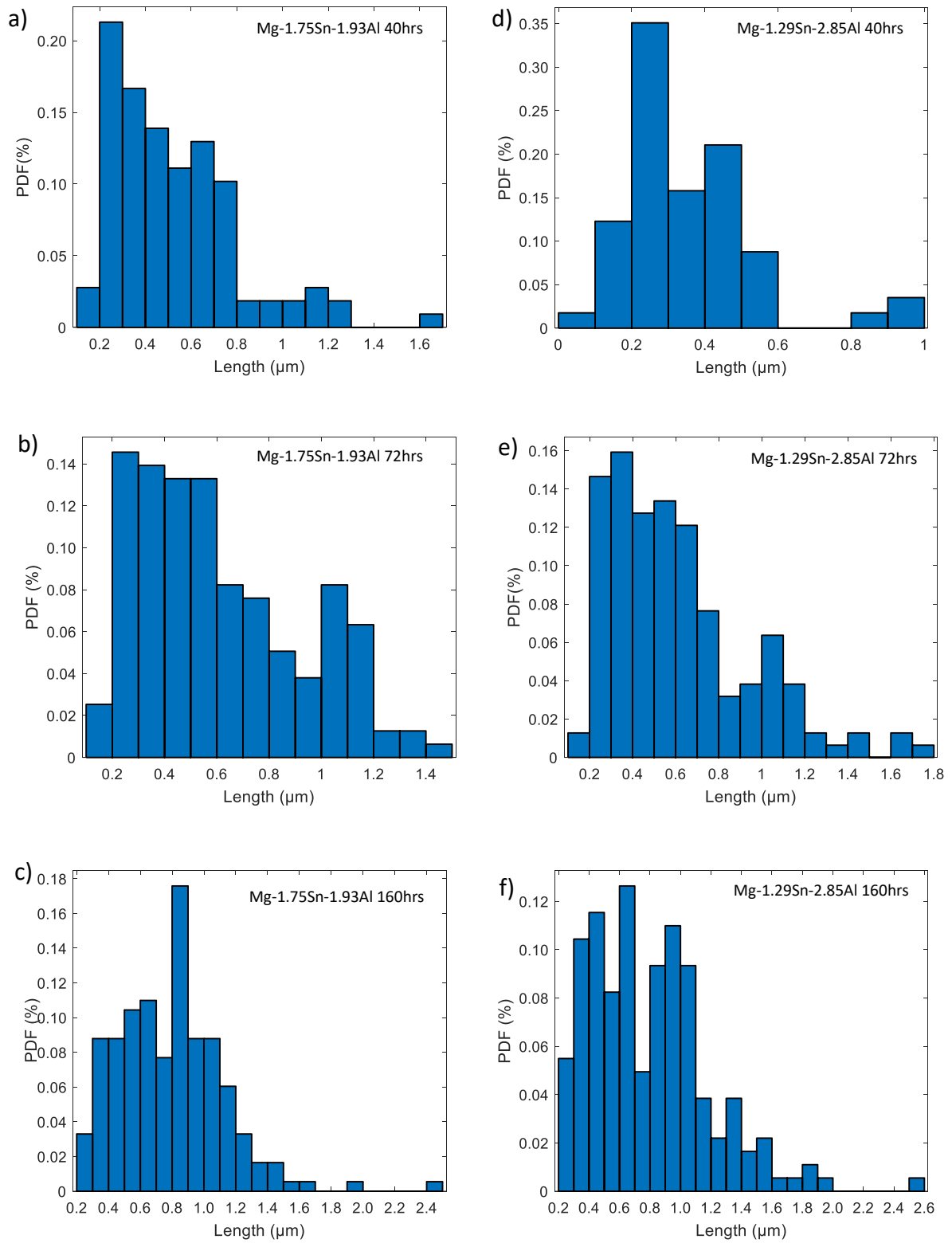
**Fig 5.11:** *a-f) size distributions as probability density functions of the $\langle 11\bar{2}0 \rangle_\alpha$ laths precipitates in the different samples*

**Table 5.1:** *Size of $\langle 11\bar{2}0 \rangle_\alpha$ laths as measured by HAADF image*

| Compo (at%) | Ageing time (hrs) | Length (um) | Height (um) | l/h |
|---|---|---|---|---|
| Mg-1.75Sn-1.93Al | 40 | 0.45 ±0.24 | 0.04 ±0.01 | 11.25 |
|  | 72 | 0.53 ±0.27 | 0.04 ±0.02 | 13.25 |
|  | 160 | 0.68 ±0.29 | 0.06 ±0.02 | 11.33 |
| Mg-1.29Sn-2.85Al | 40 | 0.30 ±0.16 | 0.02 ±0.01 | 15 |
|  | 72 | 0.53 ±0.29 | 0.04 ±0.02 | 13.25 |
|  | 160 | 0.69 ±0.34 | 0.06 ±0.02 | 11.5 |

### 5.4.2 &lt;c&gt; Rods

A simple average is used for the &lt;c&gt; rods due to the smaller number in the samples, this

is given in Table 5.2.

**Table 5.2:** *Size of &lt;c&gt; rods as measured by HAADF image in model alloys*

| Compo (at%) | Ageing time (hrs) | Height (um) | Width (um) |
|---|---|---|---|
| Mg-1.75Sn-1.93Al | 40 | 0.28 ±0.12 | 0.04 ±0.01 |
|  | 72 | 0.39 ±0.16 | 0.05 ±0.01 |
|  | 160 | 0.59 ±0.26 | 0.06 ±0.02 |
| Mg-1.29Sn-2.85Al | 40 | 0.14 ±0.20 | 0.04 ±0.03 |
|  | 72 | 0.24 ±0.10 | 0.05 ±0.01 |
|  | 160 | 0.47 ±0.18 | 0.06 ±0.02 |

### 5.4.3 Pyramidal Rods

Unfortunately the measurement of pyramidal precipitates is far more complicated than

that of the prismatic or basal. Measurements are made of a number of parameters, as

shown in Fig 5.12.
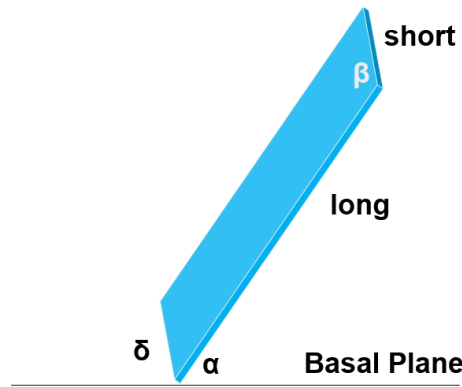
***Fig 5.12:*** *Schematic diagram of the projection produced by pyramidal rod as seen when observed from a $\langle 11\bar{2}0 \rangle_\alpha$ beam direction.*

Using these parameters it is possible to calculate a number of things including the actual length of the facets, the angle between the long and short sides and the elevation from the basal plane. The long facet is broken down into an $x$ and $y$ component using angle $\alpha$. $y$ is invariant when rotating in the basal plane however $x$ varies in the same manner as the $\langle 11\bar{2}0 \rangle_\alpha$ laths. Using the same calculation, a value $x'$ is given which is recombined with the $y$ to give the actual length. This relies on the assumption that the majority of the precipitates grow in a $\langle 11\bar{2}X \rangle_\alpha$ direction. It can be seen that there is a large variation in growth direction within the alloy, as such and considering the measurements in chapter 4, it is concluded that this is a results of differing growth rates due to the anisotropy of the matrix. A more 3D technique either using tomography or high angle tilting is required to shed further light on this. The average length of pyramidal precipitates Table 5.3 in the same manner as with the $\langle 11\bar{2}0 \rangle_\alpha$ laths with the length distributions given in Fig 5.13.

**Table 5.3:** *Lengths of pyramidal rods*

| Compo (at%) | Ageing time (hrs) | Length (um) |
|---|---|---|
| Mg-1.75Sn-1.93Al | 40 | 0.36 ±0.18 |
| | 72 | 0.55 ±0.37 |
| | 160 | 0.75 ±0.50 |
| Mg-1.29Sn-2.85Al | 40 | 0.22 ±0.20 |
| | 72 | 0.51 ±0.25 |
| | 160 | 0.72 ±0.41 |

## 5.5 Summary

Good agreement was found between the SEM and TEM measurements of number density as well as both alloys exhibiting similar number densities to that found in the literature. What's more, unlike most measures of number density made in the literature, the relative fractions of each precipitate type is established. This, coupled with the measured size, will allow a more realistic picture of the microstructure to be considered when modelling the strengthening effect of the precipitates. Moreover, in comparing the two alloys, we can see that the Mg-1.29Sn-2.85Al exhibits a larger number density corresponding to the greater increment in hardness observed in Chapter 4.
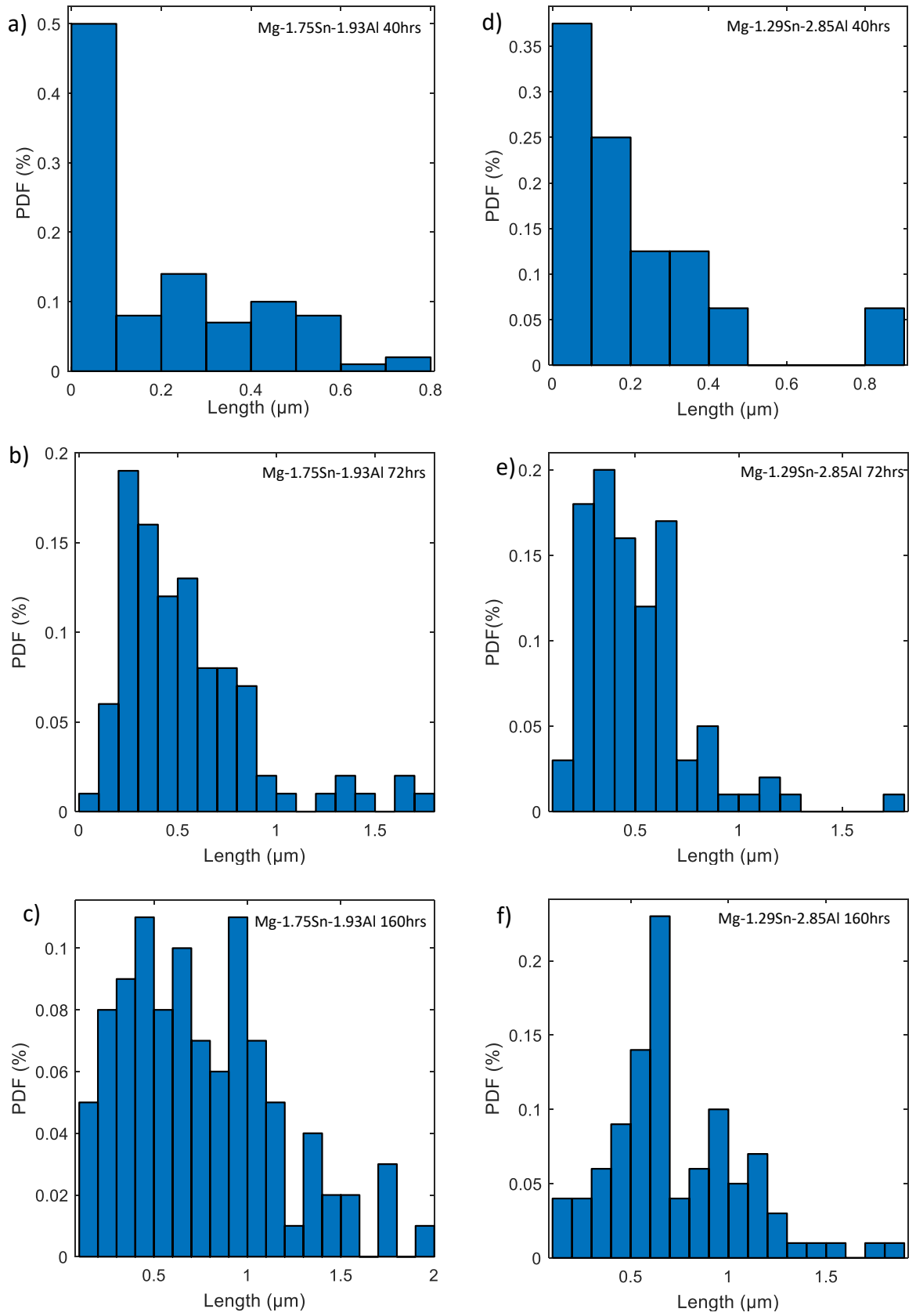
***Fig 5.13:*** *a-f) size distributions as probability density functions of the pyramidal precipitates in the different samples.*

# 6 MODELLING THE STRENGTHENING OF MG-SN-AL

## 6.1 Stating the Problem

Having characterised the alloy, we will now attempt to model the change in the microstructure during heat treatment. This will focus on the nucleation of precipitates as a function of the Gibbs free energy (Eqn 3.10-3.14), and the subsequent grow due to the supersaturation of tin in the matrix (Eqn 3.15) in line with their use in the literature[37,118,125–131] as part of a Kampman-Wagner Numerical (KWN) model. This is used to fit the diffusion rate, $D_0$, of Sn in a Mg-Sn-Al ternary, using the figure for the binary alloy as a starting point. While figures exist[171,172] for diffusion in the Mg-Sn binary, one suggestion for the increased age hardening response of ternary Mg-Sn-Al/Zn alloys is an increased diffusion rate due to the interaction between the two solute elements. The KWN model is shown and the output compared to the data given in chapter 5. Unlike in the literature, 3 morphologies of precipitate, $\langle 11\bar{2}0\rangle_\alpha$ laths, pyramidal laths and prismatic rods, will be included, in line with the observations in chapter 4.

Once this has been completed, an effort will be made to link the precipitation number density and size to the strengthening. The more well-established strengthening mechanisms, grain size (Hall-Petch) and solution strengthening, will be calculated initially and the method of combining these compared with strength values measured by Luo et al[113]. The Hall-Petch and solution strengthening will then be calculated for the alloys in this study and assessed against the solution treated samples to determine the accuracy of the conversion from hardness to strength. From this we establish an as solution treated strength  strength which we can use to assess the strengthening increase due to the precipitates. Once this has been fitted to the measurements, the data from the precipitate

growth model will then be used to model the yield strength as a function of time for the alloy.

## 6.2 Precipitate Growth Model

The initial values of $D_0$ and the interfacial energy of the precipitate, γ, are taken from the literature. As previously stated a figure for the diffusion rate is given as approximately $10^{-20} m^2 s^{-1}$ in the literature[172]. Similarly Hutchinson et al[37] give a figure of $0.114\, Jm^{-2}$ for the surface energy $\gamma$ of Mg₁₇Al₁₂ precipitates. This arises from their simulation which contrasts with the figure of $0.45 Jm^{-2}$ Hutchinson et al calculate from their experimental data which is used for coarsening in the same work. Equally Robson[118] when modelling MgZn precipitate formation give a surface energy for nuclei, $\gamma_n$, as $0.02\, Jm^{-2}$. This value is linearly increased to reach the value of $\gamma$ at a selected size for normal growth of $20nm$. For the current work $0.02 Jm^{-2}$ will be used as a starting point for the nucleation energy and $0.1 Jm^{-2}$ for the precipitate growth. The size for the transition between nucleation and growth is set at $10nm$.

Likewise we have the values of $\alpha$ and $N_0$ are fitted using the initial values of 1.7 from Hutchinson et al [37] and $10^9$ from Robson et al [118]. Lastly, no figure exists for the solute content on the precipitate interface, $C_e$, or the critical radius for growth, $R_c$, for Mg-Sn alloys and as such these are fitted in the model. All of the fitted values are given in Table 6.1, including descriptions of their purpose. Below the average precipitate length (Fig 6.1), the solute content in the matrix (Fig 6.2) and the number density of precipitates (Fig 6.3 and Fig 6.4) are given as a function of time for both alloys. Tables 6.2 and 6.3 give the figures calculated.

*Table 6.1: Fitted values from KWN model for the two alloys*

| Value | Description | Mg-1.75Sn-1.93Al | Mg-1.29Sn-2.85Al |
|---|---|---|---|
| $D(x10^{-18}m^2s^{-1})$ | Diffusion rate | 1.762 | 1.553 |
| $\gamma_n(Jm^{-2})$ | Interfacial energy for nucleation | 0.0102 | 0.0107 |
| $\gamma_g(Jm^{-2})$ | Interfacial energy for growth | 0.092 | 0.119 |
| $\gamma_c(Jm^{-2})$ | Interfacial energy for coarsening | 0.091 | 0.060 |
| $C_e$ $(at\%)$ | Solute content on precipitate interface | 0.89% | 0.76% |
| $\alpha$ | Growth scaling factor | 2.45 | 2.12 |
| $N_0$ $(x10^{15}m^{-3})$ | Number of nucleation sites per cu. metre | 7.7 | 7.2 |
| $\tau_i$ $(mins)$ | Incubation Time | 2540 | 2140 |
| $R_c(nm)$ | Critical Radius | 3.1 | 8.0 |
| $k$ | Ratio of l:r from Eqn [3.18] | 6.36 | 8.05 |

*Table 6.2: Comparison of measured values and those fitted by the simulation for Mg-1.75Sn-1.93Al*

| Value | Time (hrs) | Measured | Simulated |
|---|---|---|---|
| Average length of $\langle 11\bar{2}0 \rangle_\alpha$ laths (μm) | 40 | 0.45 | 0.44 |
| | 72 | 0.53 | 0.55 |
| | 160 | 0.68 | 0.69 |
| Total Number Density (μm⁻³) TEM | 40 | 7.62 | 8.03 |
| | 72 | 7.94 | 8.08 |
| | 160 | 5.04 | 4.57 |
| Number Density Ratio | 40/72 | 0.960 | 0.994 |
| | 160/72 | 0.635 | 0.566 |

*Table 6.3: Comparison of measured values and those fitted by the simulation for Mg-1.29Sn-2.85Al*

| Value | Time (hrs) | Measured | Simulated |
|---|---|---|---|
| Average length of $\langle 11\bar{2}0 \rangle_\alpha$ laths (μm) | 40 | 0.30 | 0.40 |
| | 72 | 0.53 | 0.46 |
| | 160 | 0.69 | 0.67 |
| Total Number Density (μm⁻³) TEM | 40 | 8.1 | 8.3 |
| | 72 | 14.0 | 13.8 |
| | 160 | 5.2 | 5.9 |
| Number Density Ratio | 40/72 | 0.577 | 0.601 |
| | 160/72 | 0.369 | 0.428 |

As can be seen from Fig 6.1, in both alloy the precipitate length grows rapidly to begin with before the rate of growth reduces as the amount of solute (Fig 6.2) drops toward the equilibrium level ($C_e$ in Table 6.1). In both alloys a drop in the average length is seen at around 2400 minutes (40hrs). This is due to a mixture of the $1/r$ dependence of the growth rate slowing the growth of the larger precipitates and the dropping supersaturation due the lack of solute in the matrix. Likewise at this point the number density is increasing rapidly (Fig 6.3) meaning that a greater proportion of precipitates have a shorter length. A breakdown of the number density of the different precipitate morphologies is given in Fig 6.4. This is demonstrated by Fig 6.5 that shows the length of precipitates nucleated during different time steps. The growth in both cases becomes approximately linear after 5000 mins (~80hrs) in line with the Liftshitz-Slyozov-Wagner model[37], demonstrating that the alloys are in the coarsening phase.
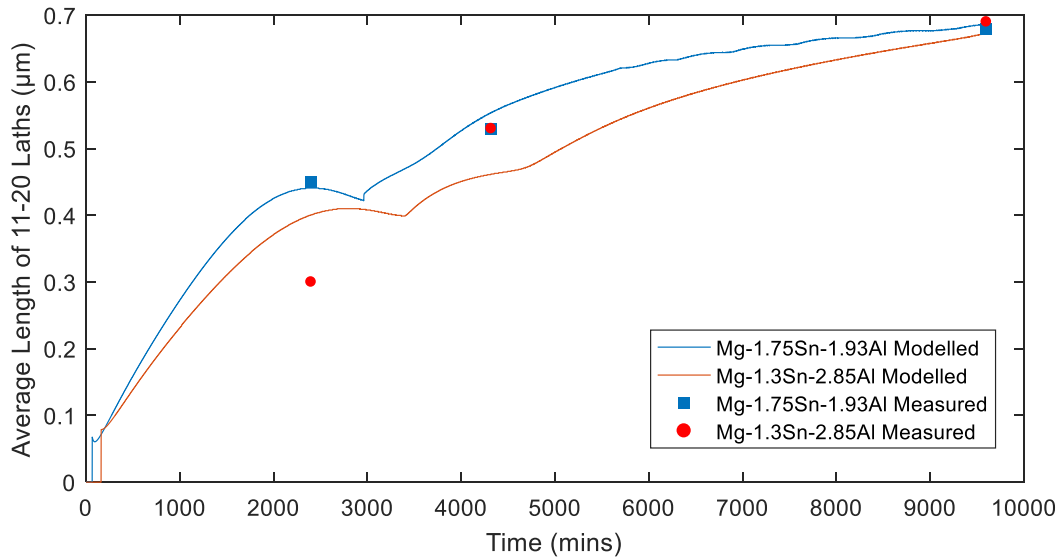


**Fig 6.1:** *Average length of $\langle 11\bar{2}0 \rangle_\alpha$ laths in Mg-1.75Sn-1.93Al(blue) and Mg-1.29Sn-2.85Al(red) alloys. Both exhibit a dip in the average length of the precipitates at around 2500-3500 minutes. This is due to a relatively low growth rate of precipitate coupled with a rapidly increasing number density*

Fig 6.3a shows a sharp peak in the number density at approximately 3000 mins (50hrs) in the Mg-1.75Sn-1.93Al. This is due to the overlap of nucleation and coarsening, whereby the precipitates nucleating close to this point are not able to grow sufficiently due to the lack of solvent and as such rapidly dissolve. The Mg-1.29Sn-2.85Al alloy (Fig 6.3b) on the other hand shows clear separation between the nucleation period and the coarsening, demonstrated by the plateau between 3000 and 5000 mins (~50 and 80 hrs).

What is also available to us from this model is the size distribution of the precipitates. These are given above in Fig 5.11 and are repeated here with a comparison to the model. It is clear there are a number of differences between the model and the measured results, most clear is the shorter peak length given in the model compared to that of the measurements. This is mainly attributed to the fact that there is no geometric consideration which would for example supress growth where two precipitates were in close proximity.
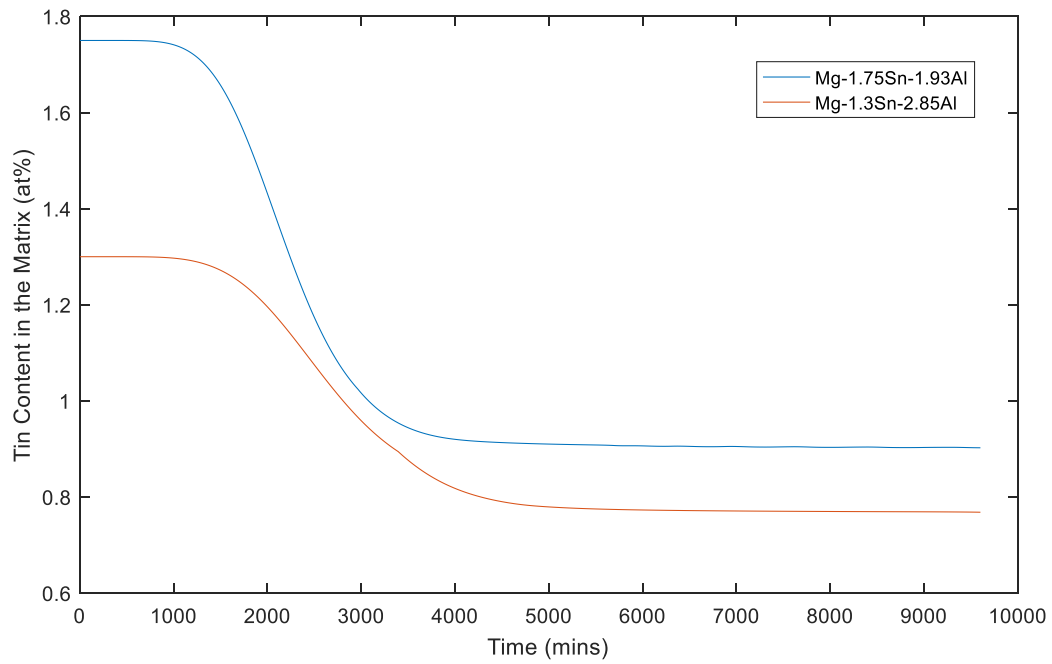
***Fig 6.2:*** *Simulated solute content as a function of time in a) Mg-1.75Sn-1.93Al and b) Mg-1.29Sn-2.85Al alloys*
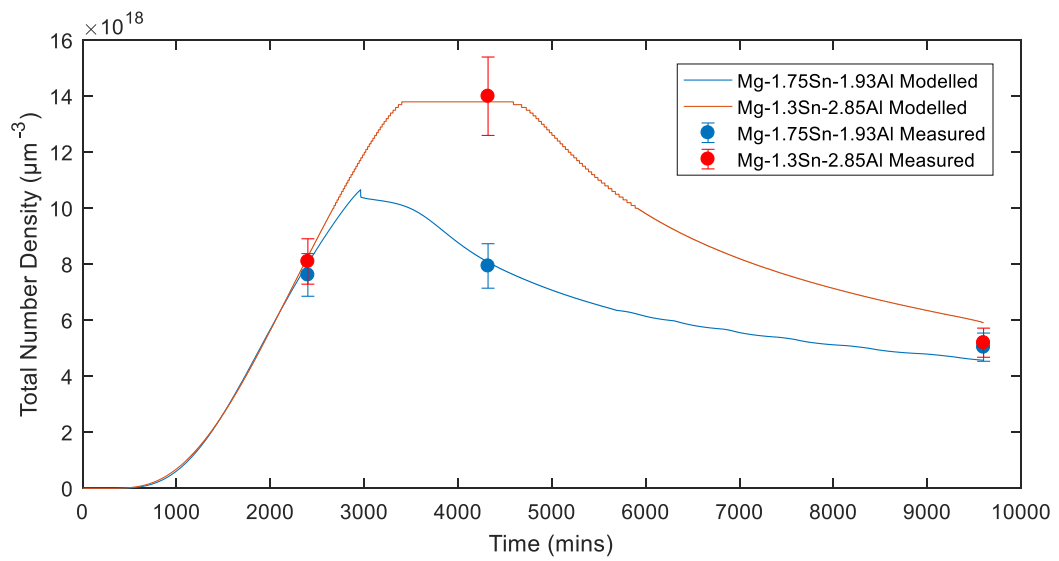


***Fig 6.3:*** *Total number density modelled as a function of time. Measured values are given with error bars*

133
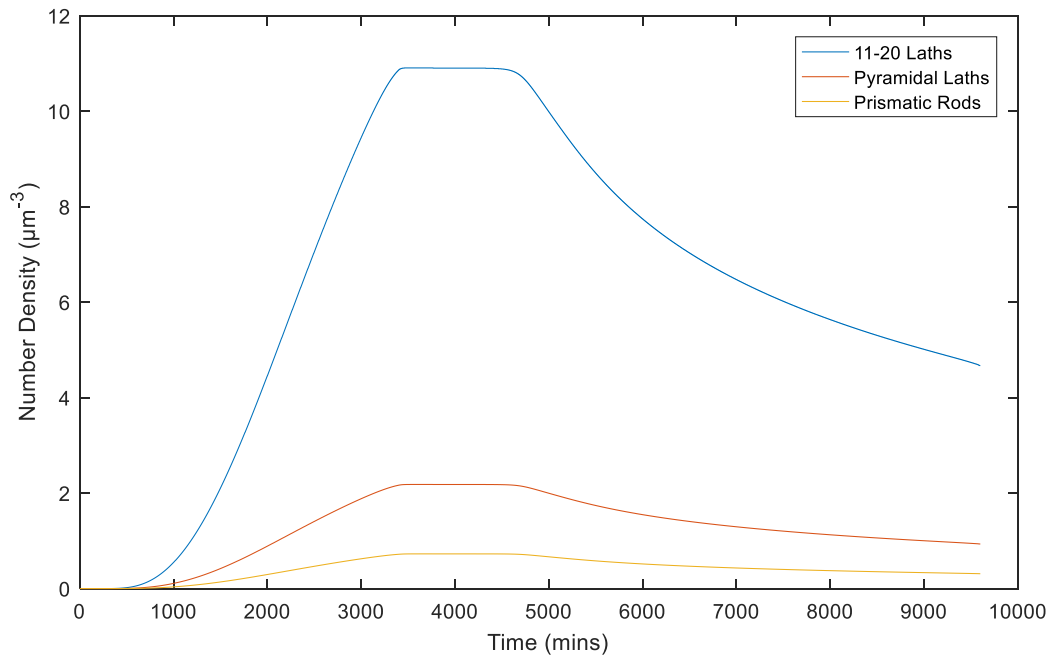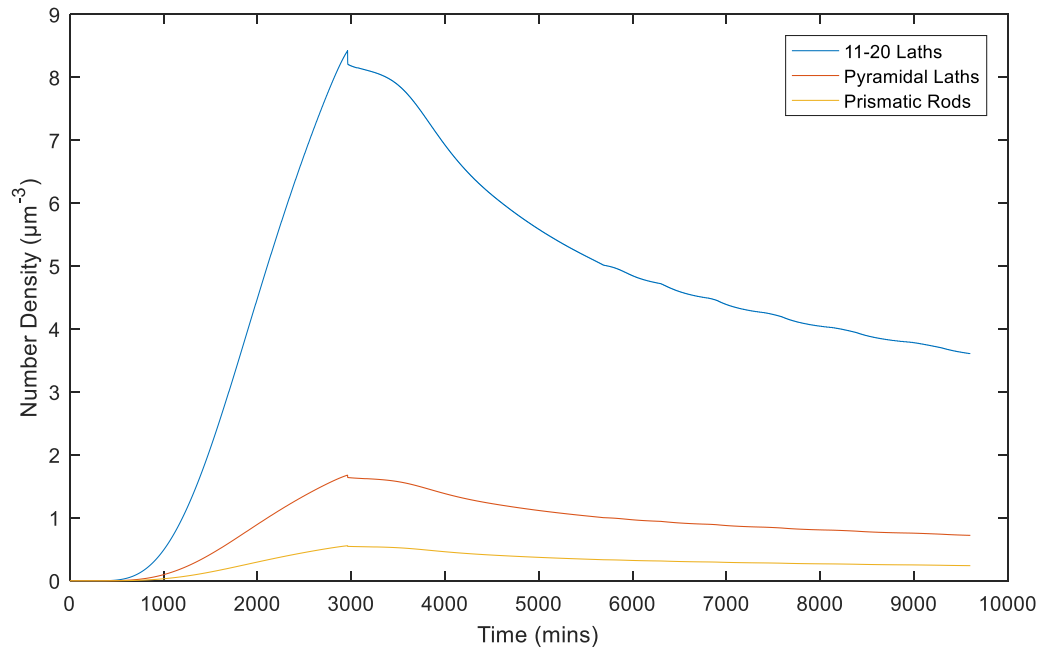
***Fig 6.4:*** *Number density in a) Mg-1.75Sn-1.93Al and b) Mg-1.29Sn-2.85Al.*
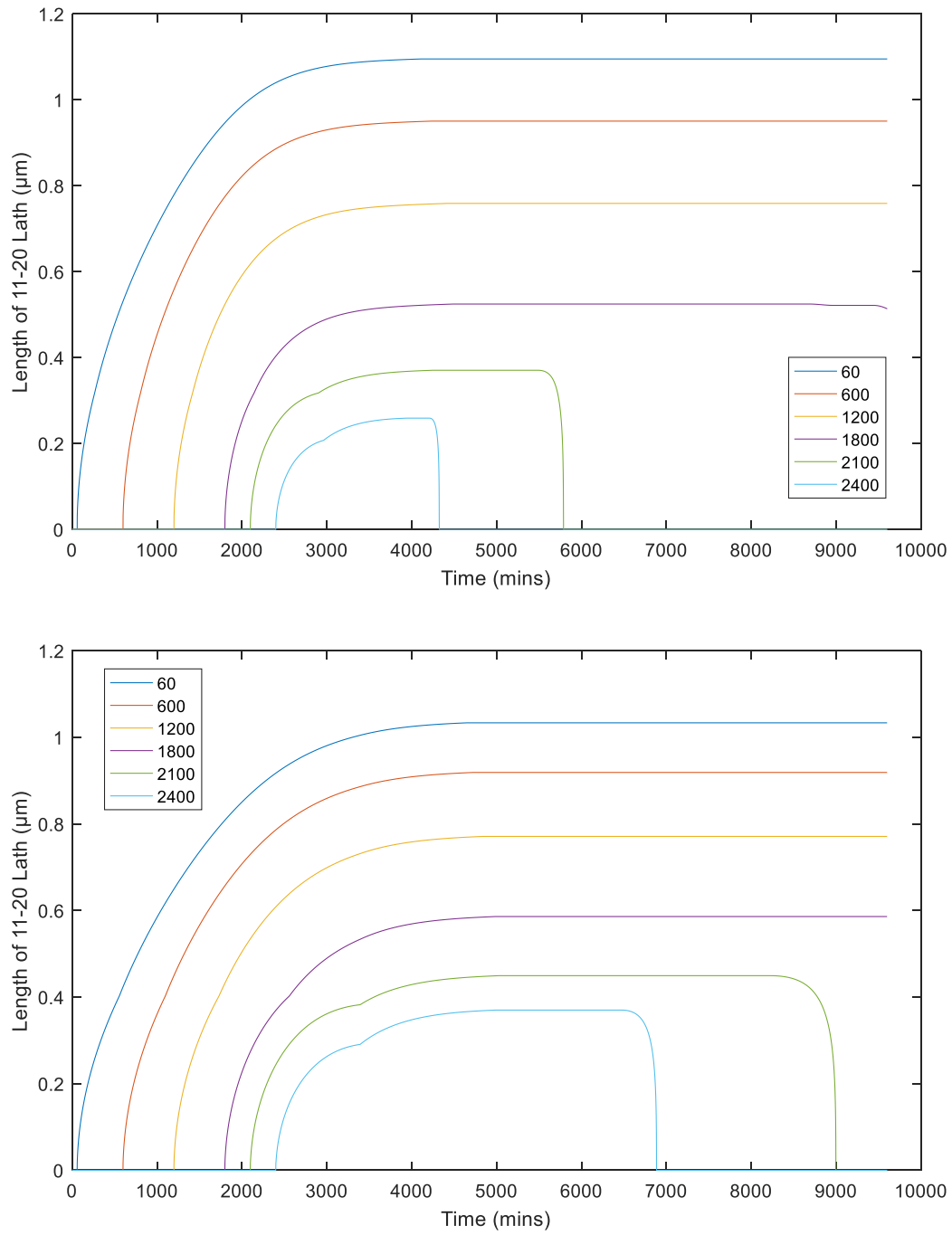
***Fig 6.5:*** *Growth of precipitates nucleated at 60, 600, 1200, 1800, 2100 and 2400 minutes (1,10,20,30, 35,40 hrs) for a) Mg-1.75Sn-1.93Al and b) Mg-1.29Sn-2.85Al.*
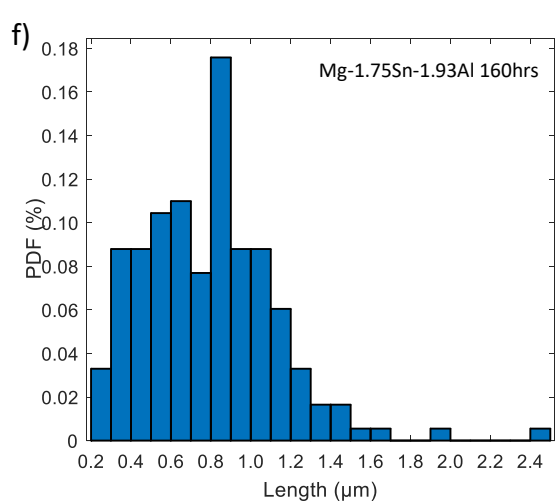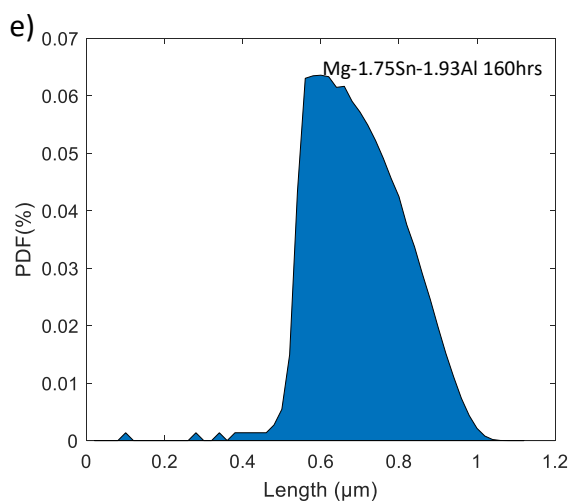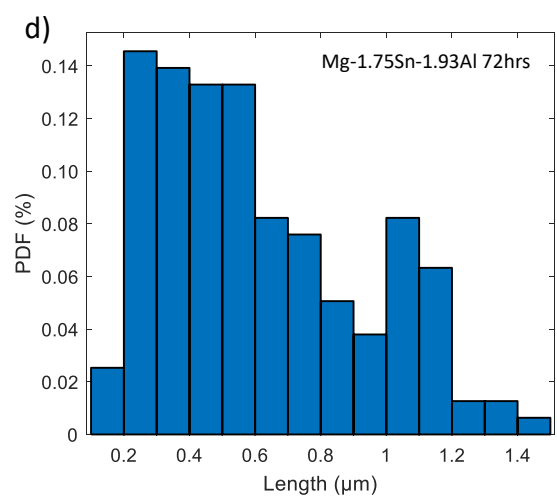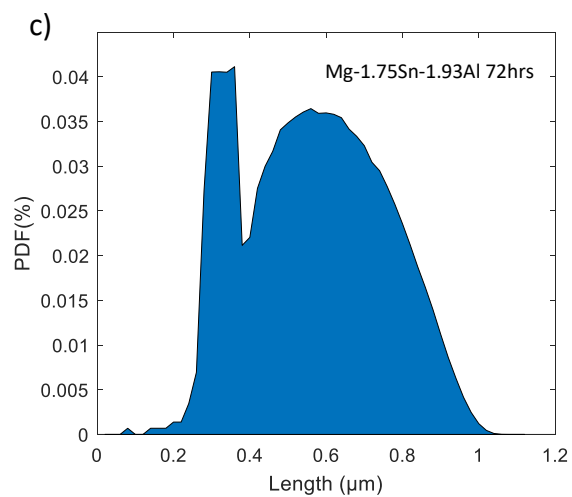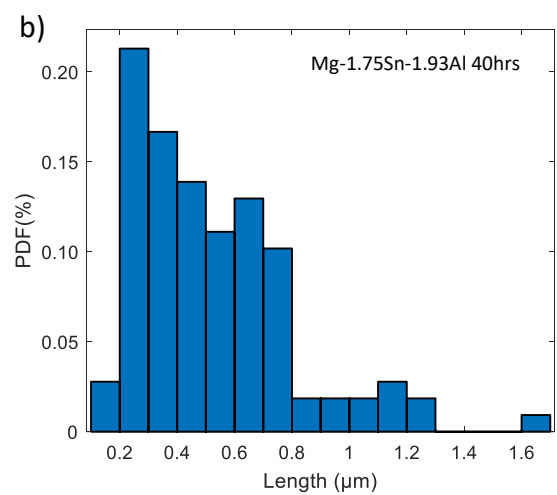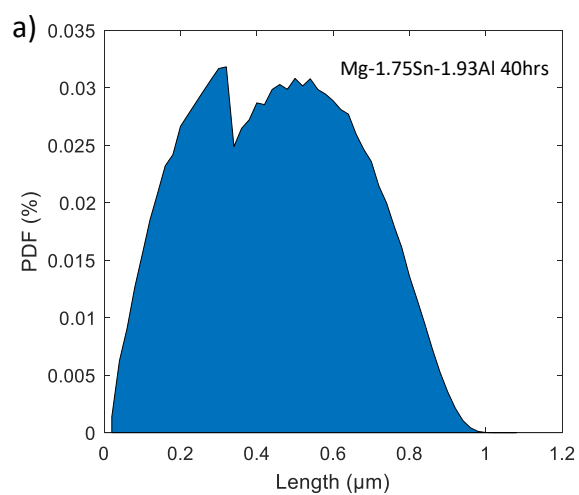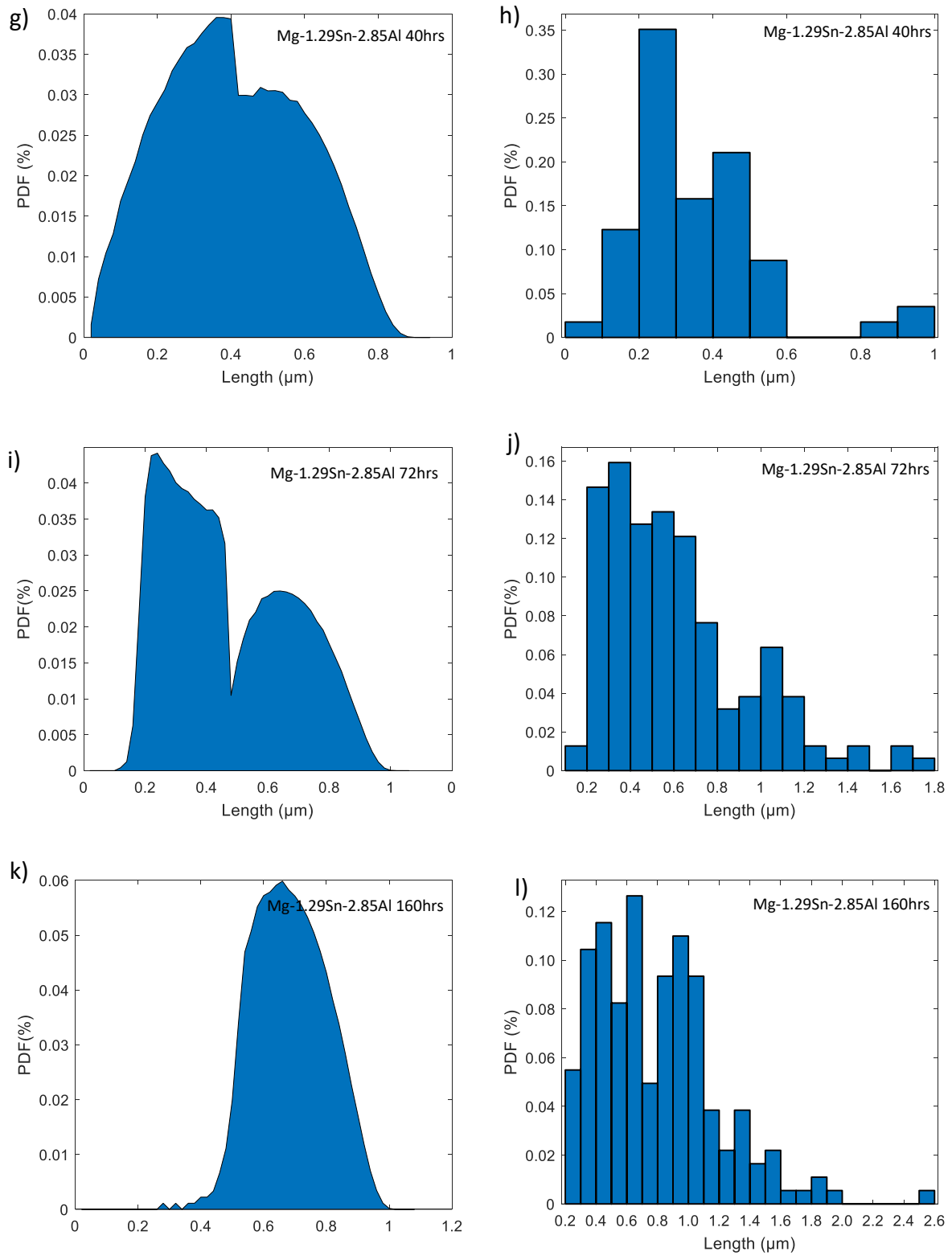
**Fig 6.5:** *Comparison of modelled number density against measured. Compositions and ageing times are given on graph a),c),e),g),i),k) are modelled and b),d),f),h),j),l) are measured.*

## 6.3　Strength Model

Now that a model for the evolution of the microstructure has been established, this must

be put in the context of the mechanical properties of the alloy.

### 6.3.1　Modelling Strength of Alloys from Solution Strengthening and Grain Size

The grain size of the sample is of the order of a few millimetres, due to the relatively small

size of the cast sample. This has not allowed the grain size to be determined accurately.

The Hall-Petch strengthening mechanism is:

$$\sigma_{HP} = \sigma_0 + \frac{k}{\sqrt{d}}, \qquad\qquad [6.1]$$

where $\sigma_0$ is the materials intrinsic resistance to slip and $k$ is a constant as defined by the

metal. From the work of Caceres et al, the values of $\sigma_0$ and $k$ are 11MPa and 0.37MPam$^{1/2}$

for Mg.  Taking $d$ as 5mm we get a result of 16.2 MPa. This is relatively little compared to

that achieved in typical alloys where the grain size is refined.

Next considering strengthening via solid solution, fortunately the low level of Al solute

means that the $\gamma$ phase hasn't formed, thus we can consider the solid solution

strengthening of Al to be constant throughout the ageing treatment. Caceres and

Rovera[36] give the equation:

$$\sigma_{SS} = CX^{2/3} \qquad\qquad [6.2]$$

where $C$ is a constant depending on the solute in question, given as 197MPa for Al, and

$X$ is the atomic percentage added to the alloy. Similarly Shi et al[87] have investigated the

solid solution strengthening of Mg by Sn, although the situation appears less well defined.

Instead the equation is given with two possible exponents, either $2/3$, as above, or $1/2$. Each

has their own constant, 286 and 192.5 MPa. For consistency however, the factor of $2/3$ will

be used. Table 6.4 below gives the increment in strength from the solutes for the prepared

alloys. The values given in Table 6.4 for Sn are for the solution treated state. This will decrease with the growth of the $Mg_2Sn$ precipitates, thus for the aged samples the portion of Sn expended in the formation of the $Mg_2Sn$ will be calculated using the volume fraction found via XRD.

*Table 6.4:* *Solid solution strengthening for the alloys used in this study*

| Alloy (wt%(at%)) | Al (MPa) | Sn (MPa) | Total (MPa) |
|---|---|---|---|
| Mg-1.75Sn-1.93Al | 14.2 | 19.3 | 33.5 |
| Mg-1.29Sn-2.85Al | 18.4 | 15.7 | 34.1 |

Despite this, no study to the author's knowledge has investigated the combined effect of ternary elements in solid solution strengthening, that is to say can the strengthening effects of two elements be combined linearly? The work of Caceres has been successfully applied to AZ91 and Mg-RE alloys with reasonable success[173–176], and given the dilute nature of the alloys (less than 5at% alloying), for now the two strengthening effects will be modelled as separate.

### 6.3.2 Combination of Strengthening Mechanisms

Unfortunately, there is no widely agreed upon method with which to combine the different strengthening mechanisms discussed above. The most simple method is a summative method where the additions are added linearly, but this has been found to be inaccurate, thus adding in quadrature has been proposed as a more reasonable way of estimating total strength[177–179].

In order to ascertain which is suitable, the data from Luo et al's work[113] on Mg-Al-Sn ternaries will be modelled, given that grain size, secondary phase area fraction and solute content are readily determined as well as the tensile yield strength. The one issue will be the difficulty in modelling the contributions of the precipitates in the as cast sample as there is no quantification of their size and number density, thus this is omitted.

*Table 6.5: Calculated strength of Mg-Sn-Al allosys in comparison to the work of Luo et al.[113]The base Mg strength used is 17.7MPa*

| Alloy (wt%) | Al (at%) | Sn (at%) | Grain Size (um) | Yield Strength (MPa) | Solute Strengthening (MPa) | Hall Petch (MPa) | Summative (MPa) | Difference between measured and summative (MPa) | Quadrature (MPa) | Difference between measured and quadrature (MPa) |
|---|---|---|---|---|---|---|---|---|---|---|
| Mg-5Al-1Sn | 4.505 | 0.206 | 295 | 64.7±1.4 | 29.6 | 32.5 | 79.8 | -15.1 | 61.7 | 3.0 |
| Mg-5Al-3Sn | 4.579 | 0.629 | 149 | 75.5±3.0 | 35.0 | 41.3 | 94.0 | -18.5 | 71.8 | 3.7 |
| Mg-5Al-5Sn | 4.656 | 1.065 | 135 | 82.5±4.0 | 39.3 | 42.8 | 99.9 | -17.4 | 75.9 | 6.6 |
| Mg-7Al-2Sn | 6.373 | 0.417 | 147 | 91.9±2.1 | 38.8 | 41.5 | 98.1 | -6.2 | 74.6 | 17.3 |
| Mg-7Al-3Sn | 6.426 | 0.63 | 121 | 88.8±3.6 | 41.4 | 44.6 | 103.7 | -14.9 | 78.6 | 10.2 |
| Mg-7Al-5Sn | 6.533 | 1.068 | 81 | 110.1±10.1 | 45.8 | 52.1 | 115.6 | -5.5 | 87.1 | 23.0 |
| Mg-9Al-2Sn | 8.213 | 0.418 | 119 | 102.5±3.3 | 44.6 | 44.9 | 107.3 | -4.8 | 81.0 | 21.5 |
| Mg-9Al-4Sn | 8.35 | 0.849 | 74 | 120.4±6.9 | 49.5 | 54.0 | 121.2 | -0.8 | 91.0 | 29.4 |
| Mg-9Al-5Sn | 8.42 | 1.07 | 91 | 127±1.3 | 51.7 | 49.8 | 119.2 | 7.8 | 89.5 | 37.5 |

As can be seen from Table 6.5, the quadrature method is more accurate in the cases where the solute concentration is lower (below 6 at%, this being the Mg-5Al-XSn series), consistently falling within 2 standard deviations of the given yield strength value, whereas in the higher solute case the summative method is more accurate. For the one outlier, Mg-7Al-5Sn, it should be noted that the experimental error was by far the largest. As such calculations were made for the alloys used for this study using the quadrature method and the results are given in Table 6.6.

As discussed, the Orowan mechanism is not considered for either mechanism. Given that the quadrature method diverges with increasing solute, i.e. when we would expect to encounter more secondary phase, perhaps this gives the reason for this discrepancy. It must also be realised that the majority of the secondary phase forms as a eutectic in the as cast form, strengthening the grain boundaries, this is not considered within the current approach.

Nonetheless, as the alloys used are considered to be dilute, the quadrature method is considered as appropriate and thus the following strengths are calculated for the solution treated alloys. Considering the above, we can approximately model the strength of a Mg-Sn-Al alloy in the solution treated state. The measurement of mechanical properties of the alloys in this study was conducted with Vickers hardness tests and thus the above must be converted to a hardness in order to provide a comparison.

**Table 6.6**: *Calculated strength increments in experimental alloys from both solute strengthening and the Hall-Petch effect in the solution treated state*

| Alloy | Solute Strengthening (MPa) | Hall-Petch (MPa) | Strength of Solution Treated alloy (MPa) |
|---|---|---|---|
| Mg-1.75Sn-1.93Al | 33.5 | 16.2 | 54.9 |
| Mg-1.29Sn-2.85Al | 34.1 | 16.2 | 55.5 |

### 6.3.3 Precipitation Hardening

When the metal is aged we must consider the contribution of the precipitates to the overall strength of the alloy. Two mechanisms of strengthening, either Orowan or precipitate shearing, compete when the dislocation interact with the precipitates. As Hutchinson et al[37]. show for $Mg_{17}Al_{12}$ in a Mg matrix, the critical radius for shearing is 3nm. Given the similarities between the two systems, we can use a similar assumptions, only changing the shear modulus of the precipitate phase. Given the similarity in the two shear modulus values ($\sim$30GPa in $Mg_{17}Al_{12}$ against $\sim$27GPa in $Mg_2Sn$[180]) it is a safe assumption that the shearing can widely be disregarded as typically the smallest dimension of the precipitates is 10s of nm.

Thus we deal only with an Orowan mechanism, whereby precipitates are sufficiently large and strong for a dislocation loop to form around the precipitate without shearing occuring. This relies of course on the strength of the precipitate but more so on the average spacing of the precipitates, $\lambda$. While it might be the case that the pyramidal or prismatic precipitates are stronger in isolation, they are clearly far too few in number to effectively strengthen the alloy. We can consider the fact that by crossing a number of basal planes, the non-basal precipitates effectively prevent slip on more planes than those precipitates confined to the basal plane. These have been successfully modelled[20,122–124,181,182] as multiple precipitates on the basal plane with size equal to the cross section on the basal plane. These studies have considered the differing strength for systems where we have a single precipitates type, but the subject of mixed precipitate types is not approached widely[183]. Thus this will be the focus of the model, considering a less uniform microstructure as found in real samples.

Thus we must consider the cross section of the precipitates in the basal plane and act from there. The <a> type dislocation is far more easily activated in ambient conditions[25,26], so for now it will be assumed that this is the only deformation mechanism. Consider slip in the three basal directions and how this will interact with the precipitates in the alloy. The starting point will be finding the effective spacing in the basal plane.

### 6.3.4   Orowan Strengthening

Eqn [2.3] from the literature review is used to model the inter precipitate spacing in the current alloy.

$$\sigma_{Orowan} = \frac{MG\boldsymbol{b}}{2\pi\lambda.\sqrt{1-\nu}}.\ln\left(\frac{d_p}{\boldsymbol{b}}\right) \qquad\qquad [2.3]$$

A number of studies [10,20,37,117,19,118,122,123] have approached the problem of different morphologies, particularly in H.C.P. where basal deformation is more likely. These focus however on very uniform cases, i.e. comparing a constant volume fraction of different precipitate morphologies in order to justify which is more effective and thus desirable. To the authors knowledge, none have attempted to calculate a microstructure of multiple morphologies in Mg. In order to do this we will simplify the situation to only consider basal deformation as Hutchinson[37] does. In order to do this we borrow the approach from the literature [10,20,122–124] in defining the precipitates as a projection in the basal plane and disregard any deformation that does not fall in this plane. Thus we define $\lambda$ as:

$$\lambda = \frac{1}{\sqrt{N_v.t}} - d_p \;, \qquad\qquad [6.4]$$

where the precipitates height (thickness) in the c direction, $t$, accounts for precipitates crossing multiple basal planes, converting the number density as a volume to the number

density on the slip plane. Obviously taking the average thickness between all precipitates regardless of their morphology would not be sensible. Therefore we further expand the $\sqrt{N_v.t}$ term, now referred to as $N_{eff}$ for convenience:

$$N_v.t = N_{eff} = (N_v.t)_{Basal} + (N_v.t)_{Pyr} + (N_v.t)_{Prism} \; etc. \tag{6.5}$$

### 6.3.5 Calculating $\langle d_p \rangle$

When we consider spherical precipitates or any that can be broadly approximated as one such as the <c> rods seen in the current sample, it is relatively trivial to calculate the average distance from the centre to the edge of the precipitate, $\langle d_p \rangle$, as it can be taken as the radius of the sphere. Alternatively we have cross sections for the precipitates that are rectangles with large aspect ratio. We calculate the average distance to the edge of a rectangle from the centre, by defining the rectangle as two functions and applying the mean value theorem:

$$\langle f(x) \rangle = \frac{1}{b-a} \int_a^b f(x) \; dx \tag{6.6}$$

Initially we define our rectangle as two functions:

$$y = \begin{matrix} \pm t \; if \; x < |l| \\ 0 \; if \; x > |l| \end{matrix} \tag{6.7a}$$

$$x = \begin{matrix} \pm l \; if \; y < |t| \\ 0 \; if \; y > |t| \end{matrix} \tag{6.7b}$$

On a 2D Cartesian grid, we can define the length of a vector as:

$$f(x,y) = \sqrt{x^2 + y^2} \tag{6.8}$$

As we restrict this vector to only the edge of the rectangle we can express it as either $f(x,t)$ or $f(l,y)$; by finding the average of both functions and weighting them appropriately we can find $\langle d_p \rangle$. As the function is even we can reduce the functions range to only the positive thus:

144

$$\langle d_p \rangle^l = \frac{1}{l} \int_0^l \sqrt{l^2 + t^2} \; dl \qquad \text{[6.9]}$$

$$\langle d_p \rangle^l = \frac{1}{2l} \left[ l.\sqrt{l^2 + t^2} + t^2.\ln\left(l + \sqrt{l^2 + t^2}\right) \right]_0^l$$

$$\langle d_p \rangle^l = \frac{1}{2l} \left( l.\sqrt{l^2 + t^2} + t^2.\ln\left(l + \sqrt{l^2 + t^2}\right) - t^2.\ln(t) \right) \qquad \text{[6.10]}$$

This can be inverted due to the symmetry of the function such that:

$$\langle d_p \rangle^t = \frac{1}{t} \int_0^t \sqrt{l^2 + t^2} \; dt = \frac{1}{2t} \left( t.\sqrt{l^2 + t^2} + l^2.\ln\left(t + \sqrt{l^2 + t^2}\right) - l^2.\ln(l) \right) \quad \text{[6.11]}$$

Thus we have $\langle d_p \rangle$ expressed in two parts whereby each factor is weighted:

$$\langle d_p \rangle = A.\langle d_p \rangle^l + B.\langle d_p \rangle^t \qquad \text{[6.12a]}$$

The only remaining need is to find an expression for this weighting. This can be achieved using the aspect ratio, $R$:

$$\langle d_p \rangle = \left( \frac{2}{\pi} \text{atan}(R) \right).\langle d_p \rangle^l + \left( 1 - \frac{2}{\pi} \text{atan}(R) \right).\langle d_p \rangle^t \qquad \text{[6.12b]}$$

The following is applied to the lath, pyramidal and other precipitates; as mentioned above the prismatic rods however will be modelled using the width as the diameter of the precipitate given their near circular cross-section.

### 6.3.6 Converting Hardness to Strength

We thus are left with two sets of results, that measured as a hardness and that simulated as a strength. Hardness is related to the yield strength, σ, via:

$$\sigma(GPa) = H_v.L.g_\oplus \qquad \text{[6.13]}$$

Where $H_v$ is the Vickers hardness measured, $L$, the load during testing, 0.1kg in the current work, and $g_\oplus$ the earths gravitational acceleration ($9.81 ms^{-2}$). The values are summarised in Table 6.7 and plotted in Fig 6.6.

**Table 6.7:** *Comparison of strengths calculated from hardness measurements and calculated from precipitation model.*

| Alloy (at%) | Ageing time (hrs) | Vickers Hardness ($V_H$) | Yield Strength Calculated From Hardness (MPa) | Calculated Strength (Quadrature Method) (MPa) | Difference (MPa) |
|---|---|---|---|---|---|
| Mg-1.75Sn-1.93Al | 0 | 49.9 ± 1.7 | 48.9 ± 1.6 | 46.6 | 2.3 |
| | 40 | 52.4 ± 1.6 | 51.4 ± 1.6 | 50.6 | 0.8 |
| | 72 | 66.6 ± 3.1 | 65.3 ± 3.1 | 68.4 | -3.1 |
| | 160 | 58.8 ± 1.7 | 57.7 ± 1.7 | 58.1 | -0.4 |
| Mg-1.29Sn-2.85Al | 0 | 50.8 ± 2.9 | 49.8 ± 2.8 | 46.8 | -3.0 |
| | 40 | 57.6 ± 2.7 | 56.5 ± 2.6 | 48.3 | 8.2 |
| | 72 | 68.4 ± 2.8 | 67.1 ± 2.7 | 73.1 | -6 |
| | 160 | 64.9 ± 3.4 | 63.6 ± 3.3 | 63.6 | 3.8 |

Considering Orowan strengthening generally will overestimate the strengthening effect of the particles, along with the fact that is assumes the particle size is uniform. The calculated strengths infact show reasonable agreement with the measured values. The largest divergence is seen when the volume fraction is greatest, perhaps hinting at the fallibility of the model as the precipitate density rises.

## 6.4 Combination of the Models

Given that the model in section 6.2 outputs the volume and number density of the precipitates as a function of time, we can link this to the strengthening model fitted using the measured values of size and number density. We can then look at the progression of the yield strength as a function of time. Fig 6.6 gives a breakdown of the contributions from the different strengthening mechanism from the two alloys as a function of time, with Fig 6.7 showing a comparison of the two alloys again using the quadrature addition method as described above. Due to the slower coarsening rate in the number density model, the strength of the alloy is over estimated in this period, but as with the mechanical measurements, the Mg-1.29Sn-1.93Al alloy exhibits a greater peak strength.
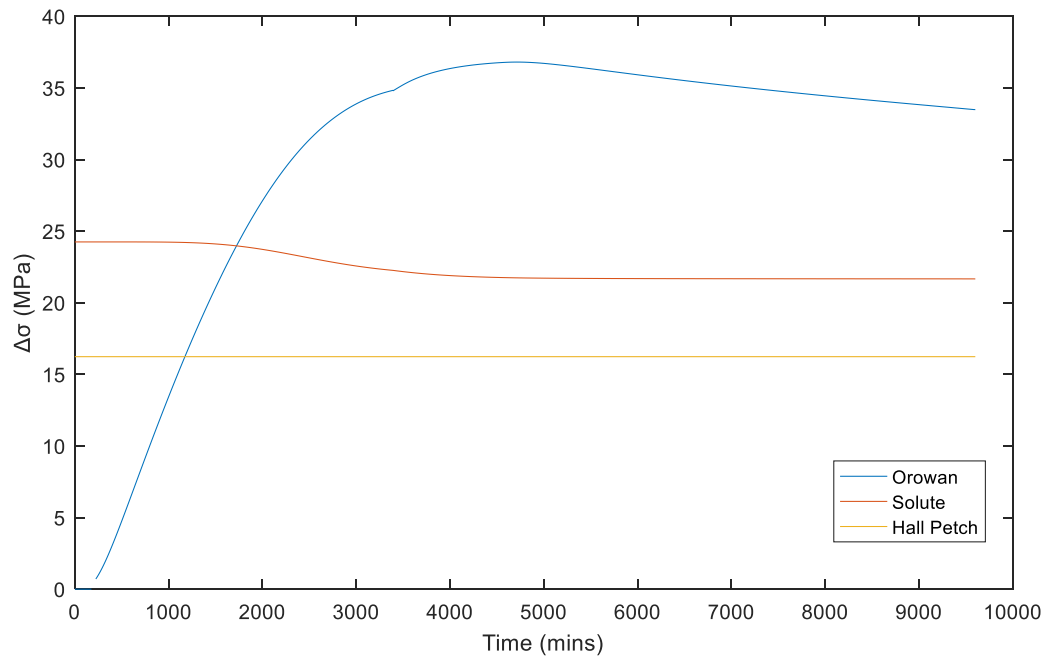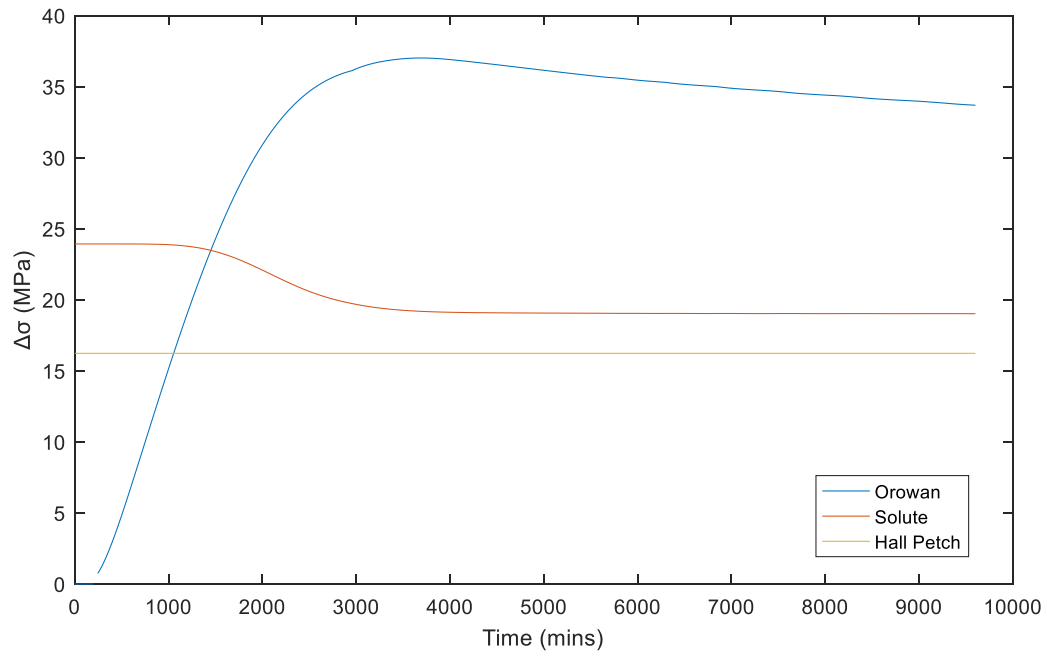
***Fig 6.6:*** *Breakdown of contributions from different mechanisms for a) Mg-1.75Sn-1.93Al and b) Mg-1.29Sn-2.85Al alloys*
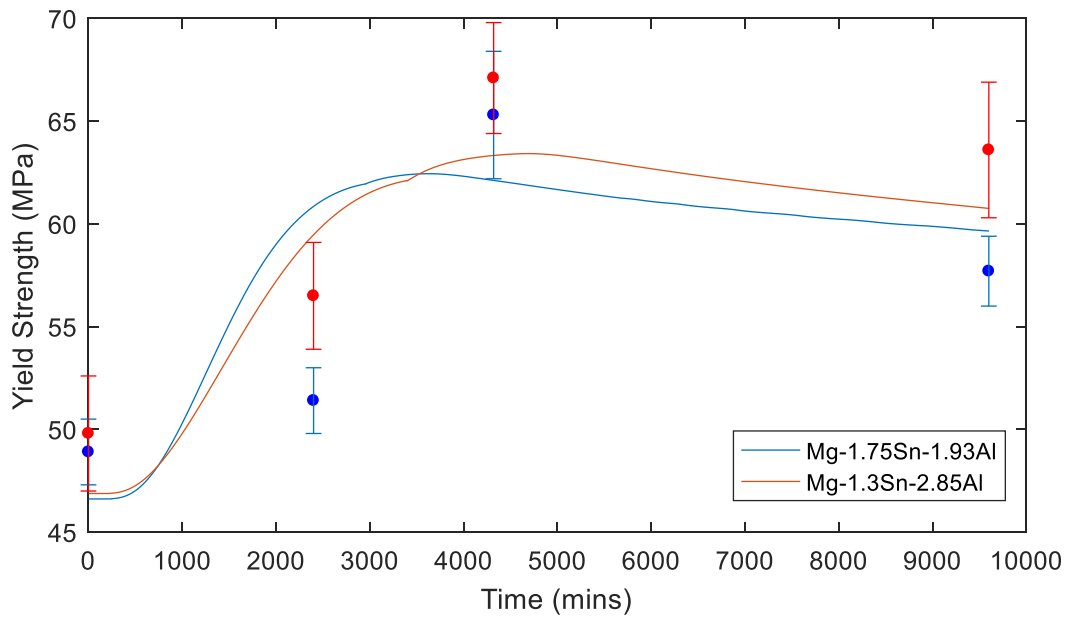
*Fig 6.7: Comparison of the Mg-1.75Sn-1.93Al and Mg-1.29Sn-2.85Al*

## 6.5 Discussion

The size results and the modelling of the precipitate growth are useful in terms of practical application of the alloy. Regardless of the OR, the greater number density of precipitates and smaller size in the Mg-1.29Sn-2.85Al alloy explain the greater strength. It is seen that the relative fractions of each precipitate morphology do not vary greatly with time or between the two compositions, thus the overall number density is of far more importance than the precipitate morphology. This is backed up by the far greater strength seen in the Mg-Sn-Al-Na quarternaries in the literature[108,109,155], that lack non basal precipitates. Microalloying has proven effective in improving the nucleation rate compared to a binary alloy though it is not yet understood whether this is a result of an increased diffusion rate of more nucleation sites or even a combination of the two.

The fitted parameters in the model indicate that the diffusion rate is greater in the ternaries which had been suggested in the literature. Further work needs to be done on the relative effectiveness of each element in increasing the diffusion rate. This could be

achieved by using a series of Mg-Sn-Al/Zn alloys. This would need to be verified in another manner, perhaps a diffusion couple between Mg-Al/Zn and Sn. Additionally, only a single ageing temperature has been investigated; further temperatures would be required to fully understand and model the effect on the diffusion rate.

Aside from the diffusion rate, the fitted interfacial energy during the growth stage indicates that in the case of the Mg-1.75Sn-1.93Al alloy is lower than that for the $Mg_{17}Al_{12}$ precipitates in AZ91, with the Mg-1.29Sn-2.85Al alloy having a similar value to that used by Hutchinson et al[37] and Robson et al[131]. Conversely the fitted value for coarsening is far lower than that which Hutchinson et al use for AZ91. However no comparison can be made to the binary Mg-Sn alloy; further data is needed though it is expected that both values of $\gamma$ would be higher in the binary. Likewise the interfacial energy for nucleation is expected to be greater due to the lower nucleation rate in the binary.

Of interest would be a comparison of the various Mg-Sn ternaries with and without the Na additions to isolate improvement in nucleation sites as it is presumed that nucleation on Na clusters is the dominant nucleation mechanism, given that the inclusion of Na resulted in number densities that are far larger than for alloys without Na.

The most interesting feature of the precipitate growth model is the overlap of growth and coarsening in the Mg-1.75Sn-1.93Al alloy. There is no clear division between the growth and coarsening stages (Fig 6.4), most likely due to the large amount of solute and slow growth rate compared to Mg-Al alloys. Despite the extra solute, nucleation is restricted when it becomes more favourable for precipitates to grow. This leads to a quicker drop off in strength and a lower number density compared to that seen in the Mg-1.29Sn-2.85Al alloy, as the smaller precipitates coarsen and are removed from the microstructure. The nucleation interfacial energy is very similar for both alloys and thus this is not the cause

of this effect. Likewise the mechanical properties and sizes are similar at the 40 hour point; therefore we conclude that it is the effect of the extra Al content in the Mg-1.29Sn-2.85Al alloy that prevents the earlier onset of coarsening. In the Mg-1.29Sn-2.85Al alloy, the growth and coarsening are well separated; thus the microstructure is slowly changing between these two points giving a consistent strength for a greater period of time as well as allowing for continued nucleation to raise the number density.

Overall the modelling of the strength of the alloys is consistent with the measurements, although no attempt has been made to model the strengthening on different slip planes due to the much greater CRSS of the non-basal planes in Mg. The characterisation needs to be taken further to include the high temperature strength as the main interest in Mg-Sn alloys is their potential as a cheap alternative to Mg-RE alloys. This should involve high temperature strength measurements, either by hardness indent as above or by measuring the strength directly. At the higher temperatures these additional slip planes become more easily activated and thus would be of greater consequence when modelling the alloy.

### 6.5.1  Critique of Growth Model
 The main flaw of the growth model is the assumed constant aspect ratio. In the actual alloy the precipitates have a variety of aspect ratios meaning that the results of the model must be used cautiously. A more in-depth look at the growth of a single precipitate category in the different directions would require the Gibbs Thomson equation to be evaluated for each face at each time step. This is still not well understood[132] and thus approximate methods such as that above must be used. Certainly an investigation of this type may shed light on the development of the various different precipitate morphologies. It is clear that the energy required for each precipitate type all fall close to each other and

as such the variation is a result of perturbations from the average alloy such as slightly higher solute levels, dislocations and impurities.

Likewise it is always assumed that the environment in which the precipitate is growing is consistent over time. The ternary element has been given as the reason for the lower interfacial energy; in fact it has been shown by Liu et al[112] that Zn forms a layer between the matrix and the precipitate. The development of this layer is most likely not consistent during the growth of the precipitate and thus using a constant interfacial energy for the precipitates may not be suitable for Mg-Sn-Zn alloys; this effect has not been seen for Al. Likewise the role the Al plays in this growth is not accounted for by the model, leading to some differences between the measured size distribution and the modelled one. That being said, the average precipitate sizes are in good agreement. Moreover Orowan's equation only makes use of the mean precipitate size and thus the difference in size distributions will not affect the strength simulation if the mean precipitate size is the same in both instances.

The strength modelling itself shows a similar profile to that found by Hutchinson et al [37] and Robson and Paa-Rai[118], fitting the measured data with reasonable accuracy. In the earlier stages the strengths are overestimated, as the volume fraction of secondary phase is low. There is the possibility that the approximation used by Orowan that all particles are spaced equally does not hold entirely, thus the lower measured strength. This again links back to the poor understanding of the nucleation and early stages of growth. It is possible that there is an as yet unobserved step between nucleation and normal growth that would explain this disparity.

## 6.6 Summary

A KWN model has been used to predict the growth of precipitates in the microstructure of Mg-Sn-Al alloys. The model has been iterated to fit a number of parameters given in Table 6.1. In contrast to the literature, the coarsening is modified to account for growth/coarsening anisotropy. This is discussed as well as a number of different models investigated.

Moreover, the observed microstructure has been linked to the change in mechanical properties of the Mg-Sn-Al alloys during heat treatment. The different precipitate types have been treated separately when considering strengthening while still considering the effective number density, $N_{eff}$, of all of the precipitates. Aside from this a calculation has been presented to calculate $\langle d_p \rangle$ for the various morphologies, which has shown good success in predicting the strengthening effect of the precipitates when the precipitates are well separated. Despite their smaller number density, the combination of the different precipitate morphologies represents a greater strengthening effect than would be expected for basal precipitates of the same volume fraction in accordance with the literature. This has then been linked to the simulation of the microstructure to give a predicted strength across the ageing process.

# 7 DISCUSSION AND FUTURE WORK

## 7.1 Summary of Results

Two dilute Mg-Sn-Al alloys, Mg-1.75Sn-1.93Al and Mg-1.29Sn-2.85Al, have been cast and heat treated for varying times (solution treatment at 520°C followed by 40, 72 and 160hrs respectively at 200°C). The microstructure was seen via TEM and XRD to consist of a variety of precipitates, but all of the $Mg_2Sn$ type. These precipitates form in a number of morphologies: hexagonal plates on the basal plane, laths elongated in the $\langle 11\bar{2}0 \rangle_\alpha$ directions, prismatic rods along the $[0001]_\alpha$ direction and pyramidal laths. All morphologies except the pyramidal laths were found to have the OR $(0001)_\alpha //$ $(111)_\beta, [11\bar{2}0]_\alpha //[110]_\beta$ (OR-3) fitting that which is widely reported in the literature for Mg-Sn ternary alloys and confirming the shared OR between different morphologies. On the other hand the pyramidal precipitates were found to have no currently determinable OR.

The dimensions of each of the precipitate varieties has been measured via SEM and TEM and the number density calculated. The area and volume fraction were established using SEM and XRD. This data has been input to a strength model based on a modified version of the Orowan equation to explain the mechanical data.

## 7.2 Conclusions

- 4 $Mg_2Sn$ precipitate morphologies identified via tilting experiments that are present in both alloys. These match those observed in similar alloys in the literature.

- Small deviations from the low index planes are observed for the precipitate facets in both alloys. Similarly, pyramidal precipitates are shown to not sit on a single low index plane.

- OR observed as follows:

  - Basal plates, $11\bar{2}0$ laths and prismatic precipitates all exhibit OR $(0001)_\alpha//(111)_\beta$, $[11\bar{2}0]_\alpha//[\bar{1}10]_\beta$

  - Pyramidal precipitates exhibits an irregular OR

- Precipitates number densities measured via TEM and SEM. The peak number densities are 7.9µm$^{-3}$ in the Mg-1.75Sn-1.93Al alloy and 14.1µm$^{-3}$ in the Mg-1.29Sn-2.85Al alloy. A full breakdown of the number density for both alloys and at each ageing time is given in Fig 5.10.

- The average size of the precipitates is given in Tables 5.1 to 5.3. Additionally the size distribution is given for $\langle 11\bar{2}0 \rangle$ laths in Fig 5.11 and pyramidal precipitates in Fig 5.13.

- Precipitate growth model established using a KWN model finding diffusion rates of $1.76x10^{-18}m^2s^{-1}$ in the Mg-1.75Sn-1.93Al alloy and $1.55x10^{-18}m^2s^{-1}$ in the Mg-1.29Sn-2.85Al alloy.

- Strength modelled giving values in line with hardness measurements

## 7.3  Future Work

- Verify the combination of the strength and precipitation models (Section 6.4) through further measurement, using different ageing times and temperatures.

- Tensile and compression mechanical tests to firstly confirm the relation between hardness and strength. This will allow researchers to assess the anisotropy between compressive and tensile strength and factor this effect into the modelling

of strength. Likewise, more directed studies could be used to determine the change in CRSS for each slip system, for example for *in situ* SEM pillar compression.

- High temperature mechanical tests are required to quantify the benefit of the $Mg_2Sn$ precipitates in comparison to those in Mg-Al(-RE) and Mg-RE alloys. This is key to assessing the viability of Mg-Sn ternaries as an alternative.

- Study of the effect of Al on the nucleation of precipitates and the diffusion coefficient of Sn in Mg-Sn-Al ternaries to refine the model of precipitate growth. This should later be extended to Zn and other common additions. This could be investigated by using precipitate growth as with the current work.

- Investigate effect of microalloying of Mn, Zn etc on the precipitation mechanism, particularly the size distribution of precipitates, to ascertain the effect on growth and nucleation and the ratios of basal/prismatic and pyramidal precipitates. In particular consideration should be given to Mn as it is an effective grain refiner in Al containing Mg alloys and thus would increase the Hall-Petch strengthening for Mg-Sn-Al.

- TEM dislocation study to confirm the effectiveness of different precipitates, particularly looking at <a> type dislocations interacting with pyramidal precipitates given the lack of a clear OR between the two lattices. This would be best achieved through in-situ TEM deformation.

- Develop the nucleation and growth model by accounting for growth in more than a single direction via a more complete treatment of the Gibbs-Thomson equation. This could be developed to consider the stress arising from the lattice mismatch as well as the chemical driving force. Likewise the nucleation could be further

developed to consider both homogeneous nucleation (as used above) and heterogeneous nucleation as is observed in the Mg-Sn-Al-Na alloys.

- Study of difference between undeformed and predeformed samples in terms of effective nucleation of precipitates on dislocations as is seen in AZ91[41] as an alternative to the homogeneous nucleation currently assumed. This could serve as a method to reduce the time required to nucleate precipitates and thus decrease the ageing time required.

# 8 REFERENCES

[1] B.L. Mordike, T. Ebert, Mater. Sci. Eng. A 302 (2001) 37–45.

[2] B.L. Mordike, H.E. Friedrich, Magnesium Technology: Metallurgy, Design Data, Applications, Springer-Verlag Berlin, Heidelberg, 2006.

[3] C. Grard, C.M. Phillips, H.W.. Phillips, Aluminium and Its Alloys, Their Properties, Thermal Treatment and Industrial Applications, Constable and Company, London, 1923.

[4] P.C. Sharm, A Textbook of Production Technology: Manufacturing Processes, S.Chand, 2008.

[5] J.R. Davis, ASM Handbook: Aluminium and Aluminium Alloys, ASM International, 1993.

[6] J.R. Davis, ASM Handbook: Cast Irons, ASM International, 1996.

[7] G. Song, A. Atrens, Adv. Eng. Mater. 5 (2003) 837–858.

[8] K.W. Guo, Recent Patents Corros. Sci. 2 (2010) 13–21.

[9] A. Atrens, G. Song, M. Liu, Z. Shi, F. Cao, M.S. Dargusch, Adv. Eng. Mater. 17 (2015).

[10] J.-F. Nie, Metall. Mater. Trans. A 43 (2012) 3891–3939.

[11] Z. Yang, J. Li, J. Zhang, G.W. Lorimer, J.D. Robson, Acta Metall. Sin. (English Lett. 21 (2008) 313–328.

[12] F. Czerwinski, Adv. Mater. Process. 2 (2014) 28–31.

[13] Y.M. Kim, C.D. Yim, H.S. Kim, B.S. You, Scr. Mater. 65 (2011) 958–961.

[14] X. Gu, Y. Zheng, Y. Cheng, S. Zhong, T. Xi, Biomaterials 30 (2009) 484–498.

[15] N. Hort, Y. Huang, D. Fechner, M. Störmer, C. Blawert, F. Witte, C. Vogt, H. Drücker, R. Willumeit, K.U. Kainer, F. Feyerabend, Acta Biomater. 6 (2010) 1714–25.

[16] H. Hornberger, S. Virtanen, A.R. Boccaccini, Acta Biomater. 8 (2012) 2442–2455.

[17] Y. Chen, Z. Xu, C. Smith, J. Sankar, Acta Biomater. 10 (2014) 4561–4573.

[18] M. Avedesian, H. Baker, ASM Handbook: Magnesium and Magnesium Alloys, ASM International, 1999.

[19] N. Stanford, J. Geng, Y.B. Chun, C.H.J. Davies, J.-F. Nie, M.R. Barnett, Acta Mater. 60 (2012) 218–228.

[20] J.-F. Nie, Scr. Mater. 48 (2003) 1009–1015.

[21] C.S. Roberts, Magnesium and Its Alloys, Wiley, 1960.

[22] F. Czerwinski, Magnesium Injection Molding, Springer-Verlag Berlin, 2014.

[23] D. Hull, D.J. Bacon, Introduction to Dislocations, Elsevier Ltd, 2011.

[24] P.B. Hirsch, Electron Microscopy of Thin Crystals, Krieger Publsihing Company, 1965.

[25] P. Ward Flynn, J. Mote, J.E. Dorn, Trans. Metall. Soc. AIME 221 (1961) 1148–1154.

[26] A. Akhtar, E. Teghtsoonian, Acta Metall. 17 (1969) 1351–1356.

[27] F. Kang, Z. Li, J. Tao, J. Mater. 47 (2012) 7854–7859.

[28] R.E. Reed-Hill, W.D. Robertson, Trans. Metall. Soc. AIME 221 (1958) 256–259.

[29] T. Obara, H. Yoshinga, S. Morozumi, Acta Metall. 21 (1973) 845–853.

[30] H. Yoshinga, R. Horiuchi, Trans. Japan Inst. Met. 4 (1963) 1–8.

[31] R. Von Mises, Zeitschrift Für Angew Math Und Mech 8 (1928) 161–185.

[32] A. Galiyev, O. Sitdikov, R. Kaibyshev, Mater. Trans. 44 (2003) 426–435.

[33] A. Akhtar, E. Teghtsoonian, Acta Metall. 17 (1969) 1339–1349.

[34] N. Stanford, M.R. Barnett, Int. J. Plast. 47 (2013) 165–181.
[35] W.B. Hutchinson, M.R. Barnett, Scr. Mater. 63 (2010) 737–740.
[36] C.H. Caceres, D.M. Rovera, J. Light Met. 1 (2001) 151–156.
[37] C.R. Hutchinson, J.-F. Nie, S. Gorsse, Metall. Mater. Trans. A 36 (2005) 2093–2105.
[38] D. Duly, J.P. Simon, Y. Brechet, Acta Metall. 43 (1995) 101–106.
[39] K.N. Braszczyńska-Malik, J. Alloys Compd. 487 (2009) 263–268.
[40] S. Celotto, Acta Mater. 48 (2000) 1775–1787.
[41] J.B. Clark, Acta Metall. 16 (1968) 141–152.
[42] D. Duly, M. Audier, Y. Brechet, Scr. Metall. Mater. 29 (1993) 1593–1596.
[43] B. Amir Esgandari, H. Mehrjoo, B. Nami, S.M. Miresmaeili, Mater. Sci. Eng. A 528 (2011) 5018–5024.
[44] A. Srinivasan, U.T.S. Pillai, B.C. Pai, Mater. Sci. Eng. A 452–453 (2007) 87–92.
[45] N. Balasubramani, A. Srinivasan, U.T.S. Pillai, B.C. Pai, Mater. Sci. Eng. A 457 (2007) 275–281.
[46] K.-C. Wu, J.-W. Yeh, S.-Y. Chang, Mater. Chem. Phys. 162 (2015) 757–763.
[47] I.C. Jung, Y.K. Kim, T.H. Cho, S.H. Oh, T.E. Kim, S.W. Shon, W.T. Kim, D.H. Kim, Met. Mater. Int. 20 (2014) 99–103.
[48] R.G. Li, Y. Xu, W. Qi, J. An, Y. Lu, Z.Y. Cao, Y.B. Liu, Mater. Charact. 59 (2008) 1643–1649.
[49] Y. Turen, Mater. Des. 49 (2013) 1009–1015.
[50] M. Zhang, P.M. Kelly, Scr. Mater. 48 (2003) 647–652.
[51] A.F. Crawley, B. Lagowski, Metall. Trans. 5 (1974) 949–951.
[52] A.F. Crawley, K.S. Milliken, Acta Metall. 22 (1974) 557–562.
[53] J. Gjønnes, T. Østmoe, Zeitschrift Für Met. 61 (1970) 604–606.
[54] D. Duly, Acta Metall. Mater. 41 (1993) 1559–1566.
[55] D. Duly, W. Zhang, M. Audier, Philos. Mag. 71 (1995) 187–204.
[56] R.A. Fournelle, J.B. Clark, Metall. Trans. 3 (1972) 2757–2767.
[57] D. Bradai, P. Zi, E. Bischoff, W. Gust, Mater. Chem. Phys. 78 (2002) 222–226.
[58] C.L. Mendis, K. Hono, 57 (2007) 485–488.
[59] C.L. Mendis, K. Oh-ishi, Y. Kawamura, T. Honma, S. Kamado, K. Hono, Acta Mater. 57 (2009) 749–760.
[60] C.L. Mendis, K. Oh-ishi, K. Hono, Mater. Sci. Eng. A 527 (2010) 973–980.
[61] D.K. Xu, L. Liu, Y.B. Xu, E.H. Han, Mater. Sci. Eng. A 420 (2006) 322–332.
[62] X. Gao, J.F. Nie, Scr. Mater. 56 (2007) 645–648.
[63] A. Singh, A.P. Tsai, Scr. Mater. 57 (2007) 941–944.
[64] A. Singh, J.M. Rosalie, H. Somekawa, T. Mukai, A. Singh, J.M. Rosalie, H. Somekawa, T. Mukai, Philos. Mag. Lett. 90 (2010) 641–651.
[65] E. Aghion, B. Bronfin, in:, G.W. Lorimer (Ed.), Proc. 3rd Int. Magnes. Conf., Institute of Materials, London, 1997, pp. 313–325.
[66] S. Celotto, T.J. Bastow, Acta Mater. 49 (2001) 41–51.
[67] F. Czerwinski, A. Zielinska-Lipiec, 51 (2003) 3319–3332.
[68] A.A. Luo, Int. Mater. Rev. 49 (2004) 13–30.
[69] M.S. Dargusch, M.A. Easton, S.M. Zhu, G. Wang, Mater. Sci. Eng. A 523 (2009) 282–288.
[70] M.O. Pekguleryuz, A.A. Kaya, Adv. Eng. Mater. 5 (2003) 866–878.
[71] F. Khomamizadeh, B. Nami, S. Khoshkhooei, Metall. Mater. Trans. A 36 (2005) 3489–3494.

[72] B. Nami, H. Razavi, S. Mirdamadi, S.G. Shabestari, S.M. Miresmaeili, Metall. Mater. Trans. A 41 (2010) 1973–1982.

[73] B. Nami, S.G. Shabestari, H. Razavi, S. Mirdamadi, S.M. Miresmaeili, Mater. Sci. Eng. A 528 (2011) 1261–1267.

[74] B.R. Powell, V. Rezhets, M.P. Balogh, R.A. Waldo, Jom 54 (2002) 34–38.

[75] A. Kielbus, T. Rzychon, Mater. Sci. Forum 638–642 (2010) 1546–1551.

[76] M. Suzuki, H. Sato, K. Maruyama, H. Oikawa, Mater. Sci. Eng. A 252 (1998) 248–255.

[77] M. Xuegang, D. Wenwen, X. Feng, Chinese Sci. Bull. 47 (2002) 1082–1086.

[78] Y. Wang, M. Li, C. Li, X. Li, L. Fan, T. Jia, Mater. Corros. 63 (2012) 497–504.

[79] G. Pettersen, H. Westengen, R. Høier, O. Lohne, 207 (1996) 115–120.

[80] Y. Lü, Q. Wang, X. Zeng, W. Ding, C. Zhai, Y. Zhu, Mater. Sci. Eng. A 278 (2000) 66–76.

[81] F. Kabirian, R. Mahmudi, Metall. Mater. Trans. A Phys. Metall. Mater. Sci. 40 (2009) 116–127.

[82] E. Sieracki, J. Velazquez, K. Kabiri, SAE Tech. Pap. (1996) 960421.

[83] A. Kielbus, Arch. Mater. Sci. Eng. 28 (2007) 345–348.

[84] A.A. Nayeb-Hashemi, J.B. Clark, Bull. Allot Phase Diagrams 5 (1984) 466–476.

[85] M.E. Drits, Z.A. Sviderskaya, L.L. Rokhlin, N.I. Nikitina, Metalloved. I Termicheskaya Obrab. Met. 11 (1979) 62–64.

[86] J. van der Planken, A. Deruyttere, Acta Metall. 17 (1969) 451–454.

[87] B.Q. Shi, R.S. Chen, W. Ke, J. Alloys Compd. 509 (2011) 3357–3362.

[88] A.A. Nayeb-Hashemi, J.B. Clark, Phase Diagrams of Binary Magnesium Alloys, ASM, 1988.

[89] G.H. Grosch, K.-J. Range, J. Alloys Compd. 235 (1996) 250–255.

[90] L.L. Rokhlin, Diagrams, Ternary Alloys: A Comprehensive Compendium of Evaluated Constitutional Data and Phase: Vol.7, Al-Mg-Se to Al-Ni-TA, VCH, Cambridge, 1993.

[91] R. Mahmudi, S. Moeendarbari, Mater. Sci. Eng. A 566 (2013) 30–39.

[92] H. Sevik, S. Açıkgöz, S. Can Kurnaz, J. Alloys Compd. 508 (2010) 110–114.

[93] Y. Mingbo, P. Fusheng, C. Renju, S. Jia, Mater. Sci. Eng. A 489 (2008) 413–418.

[94] J.M. Peng, M.B. Yang, Int. J. Cast Met. Res. 25 (2012) 103–109.

[95] J. Chen, Z. Chen, H. Yan, F. Zhang, K. Liao, J. Alloys Compd. 461 (2008) 209–215.

[96] X. Shi, D. Li, A.A. Luo, B. Hu, L. Li, X. Zeng, W. Ding, Metall. Mater. Trans. A 44 (2013) 4788–4799.

[97] L. Jiang, D. Zhang, X. Fan, F. Guo, G. Hu, H. Xue, F. Pan, J. Alloys Compd. 620 (2015) 368–375.

[98] C. Liu, H. Chen, C. He, Y. Zhang, J. Nie, Mater. Charact. 113 (2016) 214–221.

[99] J. Wei, J. Chen, H. Yan, B. Su, X. Pan, J. Alloys Compd. 548 (2013) 52–59.

[100] G. Zhang, J. Chen, H. Yan, B. Su, X. He, M. Ran, J. Alloys Compd. 592 (2014) 250–257.

[101] H. Liu, Y. Chen, Y. Tang, S. Wei, G. Niu, J. Alloys Compd. 440 (2007) 122–126.

[102] S. Behdad, L. Zhou, H.B. Henderson, M. V Manuel, Y. Sohn, A. Agarwal, B. Boesl, Mater. Sci. Eng. A 651 (2016) 854–858.

[103] X. Huang, W. Zhang, Y. Ma, M. Yin, Philos. Mag. Lett. 94 (2014) 460–469.

[104] T.T. Sasaki, J.D. Ju, K. Hono, K.S. Shin, Scr. Mater. 61 (2009) 80–83.

[105] Y. Chen, L. Jin, W. Li, Y. Song, L. Hao, Mater. Sci. Technol. 31 (2015) 73–78.

[106] M. Zhang, W.Z. Zhang, G.Z. Zhu, K. Yu, Trans. Nonferrous Met. Soc. China (English Ed. 17 (2007) 1428–1432.

[107] J.-G. Jung, S.H. Park, B.S. You, J. Alloys Compd. 627 (2015) 324–332.

[108] C.L. Mendis, C.J. Bettles, M.A. Gibson, C.R. Hutchinson, Mater. Sci. Eng. A 435–436 (2006) 163–171.

[109] C.L. Mendis, C.J. Bettles, M.A. Gibson, S. Gorsse, C.R. Hutchinson, Philos. Mag. Lett. 86 (2006) 443–456.

[110] F.R. Elsayed, T.T. Sasaki, C.L. Mendis, T. Ohkubo, K. Hono, Mater. Sci. Eng. A 566 (2013) 22–29.

[111] T.T. Sasaki, K. Oh-ishi, T. Ohkubo, K. Hono, Mater. Sci. Eng. A 530 (2011) 1–8.

[112] C. Liu, H. Chen, J. Nie, Scr. Mater. 123 (2016) 5–8.

[113] A.A. Luo, P. Fu, L. Peng, X. Kang, Z. Li, T. Zhu, Metall. Mater. … 43 (2012) 360–368.

[114] P. Zhang, S.X. Li, Z.F. Zhang, Mater. Sci. Eng. A 529 (2011) 62–73.

[115] J. van der Planken, J. Mater. Sci. 4 (1969) 927–929.

[116] T.T. Sasaki, K. Oh-ishi, T. Ohkubo, K. Hono, Scr. Mater. 55 (2006) 251–254.

[117] C.H. Cáceres, P. Lukac, (2008).

[118] J.D. Robson, C. Paa-Rai, Acta Mater. 95 (2015) 10–19.

[119] W.D. Callister Jr, Materials Science and Engineering An Introduction, 7th ed., Wiley, 2006.

[120] J.B. Ferguson, H. Lopez, D. Kongshaug, B. Schultz, P. Rohatgi, Metall. Mater. Trans. A 43 (2012) 2110–2115.

[121] M.F. Ashby, Strengthening in Crystals, Elsevier Pub. Co., New York, NY, 1971.

[122] F. Wang, J.J. Bhattacharyya, S.R. Agnew, Mater. Sci. Eng. A 666 (2016) 114–122.

[123] P. Hidalgo-Marique, J.D. Robson, M.T. Perez-Prado, Acta Mater. 124 (2017) 456–467.

[124] J.D. Robson, N. Stanford, M.R. Barnett, Metall. Mater. Trans. A Phys. Metall. Mater. Sci. 44 (2013) 2984–2995.

[125] R. Kampmann, R. Wagner, Decomposition of Alloys: The Early Stages, Pergamon Press, Oxford, 1984.

[126] R. Kampmann, R. Wagner, (1991).

[127] O.R. Myhr, O. Grong, Acta Mater. 48 (2000) 1605–1615.

[128] J.D. Robson, M.J. Jones, P.B. Prangnell, 51 (2003) 1453–1468.

[129] J.D. Robson, Acta Mater. 52 (2004) 4669–4676.

[130] J.D. Robson, D.T. Henry, B. Davis, Acta Mater. 57 (2009) 2739–2747.

[131] J.D. Robson, Acta Mater. 61 (2013) 7781–7790.

[132] X. Li, K. Thornton, Q. Nie, P.W. Voorhees, J.S. Lowengrub, Acta Mater. 52 (2004) 5829–5843.

[133] M. Hillert, L. Hoglund, J. Agren, Acta Mater. 51 (2003) 2089–2095.

[134] H.B. Aaron, G.R. Kotler, Metall. Trans. 2 (1971) 393–408.

[135] U. Dahmen, Acta Metall. 30 (1982) 63–73.

[136] M.-X. Zhang, S.-Q. Chen, H.-P. Ren, P.M. Kelly, Metall. Mater. Trans. A 39 (2008) 1077–1086.

[137] A.R.S. Gautam, J.M. Howe, Philos. Mag. 91 (2011) 3203–3227.

[138] A.R.S. Gautam, J.M. Howe, Philos. Mag. 93 (2013) 3472–3490.

[139] W. Bollmann, Philos. Mag. 16 (1967) 363–381.

[140] W. Bollmann, Philos. Mag. 16 (1967) 383–399.

[141] W. Bollmann, Crystal Defects and Crystalline Interfaces, Springer-Verlag Berlin,

Heidelberg, 1970.

[142] Y. Mout, H.I. Aaronson, 42 (1994) 2133–2144.

[143] Y. Mout, H.I. Aaronson, Acta Metall. Mater. 42 (1994) 2145–2157.

[144] M. Zhang, P.M. Kelly, Scr. Mater. 52 (2005) 963–968.

[145] M.-X. Zhang, P.M. Kelly, Acta Mater. 53 (2005) 1073–1084.

[146] M.-X. Zhang, P.M. Kelly, Acta Mater. 53 (2005) 1085–1096.

[147] J. Yang, J.L. Wang, Y.M. Wu, L.M. Wang, H.J. Zhang, Mater. Sci. Eng. A 460–461 (2007) 296–300.

[148] M. Zhang, W.Z. Zhang, G.Z. Zhu, Scr. Mater. 59 (2008) 866–869.

[149] Z.-Z. Shi, W.-Z. Zhang, X.-F. Gu, Philos. Mag. 92 (2012) 1071–1082.

[150] Z.-Z. Shi, F.Z. Dai, M. Zhang, X.F. Gu, W.Z. Zhang, Metall. Mater. Trans. A Phys. Metall. Mater. Sci. 44 (2013) 2478–2486.

[151] G. Derge, A.R. Kommel, R.F. Mehl, Trans. Metall. Soc. AIME 124 (1937) 367–378.

[152] S. Henes, V. Gerolt, Zeitschrift Für Met. 53 (1962) 743.

[153] C.L. Mendis, K. Oh-ishi, T. Ohkubo, K. Hono, Scr. Mater. 64 (2011) 137–140.

[154] Y.M. Zhu, M. Weyland, N. V Medhekar, C. Dwyer, C.L. Mendis, K. Hono, J.F. Nie, Scr. Mater. 101 (2015) 16–19.

[155] F.R. Elsayed, T.T. Sasaki, C.L. Mendis, T. Ohkubo, K. Hono, Scr. Mater. 68 (2013) 797–800.

[156] X. Nie, Y. Guan, D. Zhao, Y. Liu, J. Gui, J. Appl. Crystallogr. 47 (2014) 1729–1735.

[157] T.T. Sasaki, K. Yamamoto, T. Honma, S. Kamado, K. Hono, Scr. Mater. 59 (2008) 1111–1114.

[158] D.H. Kang, S.S. Park, Y.S. Oh, N.J. Kim, Mater. Sci. Eng. A 449–451 (2007) 318–321.

[159] Y. Kubota, K. Kifune, K. Yamamoto, Thin Solid Films 6090 (1996) 2–6.

[160] J. Sutton, Private Communication, 2016.

[161] C. a Schneider, W.S. Rasband, K.W. Eliceiri, Nat. Methods 9 (2012) 671–675.

[162] H.M. Rietveld, Acta Crystallogr. 22 (1967) 151–152.

[163] Albinati, (n.d.).

[164] R.A. Young, The Rietveld Method, Oxford, 1993.

[165] M.W. Phaneuf, Micron 30 (1999) 277–288.

[166] L.A. Giannuzzi, F.A. Stevie, Micron 30 (1999) 197–204.

[167] L.A. Giannuzzi, F.A. Stevie, Introduction to Focused Ion Beams: Instrumentation, Theory, Techniques and Practice, Springer Science and Business Media, 2005.

[168] D.H. Kang, S.S. Park, N.J. Kim, Mater. Sci. Eng. A 413–414 (2005) 555–560.

[169] T.B. Massalski, H. Okamoto, P.R. Subramanian, Binary Alloy Phase Diagrams, 2nd ed., ASM International, 1990.

[170] M.H. Loretto, R.E. Smallman, Defect Analysis in Electron Microscopy, Chapman & Hall, 1975.

[171] B.C. Zhou, S.L. Shang, Y. Wang, Z.K. Liu, Acta Mater. 103 (2016) 573–586.

[172] S. Ganeshan, L.G.H. Jr, Z. Liu, Acta Mater. 59 (2011) 3214–3228.

[173] G. Nussbaum, P. Sainfort, G. Regazzoni, H. Gjestland, N. Hydro, Scr. Metall. 23 (1989) 1079–1084.

[174] C. Shaw, H. Jones, Mater. Sci. Eng. A 226–228 (1997) 856–860.

[175] L. Gao, R.S. Chen, E.H. Han, J. Alloys Compd. 481 (2009) 379–384.

[176] Z. Li, P. Fu, L. Peng, Y. Wang, H. Jiang, J. Mater. Sci. 48 (2013) 6367–6376.

[177] T.W. Clyne, P.J. Withers, An Introduction to Metal Matrix Composites, Cambridge University Press, Cambridge, 1995.

[178] D. Hull, T.W. Clyne, An Introduction to Composite Materials, Cambridge University Press, Cambridge, 1996.

[179] C.-S. Kim, I. Sohn, M. Nezafati, J.B. Ferguson, B.F. Schultz, Z. Bajestani-Gohari, P.K. Rohatgi, K. Cho, J. Mater. Sci. 48 (2013) 4191–4204.

[180] W.-C. Hu, Y. Liu, X.-W. Hu, D.-J. Li, X.-Q. Zeng, X. Yang, Y.-X. Xu, X. Zeng, K.-G. Wang, B. Huang, Philos. Mag. 95 (2015) 1626–1645.

[181] J.D. Robson, N. Stanford, M.R. Barnett, Acta Mater. 59 (2011) 1945–1956.

[182] J. Robson, Metall. Mater. Trans. A 45A (2014) 5226–5235.

[183] M.R. Ahmadi, E. Povoden-karadeniz, K.I. Öksüz, A. Falahati, E. Kozeschnik, Comput. Mater. Sci. 91 (2014) 173–186.